UC Santa Barbara

UC Santa Barbara Electronic Theses and Dissertations

Title

Illuminating the photophysical effects of light-responsive molecules on fluid properties

Permalink

https://escholarship.org/uc/item/9949b120

Author

Seshadri, Serena

Publication Date

2022

Peer reviewed|Thesis/dissertation

UNIVERSITY OF CALIFORNIA

Santa Barbara

Illuminating the photophysical effects of light-responsive molecules on fluid properties

A dissertation submitted in partial satisfaction of the

requirements for the degree Doctor of Philosophy

in Chemistry

by

Serena Seshadri

Committee in charge:

Professor Javier Read de Alaniz, Co-Chair

Professor Matthew Helgeson, Co-Chair

Professor Megan Valentine

Professor Thuc-Quyen Nguyen

Professor Songi Han

June 2022

The dissertation of Serena Seshadri is approved.

_____

Songi Han

_____

Thuc-Quyen Nguyen

_____

Megan Valentine

_____

Matthew Helgeson, Committee Co-Chair

_____

Javier Read de Alaniz, Committee Co-Chair

March 2022

Illuminating the photophysical effects of light-responsive molecules on fluid properties

ACKNOWLEDGEMENTS

This degree belongs to all of you, as much as it belongs to me. Without the support, and joy I shared with all of you, I would not be half the scientist, artist, advocate and person I am. So much of my strength and my curiosity comes from you.

First, to my advisors Javier and Matt, I thank you for saying "yes". To this day, I'll never know why you took a chance on me boldly and naively walking into your offices proposing an idea. I am eternally grateful for every time you took a chance on me after that moment, letting me take us down some crazy research paths, and trusting my visions. Javier, I thank you for all the times you brainstormed with me, laughed with me, challenged me, pushed me, listened to me. Your mentorship allowed me to flourish both as a scientist and as a human; I owe so much to you. Matt, I thank you for teaching me and giving me confidence to pursue paths well beyond my expertise. Your patience with me as I often stumbled at becoming a ~chemical engineer is something I will always be thankful for.

Getting to work with so many amazing collaborators in chemistry and engineering was my favorite part of the whole thing. Thank you to my collaborators Megan, Elliot, Yangying and Paolo, who were always eager to learn alongside me on these crazy paths! I am grateful to have labmates and collaborators who have shaped me into the scientist I am today and who have become the greatest of friends. Miranda, Fritz, Julie and Yvonne- thank you for teaching me everything I know about DASAs, most importantly to laugh when nothing ever made sense (which was always!).

To my best friends, who are my family, how can I ever thank you enough? I could never in a million years have done this without you. I have had the best time getting to know and love you all; thank you for the joy. Cloe, you have been there every single step of the

way. You've grown with me, inspired me, laughed and cried and danced and protested with me. Thank you will never be enough. Valentina, I smile at all the ways in which you've teased me and fed me and guided me in your "old age." Our friendship is eternal. Maya, my forever person, thank you for being a phone call and a flight away for this whole Ph.D. Your support from afar has kept me grounded more than you could ever imagine, thanks for letting me rant every day. Luke, I can't believe we aren't the same person sometimes; I've loved sharing in moments of childlike excitement with you in research and in life. I would not be as courageous or as silly if it weren't for you. Miya, your compassion and joy has been a rock for me all these years, your support and friendship is the world to me. Timnit, you taught me what it means to hold space for people and to do so with such strength. Sophia, I owe so much of my curiosity and my love of pie to you. Tanvi and Josh, I know that gnomatter what, I can count on you to have my back- you've made me laugh way too much. Asha, I've cherished every ambush facetime all these years, you've inspired so much of my art and my worldview. Iman, thank you for the laughter and for seeing me. Jon, I could not have asked for a better adventure buddy. Cristina and Bella, you taught me so much about community, advocacy and fighting for what matters. To all the other MANY incredible friends I've made along the way, thank you and I love you.

Finally, thank you to my family. My parents, my brother Nilesh- you have been there for it all! My beautiful family from afar, from India to Switzerland to London to New York, I love all of you. Even when you had no idea what any of my papers were about, thank you for pretending to read them and being so very excited for me. Thank you for the relentless love and support, not just now but always, and for shaping me into someone who is creative and curious and for nurturing all those sides of me. This is for you!

VITA OF SERENA SESHADRI
June 2022

EDUCATION

Bachelor of Science in Chemistry and Education, Inquiry and Justice, Georgetown University, May 2017
Doctor of Philosophy in Chemistry, University of California, Santa Barbara, June 2022 (expected)

PROFESSIONAL EMPLOYMENT

Graduate Student Researcher, University of California, Santa Barbara, CA. July 2017 – June 2022

Chemistry Teaching Assistant, University of California, Santa Barbara, CA. September 2017 – June 2018, January-March 2021

Undergraduate Researcher, Georgetown University, Washington, DC. April 2014 – March 2017

Undergraduate Researcher, Drexel University, Philadelphia, PA. June-August 2014.

PUBLICATIONS

Seshadri, S.*, Stricker, F.*, Read de Alaniz, J.R. "Molecular Photoswitches. Chemistry, Properties, and Applications: Donor-Acceptor Stenhouse Adducts." *Molecular Photoswitches: Chemistry, Properties, and Applications* **2022.**

Seshadri, S.; Zhao, L.*; Lang, X.; Baile, S. J.; et al. "Depinning of Multiphase Fluid Using Light and Photo-Responsive Surfactants" *ACS Central Science* **2022.**

Seshadri, S.; Bailey, S. J.; Zhao, L.; Fisher, J.; Sroda, M. M.; Chiu, M.; et al. "Influence of polarity change and photophysical effects of photosurfactant-driven wetting" *Langmuir* **2021**, *37*, 33, 9939-9951.

Sroda, M. M**.;** Lee, J; Kwon, Y.; El-Arid, S.; **Seshadri, S**.; Valentine, M.; Read de Alaniz, J.; et al. "Tunable photothermal actuation enabled by photoswitching of DASAs" *ACS Appl. Mater. Interfaces* **2020**, *12*, 48, 54075-54082.

Seshadri, S.*; Gockowski, L. F.*; Lee, J.; Sroda, M. M**.;** Read de Alaniz, J, et al. "Self-regulating photochemical Rayleigh-Bénard convection using a highly-absorbing organic photoswitch" *Nature Communications*. **2020**, *11*, 2599.

Seshadri, S.*; Sheth, T.*; Prileszky, T.*; Helgeson, M. E. "Multiple nanoemulsions." *Nature Reviews Materials*, **2020**, *5*(3), 214-228.

*authors contributed equally to the work.

AWARDS

Department of Chemistry and Biochemistry Chair's Fellowship, UC Santa Barbara 2021

Mananya Tantiwiwat Fellowship, UC Santa Barbara 2021

FIELDS OF STUDY

Major Field: Photoresponsive fluid systems

Studies in Soft Robots with Professor Elliot Hawkes

Studies in Photothermal Actuation with Professor Megan Valentine

Studies in Microgravity Heat Transfer with Professor Yangying Zhu

Studies in Surfactants with Paolo Luzzatto-Fegiz

ABSTRACT

Illuminating the photophysical effects of light-responsive molecules on fluid properties

by

Serena Seshadri

The question my PhD research aims to answer is how light-responsive molecular switches can be used to develop accessible and versatile actuating materials through the control of fluid properties. Light is one of the most abundant natural resources and presents an opportunity to develop materials that can be controlled remotely, precisely and through both intensity and wavelength. Moreover, light-driven processes, particularly when leveraging visible light, provide clean, accessible methods by which scientific advancement can harness an abundant resource to do work; this is important now more than ever as we seek alternative energy sources to mitigate consumption of natural resources contributing to the global climate crisis.

My research aims to use photoswitches to control fluids by harnessing changes in polarity and absorbance for changes in interfacial tension and temperature, respectively. To accomplish this, we focus on the molecular photoswitches donor–acceptor Stenhouse adducts (DASAs) and spiropyran. Before we can engineer such actuators, it is crucial that we understand the photophysical properties that drive large changes in interfacial tension and temperature in order to most effectively leverage these properties.

First, we developed and synthesized a library of photo-responsive surfactants and provide a comparative study on the influence of polarity change and photophysical effects on wetting at a multiphase interface. Following, we exploit the large change afforded by the photo-responsive surfactants for the depinning of multiphase fluid in microgravity. In this effort, we work to address the challenges associated with boiling in microgravity conditions.

Second, we leverage the photothermal effect to drive self-regulating Rayleigh-Bénard convection and phase change actuation. DASA is especially promising for raising the temperature of a solution due to its negative photochromism and its sensitivity to the environment. We exploit the switching and large change in absorption afforded by DASA molecules upon photoswitching to generate thermal gradients in solution which lead to convection. This convection can be turned on/off based on factors that control the extent of bleaching under irradiation. Furthermore, by tuning the environment using additives, we instill another knob by which we may control the switching kinetics to generate or dissipate heat within a fluid system. Through an understanding of these effects, we work towards the goal of developing actuators that could oscillate under constant irradiation.

The integration of chemistry and engineering principles presented in this work aims to guide future research in both photochemistry and soft materials fields through a consideration of factors that affect and optimize photoswitching within fluid systems to lay foundations for the development of photo-responsive actuator systems.

TABLE OF CONTENTS

I. Introduction

Light is one of the most abundant natural resources and is the source of some of nature's greatest wonders as well as human discoveries. Color, art, photosynthesis and vision represent some of the most extraordinary ways in which light manifests in our everyday lives. This resource has been used by researchers in order to develop profound scientific advancements that rely on the use of light-driven chemical processes most notably in the form of solar energy. Light is highly attractive to scientists as a result of the ability to be controlled remotely and precisely through both intensity and wavelength. Moreover, light-driven processes, particularly when leveraging visible light, provide clean, accessible methods by which scientific advancement can harness an abundant resource to do work; this is important now more than ever as we seek alternative energy sources to mitigate consumption of natural resources contributing to the global climate crisis.

The objective of this work is to use light to control fluid properties such as interfacial tension, heat generation and phase change in order to lay foundations for the development of photo-responsive actuator systems. It is necessary to study these fundamentals before pursuing applications in actuation in order to be able to tune and predict the behaviors that we would anticipate for the development of efficient smart materials. The integration of chemistry and engineering principles presented in this thesis aims to guide future research in both photochemistry and soft materials fields through a thorough consideration of factors that affect and optimize photoswitching within fluid systems.

1.1 Photoswitches

Photochromism – the property to undergo a light-induced reversible change of color based on a chemical reaction – is the basis for the development of many new classes of photochromic molecules such as photoswitches, that undergo a reversible conversion between their stable and metastable isomers triggered by light.[1] Several types of chemical reactions can drive transformation upon light irradiation including *E/Z* isomerization as well as electrocyclizations and cycloadditions. Photoswitches are deemed either positively or negatively photochromic where positive/negative photochromes have an absorption that increases/decreases upon irradiation at the excitation wavelength, respectively.[2] Photoswitches are also defined as P- or T-type by their relaxation mechanism; where T-type photoswitches thermally revert to their original form, while P-type photoswitches require an additional excitation wavelength to revert to their original form. The most commonly used photoswitch is azobenzene[3,4], a T-type switch which typically undergoes a *trans-cis* isomerization under UV irradiation. In addition to azobenzenes, photoswitches such as spiropyrans (T-type) [5–7], diarylethenes (P-type) [8,9] and more recently donor-acceptor Stenhouse adducts (DASA)[10] are commonly used photoswitchable molecules. This thesis will primarily focus on spiropyran and DASA-based systems.
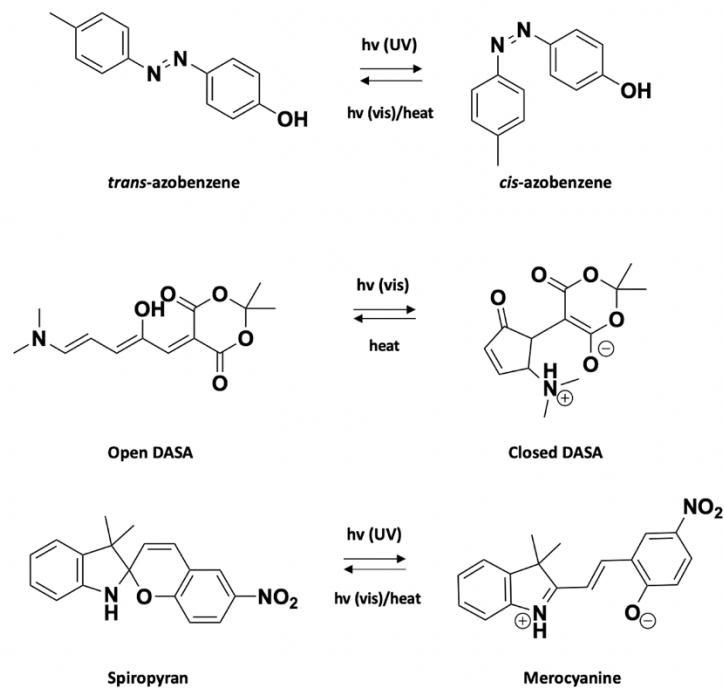
Figure 1.1 Common molecular photoswitches: azobenzene, DASA and spiropyran and the reversible conformational changes.

1.2 Spiropyran

One of the most widely studied photoswitches is spiropyran; under irradiation with UV light, spiropyran undergoes an electrocyclization leading to ring opening via carbon-oxygen bond cleavage, followed by *Z/E* isomerization. This process converts the initially clear, closed-ring spiropyran molecule to a colored, zwitterionic or quinoidal merocyanine structure (**Figure 2**).[5] With the electrocyclization comes a particularly large change in polarity as the merocyanine form is charged compared to the neutral spiropyran. The merocyanine can exist as both the zwitterionic MC form and the protonated MCH+ form

dependent on the environment. [11] In most non-polar solvents, the quinoidal form is stabilized such that the λ_{max} of the MC is 500-600 nm. In the presence of polar media, the merocyanine form becomes protonated, leading to a shift to around 400 nm.
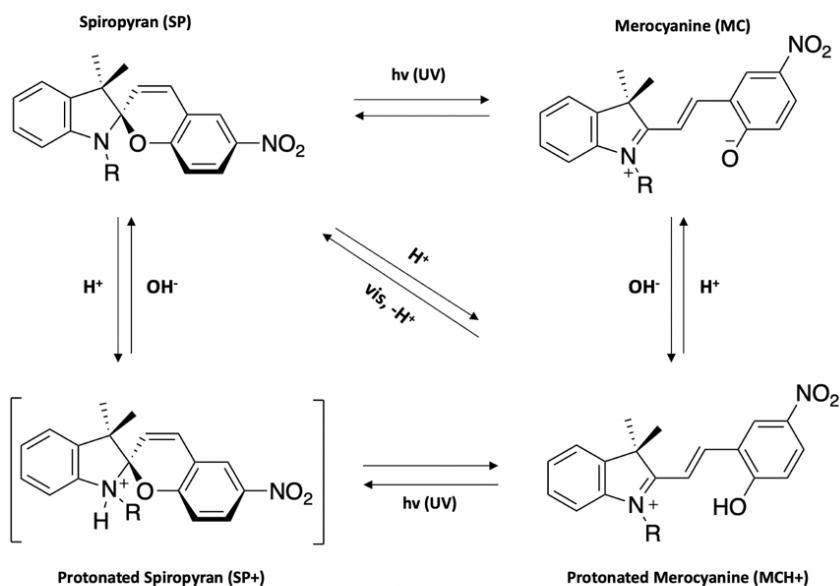
Figure 1.2 Switching mechanism of spiropyran. Different isomeric states are accessed via different stimuli.

One unique element of spiropyran is the fact that multiple stimuli can be used in order to drive the reversible conversion between SP and MC including salts, temperature, acids and bases, redox potential and mechanical force.[5,12] The versatility of the switch has led to an exciting and widespread use of spiropyran molecules for applications that extend beyond its photoswitching capabilities such as the control of optical properties, expansion of hydrogels, control of wetting amongst others. The multitude of stimuli, however, can also present several challenges in maintaining the stability of the switch in a desired form under simultaneous co-existing environmental conditions. Another challenge with the use of

spiropyran is degradation due to its tendency toward hydrolysis resulting in low fatigue resistance. Additionally, the use of UV light is harmful and prevents applications in biology; as such, recent work has looked toward the stabilization of merocyanine which can be converted to spiropyran upon irradiation with visible light and allows for solubility in aqueous environments.

1.2.1 Applications of spiropyran

The SP and MC isomers differ drastically in their properties; the color, dielectric, volume and solubility differences result in a number of widespread uses of both spiropyran and merocyanine isomers. Many of the applications of spiropyran have taken advantage of the large change in polarity in order to develop systems that can change solubilities and aggregation, as well as leverage a potentially large disruption in interfacial stability.[12–21] Spiropyran-functionalized polymeric materials have been developed for use in fluorescence, micellar disassembly, ion complexation as well as photo-control of transport through microfluidic systems. Spiropyran has also been used to functionalize biopolymers to influence polypeptide formation, protein folding and DNA hybridization using light.[5] The many applications of spiropyran in biological, organic and inorganic chemistry fields indicate the impressive nature of this photoswitch and its fast-growing impact on science.
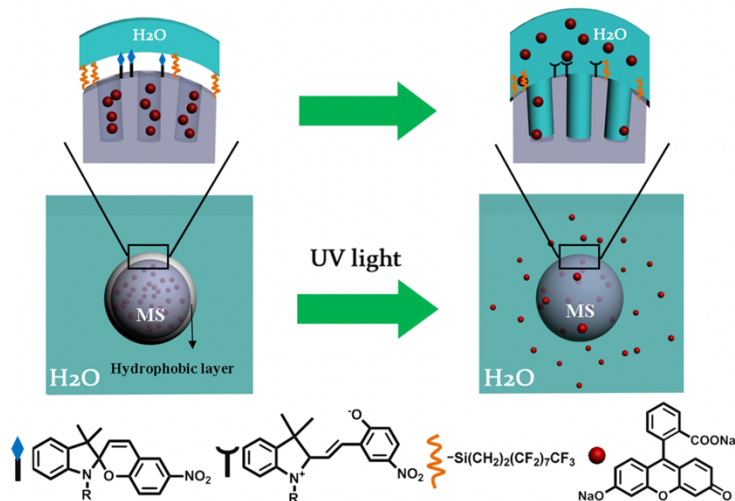
Figure 1.3 Example of a light-responsive release system of spiropyran-based materials. In this work, the outer surface of the nanoparticle was functionalized with spiropyran and perfluorodecyltriethoxysilane to prevent the surface from being wetted by water and block the loaded cargos. After irradiation with 365 nm UV light, the surface became wetted upon conversion of spiropyran to merocyanine and released the encapsulated fluorescein disodium molecules from the pores. This figure is reproduced with permission from Chen et al. [13]

1.3 Donor-Acceptor Stenhouse Adducts

One newly developed class of photoswitch is of particular interest for this work due to its multitude of advantageous properties including its activation by visible light and negative photochromism. Donor-acceptor Stenhouse adducts (DASA) are an emerging class of negatively photochromic photoswitches first reported by the Read de Aleniz group in 2014 (**Figure 4**) [22] whose history dates back hundreds of years to early discoveries in 1850.[23] Despite pioneering reports by Stenhouse and Schiff [24], it would take nearly a century before their photochromic properties were investigated by Honda in 1982 and more thoroughly understood by the Read de Aleniz group.[25]

DASA-based photochromes are easily synthesized and synthetically tunable. They are derived from a modular two-step synthesis using abundant furfural activated with carbon acid acceptor moieties via a Knoevenagel condensation. Subsequently, a secondary amine nucleophile initiates a ring opening reaction of the activated furan core, resulting in the visible light responsive DASA photochrome. This modularity allows straightforward design of DASA photochromes, and has played a major role in the rapid exploration of this new class of photochromic material and the development of three generations of DASA since 2014.

This first generation of DASA was originally based on the strongly nucleophilic dialkylamines and relatively weak electron withdrawing acceptor groups (e.g., Meldrum's acid and barbituric acid). When the dialkylamine possesses groups larger than ethyl they can suffer from a number of drawbacks including limited range of solvents that they undergo efficient switching.[22] More recently, improved photochromic performance of first generation DASA has been achieved by modifying the steric properties of the donor sidechains using asymmetric alkylamines[26]. In 2016, a second generation DASA was introduced with weaker electron donating arylamines (N-methylaniline and indoline derivatives) to address a range of shortcomings of the first generation including wavelength tuneability, low photostationary state, higher solvent compatibility, and solid-state switching.[27] Despite improved photoswitching properties, the arylamines also introduced several drawbacks, most notably compromised thermodynamic (~50–7% open form in the absence of light). As a result, a third generation was developed in 2018 which introduced new classes of more

electron-withdrawing acceptor moieties to overcome the drawbacks while maintaining the improvements of the second generation most notably by improving thermal equilibria.[28]
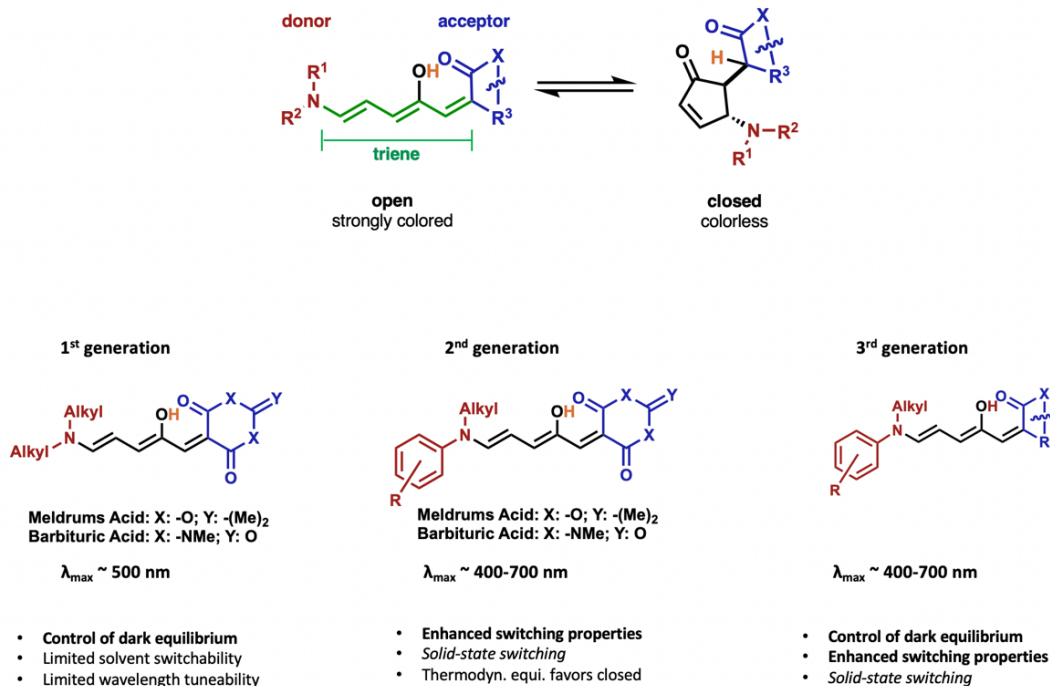
Figure 1.4. Three generations of DASA photochromes and the isomerization induced by visible light. Adapted from book chapter in Molecular Photoswitches: Chemistry, Properties, and Applications.

All DASA molecules share a general architecture with a triene backbone bearing a hydroxy group in the C2-position, an electron withdrawing carbon acid acceptor and an electron donating secondary amine at the terminal end (**Figure 3**) and undergo a conformational switch upon irradiation with visible light. The underlying mechanism of DASA photochromes is rather complicated and has been extensively studied by Feringa, Martinez, our group and coworkers.[29–35] The currently proposed mechanism consists of an actinic step followed by a series of thermal steps to fully transition from the colored "open"

form to the colorless "closed" isomer. The switching kinetics as well as the mechanism are

highly dependent on several factors including the DASA architecture, the surrounding

environment as well as the concentration. Each of these factors can be tuned in order to

highlight specific properties of DASA and have opened the door for a number of

applications for sensing,[36–41] wettability[42–45] and wavelength selectivity[46–51] amongst others.
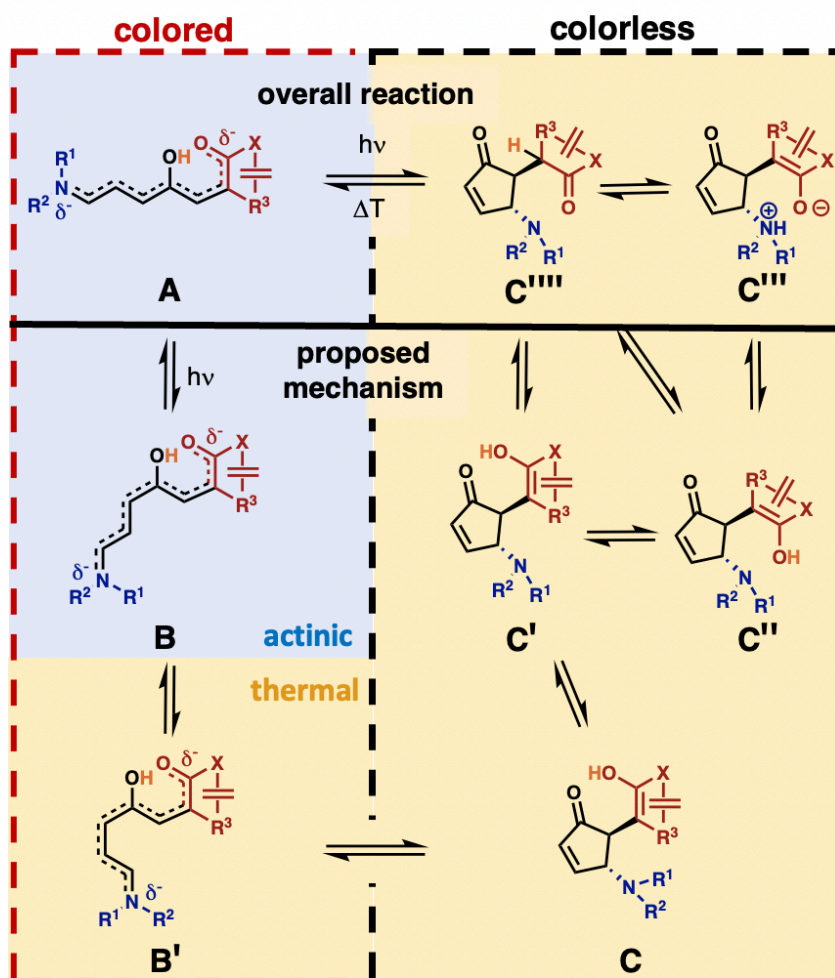
Figure 1.0-5. Proposed photoswitching mechanism of donor–acceptor Stenhouse adducts. Adapted from book chapter.

1.3.1 Applications of DASA

DASA's unique photoswitching properties enable applications primarily based on properties such as high degree of polarity change, high extinction coefficients (>100,000 $M^{-1}cm^{-1}$) as well as a large change in spectral absorption. One of the most promising properties of DASA photochromes is their activation by visible light; the benign properties and easy accessibility of long wavelength light make the wide range of wavelength tunability of DASA especially desirable for biomedical and material applications. Different from spiropyran, this response to visible light and the negative photochromism allows for more light penetration and mitigation of harmful side effects of using UV irradiation. Polarity change presents one of the primary properties of DASA that has been harnessed for practical applications as the control of wettability has potential practical applications in stimuli responsive materials and the ability to selectively direct adhesion and deadhesion.[42–45,52–54] The conformational change of DASA from an open form that is neutral or slightly polar to a highly polar, often zwitterionic closed form upon irradiation leads to a drastic and reversible polarity change, that is ideal for a range of applications including drug delivery, wettability, photopatterning, sensing, microfluidics and actuation. Further applications in engineering and materials fields require deeper understanding of factors such as concentration and role of the to produce favorable properties of DASA for exploitation in applications.

1.4 Light driven control over fluid systems

The control over fluid systems broadly encompasses a number of important applications in industry. Liquid motion as well as the motion of droplets in both liquid and solid systems is highly important for fields that rely on fluid pumping as well as droplet migration. Recently, light has been recognized as a formidable tool for non-invasive, wavelength-selective, remote control over liquid motion with high spatial and temporal resolution. Recent studies have sought to harness light energy for mixing[55,56], particle arrangement[57,58], and actuation[56,59,60] in solution. Typical systems for such applications make use of photothermal plasmonic nanoparticles and complex nanostructures[58,61–64], electrochemically activated substrates[65,66], or rely on interfacial control to drive fluids.[67–70] Manipulation of interfacial properties by external stimuli allows for the control of droplets and particles at air/water[70–74] and solid/liquid[75–77] interfaces, emulsion and micelle aggregation and separation,[78–82] and foams[83,84]. For this reason, photoswitches and light-responsive materials are highly attractive in order to provide tailored methods of fluid control for a range of applications. We explore in the following chapters methods by which photo-responsive surfactants can be designed, synthesized, and optimized within fluid systems for the control of wetting and actuation.
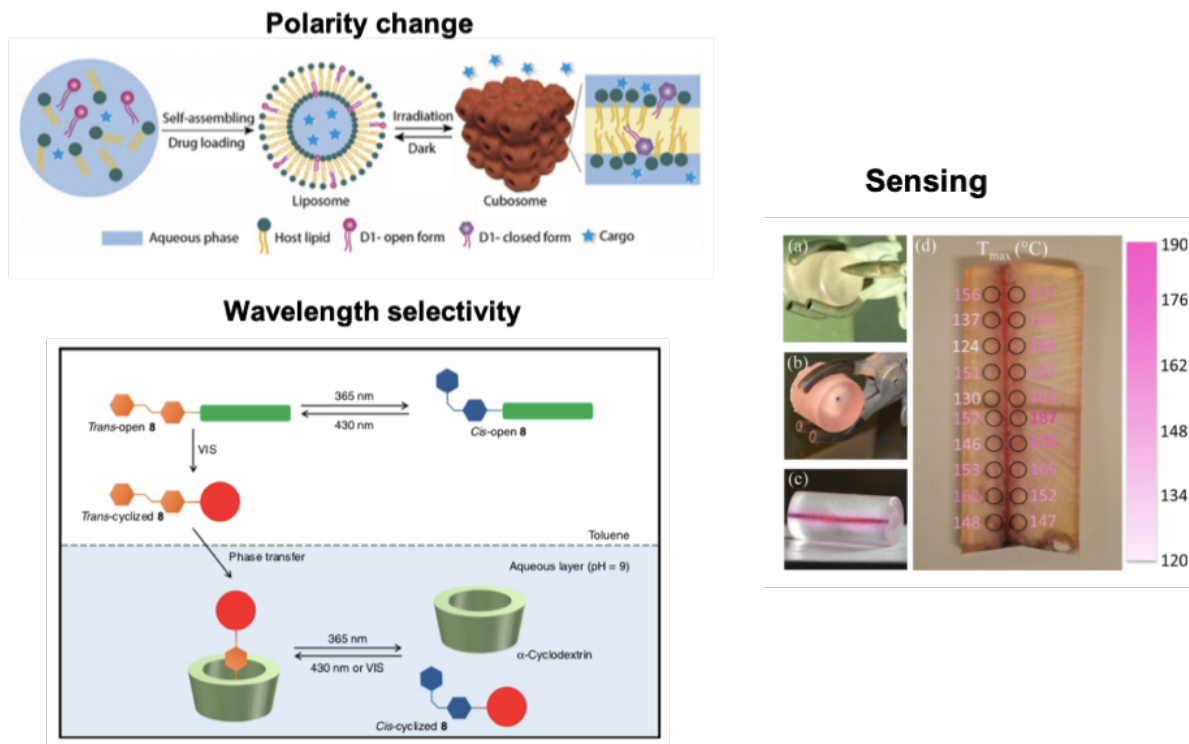
Figure 1.0-6. Illustrative applications that leverage the photophysical properties of DASA. DASA is shown in these examples in a) liquid crystal nanocarriers used for drug delivery,[43] b) orthogonal wavelength selective molecular systems,[85] c) thermochromic sensor.[41] Images were adapted with permission.

1.5 Photothermal driven processes

The photothermal effect involves the excitation of a material using light to generate thermal energy. Common photothermal agents include dyes, carbon-based materials and nanoparticles due to their ability to efficiently convert light energy to heat.[61–66] Photoswitches have rarely been utilized for their photothermal capabilities as many of the commonly used photoswitches are not very efficient photothermal agents and possess positive photochromic properties (i.e., are colored in both states). As such, they do not offer an advantage over commonly used dyes. However, the negatively photochromic nature of DASA opens the space for its use in generating heat as well as thermal gradients when

coupled to switching kinetics. The highly colored, thermodynamically stable state is a great photothermal agent but upon switching it is colorless. The absorption shift that results from the switch leads to the photothermal properties being extinguished. For negative photoswitches such as DASA the reversibility and tunability allow for control over the degree of switching and therefore heat generation.

The photothermal effect leads to advanced opportunities for generating work through photo-actuation.[86–88] Photothermal actuation can be a powerful tool in both solid and liquid networks- the former of which has been explored to generate deformation due to local temperature changes that enable macroscopic motion. Most recently, the spectral change of DASA has been utilized to elicit a photothermal gradient for the purpose of actuation. This has been studied and presented in Chapter 4 and 5 of this work in fluid systems, which enabled further work in thin films to create self-actuating materials that can lift weight against gravity, as well as a simple light-powered crawler that exploits photothermal energy conversion. Control of the magnitude of actuation is achieved by slowly converting a highly-absorbing DASA photochrome into a non-absorbing form upon irradiation. These examples mark the first uses of DASA towards photothermal actuation and invite further investigation into other applications. I seek with this work to leverage the photochemical and photothermal properties of DASA to enable actuation in materials that might eventually be accomplished in sunlight so as to develop widely accessible solutions to universal challenges. These topics will be further explored in this dissertation with the aims of better understanding DASA molecules' role in generating and dissipating heat with the goal of developing soft robotic actuating systems.

1.6 References

1. Fritzsche, M. Note sur les carbures d'hydrogene solides, tires du goudron de houille. *C. R. Acad. Sci.* **69**, (1867).

2. Bouas-Laurent, H. & Dürr, H. *INTERNATIONAL UNION OF PURE AND APPLIED CHEMISTRY ORGANIC CHEMISTRY DIVISION COMMISSION ON PHOTOCHEMISTRY* ORGANIC PHOTOCHROMISM (IUPAC Technical Report) Organic photochromism (IUPAC Technical Report). Pure Appl. Chem* vol. 73 (2001).

3. Bandara, H. M. D. & Burdette, S. C. Photoisomerization in different classes of azobenzene. *Chemical Society Reviews* **41**, 1809–1825 (2012).

4. Birnbaum, P. P. & Style, D. W. G. The photo-isomerization of some azobenzene derivatives. *Transactions of the Faraday Society* **50**, 1192–1196 (1954).

5. Klajn, R. Spiropyran-based dynamic materials. *Chemical Society Reviews* **43**, 148–184 (2014).

6. Minkin, V. I. Photo-, thermo-, solvato-, and electrochromic spiroheterocyclic compounds. *Chemical Reviews* **104**, 2751–2776 (2004).

7. Berkovic, G., Krongauz, V. & Weiss, V. Spiropyrans and Spirooxazines for Memories and Switches. *Chemical Reviews* **100**, 1741–1753 (2000).

8. Irie, M. Photochromism of diarylethene molecules and crystals. *Proceedings of the Japan Academy Series B: Physical and Biological Sciences* vol. 86 472–483 (2010).

9. Matsuda, K. & Irie, M. Diarylethene as a photoswitching unit. *Journal of Photochemistry and Photobiology C: Photochemistry Reviews* **5**, 169–182 (2004).

10. Helmy, S., Oh, S., Leibfarth, F. A., Hawker, C. J. & Read De Alaniz, J. Design and synthesis of donor-acceptor stenhouse adducts: A visible light photoswitch derived from furfural. *Journal of Organic Chemistry* **79**, 11316–11329 (2014).

11. Swansburg, S., Buncel, E. & Lemieux, R. P. Thermal racemization of substituted indolinobenzospiropyrans: Evidence of competing polar and nonpolar mechanisms. *Journal of the American Chemical Society* **122**, 6594–6600 (2000).

12. Kortekaas, L. & Browne, W. R. The evolution of spiropyran: Fundamentals and progress of an extraordinarily versatile photochrome. *Chemical Society Reviews* vol. 48 3406–3424 (2019).

13. Chen, L. *et al*. A light-responsive release platform by controlling the wetting behavior of hydrophobic surface. *ACS Nano* **8**, 744–751 (2014).

14. Son, S., Shin, E. & Kim, B. S. Light-responsive micelles of spiropyran initiated hyperbranched polyglycerol for smart drug delivery. *Biomacromolecules* **15**, 628–634 (2014).

15. Kessler, D., Jochum, F. D., Choi, J., Char, K. & Theato, P. Reactive surface coatings based on polysilsesquioxanes: Universal method toward light-responsive surfaces. *ACS Applied Materials and Interfaces* **3**, 124–128 (2011).

16. Rosario, R. *et al*. Photon-modulated wettability changes on spiropyran-coated surfaces. *Langmuir* **18**, 8062–8069 (2002).

17. Vlassiouk, I., Park, C. do, Vail, S. A., Gust, D. & Smirnov, S. Control of nanopore wetting by a photochromic spiropyran: A light-controlled valve and electrical switch. *Nano Letters* **6**, 1013–1017 (2006).

18.   Zhu, M. Q. *et al*. Spiropyran-based photochromic polymer nanoparticles with optically switchable luminescence. *Journal of the American Chemical Society* **128**, 4303–4309 (2006).

19.   Edahiro, J. I., Sumaru, K., Takagi, T., Shinbo, T. & Kanamori, T. Photoresponse of an aqueous two-phase system composed of photochromic dextran. *Langmuir* **22**, 5224–5226 (2006).

20.   Ipe, B. I., Mahima, S. & Thomas, K. G. Light-induced modulation of self-assembly on spiropyran-capped gold nanoparticles: A potential system for the controlled release of amino acid derivatives. *Journal of the American Chemical Society* **125**, 7174–7175 (2003).

21.   Li, C., Iscen, A., Palmer, L. C., Schatz, G. C. & Stupp, S. I. Light-Driven Expansion of Spiropyran Hydrogels. *Journal of the American Chemical Society* **142**, 8447–8453 (2020).

22.   Helmy, S., Oh, S., Leibfarth, F. A., Hawker, C. J. & Read De Alaniz, J. Design and synthesis of donor-acceptor stenhouse adducts: A visible light photoswitch derived from furfural. *Journal of Organic Chemistry* **79**, 11316–11329 (2014).

23.   Stenhouse, J. Ueber die Oele, die bei der Einwirkung der Schwefel-. *Justus LIebigs Annalen der Chemie* **74**, 278–297 (1850).

24.   Schiff, H. Ueber Farbstoff basen. *Justus LIebigs Annalen der Chemie* **239**, 349–385 (1887).

25.   Honda, K., Komizu, H. & Kawasaki, M. *Reverse Photochromism of Stenhouse Salts*. *J. CHEM. SOC., CHEM. COMMUN*.

26.   Mallo, N. *et al*. Structure-function relationships of donor-acceptor Stenhouse adduct photochromic switches. *Chemical Science* **9**, 8242–8252 (2018).

27.   Hemmer, J. R. *et al*. Tunable Visible and Near Infrared Photoswitches. *Journal of the American Chemical Society* **138**, 13960–13966 (2016).

28.   Hemmer, J. R. *et al*. Controlling Dark Equilibria and Enhancing Donor-Acceptor Stenhouse Adduct Photoswitching Properties through Carbon Acid Design. *Journal of the American Chemical Society* **140**, 10425–10429 (2018).

29.   Zulfikri, H. *et al*. Taming the complexity of donor-acceptor stenhouse adducts: Infrared motion pictures of the complete switching pathway. *Journal of the American Chemical Society* **141**, 7376–7384 (2019).

30.   Lerch, M. M., Wezenberg, S. J., Szymanski, W. & Feringa, B. L. Unraveling the Photoswitching Mechanism in Donor-Acceptor Stenhouse Adducts. *Journal of the American Chemical Society* **138**, 6344–6347 (2016).

31.   Lerch, M. M. *et al*. Tailoring Photoisomerization Pathways in Donor-Acceptor Stenhouse Adducts: The Role of the Hydroxy Group. *Journal of Physical Chemistry A* **122**, 955–964 (2018).

32.   di Donato, M. *et al*. Shedding Light on the Photoisomerization Pathway of Donor-Acceptor Stenhouse Adducts. *Journal of the American Chemical Society* **139**, 15596–15599 (2017).

33.   Lerch, M. M. *et al*. Solvent Effects on the Actinic Step of Donor–Acceptor Stenhouse Adduct Photoswitching. *Angewandte Chemie - International Edition* **57**, 8063–8068 (2018).

34. Sroda, M. M., Stricker, F., Peterson, J. A., Bernal, A. & Read de Alaniz, J. Donor–Acceptor Stenhouse Adducts: Exploring the Effects of Ionic Character. *Chemistry - A European Journal* **27**, 4183–4190 (2021).

35. Sanchez, D. M., Raucci, U., Ferreras, K. N. & Martínez, T. J. Putting Photomechanical Switches to Work: An Ab Initio Multiple Spawning Study of Donor-Acceptor Stenhouse Adducts. *Journal of Physical Chemistry Letters* **11**, 7901–7907 (2020).

36. Diaz, Y. J. *et al.* A Versatile and Highly Selective Colorimetric Sensor for the Detection of Amines. *Chemistry - A European Journal* **23**, 3562–3566 (2017).

37. Chen, Q. *et al.* Stable Activated Furan and Donor-Acceptor Stenhouse Adduct Polymer Conjugates as Chemical and Thermal Sensors. *Macromolecules* **52**, 4370–4375 (2019).

38. Cai, Y. de, Chen, T. Y., Chen, X. Q. & Bao, X. Multiresponsive Donor-Acceptor Stenhouse Adduct: Opportunities Arise from a Diamine Donor. *Organic Letters* **21**, 7445–7449 (2019).

39. Balamurugan, A. & Lee, H. il. A Visible Light Responsive On-Off Polymeric Photoswitch for the Colorimetric Detection of Nerve Agent Mimics in Solution and in the Vapor Phase. *Macromolecules* **49**, 2568–2574 (2016).

40. Yang, S. *et al.* Fluorescent photochromic donor-acceptor Stenhouse adduct controlled by visible light. *Dyes and Pigments* **148**, 341–347 (2018).

41. Mason, B. P. *et al.* A temperature-mapping molecular sensor for polyurethane-based elastomers. *Applied Physics Letters* **108**, (2016).

42. Zhao, H. *et al.* Surface with Reversible Green-Light-Switched Wettability by Donor–Acceptor Stenhouse Adducts. *Langmuir* **34**, 15537–15543 (2018).

43. Jia, S., Tan, A., Hawley, A., Graham, B. & Boyd, B. J. Visible light-triggered cargo release from donor acceptor Stenhouse adduct (DASA)-doped lyotropic liquid crystalline nanoparticles. *Journal of Colloid and Interface Science* **548**, 151–159 (2019).

44. Mostafavi, S. H. *et al.* Photoinduced Deadhesion of a Polymer Film Using a Photochromic Donor-Acceptor Stenhouse Adduct. *Macromolecules* **52**, 6311–6317 (2019).

45. Poelma, S. O. *et al.* Controlled drug release to cancer cells from modular one-photon visible light-responsive micellar system. *Chemical Communications* **52**, 10525–10528 (2016).

46. Hansen, M. J., Velema, W. A., Lerch, M. M., Szymanski, W. & Feringa, B. L. Wavelength-selective cleavage of photoprotecting groups: strategies and applications in dynamic systems. *Chem. Soc. Rev.* **44**, 3358–3377 (2015).

47. Rufaie-Gragan 2018 JACS Wavelength-Selective Light-Responsive DASA-Functionalized Polymersome Nanoreactors.

48. Sinawang, G., Wu, B., Wang, J., Li, S. & He, Y. Polystyrene Based Visible Light Responsive Polymer with Donor–Acceptor Stenhouse Adduct Pendants. *Macromolecular Chemistry and Physics* **217**, 2409–2414 (2016).

49. Singh, S. *et al.* Spatiotemporal Photopatterning on Polycarbonate Surface through Visible Light Responsive Polymer Bound DASA Compounds. *ACS Macro Letters* **4**, 1273–1277 (2015).

50. Tang, F. Y. *et al*. A facile way to achieve all-photonic logic functions and photo-printing based on a donor-acceptor Stenhouse adduct. *New Journal of Chemistry* **41**, 6071–6075 (2017).

51. Ulrich, S. *et al*. Visible Light-Responsive DASA-Polymer Conjugates. *ACS Macro Letters* **6**, 738–742 (2017).

52. Chen, Y. *et al*. Visible Light-Controlled Inversion of Pickering Emulsions Stabilized by Functional Silica Microspheres. *Langmuir* **34**, 2784–2790 (2018).

53. Jia, S. *et al*. Investigation of Donor-Acceptor Stenhouse Adducts as New Visible Wavelength-Responsive Switching Elements for Lipid-Based Liquid Crystalline Systems. *Langmuir* **33**, 2215–2221 (2017).

54. Senthilkumar, T. *et al*. Conjugated Polymer Nanoparticles with Appended Photo-Responsive Units for Controlled Drug Delivery, Release, and Imaging. *Angewandte Chemie* **130**, 13298–13303 (2018).

55. Liu, G. L., Kim, J., Lu, Y. U. & Lee, L. P. Optofluidic control using photothermal nanoparticles. *Nature Materials* **5**, 27–32 (2006).

56. Baigl, D. Photo-actuation of liquids for light-driven microfluidics: State of the art and perspectives. *Lab on a Chip* **12**, 3637–3653 (2012).

57. Palacci, J., Sacanna, S., Steinberg, A. P., Pine, D. J. & Chaikin, P. M. Colloidal Surfers. *Science* **339**, 936–939 (2013).

58. Esplandiu, M. J., Farniya, A. A. & Bachtold, A. Silicon-Based Chemical Motors : An E ffi cient Pump for Triggering and Guiding Fluid Motion Using Visible Light. 11234–11240 (2015) doi:10.1021/acsnano.5b04830.

59. Xu, L., Mou, F., Gong, H., Luo, M. & Guan, J. Light-driven micro/nanomotors: From fundamentals to applications. *Chemical Society Reviews* **46**, 6905–6926 (2017).

60. Luo, J. *et al*. Recent advances of light-driven micro/nanomotors: toward powerful thrust and precise control. *Nanotechnology Reviews* **7**, 555–581 (2018).

61. Tansi, B. M., Peris, M. L., Shklyaev, O. E., Balazs, A. C. & Sen, A. Organization of Particle Islands through Light-Powered Fluid Pumping. *Angewandte Chemie - International Edition* **58**, 2295–2299 (2019).

62. Li, W., Wu, X., Qin, H., Zhao, Z. & Liu, H. Light-Driven and Light-Guided Microswimmers. *Advanced Functional Materials* **26**, 3164–3171 (2016).

63. Li, M., Su, Y., Zhang, H. & Dong, B. Light-powered direction-controlled micropump. *Nano Research* **11**, 1810–1821 (2018).

64. Hong, Y., Diaz, M., Córdova-Fteueroa, U. M. & Sen, A. Light-driven titanium-dioxide-based reversible microfireworks and micromotor/micropump systems. *Advanced Functional Materials* **20**, 1568–1576 (2010).

65. Ndukaife, J. C. *et al*. Photothermal heating enabled by plasmonic nanostructures for electrokinetic manipulation and sorting of particles. *ACS Nano* **8**, 9035–9043 (2014).

66. Williams, S. J., Kumar, A., Green, N. G. & Wereley, S. T. A simple, optically induced electrokinetic method to concentrate and pattern nanoparticles. *Nanoscale* **1**, 133–137 (2009).

67. Santer, S. Remote control of soft nano-objects by light using azobenzene containing surfactants. *Journal of Physics D: Applied Physics* **51**, (2018).

68. Feldmann, D. *et al*. Manipulation of small particles at solid liquid interface: Light driven diffusioosmosis. *Scientific Reports* **6**, 1–10 (2016).

69. Jadhav, A. D. *et al.* Photoresponsive microvalve for remote actuation and flow control in microfluidic devices. *Biomicrofluidics* **9**, 1–12 (2015).

70. Diguet, A. *et al.* Photomanipulation of a droplet by the chromocapillary effect. *Angewandte Chemie - International Edition* **48**, 9281–9284 (2009).

71. Kotz, K. T., Noble, K. A. & Faris, G. W. Optical microfluidics. *Applied Physics Letters* **85**, 2658–2660 (2004).

72. Florea, L. *et al.* Photo-chemopropulsion-light-stimulated movement of microdroplets. *Advanced Materials* **26**, 7339–7345 (2014).

73. Xiao, Y. *et al.* Droplets: Moving Droplets in 3D Using Light (Adv. Mater. 35/2018). *Advanced Materials* **30**, 1870259 (2018).

74. Ji, W., Li, W., Wang, Y. & Lan, D. Tunable Spreading and Shrinking on Photocontrolled Liquid Substrate. *ACS Omega* **4**, 21967–21974 (2019).

75. Lv, C., Varanakkottu, S. N., Baier, T. & Hardt, S. Controlling the Trajectories of Nano/Micro Particles Using Light-Actuated Marangoni Flow. *Nano Letters* **18**, 6924–6930 (2018).

76. Varanakkottu, S. N. *et al.* Particle manipulation based on optically controlled free surface hydrodynamics. *Angewandte Chemie* **52**, 7291–7295 (2013).

77. Pan, S., Guo, R. & Xu, W. Photoresponsive superhydrophobic surfaces for effective wetting control. *Soft Matter* **10**, 9187–9192 (2014).

78. Tabor, R. F. *et al.* Reversible light-induced critical separation. *Soft Matter* **5**, 78–80 (2009).

79. Eastoe, J. *et al.* Photo-stabilised microemulsions. *Chemical Communications* 2785–2786 (2005) doi:10.1039/b503379a.

80. Eastoe, J., Dominguez, M. S., Wyatt, P. & Heenan, R. K. A photo-responsive organogel. *Chem. commun.* **22**, 2608–2609 (2004).

81. Vesperinas, A., Eastoe, J., Jackson, S. & Wyatt, P. Light-induced flocculation of gold nanoparticles. *Chemical Communications* 3912–3914 (2007) doi:10.1039/b710502a.

82. McCoy, T. M., Liu, A. C. Y. & Tabor, R. F. Light-controllable dispersion and recovery of graphenes and carbon nanotubes using a photo-switchable surfactant. *Nanoscale* **8**, 6969–6974 (2016).

83. Chevallier, E., Saint-Jalmes, A., Cantat, I., Lequeux, F. & Monteux, C. Light induced flows opposing drainage in foams and thin-films using photosurfactants. *Soft Matter* **9**, 7054–7060 (2013).

84. Mamane, A., Chevallier, E., Olanier, L., Lequeux, F. & Monteux, C. Optical control of surface forces and instabilities in foam films using photosurfactants. *Soft Matter* **13**, 1299–1305 (2017).

85. Lerch, M. M., Hansen, M. J., Velema, W. A., Szymanski, W. & Feringa, B. L. Orthogonal photoswitching in a multifunctional molecular system. *Nature Communications* **7**, (2016).

86. Gelebart, A. H., Vantomme, G., Meijer, E. W. & Broer, D. J. Mastering the Photothermal Effect in Liquid Crystal Networks: A General Approach for Self-Sustained Mechanical Oscillators. *Advanced Materials* **29**, (2017).

87. Lee, J. *et al.* Programmable Bilayer Actuator Driven by Visible Light Using Donor – Acceptor Stenhouse Adducts. 1–8.

88. Wani, O. M., Zeng, H. & Priimagi, A. A light-driven artificial flytrap. *Nature Communications* **8**, 1–7 (2017).

2. Motivation for the development of photo-responsive surfactants

Abstract

Many challenges arise in the control of fluid systems through remote, benign actuation that also allow for spatial control. This chapter establishes the goals and motivation of the work presented in this dissertation. The motivation behind the light-driven control of fluid properties originates with our desire to control complex nanoemulsion system for the release of an internal cargo. Here we present the importance of emulsions and nanoemulsions as well as the potential for use of light in these systems. Stimuli responsive surfactants, particularly those responding to light, open up numerous applications and modes by which fluid properties can be tuned and tailored. This chapter was adapted with permission from *Nature Review Materials*. **2020**, 5, 2014-228, copyright 2020 Nature and *Langmuir*. **2021**, 37 (33), 9939-9951. Copyright 2021 American Chemical Society.

2.1. Introduction

The motivation for this work begins with the desire to control complex fluid systems using light. Generally, manipulation of interfacial properties by external stimuli allows for the control of aggregation and separation,[1–5] and stability of foams[6,7]. While this type of control is currently accomplished in a number of ways using light,[8–14] heat,[15] magnetism[16,17] and electrochemistry, light is particularly attractive because it is inexpensive, environmentally benign and widely accessible. Moreover, its tunable intensity, wavelength and spatial patterning make light a versatile input for multiplexing and remote control of interfacial fluid properties and behavior. Specifically, we sought to control the stability of nanoemulsions using light to induce droplet breakup or coalescence, and release of an internal cargo. While light has been used in numerous studies to drive micellar and droplet breakup, it has never been used to destabilize nanoemulsions. The structural and chemical uniformity of emulsions facilitates their production; however, this simplicity also limits the scope of their applications while nanoemulsions offer exciting and complex avenues for control which we aim to exploit using light.

2.2 Colloidal systems

Emulsions are highly versatile liquid composites commonly used across a range of industries and applications. For example, in cosmetic, food and pharmaceutical products, emulsions provide a dispersible platform to solubilize active ingredients and flavor compounds, while maintaining desirable mechanical properties.[2,18] Emulsions are indispensable in agriculture because of their ability to wet plant surfaces for effective

administration of pesticide formulations[4]. The utility of emulsions extends beyond the scale of single droplets: dense emulsions form continuous interfacial networks that can serve as templates for porous materials and surfactant structures can impart shape and internal structure to inorganic materials. These templating schemes — whether forming a structure using the emulsion directly or a material templated from it — take advantage of the structural flexibility and chemical versatility of emulsions, which are absent in other colloids.

Recently, it has been recognized that nanoemulsions have unique properties that make them more versatile than other emulsion systems. Nanoemulsions consist of droplets 100 nm or smaller in diameter of immiscible liquids stabilized by surface-active materials. Although similar to microemulsions in size and appearance, they are distinguished by their stability: microemulsions are indefinitely stable thermodynamic phases, whereas nanoemulsions are transient, kinetically stable structures that slowly evolve towards two macroscopic phases. The small dimensions of nanoemulsions, however, yield remarkably high kinetic stability[8]. This metastability can be advantageous: by removing the thermodynamic restrictions that limit the composition space of microemulsions, nanoemulsions can be functionalized with more diverse and greater amounts of additives. Accordingly, nanoemulsions have potential applications ranging from medicinal-delivery vectors[9] to new material templates[10], for which it is important to add a large fraction of a functional compound to the dispersed phase of the emulsion without compromising its stability or other properties.
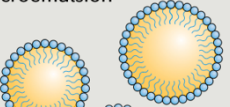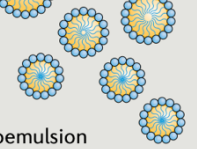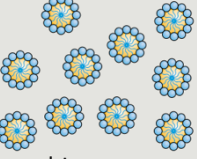
Emulsion type	Size	Stability	Requirements
Macroemulsion	Large (>1 μm), limited by large surface tension. Droplets tend to be polydisperse.	Unstable. Droplets coarsen into phase-separated mixtures in minutes or hours.	Simple to produce through low-energy agitation or, more precisely, using microfluidic devices.
Nanoemulsion	Small (~100 nm). Lower size dispersity than macroemulsions but not monodisperse.	Kinetically stable. Phase separation may be slowed to occur over weeks or months.	High-energy processing required to overcome the large energy of highly curved droplets.
Microemulsion	Very small (~ 10 nm). Monodisperse droplets from thermodynamic self-assembly.	Thermodynamic phase. Micelles remain dispersed indefinitely if state variables do not change.	Form spontaneously if immiscible phases and surfactants are in the correct concentration.

Decreasing size

Figure 2.1 Overview of different classes of emulsions. Decreasing droplet size tends to correlate with increased stability at the cost of increased energy required in their production. Figure adapted with permission from Nature Reviews Materials.

2.3 Interfacial stabilization

The production of nanoscale emulsion droplets requires the high surface energy of their interfaces to be reduced to a level that allows formation of the highly curved surfaces intrinsic to small droplets. The adsorption of amphiphilic molecules or particles at a droplet interface reduces its surface tension by reducing unfavorable interactions between the dispersed and continuous phases [19]. The reduced surface tension also lowers the energy input required to produce droplets of a given size, making nanoscale emulsion droplets accessible.

Because the type of surface-active material (that is, ionic, nonionic or particulate) strongly influences emulsion processing, they should be carefully selected before developing an emulsification protocol. Although both ionic and nonionic surfactants reduce the surface tension of an interface to allow small droplets to form, they enhance emulsion stability through different mechanisms. Ionic surfactants are amphiphilic molecules with charged head groups that tend to partition in the aqueous phase of an emulsion. The surface tension of an interface laden with charged molecules is strongly affected by the ionic strength in the surrounding continuous phase, where higher electrolyte concentrations tend to decrease interfacial tension[20]. The use of co-surfactants, particularly ionic co-surfactants, can be used in such a way to fine-tune interfacial properties. Co-surfactants which are commonly used in industrial applications provide additional methods by which we might induce interactions that stabilize or destabilize an interface, depending on the conditions of the experiment.

Nonionic surfactants provide stabilization primarily through steric repulsion by limiting molecular approach to the fluid interface. Here, the portions of surfactant molecules partitioned in the continuous phase serve as a steric barrier to interfacial contact; in addition, the increased elasticity and viscosity of surfactant-laden interfaces prevent the film fluctuations that induce coalescence [23]. Although nonionic surfactants are less affected by ionic strength and pH than ionic surfactants, changes in temperature can markedly alter their effects on surface-tension reduction[19].

For both ionic and nonionic surfactants, the relative size, geometry and phase affinities of the hydrophilic and lipophilic regions of the amphiphile are important considerations.

29

However, these properties are often difficult to measure and are only sparsely reported in the literature. Alternatively, a simple but heuristically useful descriptor of these properties is the hydrophilic– lipophilic balance (HLB). The HLB number falls between 0 and 20 for nonionic surfactants, where HLB > 10 indicates a primarily hydrophilic molecule and HLB < 10 indicates lipophilicity[23]. Ionic surfactants can have much larger effective HLB values owing to the effective size of the ionic group, with some alkyl sulfates reaching HLB > 40[24]. The phase affinity of the molecule is a strong determining factor in the colloidally stable configuration of the emulsion: surfactants with large HLB tend to favor oil-in-water (O/W) emulsions, whereas those with low HLB favor water-in-oil (W/O) emulsions. Thus, by creating a suitable co-surfactant system with a mixture of both high-HLB and low-HLB surfactants, the formation of multiple emulsions can be promoted, where the interfaces of W/O droplets are populated predominantly by low-HLB molecules and O/W interfaces are populated predominantly by high-HLB molecules [25–29].

2.4 Light for control of interfacial properties

We developed an interest in the possibility of using the light-driven polarity change of photoswitches in order to control emulsion or droplet properties through a change in interfacial properties. The most direct method by which we seek control over interfacial properties is in the development of surfactant molecules that undergo conformational changes.

Photo-responsive surfactants based on common photoswitchable molecular units such as azobenzenes,[8,10,12,30–32] spiropyrans[33–35] and donor-acceptor Stenhouse adducts (DASAs)[36,37]

30

have been developed with the majority of studies performed on azobenzene-based surfactants. Photoswitchable units such as DASA and spiropyran undergo a change in electronic configuration upon irradiation that can lead to a change in the overall charge or polarity of the surfactant. These changes in turn provide avenues for light-driven control of the interface, and a variety of unique amphiphilic molecules bearing photoswitchable units have been developed and used for solution self-assembly and wetting processes.[38] For example, photo-responsive surfactants have been used to drive aggregation and disassembly of micelles and other complex systems for applications such as drug delivery and catalysis.[7,8,11,36,38–40]

Although there have been several studies[7,8,11,36,38–40] examining the solution and interfacial behavior of photosurfactants based on common photoswitches, there have yet to be systematic comparative studies across different photoswitches that could identify molecular features that produce desirable or superior control of interfacial properties. One reason for the lack of systematic comparisons is the difficulty in measuring property changes at multiphase interfaces whilst supplying an external stimulus, as well as the predominant focus on measuring interfacial tension at air-liquid or solid-liquid interfaces. Experimentally, the switchable interfacial properties of some photosurfactants have been characterized using contact angle, Langmuir trough and interfacial tension measurements in order to quantify the magnitude of their changes in the presence of light.[7,11,12,18,32,38] These studies have demonstrated a large range of potential interfacial tension changes from 1 mN/m to 12 mN/m, consistent with the complex dependencies of photosurfactant properties on their local structural and chemical environment. For example, in the case of azobenzene

31

surfactants, several studies have shown that the magnitude of surface tension change under irradiation and the tendency to form aggregates is strongly dependent on the length of the spacer between the head and tail group.[8,38] Additionally, the influence of non-switchable co-surfactants on photosurfactant behavior remains largely unexplored, despite their potential importance for industrial applications.[11,41,42] Despite these successes, the effects of switching on interfacial properties are complex, hindering efforts to rationally design photo-responsive surfactants for which irradiation results in a significant change in interfacial properties.

2.5 Considerations for the design of photo-surfactant

In general, the interfacial response will depend on the magnitude of chemical change incurred by the switch, the solvents in which the switches are solubilized, as well the placement of the switch within the surfactant structure, i.e., as a pendant group or serving as the head or tail group. Each architecture likely provides a different response since the interfacial properties are highly governed by the local changes that result from the photoswitching reaction. Other properties of the molecule onto which the photoswitch is conjugated, including the size and composition of the head/tail group as well as the initial charge state, will dictate the relative range of control over interfacial properties upon switching. Finally, the effectiveness of the photoswitchable unit is highly affected by factors that include its switching kinetics and solvachromatism that strongly depend on the overall structural design and environment. As such, while it may be expected that an increase in polarity change in the surfactant would lead to a correspondingly large change in interfacial tension, the complicated interrelationships between the various design elements could lead to unexpected results.

As our interest lies in the formation of O/W nanoemulisons we sought to develop a photosurfactant with an HLB larger than 10. We chose a nonionic ethoxylated surfactant chassis and targeted amphiphiles in which the photo-responsive unit would initially serve as the hydrophobic tail group. We hypothesized that placing the photoswitchable unit at the surfactant tail (compared to embedded within the molecule) would enable a larger change in polarity as it would render the entire tail-group more hydrophilic upon irradiation. Poly(ethylene glycol) monomethyl ether (PEG, M_n = 550 g/mol) was chosen as the hydrophilic head group. The functional groups on the photoswitchable unit were tuned to achieve an initial hydrophile-lipophile balance (HLB) of ~16 for each type of photosurfactant, where HLB is calculated by the formula $HLB = 20 * M_h/M$ where M_h is the molar mass of the hydrophilic region and M is the molar mass of the entire amphiphilic molecule. This design allows for both synthetic tunability as well as the largest hypothesized change in interface properties.
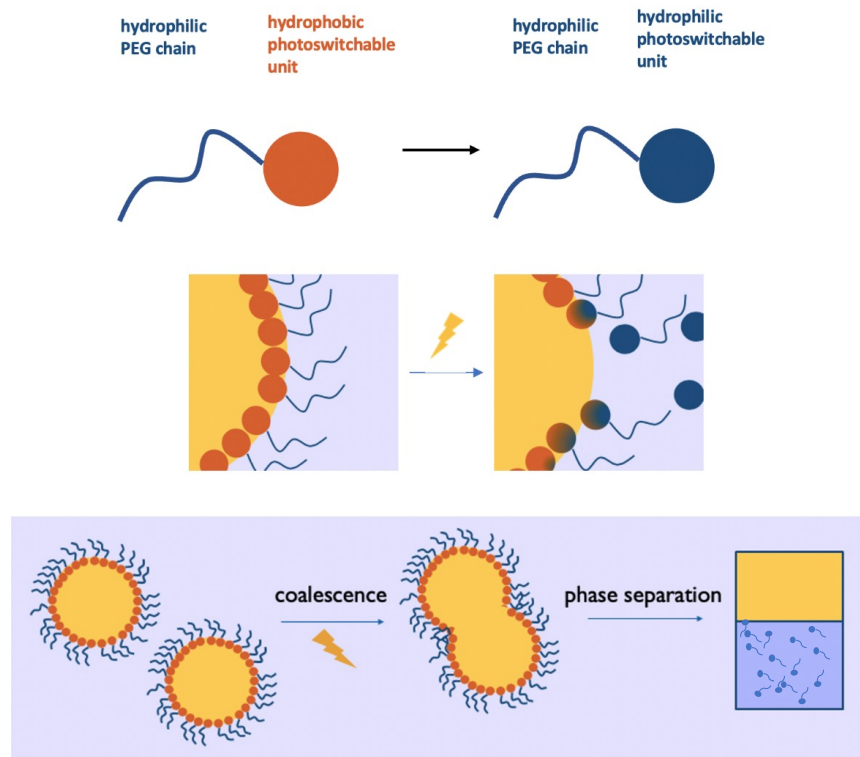
Figure 2.1 Proposed design of photoresponsive surfactant to undergo a transition upon irradiation in which the hydrophobic photoswitchable tail group is rendered hydrophilic. The proposed mechanism of droplet coalescence using photoresponsive surfactants to develop nanoemulsions for triggered release.

Early attempts at developing nanoemulsion systems for triggered release proved challenging due to the many uncertainties associated with the photo-surfactant properties. Nanoemulsions formulated with DASA-based photo-surfactants proved difficult to break and presented even more challenges in characterization. These experiments highlighted the necessity of better understanding the interfacial behavior of photo-responsive surfactants in order to confidently tailor a response from nanoemulsion systems. As a result, experimental studies were devised to finely tune the modular synthetic approach and develop a library of

photoswitchable surfactants containing azobenzene, DASA and spiropyran. The following studies aim to compare their interfacial and kinetic properties through wetting experiments and droplet migration experiments. We expect that these foundational studies of how photoswitch chemistry influences photosurfactant-induced wetting behavior will inform the design, synthesis and study of photo-responsive surfactants that will ultimately allow for the effective use of light to manipulate desired properties and to achieve specific control over fluid interfaces.

2.6 References

1.   Tabor, R. F. *et al*. Reversible light-induced critical separation. *Soft Matter* **5**, 78–80 (2009).

2.   Eastoe, J. *et al*. Photo-stabilised microemulsions. *Chemical Communications* 2785–2786 (2005) doi:10.1039/b503379a.

3.   Eastoe, J., Dominguez, M. S., Wyatt, P. & Heenan, R. K. A photo-responsive organogel. *Chem. commun.* **22**, 2608–2609 (2004).

4.   Vesperinas, A., Eastoe, J., Jackson, S. & Wyatt, P. Light-induced flocculation of gold nanoparticles. *Chemical Communications* 3912–3914 (2007) doi:10.1039/b710502a.

5.   McCoy, T. M., Liu, A. C. Y. & Tabor, R. F. Light-controllable dispersion and recovery of graphenes and carbon nanotubes using a photo-switchable surfactant. *Nanoscale* **8**, 6969–6974 (2016).

6.   Chevallier, E., Saint-Jalmes, A., Cantat, I., Lequeux, F. & Monteux, C. Light induced flows opposing drainage in foams and thin-films using photosurfactants. *Soft Matter* **9**, 7054–7060 (2013).

7.   Mamane, A., Chevallier, E., Olanier, L., Lequeux, F. & Monteux, C. Optical control of surface forces and instabilities in foam films using photosurfactants. *Soft Matter* **13**, 1299–1305 (2017).

8.   Hayashita, T., Kurosawa, T., Miyata, T., Tanaka, K. & Igawa, M. Effect of structural variation within cationic azo-surfactant upon photoresponsive function in aqueous solution. *Colloid & Polymer Science* **272**, 1611–1619 (1994).

9.   Rosslee, C. & Abbott, N. L. Active control of interfacial properties. *Current Opinion in Colloid and Interface Science* **5**, 81–87 (2000).

10.   Hubbard, F. P. & Abbott, N. L. Effect of light on self-assembly of aqueous mixtures of sodium dodecyl sulfate and a cationic, bolaform surfactant containing azobenzene. *Langmuir* **23**, 4819–4829 (2007).

11.   Shin, J. Y. & Abbott, N. L. Using light to control dynamic surface tensions of aqueous solutions of water soluble surfactants. *Langmuir* **15**, 4404–4410 (1999).

12.   Cicciarelli, B. A., Hatton, T. A. & Smith, K. A. Dynamic surface tension behavior in a photoresponsive surfactant system. *Langmuir* **23**, 4753–4764 (2007).

13.   Chevallier, E. *et al*. Pumping-out photo-surfactants from an air-water interface using light. *Soft Matter* **7**, 7866–7874 (2011).

14.   Diguet, A. *et al*. Photomanipulation of a droplet by the chromocapillary effect. *Angewandte Chemie - International Edition* **48**, 9281–9284 (2009).

15.   Crusats, J., Albalat, R., Claret, J., Ignés-Mullol, J. & Sagués, F. Influence of temperature and composition on the mesoscopic textures of azobenzene langmuir monolayers. *Langmuir* **20**, 8668–8674 (2004).

16.   Brown, P. *et al*. Magnetic control over liquid surface properties with responsive surfactants. *Angewandte Chemie - International Edition* **51**, 2414–2416 (2012).

17.   Wang, L., Dong, S. & Hao, J. Recent progress of magnetic surfactants: Self-assembly, properties and functions. *Current Opinion in Colloid and Interface Science* **35**, 81–90 (2018).

18.   Tabor, R. F. *et al*. Reversible light-induced critical separation. *Soft Matter* **5**, 78–80 (2009).

19.   McClements, D. J., Matalanis, A. & Jones, O. G. Structured biopolymer-based delivery systems for encapsulation, protection, and release of lipophilic compounds. *Food Hydrocolloids* **25**, 1865–1880 (2011).

20.   Para, G., Jarek, E., Warszyński, P. & Adamczyk, Z. Effect of electrolytes on surface tension of ionic surfactant solutions. *Colloids and Surfaces A: Physicochemical and Engineering Aspects* **222**, 213–222 (2003).

21.   Espinosa, C. E., Guo, Q., Singh, V. & Behrens, S. H. Particle charging and charge screening in nonpolar dispersions with nonionic surfactants. *Langmuir* **26**, 16941–16948 (2010).

22.   Sainis, S. K., Germain, V., Mejean, C. O. & Dufresne, E. R. Electrostatic interactions of colloidal particles in nonpolar solvents: Role of surface chemistry and charge control agents. *Langmuir* **24**, 1160–1164 (2008).

23.   Tadros, T., Izquierdo, P., Esquena, J. & Solans, C. Formation and stability of nano-emulsions. *Advances in Colloid and Interface Science* **108–109**, 303–318 (2004).

24. Li, Q. *et al*. Prediction of hydrophile–lipophile balance values of anionic surfactants using a quantitative structure–property relationship. *Journal of Colloid and Interface Science* **336**, 773–779 (2009).

25. Florence, A. T. & Whitehill, D. The formulation and stability of multiple emulsions. *International Journal of Pharmaceutics* **11**, 277–308 (1982).

26. Pal, R. Multiple O / W / O Emulsion Rheology. *Langmuir : the ACS journal of surfaces and colloids* **7463**, 2220–2225 (1996).

27. Carlotti, M. E., Gallarate, M., Sapino, S., Ugazio, E. & Morel, S. W/O/W multiple emulsions for dermatological and cosmetic use, obtained with ethylene oxide free emulsifiers. *Journal of Dispersion Science and Technology* **26**, 183–192 (2005).

28. Morais, J. M., Santos, O. D. H., Nunes, J. R. L., Zanatta, C. F. & Rocha-Filho, P. A. W/O/W multiple emulsions obtained by one-step emulsification method and evaluation of the involved variables. *Journal of Dispersion Science and Technology* **29**, 63–69 (2008).

29. Fryd, M. M. & Mason, T. G. Advanced Nanoemulsions. *Annual Review of Physical Chemistry* **63**, 493–518 (2012).

30. Birnbaum, P. P. & Style, D. W. G. The photo-isomerization of some azobenzene derivatives. *Transactions of the Faraday Society* **50**, 1192–1196 (1954).

31. Takahashi, Y., Fukuyasu, K., Horiuchi, T., Kondo, Y. & Stroeve, P. Photoinduced demulsification of emulsions using a photoresponsive gemini surfactant. *Langmuir* **30**, 41–47 (2014).

32. Eastoe, J., Dominguez, M. S., Wyatt, P., Beeby, A. & Heenan, R. K. Properties of a stilbene-containing gemini photosurfactant: Light-triggered changes in surface tension and aggregation. *Langmuir* **18**, 7837–7844 (2002).

33.   Sakai, H. *et al*. Photo-isomerization of spiropyran-modified cationic surfactants. *Journal of Colloid and Interface Science* **316**, 1027–1030 (2007).

34.   Li, C., Iscen, A., Palmer, L. C., Schatz, G. C. & Stupp, S. I. Light-Driven Expansion of Spiropyran Hydrogels. *Journal of the American Chemical Society* **142**, 8447–8453 (2020).

35.   Klajn, R. Spiropyran-based dynamic materials. *Chemical Society Reviews* **43**, 148–184 (2014).

36.   Poelma, S. O. *et al*. Controlled drug release to cancer cells from modular one-photon visible light-responsive micellar system. *Chemical Communications* **52**, 10525–10528 (2016).

37.   Chen, Y. *et al*. Visible Light-Controlled Inversion of Pickering Emulsions Stabilized by Functional Silica Microspheres. *Langmuir* **34**, 2784–2790 (2018).

38.   Eastoe, J. & Vesperinas, A. Self-assembly of light-sensitive surfactants. *Soft Matter* **1**, 338–347 (2005).

39.   Zakrevskyy, Y., Roxlau, J., Brezesinski, G., Lomadze, N. & Santer, S. Photosensitive surfactants: Micellization and interaction with DNA. *Journal of Chemical Physics* **140**, (2014).

40.   Koźlecki, T., Sokołowski, A. & Wilk, K. A. Surface activity and micelle formation of anionic azobenzene-linked surfactants. *Langmuir* **13**, 6889–6895 (1997).

41.   Xiao, Y. *et al*. Droplets: Moving Droplets in 3D Using Light (Adv. Mater. 35/2018). *Advanced Materials* **30**, 1870259 (2018).

42.   Chen, S., Costil, R., Leung, F. K.-C. & Feringa, B. L. Self-Assembly of Photoresponsive Molecular Amphiphiles in Aqueous Media. *Angewandte Chemie International Edition* 2–26 (2020) doi:10.1002/anie.202007693.

3. Influence of polarity change and photophysical effects on photosurfactant-driven wetting

Abstract

Photosurfactants have shown considerable promise for enabling stimuli-responsive control of the properties and motion of fluid interfaces. Recently, a number of photoswitch chemistries have emerged to tailor the photo-responsive properties of photosurfactants. However, systematic studies investigating how photo-responsive surfactant behavior depends on the photochemical and photophysical properties of the switch remain scarce. In this work, we develop synthetic schemes and surfactant designs to produce a well-controlled library of photosurfactants to comparatively assess the behavior of photoswitch chemistry on interfacial behavior. We employ photo-induced spreading of droplets at fluid interfaces as a model for such studies. We show that although photosurfactant response is largely guided by expected trends with changes in polarity of the photoswitch, interfacial behavior also depends non-trivially and sometimes counter-intuitively on the kinetics and mechanisms of photoswitching, particularly at the interface of two solvents, as well as on complex interactions with other surfactants. Understanding these complexities enables the design of new photosurfactant systems and their optimization toward responsive functions including triggered spreading, dewetting and destabilization of droplets on solid and fluid surfaces.

3.1 Introduction

There is an emerging interest in the remote control of the interfacial properties of fluid systems throughout the fields of chemical engineering and materials science.[1] To date, several photo-responsive surfactants based on common photoswitchable molecular units such as azobenzenes,[17–22] spiropyrans[23–25] and donor-acceptor Stenhouse adducts (DASAs)[26,27] have been developed, however, azobenzene-based surfactants have been predominately studied, and the photochromes spiropyran and DASA present a relatively new area for design and characterization of photosurfactants.[28] There have yet to be comparative studies across different photoswitches that could identify molecular features that produce desirable or superior control of interfacial properties; this chapter will provide this comparison. In this study, we aim to illuminate these effects by developing a series of photosurfactants with comparable structures and studying them *via* photoinduced droplet wetting experiments using standardized solvents and in the presence of co-surfactants, as well as quantitative measurements of surface and interfacial tension and contact angle.

3.1.1 Creation of a photosurfactant library

Using a series of photo-responsive surfactants with similar overall structure, we systematically investigated how the chemistry of a photosurfactant influences wetting and de-wetting at fluid interfaces. To do so, we first pursued a synthetic strategy to build a

tunable photosurfactant library possessing azobenzene, donor-acceptor Stenhouse adduct (DASA) and spiropyran moieties as (initially) hydrophobic tail-groups.

The photoswitches: azobenzene, donor-acceptor Stenhouse adduct (DASA), and spiropyran (**Figure 1**) each undergo different photo-driven molecular rearrangements that dictate their resulting degree of change in amphiphilicity. For azobenzene, the change in polarity upon the *cis-trans* photoisomerization was anticipated to render minimal changes relative to DASA and spiropyran in the hydrophilic-lipophilic balance (HLB) of the corresponding photosurfactant. DASA was chosen as a photoswitch based on its known polarity change that occurs upon *cis-trans* photoisomerization along with a thermal 4π electrocyclization to construct a ring-closed zwitterionic, hydrophilic product. The magnitude of polarity change of this compound, which has the potential to be quite large, is therefore tightly coupled with the overall photoswitching properties (i.e., actinic and thermal steps), which we anticipated would notably impact the overall hydrophobicity. By contrast, a third photoswitch, spiropyran, undergoes a well-defined large change in polarity upon photoisomerization to the charged merocyanine (MC) species.[25]

Synthetic design of the ethoxylated photosurfactants relied on modular click platform between the hydrophilic PEG chain and the photoswitches. Due to the potential reactivity of the photoswitches during surfactant synthesis, we chose to employ a mild, yet highly efficient Diels–Alder (DA) click reaction recently reported by our group in the preparation of block copolymers.[33,34] This approach utilizes norbornadiene (NBD) as a stable precursor to the much more reactive diene click partner, cyclopentadiene (Cp). Upon treatment with

43

3,6-di-2-pyridyl-1,2,4,5-tetrazine (DpTz), NBD is converted to Cp *in situ* and rapidly

clicked to a corresponding dienophile, maleimide. It was envisioned that the three

photoswitches could be functionalized with either a maleimide or NBD and clicked to an

appropriately functionalized PEG, yielding the desired ethoxylated photosurfactants. Using

this modular strategy, the three photosurfactants bearing DA linkages were prepared

following the NBD click procedure schematically represented in **Figure 1**. Note for

synthetic accessibility the **azo-DA-PEG** was prepared with the opposite orientation of the

malemide/Cp functional groups relative to the photochromic molecule; because of the

already small anticipated changes to interfacial behavior of azo-based photosurfactants, we

anticipate that this choice will have a negligible effect on the comparative studies to follow.

These three surfactants served as a base library of photo-responsive surfactants (**Figure 1**)

representing small (**azo-DA-PEG**), and large (**DASA-DA-PEG** and **SP-DA-PEG**) changes
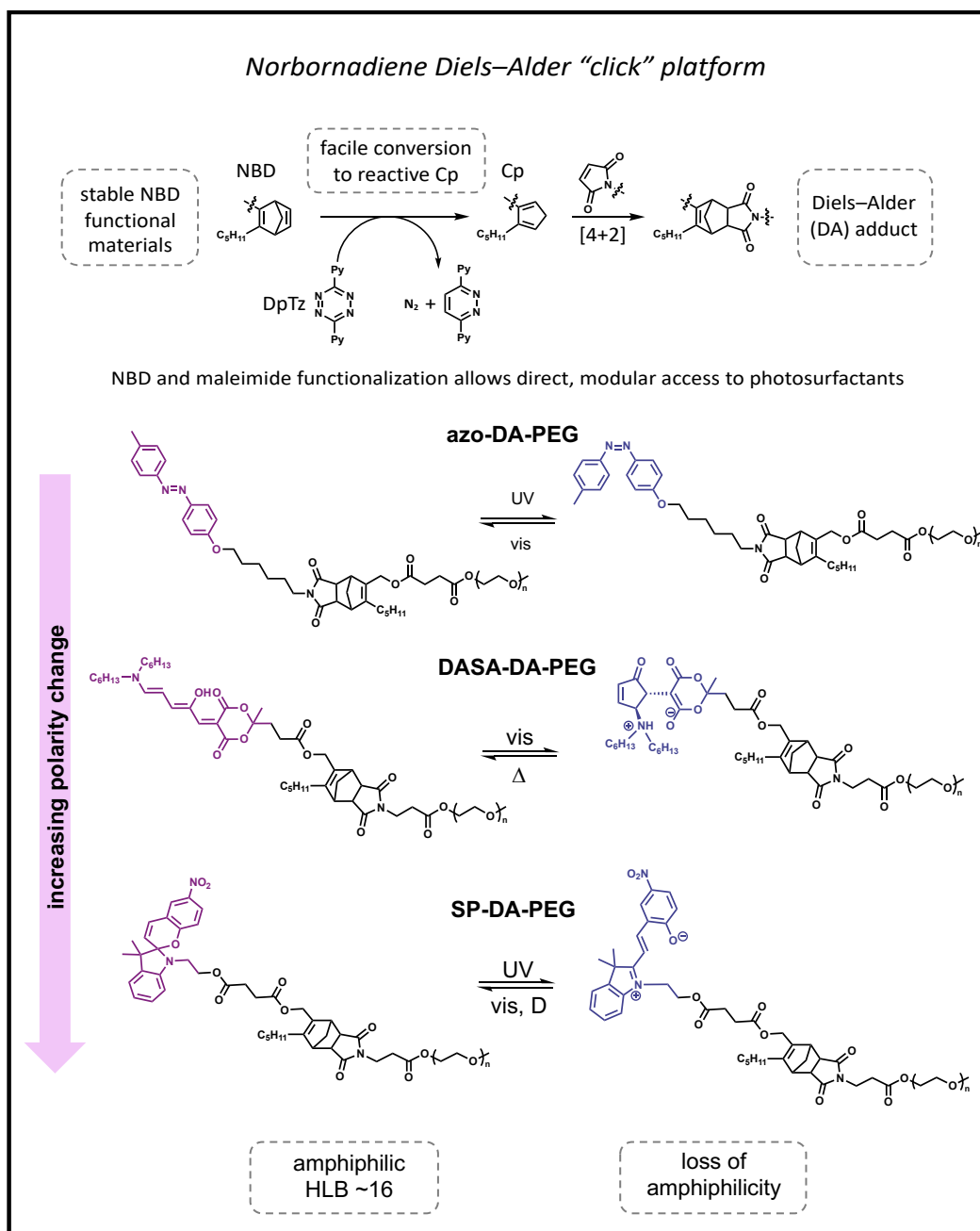
in polarity.

Figure 3.1. Synthetic schemes for developing the photosurfactant library studied in this work (top), and resulting chemical structures in their initial and irradiated conformations (bottom) where the PEG chain consists of ~12 repeat units. Reprinted with permission from Langmuir. 2021, 37 (33), 9939-9951. Copyright 2021 American Chemical Society.

3.2 Droplet wetting as a testbed for comparing photosurfactant response

Surface and interfacial tension measurements are difficult to perform with light-responsive surfactants. First, the sensitivity of photoswitching kinetics to light exposure necessitates controlled, uniform illumination of the interface, which is challenging for large area or curved interfaces. Furthermore, the photostationary state of the photoswitch may differ when the molecule is at a fluid interface compared to in bulk solution, and the adsorption equilibrium and partitioning between fluid phases may not be known (owing to the challenges with illumination just described). These challenges make the interpretation of interfacial property measurements with respect to photoswitch chemistry difficult. For example, the switching behavior and chemical pathways accessible to a photoswitch at a fluid-fluid interface will be distinct from the kinetics of the switch in either fluid phase. Because of this, a deep understanding of the interfacial properties of photosurfactants under irradiation and particularly at low surface tensions is hindered by current instrument limitations.

Due to these limitations, we propose to use droplet wetting as a facile yet sensitive and easily reproducible method by which photosurfactants' response may be compared: wetting is highly sensitive to changes in interfacial tension such that droplets composed of each photosurfactant elicit a unique response upon irradiation. To explore how light-triggered polarity changes control the differential wetting/de-wetting behaviors of photosurfactants, we observed a triphasic interface formed using a droplet of photosurfactant in toluene that was deposited at the vapor surface of an aqueous solution **(Figure 2a)**. Toluene was selected

46

as a non-polar phase to maximize surfactant solubility while allowing the droplet to sit at the air-water interface as a result of its low density. We observed that a non-photo-responsive co-surfactant must be introduced into the continuous aqueous phase to stabilize the interface; in the absence of a co-surfactant the toluene droplet containing the photosurfactant will fully wet the water:air interface. The details of this co-surfactant behavior will be investigated in further detail in the following section.

The light-triggered changes in wetting **(Figure 2b,** DASA-DA-PEG photosurfactant**)** are attributable to the varying degrees of polarity change induced by the illumination of photo-reactive surfactants, the rate at which they switch, and their interaction with any co-surfactant in the system. There exist other potential experimental factors that may contribute to spreading such as gradients in interfacial tensions generated by the flux of light. It is possible that these effects may cause or be enhanced by surface pressure driven flows, which may enhance the observed spreading. As such, these qualitative experiments are complemented by quantitative measurements and analysis of photoreactive interfacial tension tailored to each surfactant to ensure the most comprehensive experimental study possible. The combination of systematic variation in photosurfactant chemistry with an evaluation of photoinduced changes in interfacial properties holds potential for fundamental insights into the mechanisms by which photo-responsive function underlies control of interfacial activity.
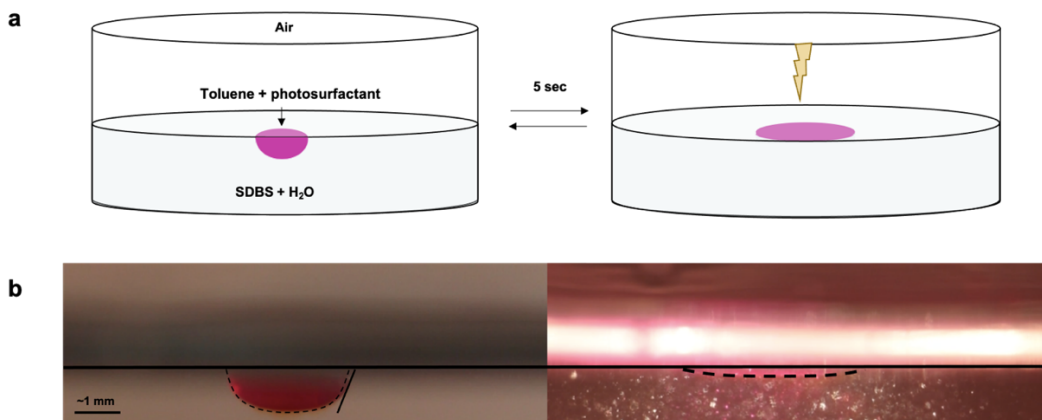
Figure 3.2. a) Schematic of droplet wetting experiment before (left) and after (right) irradiation. b) Photographic images (side view) of 10mM DASA-DA-PEG in toluene wetting to the water-SDBS interface before (left) and upon irradiation (right) with white light. Glassware was cleaned with acetone and DI water and SDBS solutions were prepared in DI water. Note that small particulates in the continuous phase or glassware are more pronounced under the visible light illumination. Reprinted with permission from Langmuir. 2021, 37 (33), 9939-9951. Copyright 2021 American Chemical Society.

3.3 Co-surfactant cooperativity drives photo-induced wetting-dewetting behavior

The photo-isomerization of photosurfactants within toluene droplets has a notable dependence of the wetting/de-wetting behavior on the constituents of the surrounding media. Specifically, it is known that photosurfactants can have significant interactions with other interfacial constituents such as co-surfactants.[31] The influence of such multi-component interactions on interfacial behavior is at present a significant knowledge gap in photosurfactant design,[28] and this motivated us to test the photowetting behavior of the

surfactant library in the presence of a range of common water-soluble co-surfactants. Specifically, we observed a significant cooperative effect between the DASA-/SP-surfactants and ionic co-surfactants, such that the latter was required to produce a meaningful level of photoresponse. When comparing toluene droplets containing **DASA-DA-PEG** in aqueous media containing non-ionic (Span80 or Tween 20), anionic (SDBS) and cationic (cetyltrimethylammonium bromide/CTAB) surfactants, we observed that the droplets only undergo measurable reversible spreading in the presence of the charged surfactants, SDBS and CTAB. The most significant response was observed over a fairly narrow range of co-surfactant concentration (**Figure S15**). At SDBS concentrations below 0.25 mM, for example, the toluene droplet spread completely when first placed at the air-water interface, indicating that the co-surfactant is necessary to stabilize droplets at the interface in the presence of the photosurfactant. Above 0.5 mM SDBS, however, droplets exhibited no change in wetting when irradiated for several minutes. We therefore utilized the anionic co-surfactant SDBS at concentrations in this range, between 0.25 mM and 0.5 mM. We speculate that this narrow range is bound on the lower end by the concentration required to observe the surfactant interactions (either in bulk solution or at the interface), and on the higher end by the CMC of the mixed surfactant system, as expected for interfacial effects involving mixed ionic surfactants.[35,36] We leave detailed investigation of this hypothesis to future work.

Within this working range of SDBS concentration, the photo-induced wetting and de-wetting is significantly larger compared to that in the absence of SDBS: changes in spreading of up to 3 times the original droplet wetted diameter of droplets were observed for

DASA-DA-PEG (**Figure 2b**). Additionally, in cases where photosurfactants with large changes in polarity (**SP-DA-PEG**) were used, the changes in spreading were so extreme that droplet breakup could be observed due to the cooperative, polarity-induced changes in surface tension (**Video 1**).

Overall, we expect that this significant co-surfactant effect will be present for any surfactant system involving an ionic co-surfactant and a photosurfactant with a charged or highly polar state as one of its photostationary states. In our view, practical applications involving photosurfactants are likely to involve a co-surfactant due to the significant cost associated with using only photosurfactants at sufficiently high concentrations to produce stable interfaces, and ionic surfactants are ubiquitous in such applications. As such, we anticipate that the observed co-surfactant interaction present in this work is likely general to a large cross-section of relevant photosurfactant systems.

3.4 Dependence of photo-induced wetting on photoswitch chemistry

Having established photo-induced wetting and dewetting at a toluene-water-air interface as a test bed for comparing the responsive interfacial properties of photosurfactants, and having established that the presence of co-surfactants is critical in driving the photowetting behavior, we turn to a systematic comparison of photowetting behavior across our library of azobenzene-, DASA- and spiropyran-based PEG photosurfactants. We summarize the results of experiments for each photoswitch separately so that the unique features of photowetting behavior for each can be clearly described.

3.4.1 Azo-DA-PEG

The smallest change in polarity with illumination is expected with azobenzene, which undergoes a reversible *trans-cis* isomerization upon irradiation with UV light. This photo-isomerization can be monitored by UV-vis spectroscopy (**Figure 3a**). Nevertheless, experiments on **azo-DA-PEG** surfactants are useful in illustrating the basic features of the photokinetic and photowetting experiments absent more complicated photoreactions and droplet behavior, which we will describe here.

Photoswitching kinetics. For a 10 μM solution of **azo-DA-PEG** in toluene, the *trans* to *cis* conformational change reached a photostationary state of 85% within approximately 100 seconds upon irradiation with 365 nm UV light (Figure 3a). Subsequent irradiation with visible light promoted isomerization back to the *trans* configuration with a photostationary state at 75% conversion within 400 seconds. We note that in the presence of the SDBS cosurfactant the ratio of *trans* to *cis* isomers may be slightly different both before and after irradiation.

Droplet photowetting. Despite the effectiveness of photo-switching under these conditions, the isomerization only leads to a small change in polarity and no HLB shift; therefore, minimal effects on the wetting/de-wetting behavior were anticipated. Analysis of video stills of **azo-DA-PEG** in SDBS/water (**Figure 3b**) indicated that the diameter of the droplet contact line only marginally increased (<10%) after 2 minutes of exposure to 365 nm

51

light, which is sufficient for the photostationary state to be achieved. Additionally, the toluene-water interfacial tension measured by the pendant drop method was unaffected by the exposure to light (**Figure 3c, 3d**). From these results, we deduce that the polarity change accompanying the *trans-cis* isomerization of azobenzene is insufficient to enact significant changes in interfacial properties under these conditions. These results are repeatably observed for droplets of various volumes.
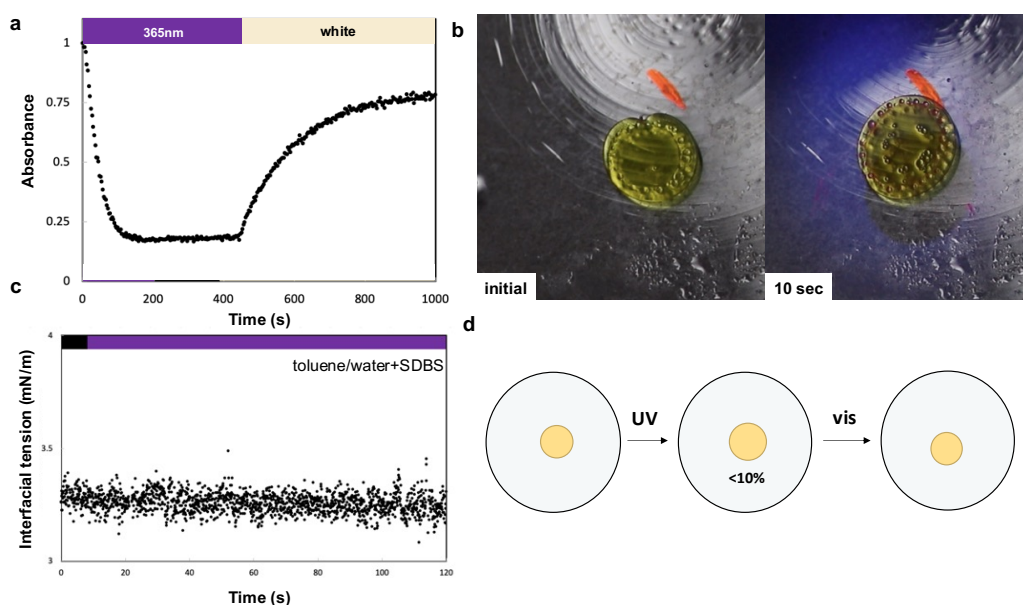
Figure 3.3 a) Pump probe kinetics of 10μM azo-DA-PEG with 365 nm light, followed by darkness and then white light to trigger the reverse reaction. Colored bars at the bottom of the plot indicate the illumination conditions. b) Droplet wetting experimental results for a droplet of 10mM Azo-DA-PEG in toluene layered onto a solution of 0.25mM SDBS in water before (left; initial) and after 10-s irradiation with 365 nm light (right), c) Interfacial tension measurements of 10mM Azo-DA-PEG in toluene vs 0.25mM SDBS in water show no change upon illumination as measured by pendant drop experiments. Colored bars at the top of the plot indicate the illumination conditions. and d) Schematic representation of the wetting changes observed during this experiment. Reprinted with permission from Langmuir. 2021, 37 (33), 9939-9951. Copyright 2021 American Chemical Society.

3.4.2 DASA-DA-PEG

We anticipated changes in interfacial properties upon photoswitching to become more pronounced in the presence of a photosurfactant that undergoes a larger change in polarity upon illumination. DASAs have a large change in polarity, along with a more complicated multi-step switching mechanism consisting of a photo-driven isomerization, followed by a thermally driven bond rotation and 4π electrocyclic ring closure and potentially accessible additional isomerization pathways.[37,38]

Unlike azobenzene-based surfactants, the large polarity changes associated with switching of both DASA- and spiropyran-based surfactants result in significant changes in solubility of the surfactant. Before irradiation, the elongated, highly conjugated DASA acts as a hydrophobic tail group (**Figure 1**) and while some of the surfactant may initially reside in the aqueous phase, it predominantly resides in the toluene phase in the dark. Exact quantification of partitioning of surfactants into each phase both before and after irradiation is complicated by the tendency to form an emulsion layer between solvents which prevents separation and analysis. Small molecule studies provide some insight into anticipated partitioning after irradiation which we expect to be enhanced by the ionic co-surfactant.[39] Visible light-induced photo-isomerization yields a zwitterionic, structurally compact isomer with a significant loss in hydrophobicity. Importantly, although this donor-acceptor architecture is known to form the zwitterionic ring-closed isomer upon photocyclization, the combination of actinic and thermal steps associated with photo-switching mechanism of

DASAs[40–44] offers multiple "productive" and "non-productive" pathways of varying polarity change that must also be considered. As a result, the overall polarity change observed for the DASA surfactant is tightly coupled to accessible switching pathways and kinetics where solvent, additives and architecture can play a significant role and multiple isomers may exist in the solution at once.[40–48]

Photoswitching kinetics. Pump-probe UV-vis spectroscopy of a bulk solution of 10 μM solution of **DASA-DA-PEG** in toluene reveals a comparably low-conversion photostationary state, with only 60% switching to the ring-closed form after 250 seconds of irradiation with white light (**Figure 4a**). The reverse reaction is similarly slow; upon removal of the light source, the DASA moiety completely reverts back to the open form after 300 seconds. Despite this slow rate of ring-closure, the zwitterionic character of the closed DASA leads to a pronounced loss of hydrophobicity in the **DASA-DA-PEG** surfactant molecules. We expect that the large changes in polarity induced by photoexposure will lead to changes in interfacial activity that result in changes in interfacial tension and therefore changes in wetting. It was not possible to conduct pump-probe UV-vis spectroscopy studies in the presence of the co-surfactant, which could influence the switching kinetics of the forward and reverse reaction.

Droplet photowetting. Using the droplet wetting platform, we found that these changes in polarity and resulting interfacial activity enabled a rapid and dramatic response of **DASA-DA-PEG**-containing droplets to light irradiation that is more pronounced than previously reported droplet behaviors. At concentrations of DASA ranging from 1 mM to 20 mM, these

droplets spread with wetted diameter increasing by ~150-200% upon irradiation with 214

mW/cm^2 white light (**Figures 4b, 4c**). By comparison, the only previous study to our

knowledge to report spreading in a multiphase liquid system have reported effects that were

an order of magnitude smaller, with ~20% increase in diameter over 120 seconds.[6] As a

result of the conversion to a hydrophilic molecule, some partitioning of DASA into the

water phase expectedly occurred over several minutes of irradiation. The observed spreading

is consistent with a measured contact angle change from 75° to nearly 0° upon irradiation

(**Figure 2b**). Additionally, the response was reversible and repeatable with the removal of

light leading to an immediate de-wetting and return to the original diameter (**Video 2**).

Notably, the time scale over which this dramatic change occurs (< 5 seconds) is

considerably shorter than that observed for complete photo-switching of **DASA-DA-PEG** in

toluene (**Figure 4a)**. Surface pressure gradient-driven flows (i.e., Marangoni flows) may be

partially responsible for the different time-scales observed for the photoswitching and

photowetting behaviors. Unfortunately, the overall low surface tension of **DASA-DA-PEG**

in toluene and the opaque initial solution precludes direct measurements of interfacial

tension using either pendant drop or Wilhelmy plate methods, and preventing direct

characterization of Marangoni flows.

Based on these results, we hypothesize that the relationship between interfacial activity

of the closed form and surface tension is nonlinear, such that it is possible for a small

fractional conversion of photoreaction to drive surface tension changes faster than the

photostationary state is reached. It is likely that intermediate photo-driven isomerization

pathways play a significant role in the surface tension changes and rapid response of DASA

droplets. These light driven pathways are not decipherable in the pump-probe kinetic measurements due to overlapping absorbances of non-ring closed DASA species; however, they have been shown to occur over picosecond timescales.[42] The switching kinetics of the DASA when situated at the interface of two solvents is also unknown and we hypothesize are what allows for alternative switching pathways and kinetics to become accessible.
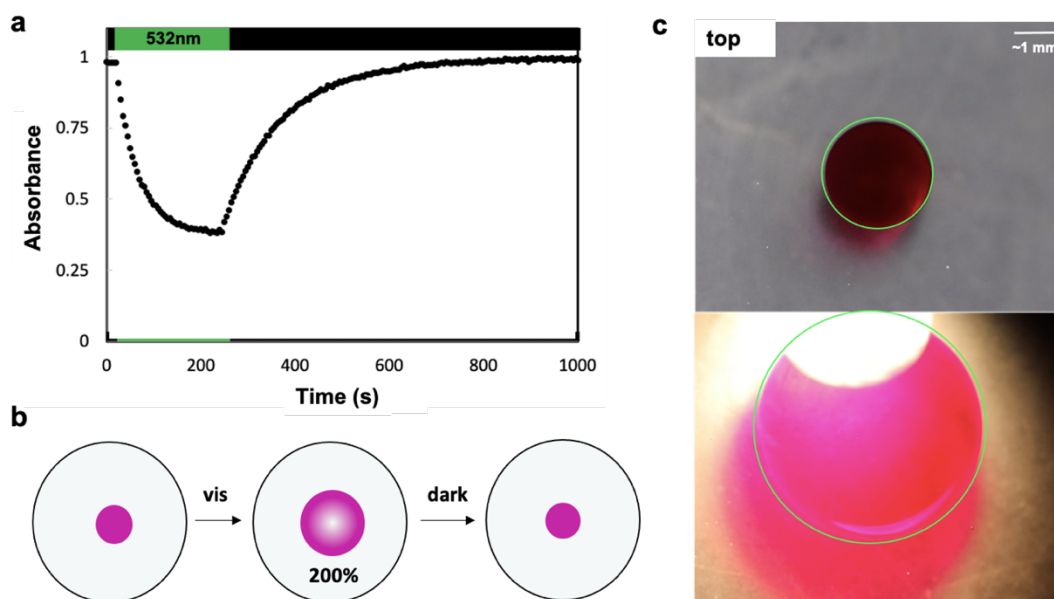

Figure 3.4. a) Pump-probe kinetic measurements of 10μM DASA-DA-PEG solution in toluene upon irradiation with 532 nm light. Colored bars at the top of the plot indicate the illumination conditions. b) Schematic depiction of wetting experiments. c) Top view of droplet wetting and de-wetting behavior for 10mM DASA-DA-PEG in toluene droplet in 0.25mM SDBS before (top) and during (bottom) irradiation. Droplets expand by ~150-200% when irradiated with white light. Droplet edges are highlighted with a thin green line in order to clearly distinguish between shadows and reflections. Reprinted with permission from Langmuir. 2021, 37 (33), 9939-9951. Copyright 2021 American Chemical Society.

3.4.3 SP-DA-PEG

The third photo-switchable surfactant studied, **SP-DA-PEG** is, like DASA, expected to undergo a large change in polarity upon irradiation. The irradiation of the photosurfactant leads to the transition of a neutral species, spiropyran (SP), to a charged species, merocyanine (MC). In principle, SP-based photosurfactants should exhibit enhanced changes in polarity upon photoswitching due to longer-range charge separation on the molecule in the open MC form (*cf*. Figure 1). However, the photokinetic behavior of spiropyran is complicated because it undergoes a multi-step switching mechanism in which the first step of the ring-opening leads to the formation of short-lived *cis*-MC isomer followed by a bond rotation which yields the *trans*-MC most commonly observed. As such, the interfacial behavior of SP-surfactants will depend on a complex equilibrium between intermediate photoreactive states of SP at the interface. These potential complicating effects will be assessed in the description of the results to follow.

Photoswitching kinetics. Reversible photoisomerization of **SP-DA-PEG** is confirmed by pump-probe UV-vis spectroscopy (**Figure 5a**). The ring-opening to **MC-DA-PEG** occurs within 50 seconds upon 365 nm light irradiation and is completely reversible when the light is removed, returning to **SP-DA-PEG** within 30 seconds, in the absence of SDBS. Like azobenzene and DASA surfactants, we similarly expect that the presence of the co-surfactant may lead to altered switching kinetics and ratio of open/closed isomers, however we still anticipate a large overall conversion. Due to the rapid conformational change combined with the relatively complete conversion a charged species, we anticipated that the

57

effects on the resulting wetting/de-wetting behavior would be even more pronounced than those observed for the DASA-based photosurfactant.

Droplet photowetting. This anticipated extreme behavior is confirmed in **Figure 5**. Notably, the strong change in photosurfactant polarity led to rapid wetting and significant droplet instability, which caused small water droplets to become temporarily entrained within the large toluene droplet as it spread on the interface at 10mM **SP-DA-PEG** (**Figure 5b, 5c, Video 2**). This effect can be mediated by tuning the concentration of the photosurfactant: at low concentrations (< 1 mM), the photo-wetting/de-wetting behavior was similar to that observed in the case of 1–20 mM **DASA-DA-PEG** droplets in which no interfacial instability was observed (**Video 3**). These droplets rapidly spread on the interface within seconds upon irradiation with 49 mW/cm^2 365 nm LED light. At these low concentrations, droplets experienced less partitioning of the **SP-DA-PEG** into the water and reverted back to their initial state after the light was removed. In all cases, **SP-DA-PEG** is converted to **MC-DA-PEG,** whose affinity for water drives its diffusion out of the droplet into the aqueous phase, leaving a plume-like trail in the water. An immediate decrease in interfacial tension reflects the rapid rate with which the photoreaction drives this interfacial behavior (**Figure 5d**). We hypothesize that at the higher concentrations, the encapsulated water droplets decrease the diffusion length between interfaces, and therefore decrease mass transport limitations of photosurfactant to the water phase driving more rapid changes in surface tension as well as phase transfer, resulting in the large observed amounts of leeching.

We infer from these results that rapid photoswitching, in combination with conformational changes that render the spiropyran photosurfactant more fully charged, are what lead to a more pronounced effect on interfacial properties than either DASA or azobenzene photosurfactants of the same design. Additionally, by tuning the concentration of photosurfactant, we can selectively trigger distinct responses to light, ranging from controlled wetting/de-wetting to triggered droplet instability.
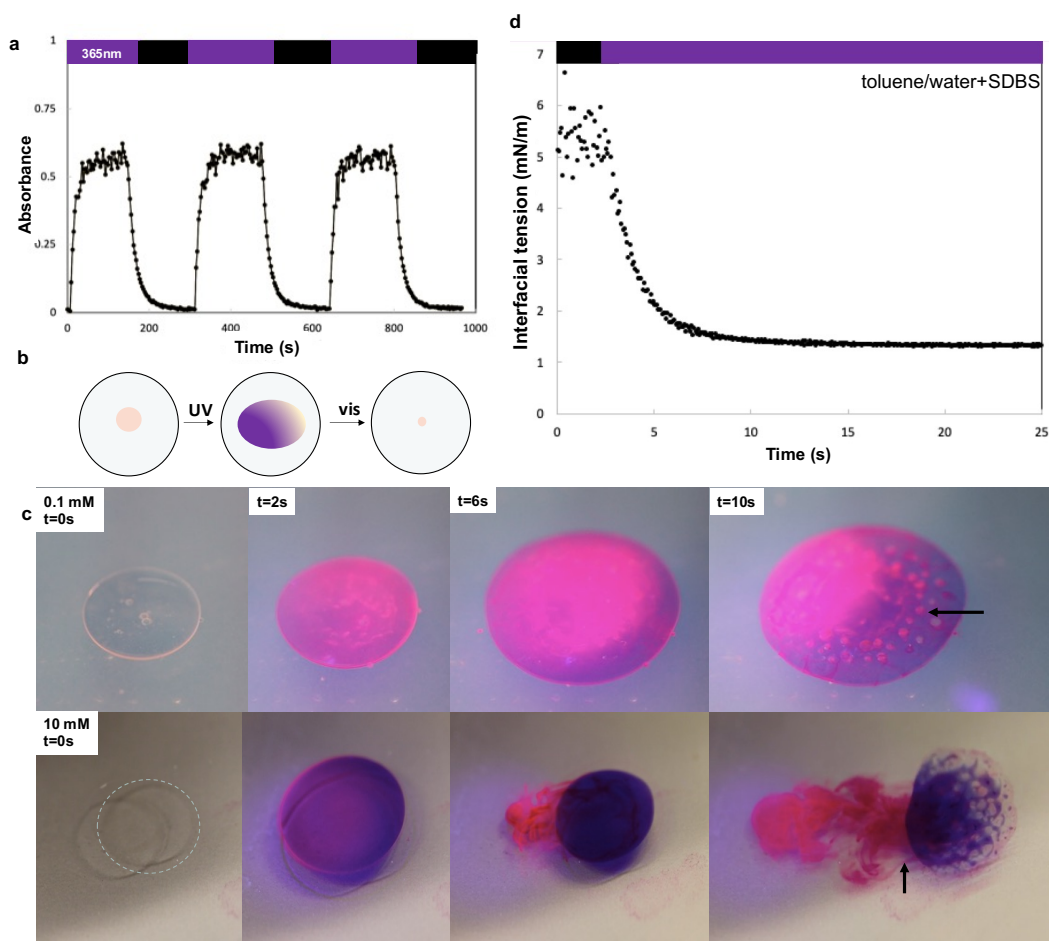

Figure 3.5. a) Pump-probe kinetics studies of 10μM SP-DA-PEG with cycled exposure to 365 nm light. Colored bars at the top of the plot indicate the illumination conditions. b) Schematic depiction of wetting experiments where the entrained droplets and jetted release of photosurfactant are indicated with arrows. c)

Images of droplet of (top row) 0.1 mM SP-DA-PEG and (bottom row) 10 mM SP-DA-PEG in toluene in 0.25mM SDBS in water upon irradiation with 365 nm light. Arrows point to entrapped water and the released plume d) Interfacial tension change of 10 mM SP-DA-PEG in toluene in an aqueous solution containing 0.25 SDBS under illumination as measured by pendant drop method. Colored bars at the top of the plot indicate the illumination conditions. Reprinted with permission from Langmuir. 2021, 37 (33), 9939-9951. Copyright 2021 American Chemical Society.

3.5 Rationalization of observed photowetting behavior from interfacial properties

Despite the ability of the previous photowetting experiments to systematically compare the photoresponsive behavior of different photosurfactants, and to reveal new previously unreported phenomena associated with extreme photowetting, the physical process is complicated. Specifically, in addition to the direct dependence on photokinetics of switching under illumination, the time scales and extent of wetting will depend on some combination of adsorption kinetics and equilibrium, mass transport effects, and co-surfactant interactions (including the co-surfactant SDBS as well as any photoreaction intermediates). As a first step toward unraveling these coupled effects, we attempt to address the simpler question of whether the observed changes in steady state contact angle of the wetting droplets can be successfully reconciled by changes in the corresponding interfacial tensions of the three biphasic interfaces involved (toluene-water, air-water, air-toluene).

3.5.1 Interfacial tension of interfaces containing DASA-ester-PEG

As discussed previously, characterizing the interfacial properties of photosurfactants in the exact conditions of the droplet wetting experiment presents challenges including limitations involving uniform illumination and differential solubility of the photosurfactants in the various phases as well as their changes upon illumination. In the previous sections, we reported the interfacial tension changes observed in biphasic toluene-water systems, which were successfully characterized *via* pendant drop experiments. Here, we report our successful attempts to measure all of the associated interfacial tensions for a single photosurfactant in the presence (where possible) of SDBS co-surfactant.

For these studies, we performed quantitative tensiometry measurements using **DASA-ester-PEG** as the model photosurfactant. Initial attempts to measure the surface tension of **DASA-DA-PEG** at the toluene-water interface or toluene-air interface failed due to the very low surface energies in the presence of open and closed **DASA-DA-PEG** and SDBS. Instead, we modified the chemistry of the DASA-based surfactant by introducing a linker chemistry that leads to a less effective surfactant molecule: **DASA-ester-PEG (Figures S12- S13**). Serendipitously, we discovered that the initially higher interfacial tension of this molecule allowed us to experimentally study the surface tension more readily than using **DASA-DA-PEG**. Importantly, although the linkage chemistry change results in slower switching kinetics and a higher initial interfacial tension, we observed the same light-responsive droplet behavior as observed from when using **DASA-DA-PEG** with regards to the change in three phase contact angle. This suggests that the interactions between the

61

surfactants in the mixture, and not the magnitude of the initial tension, dominate the photo-responsive properties.

Using **DASA-ester-PEG** as a model system, we measured the interfacial tension changes between toluene-air (σ_{TA}) and water-air (σ_{WA}) using Wilhelmy plate experiments and the three-phase contact angle (θ) using video microscopy. Results of these individual measurements can be found in **Table S1**. We were unable to measure the toluene-water interface directly; however, approximate changes in the toluene-water (σ_{TW}) interfacial tension can be inferred using the Young-Dupré equation.

$$\sigma_{TW} = \frac{\sigma_{WA} - \sigma_{TA}}{\cos \theta} \tag{1}$$
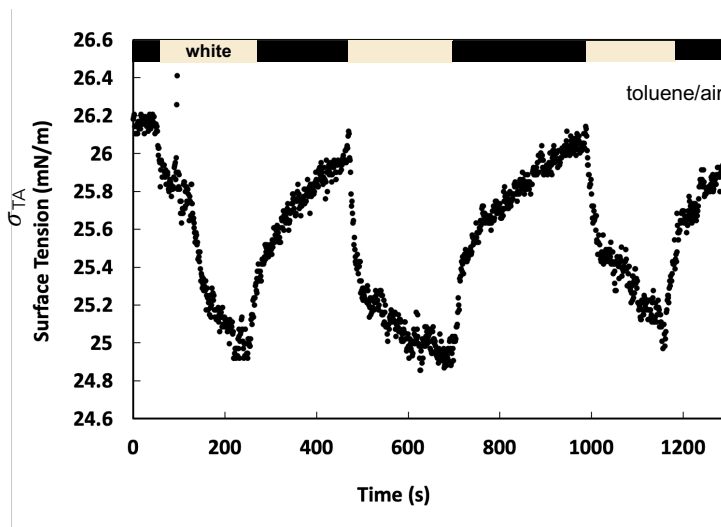

Figure 3.6. Reversible surface tension change of 20mM DASA-ester-PEG in toluene measured against air with cycled irradiation. Reprinted with permission from Langmuir. 2021, 37 (33), 9939-9951. Copyright 2021 American Chemical Society.

The light-triggered surface tension change in the presence of **DASA-ester-PEG** at the toluene-air interface was rapid and could be cycled by repeated illumination cycles, but only a modest change of only about 2 mN/m for a 20 mM solution was observed (**Figure 6**). Predictably, we measured that the interfacial tension of the water-SDBS solution and air does not change upon irradiation in the presence of DASA-ester-PEG, although we note that the presence of the photosurfactant does produce an observable change in interfacial tension, and this will be discussed further in the following section in the context of the mechanism of photowetting. Contact angle measurements of a toluene droplet containing **DASA-ester-PEG** wetting to the air-water indicated a large decrease in contact angle of nearly 70° as the droplet spreads at the interface upon irradiation.

In order to reconcile the modest change in σ_{TA} with the large change in droplet contact angle, we use eqn. (1) to estimate the light-induced change in σ_{TW} that would be necessary to explain the observed pronounced photo-induced spreading (**Table S1**). We determine this relative change to be ~22.4 mN/m. This value is almost twice the maximal change reported in previous studies.[16,20,21,30,31,49] Moreover, it is an order of magnitude larger when comparing to the equivalent change in the previously reported spreading coefficient using azo-surfactants.[6] Thus, our result underscores the untapped potential for light-mediated interface control using tailored photosurfactants in the presence of ionic co-surfactants. Finally, while this analysis was performed for **DASA-ester-PEG**, we posit this is a general effect and that

changes of similar magnitude would be observed for **DASA-DA-PEG** and **SP-DA-PEG** in similar multi-phase environments.

3.5.2 Proposed mechanism of photowetting

We now attempt to use the comprehensive results on photowetting and interfacial tensiometry for the DASA-DA-PEG/SDBS system to propose a possible mechanism of photowetting that reconciles several of the key experimental observations. First, the observed degree of photowetting and interfacial tension change for the DASA- and SP-based surfactants depends critically on the presence of an ionic surfactant initially in the aqueous subphase. Because switching of DASA and SP surfactants leads to the formation of a zwitterion, it is likely that this observation can be explained by strong electrostatic interactions between the switched photosurfactant and the ionic co-surfactant at the interface and in the aqueous subphase. Furthermore, the observed time scale for changes in toluene-water interfacial tension and wetting is significantly faster than the observed time scale for the DASA-based photosurfactant to achieve its photostationary state in toluene solution. To explain this observation, we propose that the ionic co-surfactant in the continuous phase or at the interface alters the switching and adsorption kinetics of the photosurfactant. In addition to direct electrostatic interactions between photosurfactant and co-surfactant, we also anticipate that the presence of an ionic cosurfactant would influence the photoswitching properties and interactions by modifying the dielectric properties of the continuous phase. Previous studies on the solvachromatism of DASA showed that the polarity of the continuous phase determines the initial degree of charge separation, the rate of switching

and the influence of ionic species on the photoswitching process.[50] Not only would these effects lead to altered kinetics of the photoreaction, but would also result in faster kinetics of adsorption and partitioning of photosurfactant into the aqueous phase during light irradiation. We note that any surface pressure gradient-driven flows, caused either by non-uniform irradiation or by mass transport effects, would not qualitatively alter these phenomena but could potentially enhance the kinetics of the photowetting response. Finally, the extreme degree of photowetting for DASA- and SP-based photosurfactants in the presence of an ionic co-surfactant is consistent with changes in apparent oil-water interfacial tensions that are significantly larger than have been previously reported for similar photosurfactants in the absence of a co-surfactant. Here, it is likely that the strong co-surfactant interactions, either at the toluene-water interface or in the aqueous sub-phase, lead directly to enhanced surface pressure of the photosurfactant relative to a system without ionic co-surfactant.

A clear hypothesized process that incorporates all of the various phenomena described above is illustrated in **Figure 7a**, in which the observed photowetting is explained by a combination of interactions and kinetic processes at the toluene-water interface and in the aqueous sub-phase that are driven by interactions of DASA and SP surfactants with the ionic SDBS co-surfactant. Thorough testing of this hypothesis will require detailed measurements of interfacial photoreactivity, surface pressure, and adsorption/desorption kinetics of the photosurfactants in the presence of ionic co-surfactants. Due to challenges described previously in the design of such experiments, these detailed experiments are beyond the scope of the present study. However, some initial corroborating evidence is provided by the

measurement of the surface tension change of a solution of 0.25 mM SDBS in water with and without the addition of **DASA-ester-PEG.** Specifically, we find that as the photosurfactant becomes soluble in the aqueous phase and eventually co-adsorbs to the air-water interface with SDBS, the interfacial tension of the solution increases by 5 mN/m **(Figure 7b)**. Because of this increase in air-water interfacial tension upon addition of **DASA-ester-PEG**, the spreading coefficient of the three-phase water-toluene-air system will correspondingly increase and therefore enhance the photowetting by producing a larger change in contact angle for an equivalent change in water-toluene interfacial tension. This phenomenon will similarly occur for photosurfactants such as **DASA-DA-PEG** and **SP-DA-PEG,** but not for azobenzene-containing surfactants that have a change in conformation without a large change in polarity (and therefore without change to their solubility in the aqueous phase). These results indicate that if the charged photosurfactant were to adsorb to a bare air-water interface, it would lower the air-water interfacial tension and therefore decrease the spreading coefficient and suppress photowetting. However, when the photosurfactant displaces a co-surfactant with higher specific surface pressure from the air-water interface, this increases the interfacial tension and produces the resulting enhancement of photowetting observed.
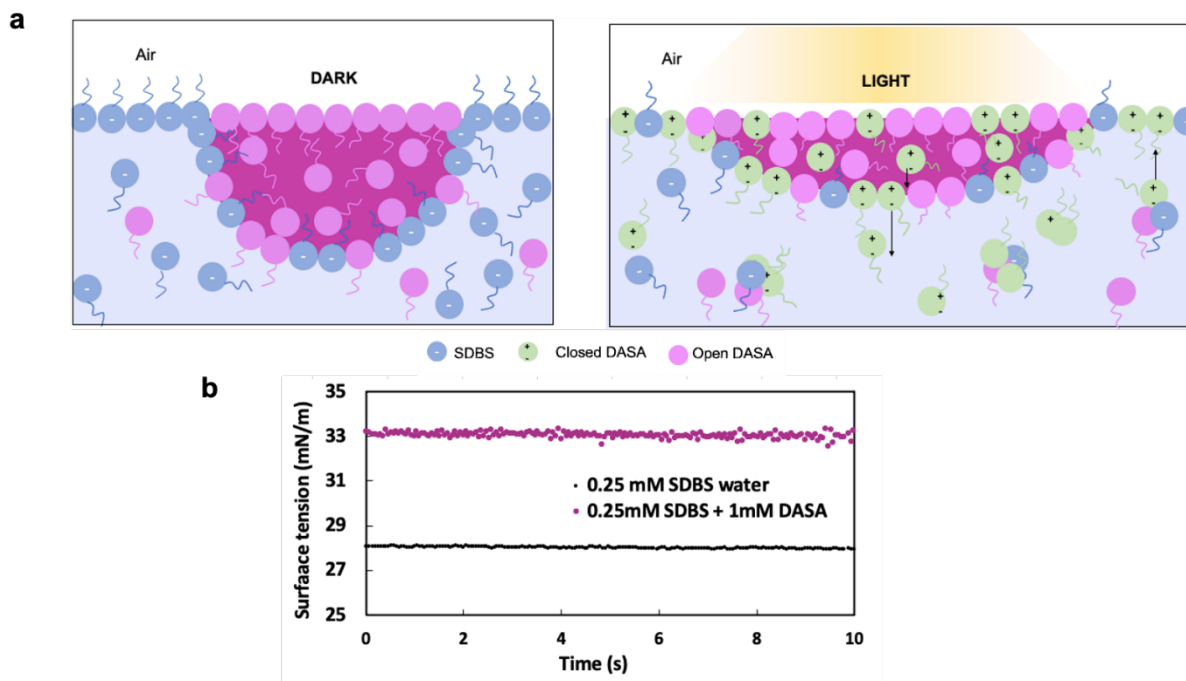
Figure 3.7. a) Cartoon schematic depicting the hypothesized mechanisms by which DASA surfactants produce photowetting in the presence of a charged co-surfactant. Both surfactants initially occupy the toluene-water interface, only DASA surfactant stabilizes toluene-air interface and only co-surfactant is present at the air-water interface (left panel). After photoconversion, changes in polarity of the photosurfactant result in (i) changes in the surface excess of photosurfactant at the toluene-water interface, and (ii) solubility-driven transport of the photosurfactant from the toluene-water interface through the aqueous phase to the air-water interface (right panel). The resulting changes in relative surfactant composition of both interfaces contributes to an increase in spreading relative to changes occurring at the water-toluene interface alone. b) Experimental measurements of air-water interfacial tension demonstrating an increase of interfacial tension due to adsorption of DASA-ester-PEG photosurfactant. Reprinted with permission from Langmuir. 2021, 37 (33), 9939-9951. Copyright 2021 American Chemical Society.

3.6 Conclusion

We performed a comparative study of three photo-responsive surfactants, **Azo-DA-PEG**, **DASA-DA-PEG**, and **SP-DA-PEG** involving photo-induced changes in wetting and interfacial properties at the toluene-water-air interface. These studies reveal that the design and photoswitching kinetics are of substantial importance in the role of photsurfactants' control of interfacial properties. Particularly in the case of photosurfactants with large changes in polarity, such as **DASA-DA-PEG** and **SP-DA-PEG**, we observed rapid and extreme responses in wetting/de-wetting behavior, and in some cases the resultant spreading was sufficient to produce droplet instability. While both surfactants undergo a conformational change from a neutral to charged species, they differ significantly in their respective switching kinetics with **SP-DA-PEG** switching to the hydrophilic, charged **MC-DA-PEG** much faster and to a higher photostationary state than **DASA-DA-PEG**. Importantly, we find that the presence and concentration of an ionic co-surfactant is of incredible importance in dictating the observed interfacial behavior. The partitioning of the photoswitch in the solvents contributes to the range of behaviors, as the adsorption and switching kinetics are influenced by the surrounding media. As such, these dramatic responses are explained not only by the photo-isomerization event, but subsequent molecular transport and interactions with the surrounding bulk phase. We anticipate this relationship between co-surfactants and ionically charged species is generalizable and relevant to industrial applications that rely on the cooperative use of co-surfactants, and moreover is a relatively unexplored aspect of photosurfactant behavior that could be exploited in future applications. Understanding these complexities enables the design of new

photosurfactant systems and their optimization toward responsive functions including triggered spreading, dewetting and destabilization of droplets on solid and fluid surfaces.

3.7 Supplementary Information

Supplementary videos can be found at Langmuir. 2021, 37 (33), 9939-9951. Copyright 2021 American Chemical Society.

Supplementary Video 1   Droplet breakup for 10 mM SP-DA-PEG in toluene in 0.25 mM SDBS in water upon irradiation with 365 nm light

Supplementary Video 2 Droplet wetting and dewetting behavior for the 10mM DASADA-PEG in toluene droplet in 0.25mM SDBS before and during irradiation

Supplementary Video 3 Droplet wetting behavior for 0.1 mM SP-DA-PEG in toluene in 0.25 mM SDBS in water upon irradiation with 365 nm light

3.7.1 Materials and Methods

All chemicals were obtained from Sigma Aldrich, TCI Europe or Fisher Scientific and, unless otherwise noted, all reagents were used as received without further purification. **SP-OH**,[1] **NBD-COOH**,[2] **NBD-OH**,[3] **FM-COOH**,[4] **3-maleimidopropionic acid**,[5] **and azo-mal**[3] were prepared following published protocols. Room temperature reactions were carried out between 22-25 ºC. Thin-layer chromatography (TLC) was performed using Merck silica gel

60 F254 pre-coated plates (0.25 mm) and visualized by exposure to UV light (254 nm) or stained with *p*-anisaldehyde. ^{1}H and ^{13}C NMR spectra were recorded on Varian 400 MHz and 600 MHz spectrometers. Data for ^{1}H NMR spectra are reported as follows: chemical shifts (δ) are reported in ppm and referenced internally from the proteo-solvent resonance. Coupling constants (*J*) are reported in Hz. Abbreviations for the peak multiplicities are *s* (singlet), *d* (doublet), *dd* (doublet of doublet), *t* (triplet), *q* (quadruplet) and *m* (multiplet). Data for ^{13}C NMR spectra are reported in terms of chemical shift (d ppm).

 White light source. A Schott Ace 150 W fiber optic white light source was chosen for all experiments requiring visible light due to its broad coverage of the absorbance spectrum of DASA-DA-PEG. Absolute irradiance of the white light source was measured using a USB 4000-UV-Vis spectrometer (OceanOptics, Inc., USA). For experiments involving SP-DA-PEG and Azo-DA-PEG, a fiber-coupled 365-nm LED (Thorlabs M365F1) with controllable intensity was used.
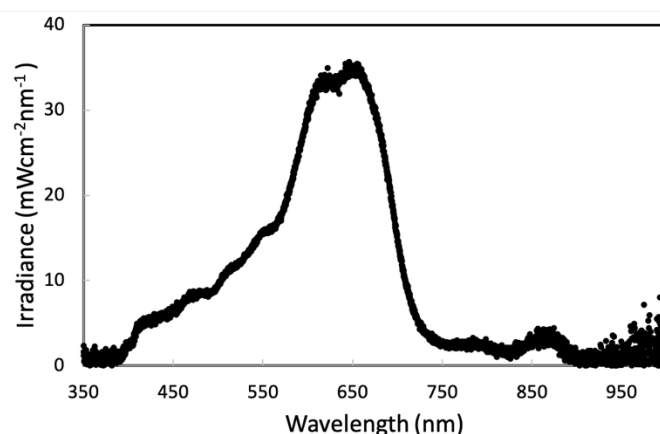

Figure S1. Absorbance spectrum and irradiance of the white light source used in the experiments.

3.7.2 Experimental Methods

Preparation of Photosurfactants by Norbornadiene (NBD). **NBD-PEG** or **mal-PEG** (1.00 eq) was dissolved in chloroform (0.05 M) in a 20 mL vial equipped with stir bar. To this solution was added the functionalized photoswitch, **azo-mal**, **DASA-NBD** or **SP-NBD** (1.20 – 1.33 eq) and 3,6-di-2-pyridyl-1,2,4,5-tetrazine (DpTz) (1.5 eq/NBD). The vial was capped under an atmosphere of air. A vent needle was placed in the cap and the solution was allowed to stir (17 – 24 h). Deprotection of NBD group to cyclopentadiene (Cp) and the subsequent Diels–Alder reaction with maleimide was monitored by ^{1}H NMR. Before purification by precipitation, excess DpTz was quenched with norbornene (1 eq/DpTz) to promote solubility and make removal by precipitation more effective. After stirring an additional 30 min, the solvent was removed under reduced pressure and the residue taken up in ethanol (EtOH). The solution was cooled to –78 °C and the surfactant was isolated by cold centrifugation. The resulting material was dried under reduced pressure to afford the desired surfactants as highly colored viscous liquids. Near quantitative incorporation of each photoswitch onto PEG was confirmed by ^{1}H NMR. Full synthetic details and ^{1}H NMR spectra can be found in the Supplemental Information.

Light source. A Schott Ace 150 W fiber optic white light source was chosen for all experiments in which DASA surfactants are utilized due to its broad coverage of the absorbance spectrum of DASA-DA-PEG (Supplementary Fig. 1). For experiments involving SP-DA-PEG and Azo-DA-PEG, a fiber-coupled 365 nm LED (Thorlabs M365F1) with controllable intensity was used.

Droplet wetting experiments. All experiments were performed using glassware cleaned by sonication in water and isopropyl alcohol to prevent contamination by residual surfactant molecules and dust. DI water containing sodium dodecylbenzene sulfonate (SDBS) at a concentration of 0.25mM was added to a glass petri dish where a $5\mu L$ droplet of toluene containing photosurfactant at the desired concentration was administered and floated atop the water:SDBS solution. The droplet was allowed to equilibrate for ~1 minute. Light was then delivered from approximately 1 inch above the droplet by either a fiber optic white light source (for DASA-DA-PEG) or a fiber-coupled 365 nm LED (for SP-DA-PEG and Azo-DA-PEG) at 230 mW/cm² and 49 mW/cm², respectively. Videos were recorded from the top and the side in order to track droplet wetting over time using a Canon Rebel SL2 (100 mm f/2.8 Macro USM fixed lens, 1x magnification, 30 frames per second).

Kinetic analysis. The photoinduced optical absorption kinetics were measured using a pump-probe setup described in previously reported procedures.[51] In addition to characterizing the kinetics of the photoreactions, these measurements also provide a measurement of the photostationary state, i.e., the equilibrium fractional conversion of the photoswitch under illumination. Unfortunately, in the presence of the co-surfactant, it is very difficult to accurately measure the photostationary state by NMR or study the kinetics at the interface of the fluids using UV-Vis spectrophotometry, and as such kinetic analysis presented is for solutions in the absence of co-surfactant.

Interfacial tension measurements. There are many challenges associated with the acquisition of accurate interfacial measurements of photosurfactants under irradiation. In order to perform a systematic study, it would be ideal to uniformly characterize each surfactant's behavior at each interface using the same methodology; however, instrumentation often limits or prohibits the ability to simultaneously administer controlled, uniform illumination during measurements, and the low interfacial tension of many photosurfactant systems can prevent accurate measurements. Thus, surface and interfacial tension measurements were obtained here *via* a combination of pendant drop, Wilhelmy plate and contact angle experiments (see Supplementary Information for full experimental details).

Pendant drop measurements were used to measure the interfacial tension changes due to irradiation for photosurfactants at a toluene-water interface. Briefly, using a curved hook needle tip, a droplet of photosurfactant solution in toluene was produced in a quartz cuvette filled with 0.25 mM SDBS in water and allowed to equilibrate for 2-5 minutes or until the initial surface tension value was steady. Measurements of droplet volume and surface tension were first recorded in a darkened room to minimize switching due to ambient light. The appropriate light source (365 nm LED for spiropyran and azobenzene-based surfactants and white light for DASA surfactants) was directed onto the droplet, and measurements were recorded from the onset of irradiation until changes in interfacial tension were no longer observed (typically within 10 minutes).

Contact angle measurements were used for some photosurfactant solution droplets to probe surface tension at the three-phase air-water-toluene interface. Video imaging was used to monitor droplet wetting from the side of a rectangular glass vial and irradiation was applied from directly above. ImageJ was used to determine the contact angle at the air-water interface before and during irradiation. Measurements were averaged across 5 recordings. Due to its initial colored state and visible light absorption, DASA was the most easily visualized by this technique.

Wilhelmy plate measurements were used to measure interfacial tension changes under irradiation for some photosurfactant solutions at the toluene-air interface. Surface pressure was measured using a filter paper Wilhelmy tensiometer (Riegler and Kirstein, Germany). Samples were pipetted into a glass petri dish which is cleaned prior to experiments by rinsing with acetone, isopropyl alcohol, and deionized water (Milli-Q). Changes in surface pressure were recorded as an overhead light source was turned on and a steady-state was reached.

3.7.3 Synthesis

Synthesis performed by Sophia Bailey.

Small molecule building blocks
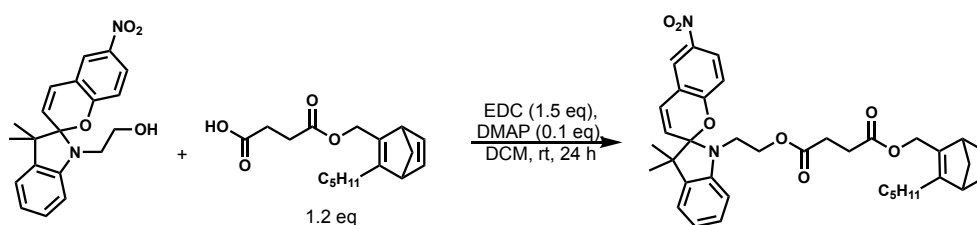
2-(3',3'-dimethyl-6-nitrospiro[chromene-2,2'-indolin]-1'-yl)ethyl ((3-pentylbicyclo[2.2.1]hepta-2,5-dien-2-yl)methyl) succinate (SP-NBD):

SP-OH[1] (1.74 g, 4.93 mmol, 1.00 eq) and **NBD-COOH**[2] (1.73 g, 5.92 mmol, 1.20 eq) were dissolved in 17.4 mL dichloromethane (DCM). To this solution was added 1-ethyl-3-(3-dimethylaminopropyl)carbodiimide (EDC, 1.42 g, 7.39 mmol, 1.50 eq) and 4-dimethylaminopyridine (DMAP, 60.2 mg, 0.493 mmol, 0.100 eq) and the resulting mixture was capped under an atmosphere of air and allowed to stir for 24 h. The solution was then washed with H_2O (3 x 20 mL), dried over $MgSO_4$ and concentrated. The residue was loaded onto a silica plug. The material was first washed with hexanes (50 mL), then the desired product (**SP-NBD**) was eluted with 5% EtOAc in hexanes and concentrated to afford **SP-NBD** as a viscous pink/green liquid (1.89 g, 3.01 mmol, 61%).

SP-NBD: R_f (Hexanes:EtOAc, 95:5): 0.22; ^{1}H NMR (600 MHz, CDCl$_3$) δ 8.03 – 8.00 (m, 2H), 7.21 – 7.19 (m, 1H), 7.09 (d, J = 7.3 Hz, 1H), 6.93 – 6.88 (m, 2H), 6.76 – 6.67 (m, 4H), 5.89 (d, J = 10.6 Hz, 1H), 4.73 (dd, J = 4.3, 12.2 Hz, 1H), 4.57 (dd, J = 4.2, 12.1 Hz, 1H), 4.29 – 4.20 (m, 2H), 3.53 – 3.36 (m, 4H), 2.60 - 2.53 (m, 4H), 2.24 – 2.10 (m, 2H), 1.93 – 1.87 (m, 2H), 1.42 – 1.25 (m, 7H), 1.21 – 1.14 (m, 5H), 0.86 (t, J = 7.4 Hz, 3H) ppm; ^{13}C NMR (100 MHz, CDCl$_3$) δ 172.2, 172.1, 159.4, 155.6, 146.6, 142.8, 142.0, 141.9, 140.8, 135.7, 128.3, 127.8, 125.9, 122.8, 121.8, 121.8, 119.9, 118.4, 115.5, 106.7, 106.5, 71.3, 62.6, 61.0, 53.8, 52.8, 52.0, 42.3, 31.4, 29.0, 28.9, 28.3, 26.8, 25.8, 22.5, 19.8, 14.0 ppm; IR (ATR) 3064, 2960, 2929, 2861, 1731, 1480, 1335, 1270, 1154, 952, 746 cm^{-1}; HRMS (ES+) Exact mass cald. for C$_{37}$H$_{42}$N$_2$O$_7$ [M+Na]$^+$: 649.2890, found: 649.2887.
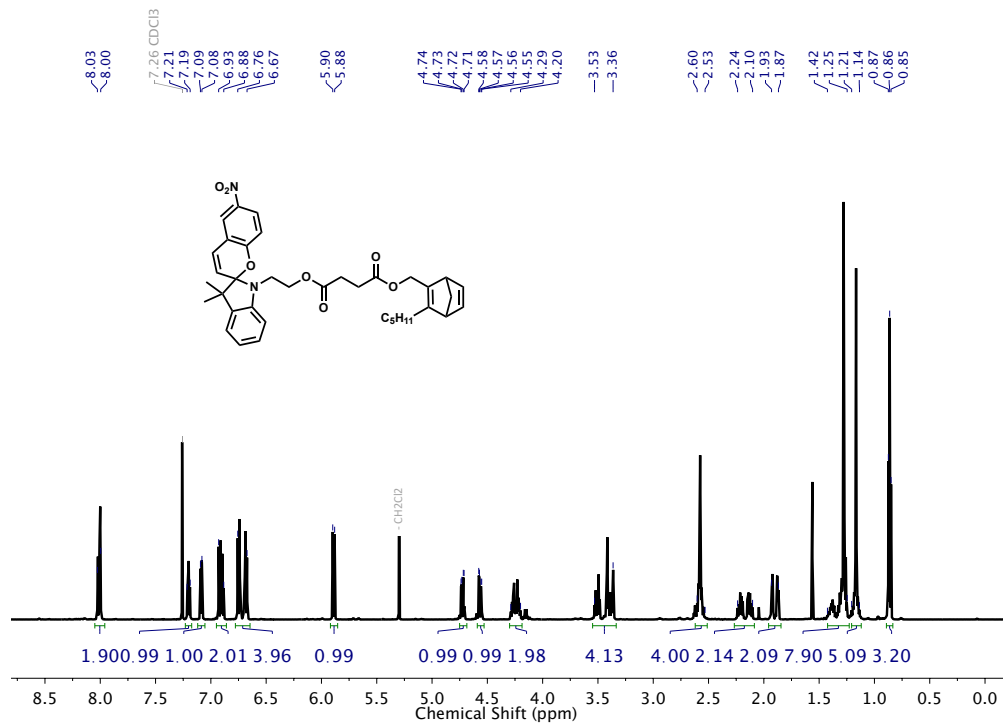
Figure S2. ^{1}H NMR (600 MHz, CDCl$_3$) **SP-NBD**
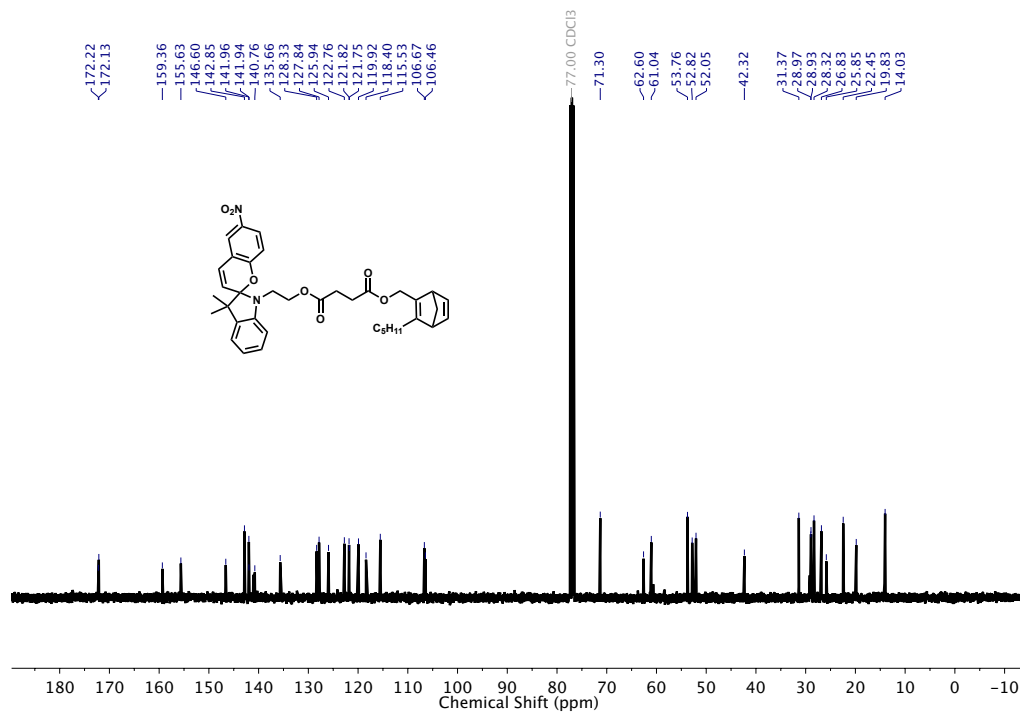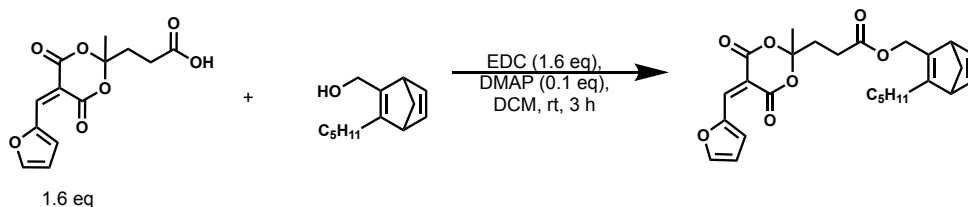

Figure S3. ^{13}C NMR (100 MHz, CDCl$_3$) **SP-NBD**

3-(5-(furan-2-ylmethylene)-2-methyl-4,6-dioxo-1,3-dioxan-2-yl)propanoic 4-oxo-4-

((3-pentyl bicyclo[2.2.1]hepta-2,5-dien-2-yl)methoxy)butanoic anhydride (FM-NBD):

FM-COOH[3] (2.80 g, 10.0 mmol, 1.50 eq) and **NBD-OH**[3] (1.28 g, 6.67 mmol, 1.00 eq)

were dissolved in 12.8 mL dichloromethane (DCM). To this solution was added EDC (1.92

g, 10.0 mmol, 1.50 eq) and DMAP (81.4 mg, 0.667 mmol, 0.100 eq) and the resulting

mixture was capped under an atmosphere of air and allowed to stir at rt while monitoring by

TLC (6:1 hexanes, EtOAc). After 2 h, consumption of the FM-COOH starting material was

observed due to some degradation, so an additional portion was added (0.280 g, 1.00 mmol,

0.100 eq), along with EDC (0.192 g, 1.00 mmol, 0.100 eq). After an additional 1 h, the

solution was then washed with H_2O (2 x 13 mL), then brine (1 x 13 mL). The solvent was

removed, and the residue loaded onto a silica plug. The product was eluted with DCM to

afford **FM-NBD** as a yellow viscous liquid (2.14 g, 4.71 mmol, 71%).

FM-NBD: R_f (DCM): 0.58; ^{1}H NMR (400 MHz, CDCl$_3$) δ 8.47 (d, J = 3.9 Hz, 1H), 8.36

(s, 1H), 7.85 (d, J = 1.2 Hz, 1H), 6.76 – 6.68 (m, 3H), 4.73 (d, J = 12.2 Hz, 1H), 4.58 (d, J =

12.2 Hz, 1H), 3.40 (d, J = 25.8 Hz, 2H), 2.61 – 2.57 (m, 2H), 2.34 – 2.31 (m, 2H), 2.26 –

2.09 (m, 2H), 1.93 – 1.87 (m, 2H), 1.74 (s, 3H), 1.45 – 1.12 (m, 6H), 0.86 (t, J = 7.2 Hz, 3H)

ppm; ^{13}C NMR (100 MHz, CDCl$_3$) δ 172.2, 162.9, 159.8, 155.8, 150.6, 150.2, 142.9, 142.0,

141.5, 140.7, 128.4, 115.4, 107.2, 105.0, 71.3, 61.1, 53.8, 52.1, 35.2, 31.4, 28.3, 28.1, 26.8,

26.1, 22.5, 14.0 ppm; IR (ATR) 2957, 2929, 2857, 1721, 1593, 1463, 1365, 1268, 1138,

946, 769 cm^{-1}; HRMS (ES+) Exact mass cald. for $C_{26}H_{30}O_7$ [M+Na]$^+$: 477.1889, found:

477.1884.
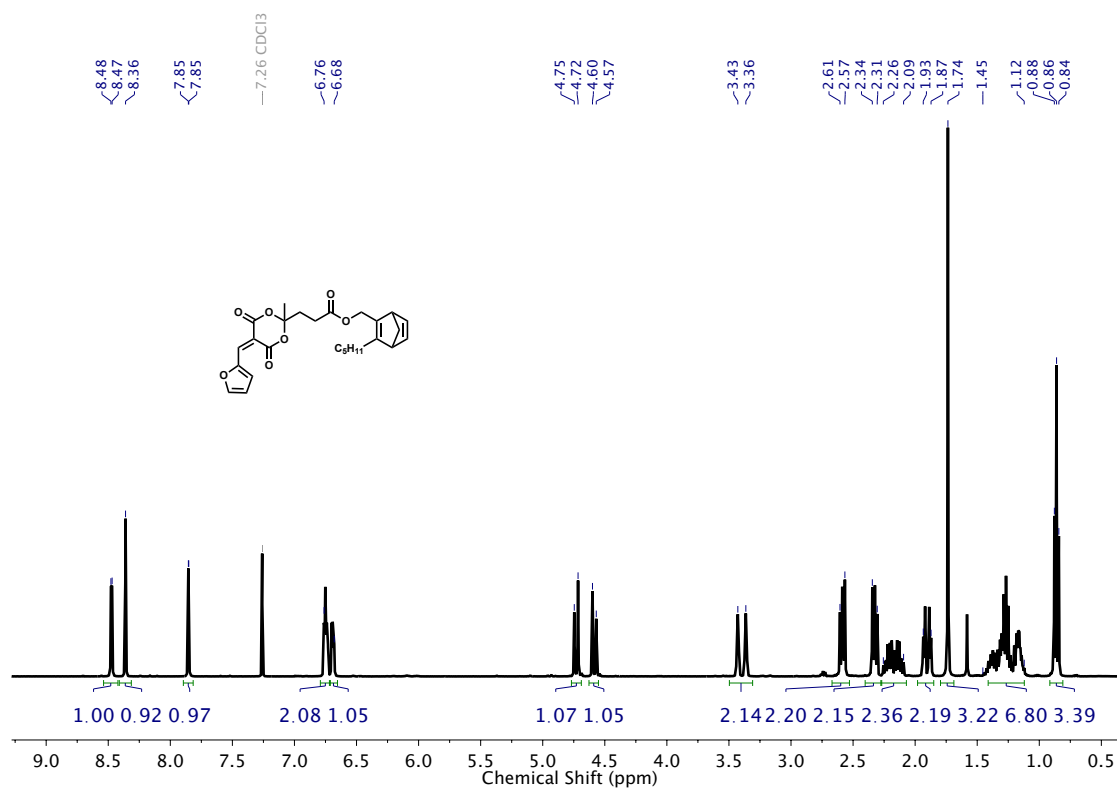
Figure S4. ^{1}H NMR (400 MHz, CDCl$_3$) **FM-NBD**
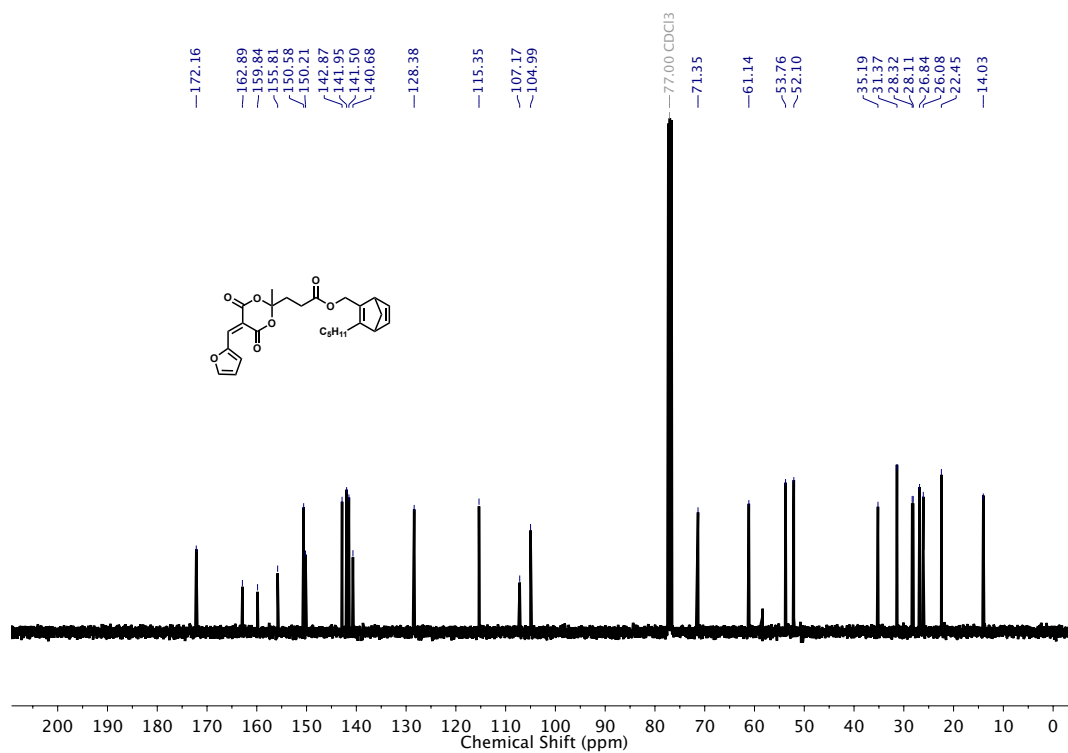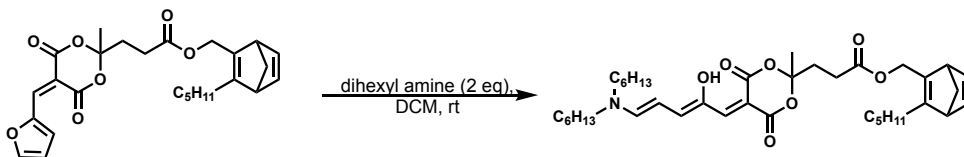
Figure S5. ^{13}C NMR (100 MHz, CDCl$_3$) **FM-NBD**

3-(5-((2Z,4E)-5-(dihexylamino)-2-hydroxypenta-2,4-dien-1-ylidene)-2-methyl-4,6-dioxo-1,3-dioxan-2-yl)propanoic 4-oxo-4-((3-pentylbicyclo[2.2.1]hepta-2,5-dien-2-yl)methoxy)butanoic anhydride (DASA-NBD)

FM-NBD (245 mg, 0.539 mmol, 1.00 eq) was dissolved in THF (1.35 mL) in a 20 mL scintillation vial equipped with stir bar. To the solution was added dihexyl amine (0.126 mL, 0.539 mmol, 1.00 eq). The solution was stirred for 10 minutes then cooled to 0 °C for 20 min. The solvent was removed by rotary evaporation and the material was precipitated in cold ether to afford 34 mg (0.0531 mmol, 10%) of **DASA-NBD** as a pink solid. An additional 69 mg (0.108 mmol, 20%) of **DASA-NBD** was recovered from the filtrate by loading the residue onto a plug of silica, rinsing with hexanes, then eluting with 1:1 EtOAc, hexanes.

FM-NBD: ^{1}H NMR (400 MHz, CDCl$_3$) δ 11.39 (s, 1H), 7.18 (d, J = 12.3 Hz, 1H), 7.06 (s, 1H), 6.76 – 6.68 (m, 3H), 6.05 (t, J = 12.3 Hz, 1H), 4.72 (d, J = 12.2 Hz, 1H), 4.57 (d, J = 12.2 Hz, 1H), 3.44 – 3.36 (m, 6H), 2.61 – 2.57 (m, 2H), 2.30 – 2.26 (m, 2H), 2.24 – 2.09 (m, 2H), 1.94 – 1.87 (m, 2H), 1.70 (s, 3H), 1.70 – 1.62 (m, 4H), 1.41 – 1.24 (m, 16H), 1.21 – 1.14 (m, 2H) 0.92 – 0.85 (m, 9H); ^{13}C NMR (100 MHz, CDCl$_3$) δ 172.7, 166.8, 164.9, 157.5, 155.5, 151.3, 144.9, 143.0, 141.9, 140.9, 139.0, 103.9, 102.3, 90.3, 71.3, 60.9, 57.7, 53.7, 52.1, 49.7, 34.8, 31.4, 31.3, 31.2, 28.9, 28.3, 28.2, 27.1, 26.9, 26.6, 26.1, 24.8, 22.5, 22.4, 14.0, 13.9 ppm; IR (ATR) 2957, 2928, 2858, 1715, 1673, 1569, 1455, 1414, 1097,

917, 747 cm^{-1}; HRMS (ES+) Exact mass cald. for C$_{38}$H$_{57}$NO$_7$ [M+Na]$^+$: 662.4033, found: 662.4037.
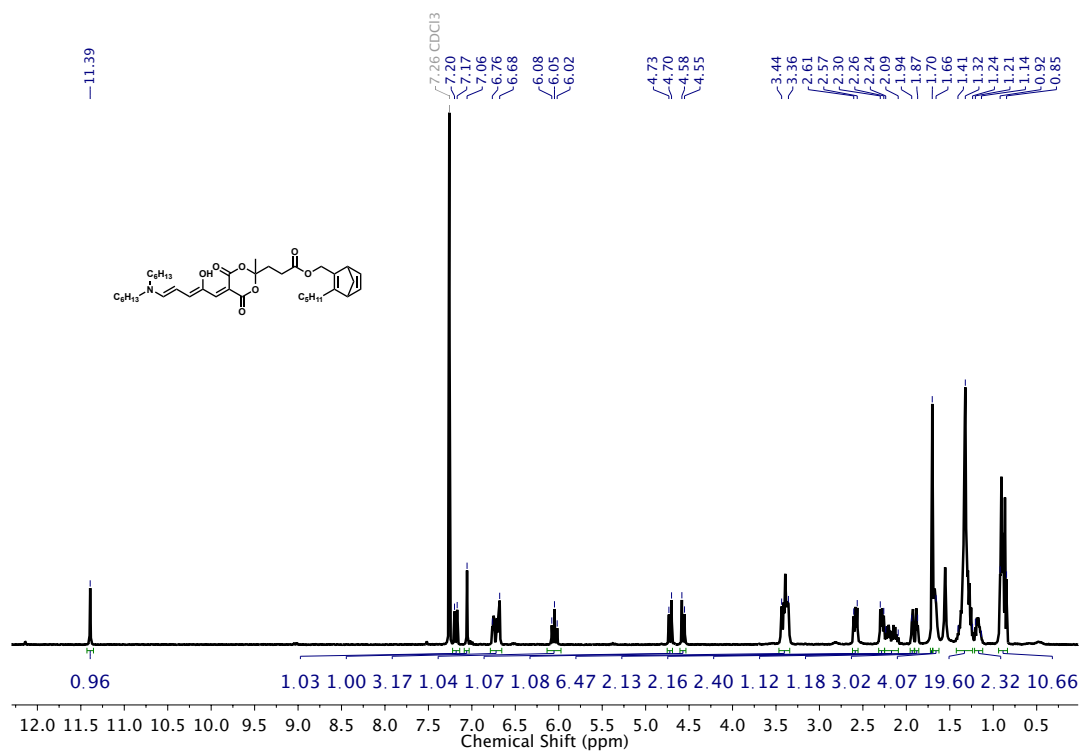
Figure S6. ^{1}H NMR (400 MHz, CDCl$_3$) **DASA-NBD**
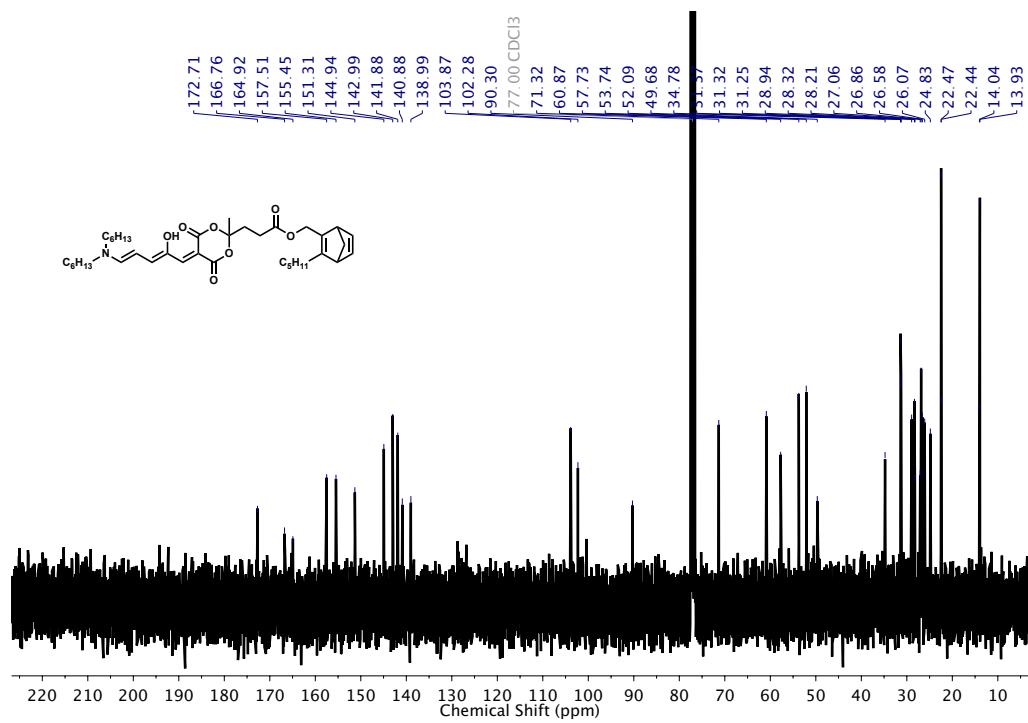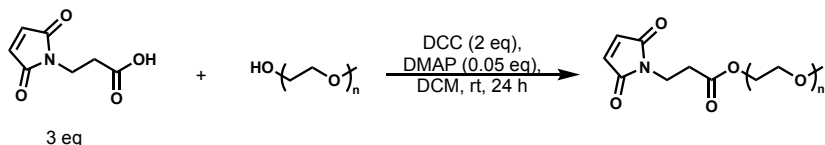
Figure S7. ^{13}C NMR (100 MHz, CDCl$_3$) **DASA-NBD**

Synthesis of polymer building blocks

Synthesis of mal-PEG:

Prepared following a modified literature procedure.[2] To a 20 mL vial equipped with stir bar was added MeO-PEG-OH (purchased from Sigma-Aldrich, M_n = 550 g/mol, 0.909 mL, 1.82 mmol, 1.00 eq), 3-maleimidopropionic acid (923 mg, 5.45 mmol, 3.00 eq), N, N'-Dicyclohexylcarbodiimide (DCC) (750 mg, 3.64 mmol, 1.50 eq), DMAP (11.0 mg, 0.0909 mmol, 0.0500 eq) and 4 mL DCM. The vial was capped under air and allowed to stir at rt for 24 h (at which complete formation of the ω-ester was confirmed by ^{1}H NMR of the crude reaction mixture). The solution was filtered to remove any insoluble solids and then the DCM was removed under reduced pressure. Ethanol (EtOH) (5 mL) was added to the residual mixture and the resulting solution was filtered before an additional 40 mL of EtOH was added and the solution was cooled to −78 °C. The functionalized polymer was isolated by cold centrifugation. The supernatant was decanted, and the cold precipitation and centrifugation was repeated once more. The resulting polymer was dried under reduced pressure to afford the desired **mal-PEG** (1.11 g, 1.54 mmol, 85%) as red/pink viscous liquid. $M_{n(\text{NMR})}$ = 800 g/mol.
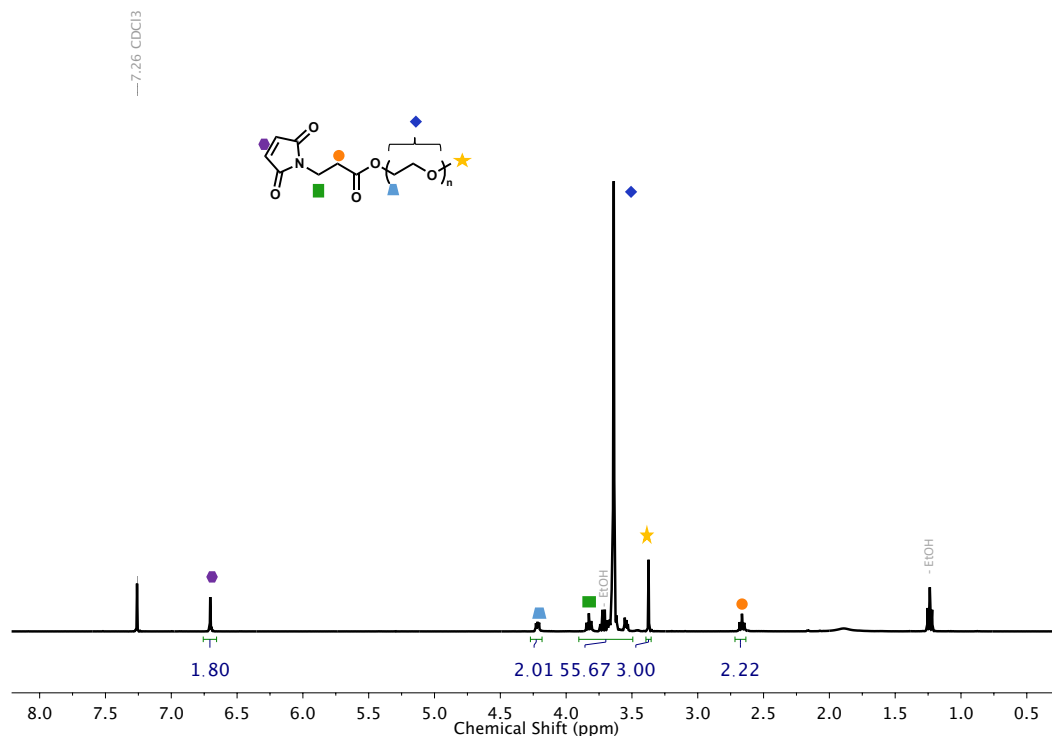
Figure S8. ^{1}H NMR (400 MHz, CDCl$_3$) **mal-PEG**
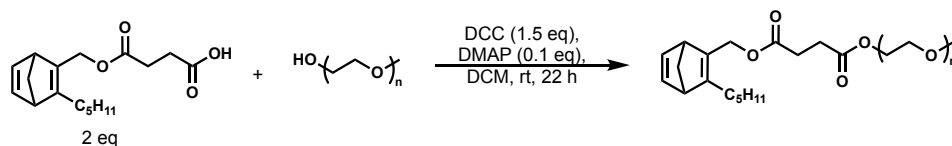
Synthesis of NBD-PEG:

Prepared following a published procedure, modified as follows.[2] To a 20 mL vial

equipped with stir bar was added MeO-PEG-OH (purchased from Sigma-Aldrich, $M_n = 550$

g/mol, 1.00 mL, 2.00 mmol, 1.00 eq), NBD-COOH[2] (1.17 g, 4.00 mmol, 2.00 eq), DCC

(620 mg, 3.50 mmol, 1.50 eq), DMAP (24.4 mg, 0.200 mmol, 0.100 eq) and 2.20 mL DCM.

The vial was capped under air and allowed to stir at rt for 22 h (at which time complete

formation of the ω-ester was confirmed by ^{1}H NMR of the crude reaction mixture). The

solution was filtered to remove any insoluble solids and the DCM was removed under

reduced pressure. Ethanol (EtOH) (24 mL) was added to the residual mixture and the

86

resulting solution was cooled to −78 °C. The functionalized polymer was isolated by cold centrifugation. The supernatant was decanted, and the cold precipitation and centrifugation was repeated twice more. The resulting polymer was dried under reduced pressure to afford the desired **NBD-PEG** (1.42 g, 1.71 mmol, 86%) as viscous liquid. $M_{n(NMR)}$ = 900 g/mol.
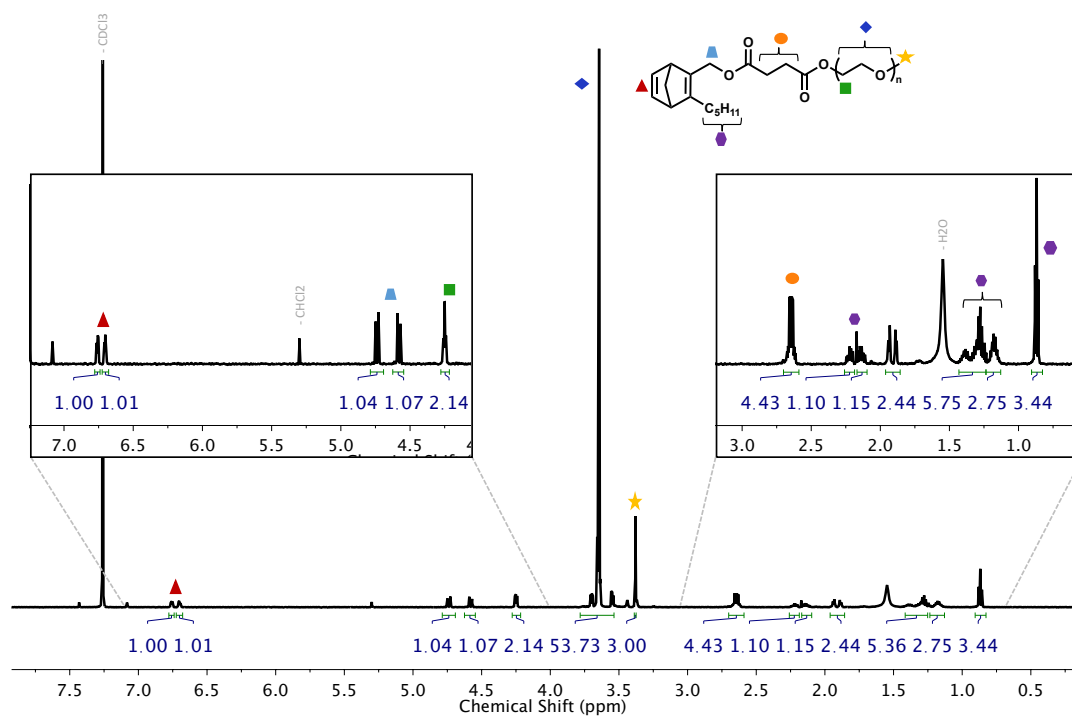
**Figure S9.** ^{1}H NMR (600 MHz, CDCl$_3$) **NBD-PEG**

3.7.4 Photosurfactant Synthesis by Norbornadiene "Click"
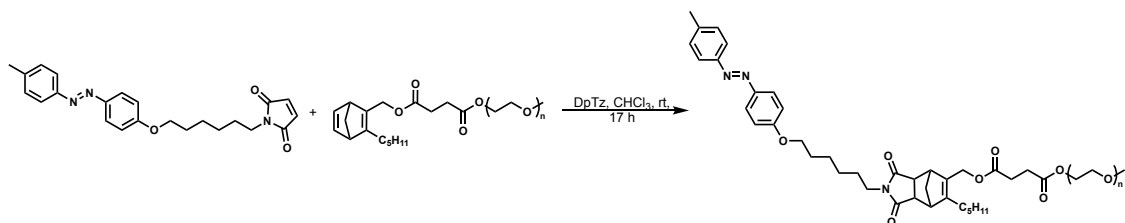
Synthesis of azo-DA-PEG

To a 20 mL vial equipped with stir bar was added **azo-mal**[6] (51.9 mg, 0.133 mmol, 1.20 eq), **NBD-PEG** (100. mg, 0.111 mmol, 1.00 eq), 3,6-di-2-pyridyl-1,2,4,5-tetrazine (DpTz) (42.7 mg, 0.181 mmol, 1.63 eq) and 2 mL chloroform. The vial was capped with a rubber septa under an atmosphere of air. A vent needle was placed in the rubber septa and the solution was allowed to stir at rt for 17 h. Reaction completion was confirmed by ^{1}H NMR of crude reaction mixture. Upon completion norbornylene (17.0 mg, 0.181 mmol, 1.63 eq) was added to the solution and stirred for 30 min. The solvent was removed under reduced pressure and the residue taken up in EtOH (10 mL). The solution was cooled to -78 °C and the surfactant was isolated by cold centrifugation. The supernatant was decanted, and the cold precipitation and centrifugation was repeated once more. The resulting material was dried under reduced pressure to afford the desired **azo-DA-PEG** (73 mg, 0.0579 mmol, 52%) as vibrant orange, viscous liquid. $M_{n(NMR)} = 1260$ g/mol.

Figure S10. ^{1}H NMR (600 MHz, CDCl$_3$) **azo-DA-PEG**
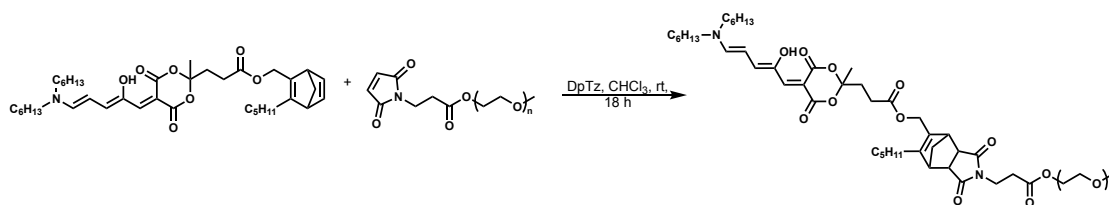
Synthesis of DASA-DA-PEG

To a 20 mL vial equipped with stir bar was added **DASA-NBD** (96.0 mg, 0.150 mmol, 1.33 eq), mal-PEG (90.0 mg, 0.113 mmol, 1.00 eq), DpTz (44.3 mg, 0.188 mol, 1.66 eq) and 2.3 mL chloroform. The vial was capped with a rubber septa under an atmosphere of air. A vent needle was placed in the rubber septa and the solution was allowed to stir for 18 h. Reaction completion was confirmed by ^{1}H NMR of crude reaction mixture. Upon completion norbornylene (17.7 mg, 0.188 mmol, 1.66 eq) was added to the solution and stirred for 1 h. The solution was passed through a silica plug. The material was rinsed with

89

1% MeOH in DCM (50 mL), then the pink product was eluted with a solution of 10% MeOH in DCM (50 mL). The solvent was removed under reduced pressure and the residue taken up in EtOH (10 mL). The solution was cooled to −78 °C and the surfactant was isolated by cold centrifugation. The supernatant was decanted, and the resulting polymer was dried under reduced pressure to afford the desired **DASA-DA-PEG** (122 mg, 0.0865 mmol, 77%) as vibrant pink, viscous liquid. $M_{n(\mathrm{NMR})} = 1410$ g/mol.
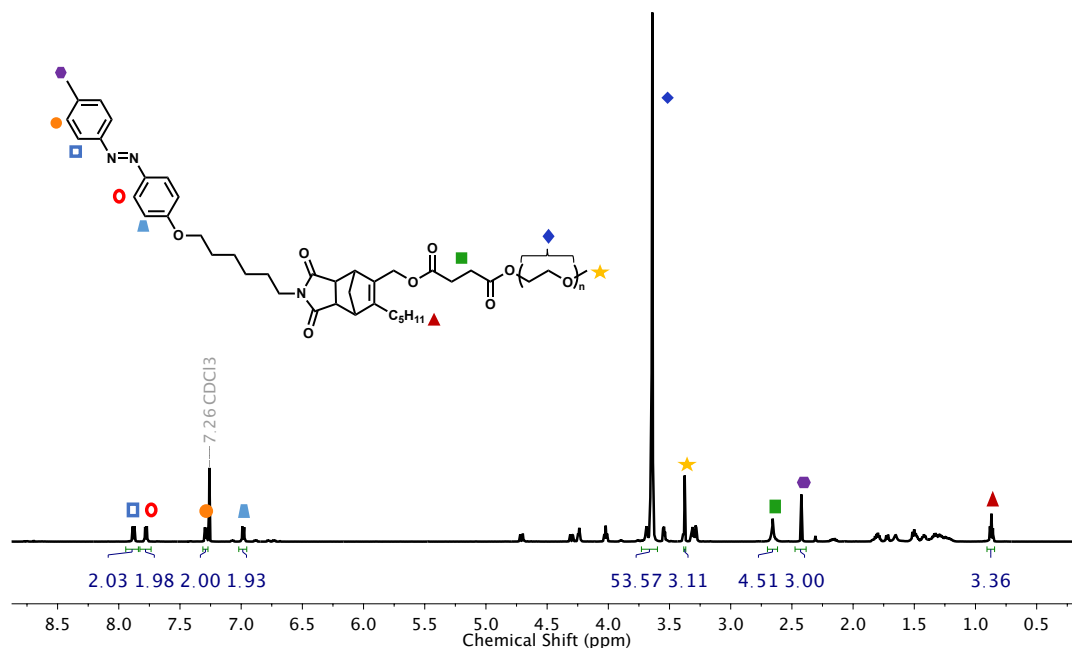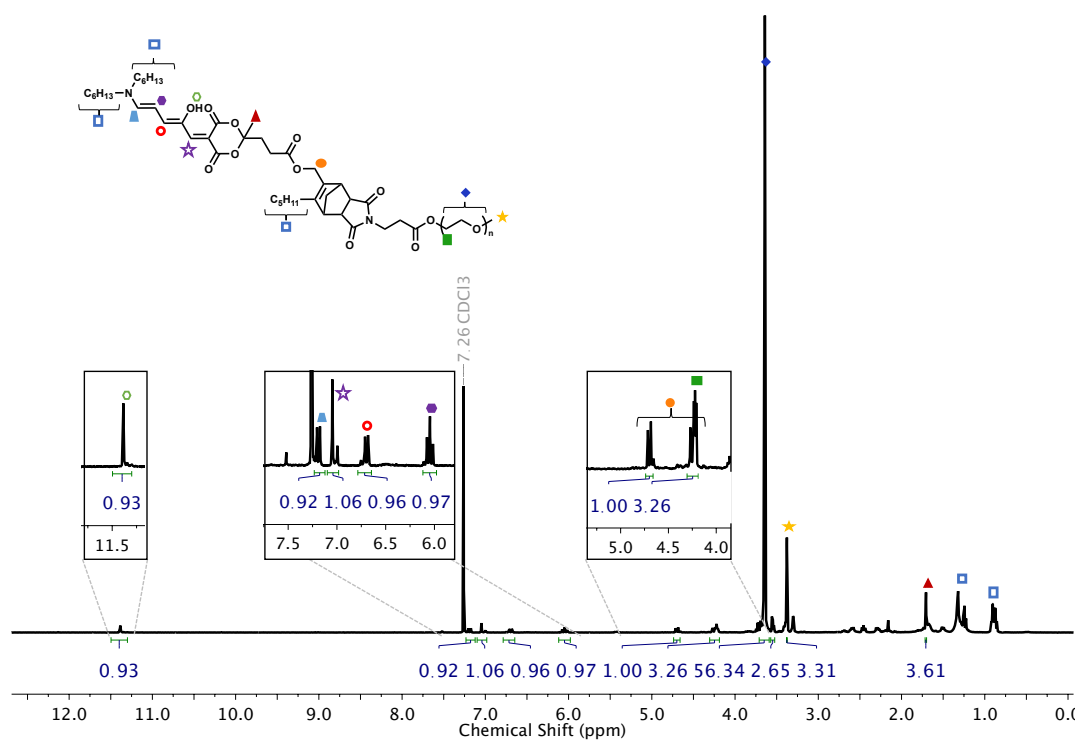

Figure S11. ^{1}H NMR (400 MHz, CDCl₃) **DASA-DA-PEG**
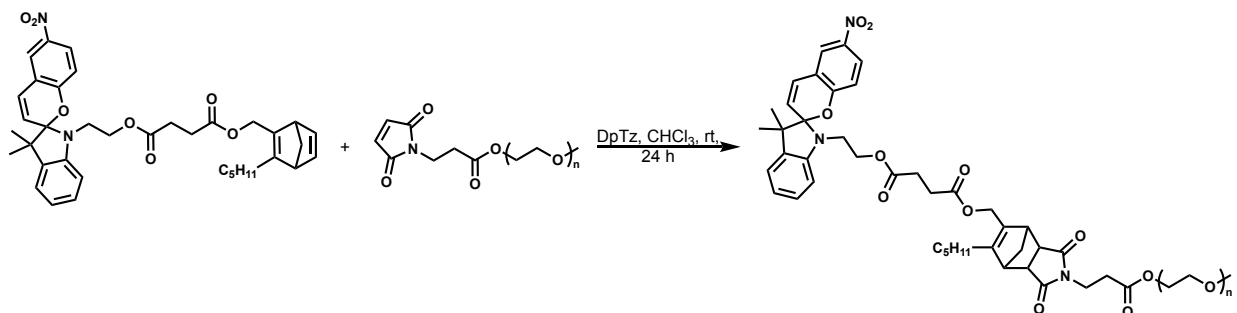
Synthesis of SP-DA-PEG

To a 20 mL vial equipped with stir bar was added **SP-NBD** (506 mg, 0.807 mmol, 1.22 eq), **mal-PEG** (528 mg, 0.660 mmol, 1.00 eq), DpTz (346 mg, 1.47 mol, 2.22 eq) and 14 mL chloroform. The vial was capped with a rubbers septa under an atmosphere of air. A vent needle was placed in the rubber septa and the solution was stirred for 15 h. Reaction progress was monitored by ^{1}H NMR of the crude reaction mixture. After 15 h, ^{1}H NMR indicated unreacted mal-PEG was still present. An additional portion of **SP-NBD** was added (128 mg, 0.204 mmol, 0.309 eq) and the solution was stirred an additional 9 h. Reaction completion was confirmed by ^{1}H NMR of the crude reaction mixture. Upon completion norbornylene (138 mg, 1.47 mmol, 2.22 eq) was added to the solution and stirred for 30 min. The solution was passed through a silica plug. The material was rinsed with DCM, then the pink product was eluted with a solution of 10% MeOH in DCM (50 mL). The solvent was removed under reduced pressure and the residue taken up in EtOH (25 mL). The solution was cooled to −78 °C and the surfactant was isolated by cold centrifugation. The supernatant was decanted, and the cold precipitation and centrifugation was repeated once more. The resulting material was dried under reduced pressure to afford the desired **SP-DA-PEG** (475 mg, 0.342 mmol, 52%) as green/pink viscous liquid. $M_{n(NMR)} = 1390$ g/mol.
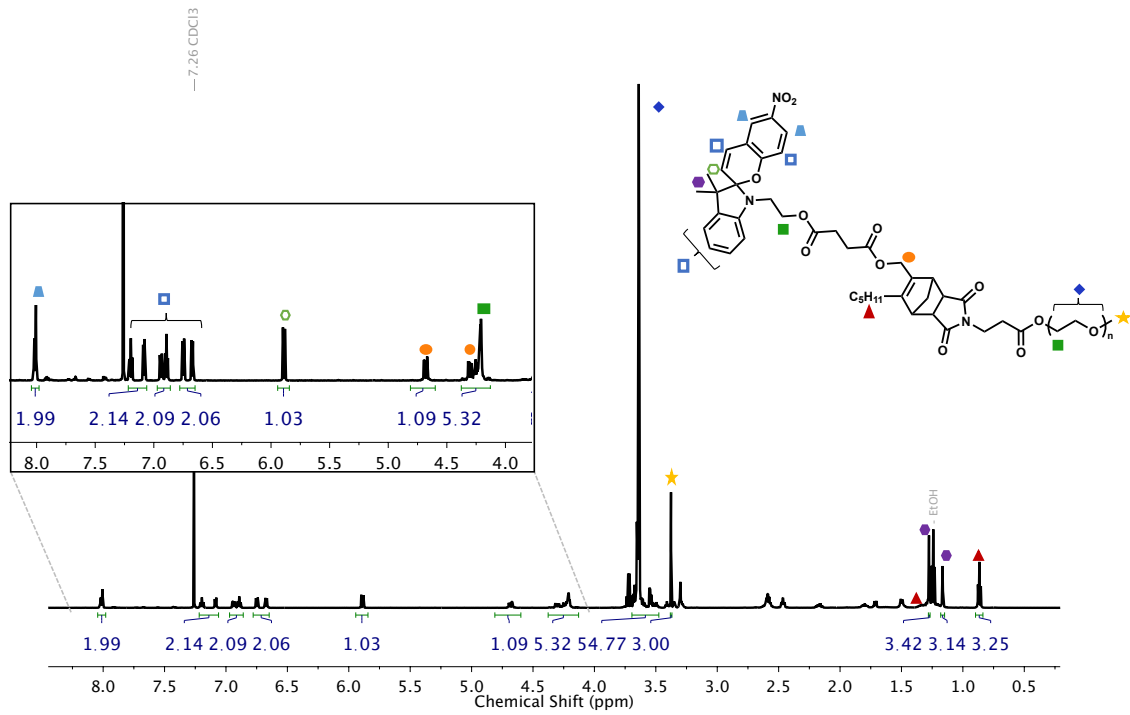
Figure S12. ^{1}H NMR (600 MHz, CDCl$_3$) **SP-DA-PEG**

3.7.5 Alternative DASA-ester-PEG Photosurfactant Synthesis
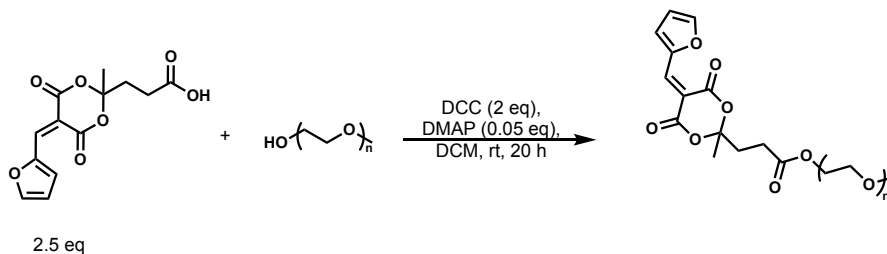
Synthesis of FM-PEG

To a 20 mL vial equipped with stir bar was added MeO-PEG-OH (purchased from Sigma-Aldrich, $M_n = 550$ g/mol, 0.30 mL, 0.60 mmol, 1.0 eq), **FM-COOH**[3] (420 mg, 1.5 mmol, 2.5 eq), DCC (250 mg, 1.2 mmol, 2.0 eq), DMAP (3.7 mg, 0.03 mmol, 0.050 eq) and 1.3 mL DCM. The vial was capped with a rubber septa under air starting and allowed to stir at rt for 20 h. Completion of the reaction was confirmed by ^{1}H NMR of the crude reaction mixture. Upon completion, the solution was filtered to remove any insoluble solids and the DCM was removed under reduced pressure. The solvent was removed under reduced pressure and the residue taken up in ethanol (EtOH) (10 mL). The solution was cooled to -78 °C and the functionalized polymer was isolated by cold centrifugation. The supernatant was decanted, and the cold precipitation and centrifugation was repeated twice more. The resulting polymer was dried under reduced pressure to afford the desired **FM-PEG** (0.176 g, 0.214 mmol, 36%) as viscous liquid. $M_{n(NMR)} = 820$ g/mol.
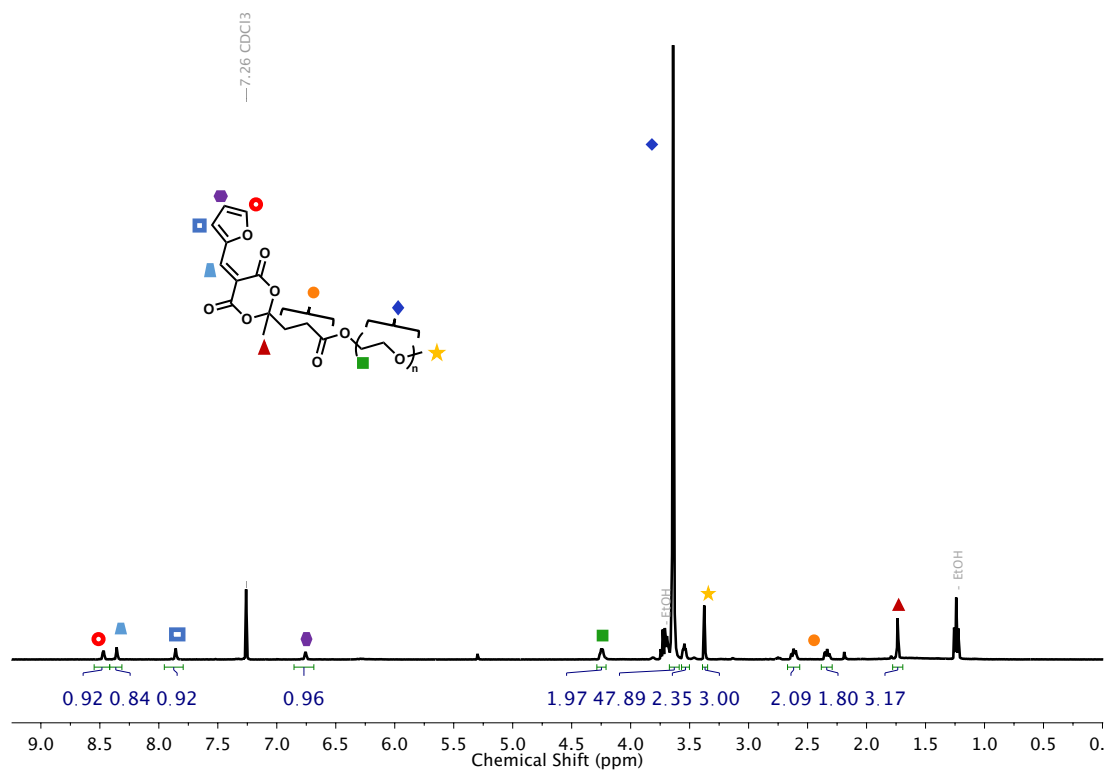
Figure S13. ^{1}H NMR (400 MHz, CDCl$_3$) **FM-PEG**
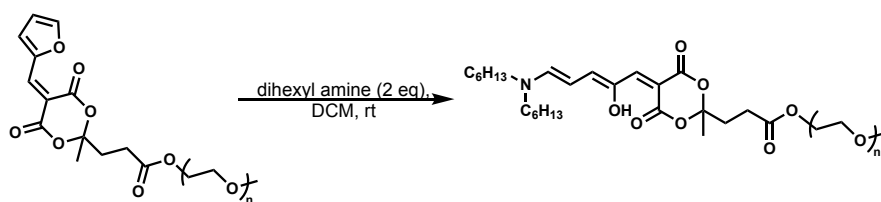
Synthesis of DASA-ester-PEG:

To a 20 mL vial equipped with stir bar was added **FM-PEG** (0.176 g, 0.220 mmol, 1.0 eq), dihexyl amine (0.103 mL, 0.428 mmol, 2.0 eq) and 10 mL DCM. The vial was capped with a rubber septa under air starting and allowed to stir at rt for 30 min. The solvent was removed under reduced pressure and the residue taken up in diethyl ether (10 mL). The

94

solution was cooled to −78 °C and the functionalized polymer was isolated by cold centrifugation. The supernatant was decanted, and the cold precipitation and centrifugation was repeated twice more. The resulting polymer was dried under reduced pressure to afford the desired **DASA-ester-PEG** (0.216 mg, 0.214 mmol, 97%) as vibrant pink, viscous liquid. $M_{n(\text{NMR})} = 1010$ g/mol.
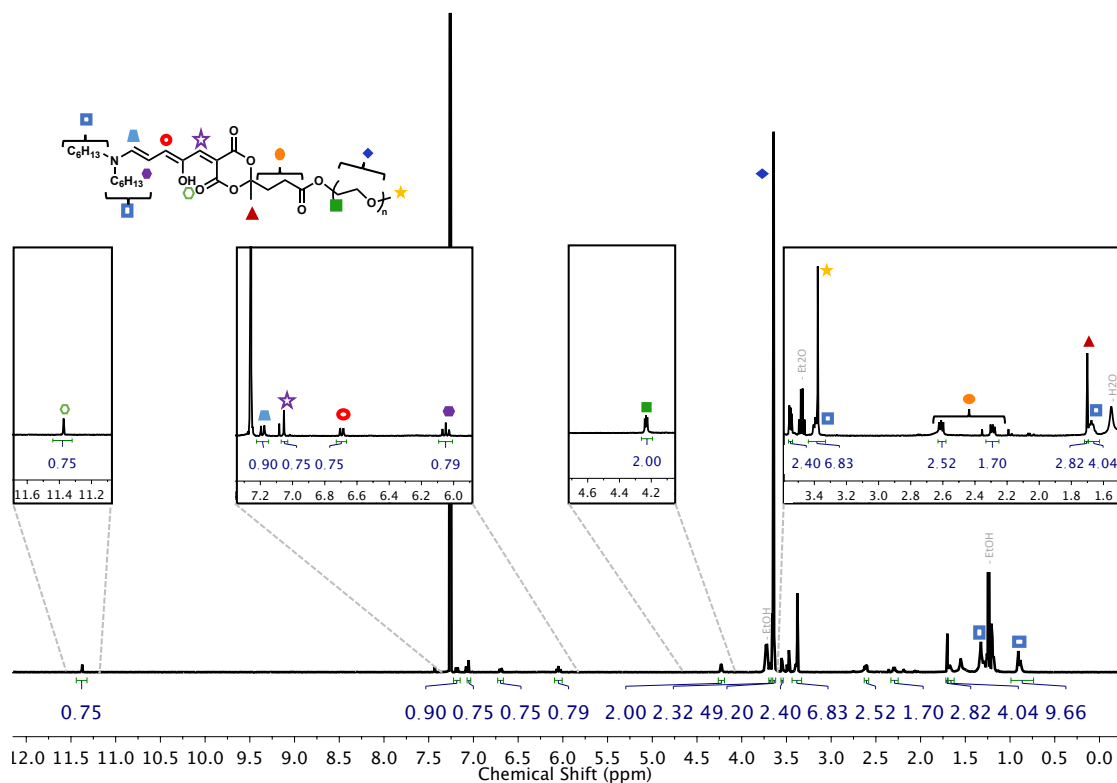
Figure S14. ^{1}H NMR (600 MHz, CDCl$_3$) **DASA-ester-PEG**

3.7.6 Co-surfactant concentration effects

The wetting behavior is dependent on the concentration of co-surfactant present in
solution. For a 20mM solution of DASA in toluene the results are shown below.

Figure S15. Concentration studies indicate that (a) for 20mM **DASA-DA-PEG** droplets reversible
wetting is observed only within the range of 0.25mM-0.5mM SDBS in water, and above 1 mM, no change in

droplet wetting is observed. Images taken before and after 5 seconds of irradiation using a 230mW/cm^2 white light, 20mM DASA-DA-PEG droplets in (b) 0.25mM SDBS exhibit significant photo-induced wetting whereas identical droplets in (c) 5mM SDBS do not respond to light. (d) Schematic demonstrating the proposed concentration-dependent effect of the co-surfactant in determining the occupancy of DASA-DA-PEG at the toluene-water interface in the dark. At low concentrations of SDBS, the DASA surfactant predominantly occupies the toluene-air interface and the toluene solution wets the air-water interface rather than forming a droplet. As the concentration of SDBS is increased, both surfactants occupy the interface and within the range of 0.25-0.5mM, the observed wetting responses are observed upon irradiation. At high concentrations of SDBS, no photosurfactant is expected to be present at the interface and thus light does not affect the droplet.

3.7.7 Interfacial tension

Due to the varied dynamic processes at play in each photo-surfactant system, interfacial tension measurements are challenging to evaluate by a singular method; thus, surface and interfacial tension measurements are obtained via a combination of tensiometer, Wilhelmy plate and contact angle experiments.
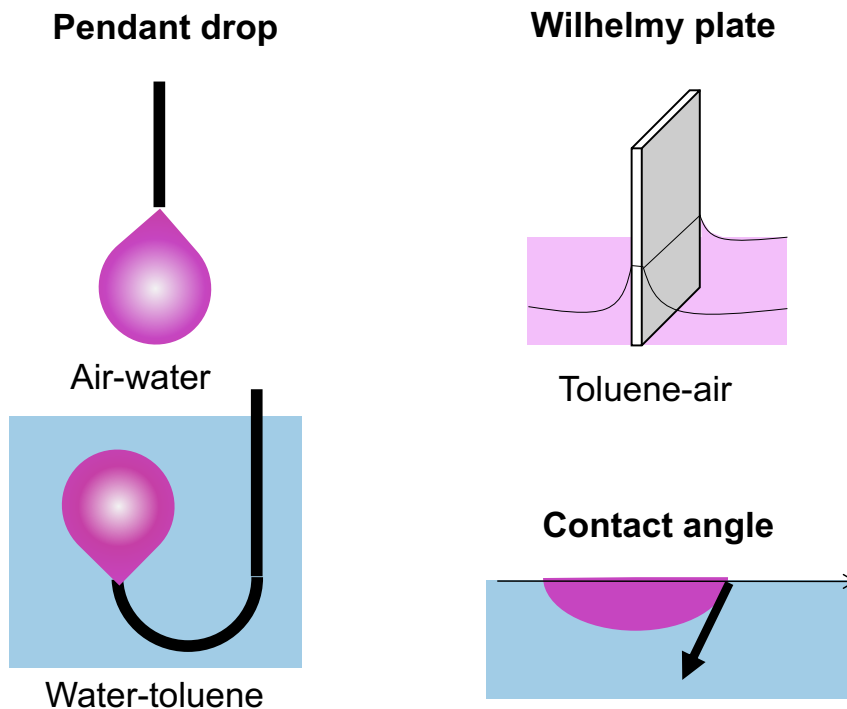
Figure S16. Schematic representations of all methods utilized to experimentally determine surface and interfacial tension.

Using Young-Dupré equation ($\sigma_{WA} = \sigma_{TA} + \sigma_{Tw}\cos(\theta)$, variables defined below) we approximated the change in interfacial tension between the toluene and water phase in the triphasic system. This was done by measuring the interfacial tension of toluene+DASA and air (σ_{TA}) using the Wilhelmy plate, water + SDBS and air (σ_{WA}) using the pendant drop and the contact angle of the system (θ). Through combination of these individual measurements we calculate the interfacial tension change of toluene + DASA and water + SDBS (σ_{Tw}) upon irradiation. Surface tension measurements are reported in mN/m. Contact angle measurements were averaged for 5 droplets ranging in size from 1-5 μL. The average initial contact angle was 71° and after irradiation 4.3° across five videos.

98

Table S1. Using the Young-Dupré equation we calculate the change in interfacial tension between the toluene-DASA droplet and the surrounding water-SDBS fluid (σ_{TW}) in the triphasic system. All values are reported for **DASA-ester-PEG.**

	σ_{WA}	σ_{TA}	θ	Calculated σ_{Tw}	% change
Before irradiation	37.3 (mN/m)	25.7 (mN/m)	71°	35.7(mN/m)	63%
After irradiation	37.3 (mN/m)	24.1 (mN/m)	4.3°	13.3(mN/m)	

3.8 References

1.   Brown, P., Butts, C. P. & Eastoe, J. Stimuli-responsive surfactants. *Soft Matter* **9**, 2365–2374 (2013).

2.   Diguet, A. *et al*. Photomanipulation of a droplet by the chromocapillary effect. *Angewandte Chemie - International Edition* **48**, 9281–9284 (2009).

3.   Kotz, K. T., Noble, K. A. & Faris, G. W. Optical microfluidics. *Applied Physics Letters* **85**, 2658–2660 (2004).

4.   Florea, L. *et al*. Photo-chemopropulsion-light-stimulated movement of microdroplets. *Advanced Materials* **26**, 7339–7345 (2014).

5.   Xiao, Y. *et al*. Droplets: Moving Droplets in 3D Using Light (Adv. Mater. 35/2018). *Advanced Materials* **30**, 1870259 (2018).

6.   Ji, W., Li, W., Wang, Y. & Lan, D. Tunable Spreading and Shrinking on Photocontrolled Liquid Substrate. *ACS Omega* **4**, 21967–21974 (2019).

7.   Lv, C., Varanakkottu, S. N., Baier, T. & Hardt, S. Controlling the Trajectories of Nano/Micro Particles Using Light-Actuated Marangoni Flow. *Nano Letters* **18**, 6924–6930 (2018).

8.   Varanakkottu, S. N. *et al.* Particle manipulation based on optically controlled free surface hydrodynamics. *Angewandte Chemie - International Edition* **52**, 7291–7295 (2013).

9.   Pan, S., Guo, R. & Xu, W. Photoresponsive superhydrophobic surfaces for effective wetting control. *Soft Matter* **10**, 9187–9192 (2014).

10.   Tabor, R. F. *et al.* Reversible light-induced critical separation. *Soft Matter* **5**, 78–80 (2009).

11.   Eastoe, J. *et al.* Photo-stabilised microemulsions. *Chemical Communications* 2785–2786 (2005) doi:10.1039/b503379a.

12.   Eastoe, J., Dominguez, M. S., Wyatt, P. & Heenan, R. K. A photo-responsive organogel. *Chem. commun.* **22**, 2608–2609 (2004).

13.   Vesperinas, A., Eastoe, J., Jackson, S. & Wyatt, P. Light-induced flocculation of gold nanoparticles. *Chemical Communications* 3912–3914 (2007) doi:10.1039/b710502a.

14.   McCoy, T. M., Liu, A. C. Y. & Tabor, R. F. Light-controllable dispersion and recovery of graphenes and carbon nanotubes using a photo-switchable surfactant. *Nanoscale* **8**, 6969–6974 (2016).

15.   Chevallier, E., Saint-Jalmes, A., Cantat, I., Lequeux, F. & Monteux, C. Light induced flows opposing drainage in foams and thin-films using photosurfactants. *Soft Matter* **9**, 7054–7060 (2013).

16.   Mamane, A., Chevallier, E., Olanier, L., Lequeux, F. & Monteux, C. Optical control of surface forces and instabilities in foam films using photosurfactants. *Soft Matter* **13**, 1299–1305 (2017).

17.   Birnbaum, P. P. & Style, D. W. G. The photo-isomerization of some azobenzene derivatives. *Transactions of the Faraday Society* **50**, 1192–1196 (1954).

18.   Takahashi, Y., Fukuyasu, K., Horiuchi, T., Kondo, Y. & Stroeve, P. Photoinduced demulsification of emulsions using a photoresponsive gemini surfactant. *Langmuir* **30**, 41–47 (2014).

19.   Hayashita, T., Kurosawa, T., Miyata, T., Tanaka, K. & Igawa, M. Effect of structural variation within cationic azo-surfactant upon photoresponsive function in aqueous solution. *Colloid & Polymer Science* **272**, 1611–1619 (1994).

20.   Eastoe, J., Dominguez, M. S., Wyatt, P., Beeby, A. & Heenan, R. K. Properties of a stilbene-containing gemini photosurfactant: Light-triggered changes in surface tension and aggregation. *Langmuir* **18**, 7837–7844 (2002).

21.   Cicciarelli, B. A., Hatton, T. A. & Smith, K. A. Dynamic surface tension behavior in a photoresponsive surfactant system. *Langmuir* **23**, 4753–4764 (2007).

22.   Hubbard, F. P. & Abbott, N. L. Effect of light on self-assembly of aqueous mixtures of sodium dodecyl sulfate and a cationic, bolaform surfactant containing azobenzene. *Langmuir* **23**, 4819–4829 (2007).

23.   Sakai, H. *et al*. Photo-isomerization of spiropyran-modified cationic surfactants. *Journal of Colloid and Interface Science* **316**, 1027–1030 (2007).

24.   Li, C., Iscen, A., Palmer, L. C., Schatz, G. C. & Stupp, S. I. Light-Driven Expansion of Spiropyran Hydrogels. *Journal of the American Chemical Society* **142**, 8447–8453 (2020).

25.   Klajn, R. Spiropyran-based dynamic materials. *Chemical Society Reviews* **43**, 148–184 (2014).

26.   Poelma, S. O. *et al*. Controlled drug release to cancer cells from modular one-photon visible light-responsive micellar system. *Chemical Communications* **52**, 10525–10528 (2016).

27.   Chen, Y. *et al*. Visible Light-Controlled Inversion of Pickering Emulsions Stabilized by Functional Silica Microspheres. *Langmuir* **34**, 2784–2790 (2018).

28.   Chen, S., Costil, R., Leung, F. K.-C. & Feringa, B. L. Self-Assembly of Photoresponsive Molecular Amphiphiles in Aqueous Media. *Angewandte Chemie International Edition* 2–26 (2020) doi:10.1002/anie.202007693.

29.   Zakrevskyy, Y., Roxlau, J., Brezesinski, G., Lomadze, N. & Santer, S. Photosensitive surfactants: Micellization and interaction with DNA. *Journal of Chemical Physics* **140**, (2014).

30.   Eastoe, J. & Vesperinas, A. Self-assembly of light-sensitive surfactants. *Soft Matter* **1**, 338–347 (2005).

31.   Shin, J. Y. & Abbott, N. L. Using light to control dynamic surface tensions of aqueous solutions of water soluble surfactants. *Langmuir* **15**, 4404–4410 (1999).

32.   Koźlecki, T., Sokołowski, A. & Wilk, K. A. Surface activity and micelle formation of anionic azobenzene-linked surfactants. *Langmuir* **13**, 6889–6895 (1997).

33.   St Amant, A. H. *et al*. Norbornadienes: Robust and Scalable Building Blocks for Cascade "click" Coupling of High Molecular Weight Polymers. *Journal of the American Chemical Society* **141**, 13619–13624 (2019).

34.   Bailey, S. J. *et al*. Norbornadiene Chain-End Functional Polymers as Stable, Readily Available Precursors to Cyclopentadiene Derivatives. *Macromolecules* **53**, 4917–4924 (2020).

35.   Feng, H. *et al*. The ultra-low interfacial tension behavior of the combined cationic/anionic-nonionic gemini surfactants system for chemical flooding. *Colloids and Surfaces A: Physicochemical and Engineering Aspects* **554**, 74–80 (2018).

36.   Wang, R., Li, Y. & Li, Y. Interaction between cationic and anionic surfactants: Detergency and foaming properties of mixed systems. *Journal of Surfactants and Detergents* **17**, 881–888 (2014).

37.   Lerch, M. M., Wezenberg, S. J., Szymanski, W. & Feringa, B. L. Unraveling the Photoswitching Mechanism in Donor-Acceptor Stenhouse Adducts. *Journal of the American Chemical Society* **138**, 6344–6347 (2016).

38.   Di Donato, M. *et al*. Shedding Light on the Photoisomerization Pathway of Donor-Acceptor Stenhouse Adducts. *Journal of the American Chemical Society* **139**, 15596–15599 (2017).

39.   Helmy, S., Oh, S., Leibfarth, F. A., Hawker, C. J. & Read De Alaniz, J. Design and synthesis of donor-acceptor stenhouse adducts: A visible light photoswitch derived from furfural. *Journal of Organic Chemistry* **79**, 11316–11329 (2014).

40.   Mallo, N. *et al*. Structure-function relationships of donor-acceptor Stenhouse adduct photochromic switches. *Chemical Science* **9**, 8242–8252 (2018).

41.   Mallo, N. *et al*. Photochromic switching behaviour of donor-acceptor Stenhouse adducts in organic solvents. *Chemical Communications* **52**, 13576–13579 (2016).

42.   Di Donato, M. *et al*. Shedding Light on the Photoisomerization Pathway of Donor-Acceptor Stenhouse Adducts. *Journal of the American Chemical Society* **139**, 15596–15599 (2017).

43.   Zulfikri, H. *et al*. Taming the complexity of donor-acceptor stenhouse adducts: Infrared motion pictures of the complete switching pathway. *Journal of the American Chemical Society* **141**, 7376–7384 (2019).

44.   Lerch, M. M. *et al*. Solvent Effects on the Actinic Step of Donor–Acceptor Stenhouse Adduct Photoswitching. *Angewandte Chemie - International Edition* **57**, 8063–8068 (2018).

45.   Helmy, S., Oh, S., Leibfarth, F. A., Hawker, C. J. & Read De Alaniz, J. Design and synthesis of donor-acceptor stenhouse adducts: A visible light photoswitch derived from furfural. *Journal of Organic Chemistry* **79**, 11316–11329 (2014).

46.   Helmy, S. *et al*. Photoswitching using visible light: A new class of organic photochromic molecules. *Journal of the American Chemical Society* **136**, 8169–8172 (2014).

47.   Hemmer, J. R. *et al*. Tunable Visible and Near Infrared Photoswitches. *Journal of the American Chemical Society* **138**, 13960–13966 (2016).

48.   Hemmer, J. R. *et al*. Controlling Dark Equilibria and Enhancing Donor-Acceptor Stenhouse Adduct Photoswitching Properties through Carbon Acid Design. *Journal of the American Chemical Society* **140**, 10425–10429 (2018).

49.   Tabor, R. F. *et al*. Reversible light-induced critical separation. *Soft Matter* **5**, 78–80 (2009).

50.   Sroda, M. M., Stricker, F., Peterson, J. A., Bernal, A. & Read de Alaniz, J. Donor–Acceptor Stenhouse Adducts: Exploring the Effects of Ionic Character. *Chemistry - A European Journal* **27**, 4183–4190 (2021).

51.   Hemmer, J. R. *et al*. Controlling Dark Equilibria and Enhancing Donor-Acceptor Stenhouse Adduct Photoswitching Properties through Carbon Acid Design. *Journal of the American Chemical Society* **140**, 10425–10429 (2018).

SI References

1. For preparation of **SP-OH**, see Raymo, F. M.; Giordani, S. Signal Processing at the Molecular Level. *J. Am. Chem. Soc.* **2001**, *123*, 4651 – 4652.:

2. For preparation of **NBD-COOH**, see Bailey, S. J.; Discekici, E. H.; Barbon, S. M.; Nguyen, S. N.; Hawker, C. J.; Read de Alaniz, J. Access to cyclopentadiene chain-end functional polmers via post-polymerization reaction with norbornadiene derivative.

3. For preparation of **NBD-OH**, **azo-mal,** see**:** St. Amant, A. H.; Discekici, E. H.; Bailey, S. J.; Zayas, M. S.; Song, J.; Shankel, S. L.; Nguyen, S. N.; Bates, M. W.; Anastasaki, A.; Hawker, C. J.; Read de Alaniz, J. *J. Am. Chem. Soc.* **2019**, *141*, 34, 13619 – 13624. **NBD-OH**, **azo-mal**

4. For preparation of **FM-COOH**, see: Chen, Q.; Diaz, Y. J.; Hawker, M. C.; Martinez, M. R.; Page, Z. A.; Zhang, S. X.-A.; Hawker, C. J.; Read de Alaniz, J. Stable

Activated Furan and Donor–Acceptor Stenhouse Adduct Polymer Conjugates as Chemical and Thermal Sensors. *Macromolecules*, **2019**, *52*, 11, 4370 — 4375.

5. For preparation of **3-maleimidopropionic acid**, see: Marcia de Figueiredo, R.; Oczipka, P.; Fröhlich, R.; Christmann, M. Synthesis of 4-maleimidobutyric Acid and Related Maleimides. *Synthesis*, **2008**, *8*, 1316 – 1318.

4. Depinning of Multiphase Fluid in Microgravity Using Photo-Responsive Surfactants

Abstract

The development of non-invasive and robust strategies for manipulation of droplets and bubbles is crucial in applications such as boiling and condensation, electrocatalysis and microfluidics. In this work, we realize the swift departure of droplets and bubbles from solid substrates by introducing photo-responsive surfactants and applying asymmetric illumination, thereby inducing a "photo-Marangoni" lift force. Experiments show that a pinned toluene droplet can depart the substrate in only 0.38 s upon illumination, and that the departure volume of air bubbles is reduced by 20%. These benefits can be achieved with moderate light intensities and dilute surfactant concentrations, without specially fabricated substrates. Simulations suggest that the net departure force includes contributions from viscous stresses directly caused by the Marangoni flow, as well as from pressure buildup due to flow stagnation at the contact line. The manipulation scheme proposed here shows potential for applications requiring droplet and bubble removal from working surfaces. This chapter was adapted with permission from *ACS Central Science*. *ACS Cent. Sci.* **2022**, *8, 2,* 235–245. Copyright 2022. American Chemical Society

4.1 Introduction

Building on previous work, this chapter utilizes the spiropyran-based photosurfactant in order to de-pin bubbles and droplets in multi-phase fluid systems. The motivation for this work is to enhance boiling in microgravity environments. The overarching goal of this study is to enhance and tune boiling heat transfer, for advanced manipulation of multi-phase fluid motion. These insights will enable exciting new capabilities for space applications, where efficient phase-change thermal transport and precision control of multi-phase fluid motion play a key role. The control of fluid motion and boiling are important for several different industrial applications such as phase-change heat transfer[1], water harvesting[2], and electro-catalysis, and on Earth is well understood[3-7]. In microgravity, we want to maintain boiling as close to the critical heat flux as possible and in the nucleate boiling regime; here bubble dynamics play a significant role and nucleation growth and departure strongly affect the boiling performance and ability to reach high critical heat flux. Bubble departure relies heavily on buoyancy, and in microgravity in the absence of buoyancy, the efficiency is decreased as dry patches form and accumulate preventing liquid paths and formation of new bubbles. With this study, we seek an alternate approach to move bubbles in the absence of gravity.

Several solutions to this challenge have been developed; however, these rely on complicated fabrication and consumption of resources. While past research efforts have focused on engineering static materials with well-designed surface structures and coatings to realize the passive control of fluid behaviors[8–10], simple methods capable of dynamically manipulating bubbles and droplets with high spatial and temporal resolutions are highly

desired to improve the performance and extend the functionality of aforementioned systems. Recent advances in developing materials that respond to thermal[11], chemical[12], electrical[13], or magnetic stimuli[14] have enabled dynamic manipulation of bubble and droplet motions. Most notably, electrowetting-on-dielectrics (EWOD) systems have been developed to move, merge, and split discrete droplets with precisely controlled volume in a programmable manner, which give rise to the concept of digital microfluidics[15]. However, these methods are still subject to several limitations; thermally and chemically actuated systems typically have long response times and reversibility issues. Electrowetting and magnetically controlled systems generally require a high voltage (2×10^2-2×10^3 V)[16] or a strong magnetic field (0.1-1.0 T)[17], which presents concerns for system reliability and safety. In addition, this approach requires sophisticated patterning of electrodes, making them difficult to implement.

Alternatively, using stimuli-responsive surfactants for dynamic manipulation is attractive because surfactants spontaneously accumulate at the interfaces, and therefore strongly influences the interfacial tension. This enables direct manipulation of multi-phase interfaces without needing to fabricate electrodes or micro/nanostructures on the substrate and apply delicate surface coatings. In this chapter, we explore how a light responsive surfactant may address some of these limitations. We employ the SP-DA-PEG for this study, as it can achieve fast, reversible, and significant interfacial changes of different solvents, thanks to its large polarity change under illumination. We demonstrate the removal of droplets and bubbles pinned on a solid substrate using photo-responsive surfactants and low-intensity lights by creating a net force on the bubble or droplet due to the Marangoni effect induced

by the non-uniform distribution of these photo-responsive surfactants (**Figure 1c**). Since light is used to induce Marangoni stresses, we refer to this phenomenon as a "photo-Marangoni" effect. This study can advance the fundamental understandings on bubble and droplet dynamics and the physical insights gained can be broadly implemented in various applications, including microgravity boiling.

4.2 Results

4.2.1 Scaling estimates of photo-Marangoni effects in drop/bubble departure

To estimate the potential significance of photo-Marangoni forces in the depinning of drops and bubbles, we perform estimates . On the SP-DA-PEG surfactant, the photo-switchable moiety can exist as two different isomers, spiropyran (SP) and merocyanine (MC). The former is thermodynamically stable in the dark, but will undergo a conformational switch to the latter initiated by illumination with a specific wavelength (**Figure 1a**). If illumination is stopped or a different wavelength of light is applied, the isomer can revert back to the thermodynamically stable form. As we have learned, the reversible photoconversion is associated with a change of surface tension or interfacial tension γ of the surfactant-containing solution (**Figure 1b**).[25,26]

Applying light to only one side of a single bubble or droplet whose surface is covered with photo-responsive surfactants (**Figure 1c**) causes a localized photo-reaction and induces a gradient of γ across the interface between the two fluids, which drives a local Marangoni flow toward the region of higher γ. The Marangoni flow drives a flow in the surrounding fluid (downward in Figure 1c), such that the bubble/droplet experiences a Marangoni-

induced force F_M in the opposite direction, easing the depinning and departure from the substrate (the fluid mechanics of generic Marangoni-induced droplet propulsion are reviewed in Ref. [12]). We propose here that, if a gradient in γ can be tuned and sustained by maintaining a constant gradient of two photo-switched isomers, bubbles and droplets can be continuously removed from the solid substrate on-demand.

To estimate the relative gradient of surface tension $\Delta\gamma/\gamma$ that is required to depin an air bubble immersed in an aqueous solution (**Figure 1c**), we consider the relative order of magnitude of the relevant forces. For a static bubble pinned to a substrate, the bubble diameter d_b at departure from a substrate is obtained by balancing buoyancy F_b, which is of order $g\Delta\rho d^3$ (where $\Delta\rho$ is the density difference), and the pinning surface force $F_{pin,vertical} \sim \gamma d \sin^2\varphi$ (where φ is the macroscopic or apparent contact angle in the
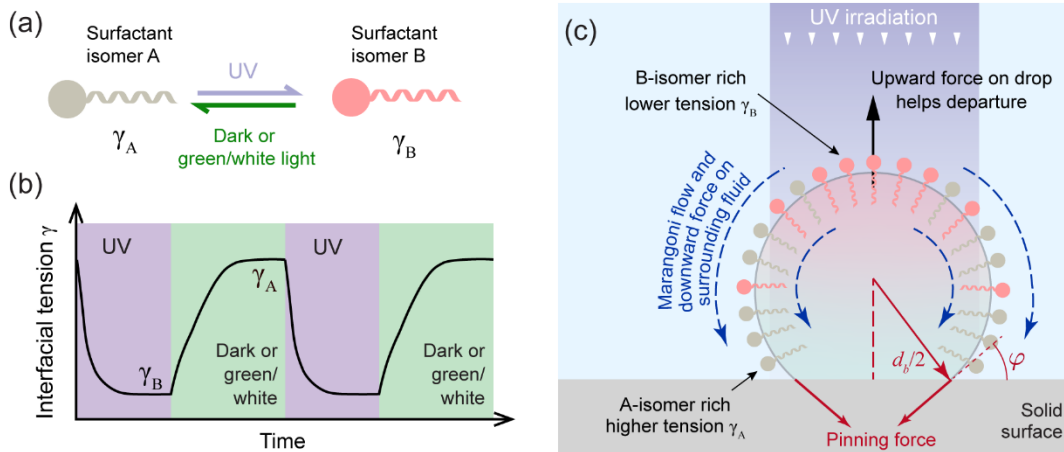
Figure 4. 1. Mechanism of photo-Marangoni effect for light-activated bubble/droplet departure. (a) Photo-responsive surfactants reversibly switching molecular conformation upon illumination of light with appropriate wavelengths. (a) Photo-responsive surfactants reversibly switching molecular conformation upon illumination of light with appropriate wavelengths. In this example, forward switching is activated by UV light. The reverse reaction occurs once UV is removed, and is accelerated by green light. (b) The surface tension is changed

reversibly by UV/green illumination. (c) A surface tension gradient can be established along the interface by applying light with an intensity gradient, or only to one region on the interface, and the subsequent Marangoni flow drives the bubble/droplet to depart. Reprinted with permission from ACS Central Science. 2022. Copyright 2022. American Chemical Society

liquid, and "~" denotes order of magnitude), yielding $d_b \sim \sin\varphi(\gamma/g\Delta\rho)^{1/2}$. For photo-Marangoni forces to assist departure, they must be significant relative to buoyancy for a bubble of size d_b or smaller. If a surface tension change of order $\Delta\gamma$ exists across the height of the bubble, and can be maintained to drive a flow, the resulting photo-Marangoni force that can assist depinning is of order $\Delta\gamma d$; requiring this to be at least 10% of the buoyancy force sets $\Delta\gamma \gtrsim 0.1 g \Delta\rho\, d_b$. In the extreme case of microgravity applications, or of immiscible fluids with matched densities, the photo-Marangoni force alone must overcome the totality of the pinning surface force $F_{p,vertical}$, which requires $\Delta\gamma \gtrsim \gamma \sin^2\varphi$. We note that the photo-Marangoni effect is only one possible mechanism by which photosurfactants can be used for de-pinning. Another, simpler mechanism is simply that if the change in contact angle due to change in photostationary state surface tension is sufficiently large, then the reduction in surface tension alone (even absent any surface tension gradients) is sufficient to depin the droplet. These order-of-magnitude estimates inform our choice of photosurfactant.

4.2.2 Selection and characterization of SP-DA-PEG

An ideal surfactant to achieve bubble departure in a multi-phase system should display a large surface tension change, good reversibility, fast switching kinetics activated by a low-

intensity light. As such, we use the spiropyran-based photo-isomerizable molecule (SP-DA-PEG) which was previously synthesized, studied and compared against other commonly used photo-surfactants azobenzene and DASA detailed in Chapter 2.
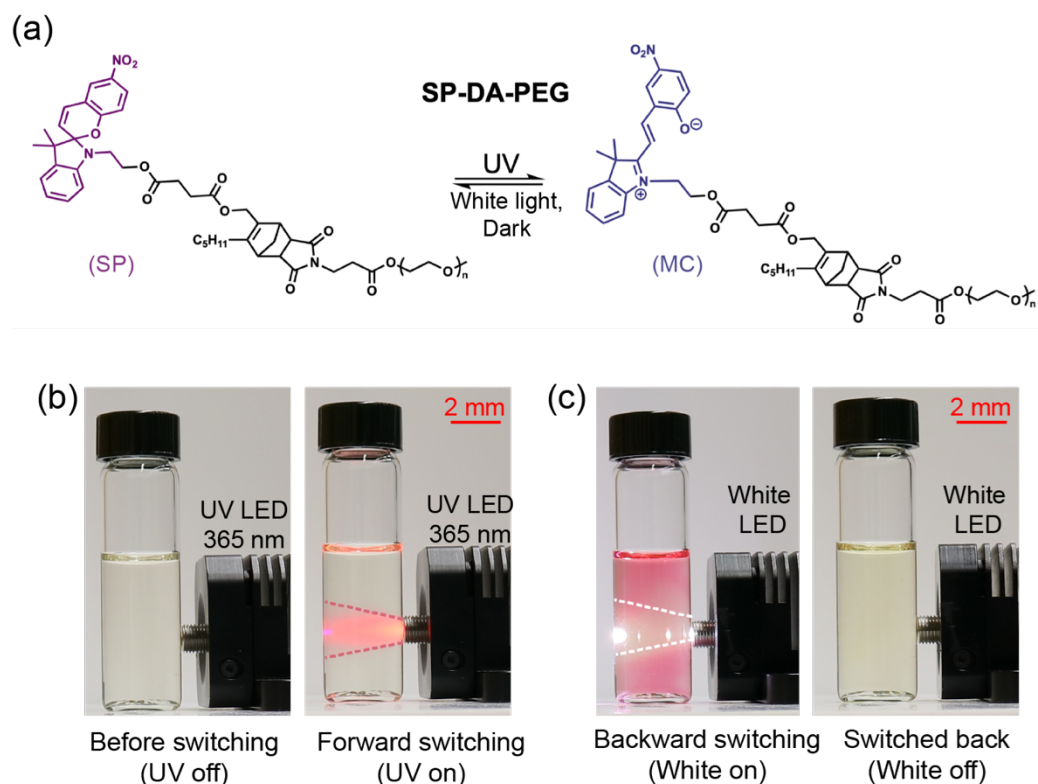
Figure 4.2. (a) The reversible photoconversion of the spiropyran (SP) isomer to the merocyanine (MC) isomer form. (b) 0.1 mM spiropyran water solution changes from transparent to light pink under 365 nm UV illumination. (c) 0.1 mM spiropyran water solution switches from MC form back to SP form, as shown by the color change from light pink to transparent Reprinted with permission from ACS Central Science. 2022. Copyright 2022. American Chemical Society

As shown in **2a**, SP-DA-PEG comprises the photo-switchable spiropyran unit at the surfactant tail and the poly(ethylene glycol) monomethyl ether (PEG, $M_n \approx 550$ g/mol) chain as the hydrophilic head group on which spiropyran is immobilized. The isomerization of the

spiropyran (SP) isomer to the merocyanine (MC) isomer is activated by UV light within 300-375 nm in wavelength, whereas the reverse photo-isomerization occurs upon the removal of UV irradiation, which can be further accelerated by application of a 500-600 nm light[22,25] (**2a**). In 2b, the color changes observed for a 0.1 mM SP-DA-PEG in water solution are shown.
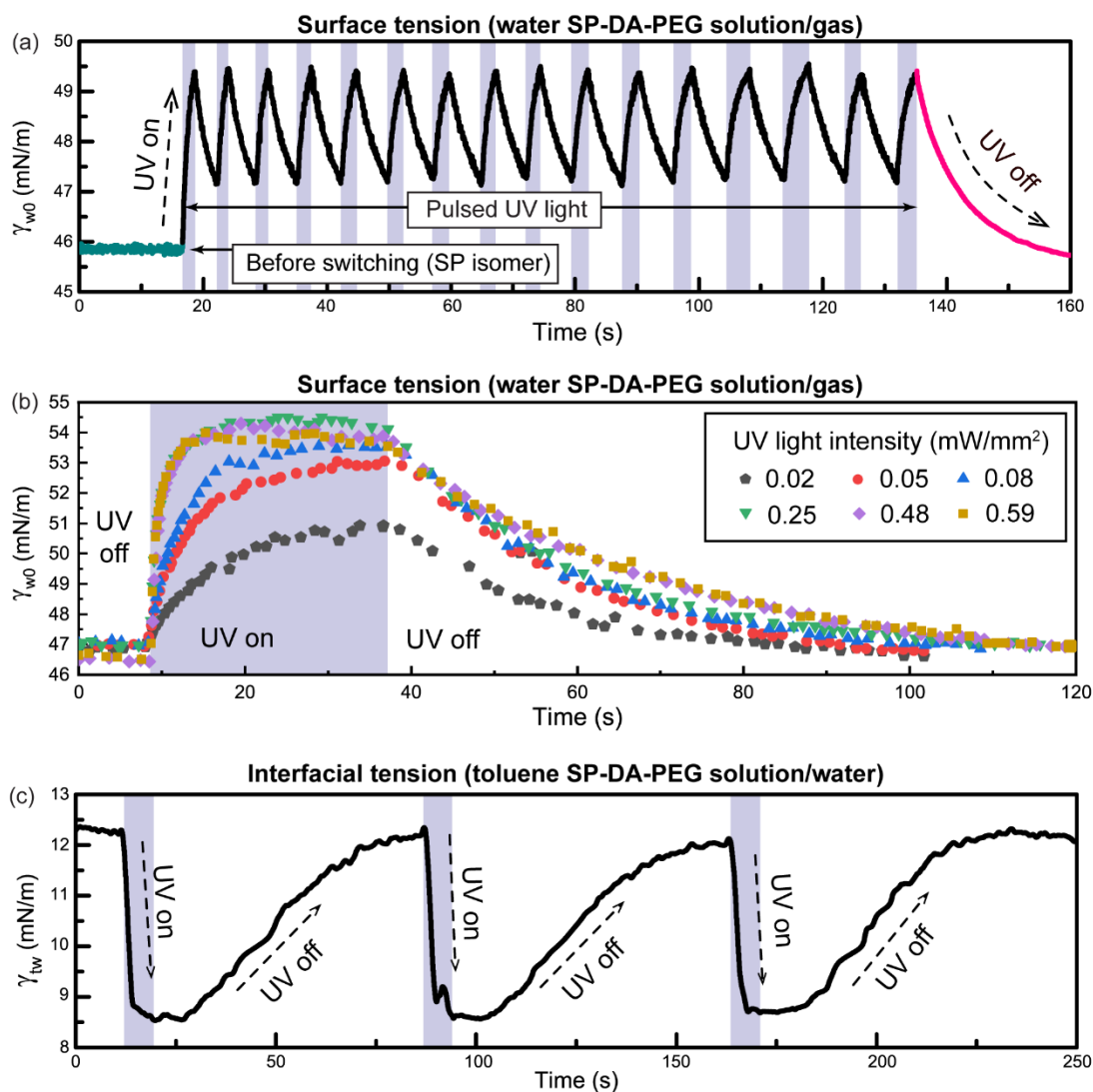
Figure 4.3 (a) The surface tension of 0.1 mM SP-DA-PEG water solution under repetitive pulsed UV light. (b) The surface tension of 0.1 mM SP-DA-PEG water solution under UV irradiation with different light intensity against air. (c) The reversible change of interfacial tension between 0.1 mM SP-DA-PEG toluene solution and

In previous work, we identified a large change in interfacial tension of SP-DA-PEG in water against toluene; here, we seek to expand these interfacial tension measurements. We measured the surface tension response of SP-DA-PEG solutions during photo-isomerization using the pendant drop method[29] using a commercial tensiometer. Although an accurate measurement of interfacial/surface tensions of surfactant solutions can be challenging, as the timescales for surfactants to diffuse to the interface and for the droplet to relax to full equilibrium can take tens of minutes[30], these pendant drop measurements are directly relevant to depinning applications, where timescales are inherently much shorter than those associated with molecular diffusion.

First, we applied alternating irradiation of 365 nm UV and white light to an aqueous SP-DA-PEG solution (0.1 mM), and observe the response of an air bubble. In Figure 3a, γ_W uickly rises to 49.5 mN/m from 46 mN/m after 1 second of UV irradiation. Once UV is removed and the white light is applied, γ_{W0} undergoes a rapid decrease. After 16 cycles of irradiation, γ_{W0} can recover its original value, which indicates that spiropyran could potentially maintain its performance through large numbers of depinning cycles.

Figure 3b shows the time evolution of γ_{W0} for 0.1 mM SP-DA-PEG in aqueous solution under different light intensities. At the smallest intensity of 0.02 mW/mm^2, γ_{W0} changes from 46.5 mN/m to around 50.4 mN/m in 38 seconds. When the light intensity is increased, more SP molecules are transformed into the open-ring conformation, MC, at a faster rate

and the resultant surface tension is increased to 54.3 mN/m within 8 seconds. In addition, most SP molecules can be converted into the open-ring form and the photo-conversion process saturates once the light intensity exceeds 0.25 mW/mm^2, which is still a relatively low intensity in most optical applications. After the UV light is removed, γ_{w0} reverts to its original value for all cases.

We also measured the dynamic response of the interfacial tension γ_{tw} between deionized (DI) water and a 0.1 mM SP-DA-PEG toluene solution, as shown in Figure 3c. Under 365 nm UV light with intensity of 0.59 mW/mm^2, γ_{tw} quickly changes from 12.33 ±0.05 mN/m (SP) to 8.59±0.10 mN/m (MC), corresponding to a 30% change.

4.2.3 Droplet departure experiments

To demonstrate the depinning, we first carried out experiments on the departure of a liquid droplet, consisting of toluene in water. The experimental setup is shown in Figure 4a. A toluene droplet is injected into a water bath through a round hole ($d = 0.61$ mm) using a syringe pump to control the injection rate. The droplet contains 0.1 mM SP-DA-PEG; this concentration showed the most significant interfacial tension change through our pendant drop experiments. The droplet is stabilized at ~15 μL (corresponding to a diameter of approximately 3 mm) and remains pinned to the hole (**Figure 4b**). Later, another equal-sized droplet is generated and equilibrated for 10 s. Then, the output from a multiline Argon Ion UV laser (351.1+363.8 nm, beam diameter of 1.3 mm) is directed to the top of the droplet (height of 3.5 mm). The incident light intensity on the bubble is 44 mW/mm^2, as measured

in the empty container. The laser enables precise targeting of the photo switch, and the higher intensity accelerates the isomerization to MC.
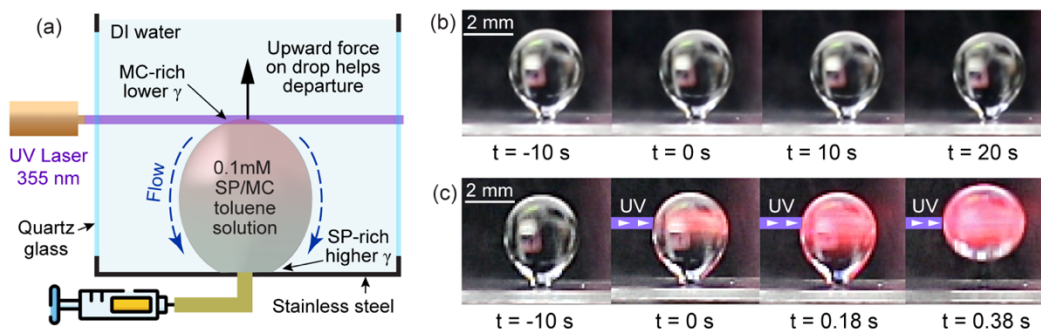
Figure 4. 3. (a) Schematic of the experimental setup for photo-induced droplet depinning. A droplet is generated by pushing the toluene solution with 0.1 mM SP-DA-PEG through a hole (0.61 mm in diameter). A collimated UV laser is directed at the top part of the droplet to trigger the photo-Marangoni effect. (b) A droplet (~15 μL) generated by pushing the toluene solution through a round hole stays static for 30 seconds. (c) Time-lapse images of an equal-sized droplet (~15 μL) depinned by photo-Marangoni effect. The droplet stays static and departs immediately after the UV laser is turned on. Reprinted with permission from ACS Central Science. 2022. Copyright 2022. American Chemical Society

Figure 4c demonstrates that the initially pinned toluene droplet departs the substrate in only 0.38 s after UV irradiation. We define the instance when the laser is turned on as $t = 0$ s. A pink region rapidly forms within the top part of the droplet where the UV beam passes through, indicative of the onset of the photo-conversion. The widening of the pink region observed at t=0.18 s suggests fluid flow from the pink MC-rich lower interfacial tension region to the clear SP-rich higher interfacial tension region. The fluid motion inside the toluene droplet is demonstrated by visual inspection of tracer particles (Supplementary Movie 1). The detailed flow field and force analysis will be discussed in the following sections. To ensure that droplet departure is activated by photo-Marangoni effect rather than the possible thermal-Marangoni effect induced by laser heating within the droplet, we

117

simulated the temperature rise ΔT within the toluene droplet (see Supplementary Information). It is found that ΔT is limited to only 0.25 °C before droplet departure (t=0.38 s). In addition, the droplet temperature is experimentally measured to have increased from 21.7±0.03 °C to 23.2±0.8 °C during 17 seconds of laser heating (see Supplementary Information). A previous work demonstrated that γ_{tw} for water/toluene decreases by 1.8% when the temperature is increased from 20 °C to 25 °C)[31]. Therefore, thermal Marangoni effects are negligible in this experiment. This estimate also illustrates the advantage of the photo-Marangoni effect over thermal Marangoni, in that a much smaller light intensity can manipulate multi-phase flow without the need to generate a substantial temperature gradient in the droplet. Furthermore, the light intensity used for photo-Marangoni experiments (44 mW/mm^2) is 2-4 orders of magnitude lower than those previously reported for thermal Marangoni examples[32,33].
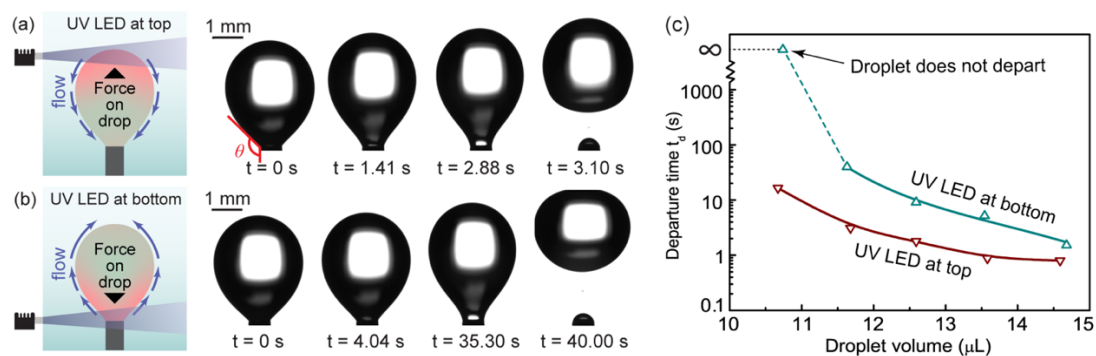
Figure 4. 4. The photo-Marangoni effect facilitates the depinning of a toluene droplet (~11.5 μL) when the droplet top is irradiated by UV. The depinning time t_d is 3.10 s. (b) The photo-Marangoni effect inhibits the departure of a same sized droplet by creating an upward Marangoni flow. The depinning time t_d increases to 40.00 s. (c) The depinning time t_d of droplets with different volumes. t_d becomes orders of magnitude higher when UV irradiation is applied at the droplet bottom. Reprinted with permission from ACS Central Science. 2022. Copyright 2022. American Chemical Society

We further demonstrate that droplet departure can be activated with even lower light intensity, and that the time for the droplet departure t_d shows a strong dependence on droplet size. Here t_d is defined as the time of droplet departure after UV irradiation. In this second set of experiments, we use a fiber-coupled UV LED with a light intensity of 0.59 mW/mm^2 (this is nearly 75 times smaller than in our experiments with the UV laser). A computer-controlled droplet dispenser is used to generate a toluene droplet with precisely controlled volume. As before, the droplet contains 0.1 mM SP-DA-PEG and is immersed in DI water. The UV LED illuminates the top part of a 11.5 μL droplet, as shown in Figure 5a. As a result, γ_{tw} locally decreases and a downward Marangoni flow drives the droplet to depart after 3.10 s. By contrast, a reverse-direction photo-Marangoni flow can be generated by illuminating the bottom part of the droplet with the UV LED. This reverse photo-Marangoni flow hinders droplet departure, as shown by the fact that t_d increases by an order of magnitude ($t_d = 40.0$ s). The droplet eventually still departs the surface; a contributing factor may be the reduced pinning force F_p as a result of the decreased interfacial tension γ_{tw} after the photo-conversion (see **Figure 3c**). In Figure 5c, we measured the depinning time t_d for toluene droplets with different volumes. As the droplet volume increases, t_d decreases exponentially due to increased buoyancy; yet the departure time is significantly shorter for droplets with UV applied at the top than at the bottom for all droplets tested.

4.2.4 Bubble departure experiments

In this section we show that the photo-Marangoni effect can also be used to assist the departure of air bubbles. The assisted departure is demonstrated by a reduction in the maximum bubble volume V_d before departure. Figure 6a shows the experimental setup. A syringe pump is used to generate an air bubble in a chamber filled with 0.1 mM SP-DA-PEG in toluene solution. The same UV LED used for the droplet experiments illuminates from 2.5 cm above the bubble. The highly diverging feature of its light naturally creates a light intensity gradient in the vertical direction along the bubble. Furthermore, a 532 nm green laser shines a beam horizontally at the bottom of the bubble. The green light irradiation accelerates reverse isomerization from MC to SP and subsequently enhances the composition gradient of surfactants along the interface. In our previous work[23], it was found that the surface tension of SP-DA-PEG toluene solutions (γ_{t0}) decreases after the photo-isomerization from SP to MC. Therefore, the bubble top is rich in MC and has a lower surface tension, leading to a downward photo-Marangoni flow which drives the bubble to depart. Using the pendant drop method, γ_{t0} is measured to reduce slightly from 23.25 mN/m to 22.75 mN/m upon UV irradiation, a modest change (only 2%) compared to that of γ_{tw}.
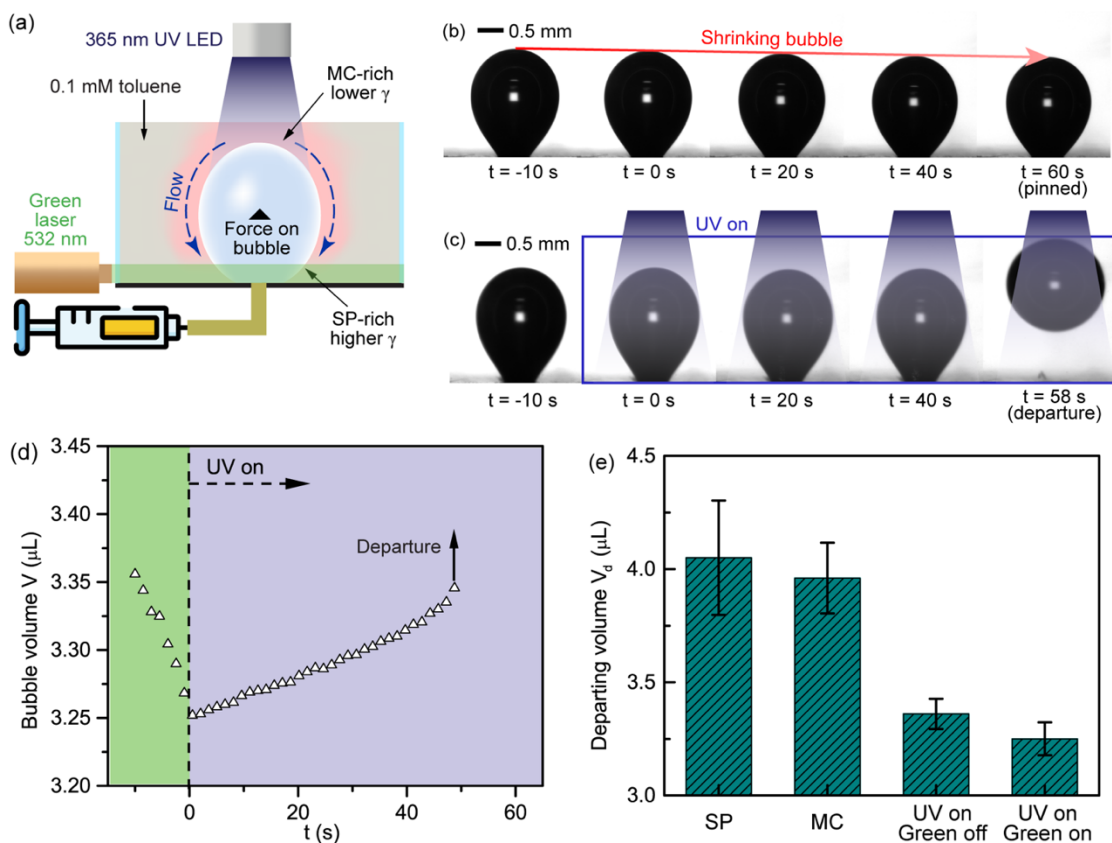
Figure 4.5. (a) Schematic of the experimental setup in the bubble experiment. The photo-Marangoni effect is driven by a UV LED shining downwards from 2.5 cm above the bubble, and it is further assisted by a collimated green laser beam shining near the bottom of the bubble. Together, these enhance the difference in isomer composition across the bubble, and thereby increase the surface tension difference. (b) A pinned air bubble (~3.36 μL) naturally shrinks in toluene solution, and fails to depart. (c) An air bubble of the same initial volume leaves the surface under the photo-Marangoni effect. (d) The volume change of an air bubble before and after UV irradiation; departure occurs at a volume that is smaller than the initial one. (e) The bubble volume at departure Vd in SP solution, MC solution, SP solution when UV LED is on and green laser is off, and SP solution when UV LED and green laser are both on. Reprinted with permission from ACS Cent. Sci. 2022, 8, 2, 235–245. Copyright 2022. American Chemical Society

We compared V_d for bubbles injected into SP solutions, MC solutions, and solutions with a mixture of SP and MC isomers by controlling the illumination conditions. Time-lapse images of the injected bubble immersed in 0.1 mM SP-DA-PEG toluene solution when no light is applied are shown in Figure 6b. At t = −10 s, the syringe pump is stopped and the bubble remains pinned to the surface. A slow shrinkage is observed over a period of 60 seconds, which is likely due to a minor leakage in the gas supply line. In contrast, when UV LED is turned on (at t = 0 s) for an equal-sized bubble generated with the same method (**Figure 6c**), the originally shrinking bubble starts to inflate due to the Marangoni lift force, and departs from the surface at t = 58 s. The time-dependent volume of the bubble during this process is shown in Figure 6d. The thermal Marangoni effect is negligible as the solution temperature is measured to increase by only 0.5 °C during 1 minute of UV irradiation (see Supplementary Information). Bubble departure volumes for SP-only solutions $V_{d,SP}$ and for MC-only solutions $V_{d,MC}$ are measured by generating a quasi-steady-state bubble using the syringe pump with a constant and low flow rate of 1 μL/min. It is found that $V_{d,SP} = 4.05$ μL and $V_{d,MC} = 3.96$ μL. The difference between $V_{d,SP}$ and $V_{d,MC}$ agrees well with surface tension change of 0.1 mM SP-DA-PEG toluene solution before and after the photo-isomerization. The bubble departure size can further be reduced to $V_{d,UV,G} = 3.25$ μL by applying UV and green light to the top and bottom of the bubble, respectively, as illustrated in Figure 6a. The photo-Marangoni force F_M, as a percentage of the buoyancy force, herein is evaluated to be $F_M/F_B \cong$

$(V_{d,SP} - V_{d,UV,G})/V_{d,SP} = 19.8\%$, even with a modest change (2.1%) of surface tension of SP-DA-PEG

solution. The above equation assumes that the bubbles are in quasi-static states and that the pinning force is relatively the same for all the cases. By designing new surfactants and characterizing the surface tension change in different solvents, the photo-Marangoni effect acting on gaseous bubbles can potentially be further enhanced.

4.2.5 Finite element simulations

Finite element simulations were performed by Lei Zhao to investigate the lift force due to the photo-Marangoni effect (details in Methods), focusing on toluene droplets in DI water. We first simulate the departure of a 10.65 μL droplet (0.1 mM SP-DA-PEG) and assume a linear interfacial tension gradient with γ_{top} = 8.59 mN/m at the top of the droplet and γ_b = 12.33 mN/m at the bottom. These values are based on the assumptions that the photoconversion equilibrium is established and the proportions of SP and MC molecules are determined by the local light intensity. Figure 7a presents the velocity field in both phases when the photo-Marangoni effect is activated. Within the droplet, the liquid travels downward near the interface due to the Marangoni stress and then circulates back to the top near the center axis. Outside the droplet, there is also a downward flow which moves faster at the interface and decays to almost zero away from the droplet. The pressure distribution is shown in Figure 7b. A high-pressure region appears near the base of the droplet in the outer phase, due to the stagnant flow near the bottom wall. This high-pressure region exerts an additional lift force on the droplet. Figure 7c plots the profiles of z-component of total stress σ_z, viscous stress τ_z, and pressure p_z from the droplet bottom to its top. Interestingly, the result shows that pressure is the dominating factor near the bottom of the droplet, but then dips at a height below the maximum width of the droplet, slightly hindering departure. In

123

contrast, the profile of τ_z is relatively flat, indicating that the outer phase is constantly

pushing the droplet upward through surface shear.

However, the above simulation may be over-predicting F_M, since it assumes that the

maximum possible interfacial tension difference is realized across the drop, whereas in

practice the finite-time kinetics of the photoconversion may not allow the MC-isomer to

fully switch back to the SP-isomer before the fluid reaches the bottom of the droplet.

Therefore, we reduced the interfacial tension difference and calculated the corresponding

photo-Marangoni force F_M, looking for the interfacial tension difference that would enable

departure. Since the forward reaction is fast (**Figure 3c**), we fixed γ_{top} at 8.59 mN/m by

assuming a complete photoconversion under UV irradiation, and gradually increased γ_b,

corresponding to a decreasing proportion of MC molecules in the surfactant mixture. Figure

7d summarizes the upward force contributed by pressure F_p and viscous stress F_v under

different $\Delta\gamma/\gamma_0$, where $\Delta\gamma = \gamma_b - \gamma_{top}$ and γ_0 is the interfacial tension before the

photoconversion. F_p and F_v are of the same order of magnitude for $\Delta\gamma/\gamma_0$ spanning from

0% to 30%, indicating that both pressure buildup at the bottom and the relatively constant

viscous shear contribute substantially to the photo-Marangoni force F_M. Note that as F_p and

F_v increase with respect to $\Delta\gamma/\gamma_0$, the net photo-Marangoni force $F_M = F_p+F_v$ eventually

exceeds buoyancy F_B at $\Delta\gamma/\gamma_0 = 29.4\%$. This suggests that the photo-Marangoni effect

could even serve to completely replace buoyancy forces if using two density-matched fluids,

or if working in microgravity environments. The net force F_N on the droplet can be

estimated by considering the pinning force $F_{pin} = \pi d_s \gamma_b \sin\theta$, buoyancy $F_B = \Delta\rho g V$,

and the photo-Marangoni force F_M, such that $F_N = F_M + F_B - F_{pin}$. In Figure 7e, it is shown that F_M is of the same order of magnitude as F_B. For small $\Delta\gamma/\gamma_0$, F_N is negative, indicative of a pinned droplet on the substrate; droplet departure ($F_N > 0$) occurs when $\Delta\gamma/\gamma_0$ exceeds 21.5%. Therefore $\Delta\gamma/\gamma_0$ required for

departure is below the maximum $\Delta\gamma_{max}/\gamma_0 = 30\%$ that we previously measured in our tensiometer experiments, which further supports the feasibility of photo-Marangoni-assisted departure.
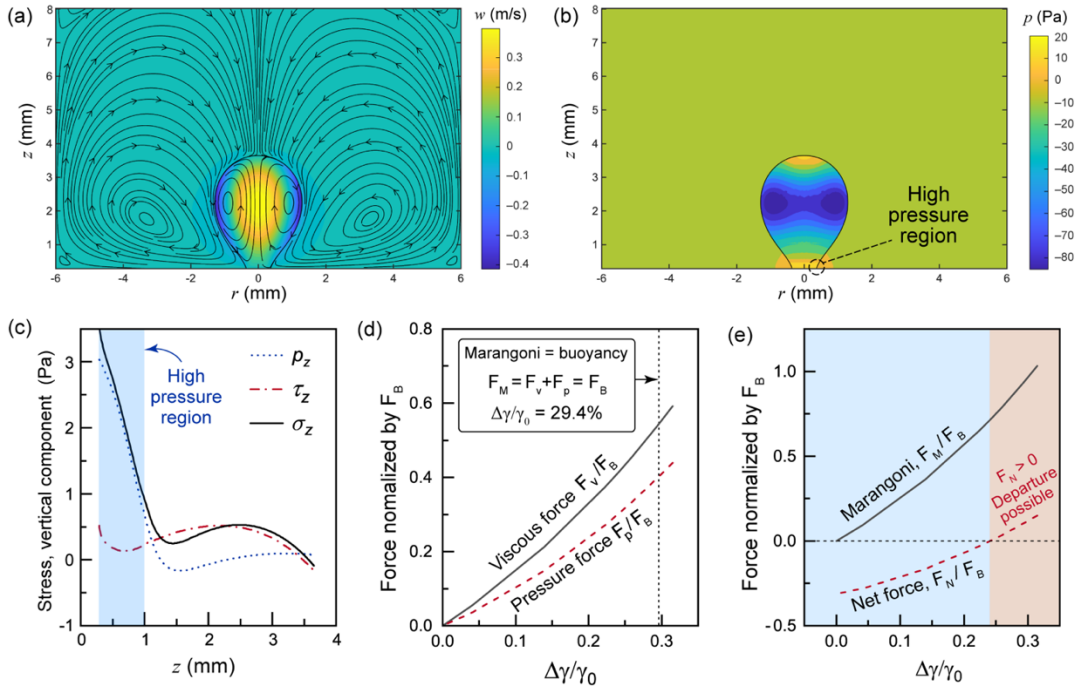
Figure 4. 6. The streamline plots and w-velocity contour and (b) pressure contour around the droplet when the photo-Marangoni effect is activated. (c) The distribution of z-stresses acting on the droplet along the droplet interface. P_z is the vertical component of the pressure, τ_z is the viscous stress, and σ_z is the total stress. All quantities are positive if they push the drop upward. (d) The force contributed by pressure and viscous stress normalized by the buoyancy F_B. $\Delta\gamma$ is the difference between γ_b and γ_{top}, and $\gamma_0 = 12.33$ mN/m is the interfacial tension before the photoconversion. (e) The Marangoni force F_M and net force F_N versus different

interfacial tension gradients. $F_N = 0$ is achieved at $\Delta\gamma/\gamma_0 = 21.5\%$. Reprinted with permission from ACS Central Science. 2022. Copyright 2022. American Chemical Society

4.3 Discussion and conclusions

In summary, we developed a dynamic, non-invasive and reversible manipulation scheme to assist bubble and droplet departure from solid surfaces using a light-responsive surfactant, namely SP-DA-PEG. The excellent reversibility, stability, sensitivity to illumination, as well as fast photo-isomerization kinetics make SP-DA-PEG ideal for applications involving bubble and droplet manipulation. In our experiments, an interfacial tension change as high as 30% and a droplet departure time of 0.38 s (for an otherwise pinned droplet) are achieved. Both experiments and simulations demonstrate that the photo-Marangoni force arises not only from the viscous shear along the interface, but also from the pressure build-up due to flow stagnation at the bottom. As a matter of fact, the photo-Marangoni flow induces a Reynolds number (based on interface velocity, drop diameter and ambient fluid properties) of approximately 600, indicative of a laminar flow where inertial effects may not be negligible. Therefore, even a modest change in surface tension (2.1%) can lead to a significant change in bubble behaviors (19.8% change in bubble departure volume).

The photo-Marangoni effect can serve as an effective yet simple platform technology for non-invasive dynamic fluid manipulation that does not require electrical voltage, magnetic field, patterning complex electrodes or engineering of well-designed surface textures. The surfactant concentration used in this work is around 0.1 mM, which is even smaller than the concentration of natural or man-made surfactants in environmental water[34]. The required

126

light intensity for complete photo-isomerization is only around 0.25 mW/mm^2, comparable to the average solar irradiance received by the earth's surface[35]. Therefore, the photo-Marangoni effect can contribute to developing new research capabilities not only in applications requiring fluid removal such as heat transfer, electrolysis, organic synthesis, but also in processes that entail biological compatibility and optical resistance, such as biochemical assays, dynamic patterning and manufacturing of novel materials. Furthermore, the physical insights gained in the theoretical analysis, experimental observations and numerical simulations will guide the design and synthesis of photo-surfactants for future photo-driven multi-phase systems.

More work can be done to improve the photo-Marangoni effect to achieve faster response and more durable performance. The mechanism of interfacial tension change during photoconversions depends on the ring-opening process of the photo-switch unit, resulting in a polarity change and charge redistribution of SP-DA-PEG. Typically, the effect of spiropyran-based surfactants on non-polar interfaces, such as the toluene-air interface, becomes less significant compared to that of an interfacial system involving polar liquids like water. Therefore, the meticulous design and optimization of molecular structures of the light-responsive surfactants is needed to achieve optimal interfacial tension change and reaction kinetics for different combinations of interfacial systems. In addition, more detailed numerical and theoretical studies on the coupling between multiphase flow, interface deformation, species transport, surfactant adsorption, and photo-reactions can provide more insights to explore the surfactant transport and fluid dynamics associated with the photo-Marangoni effect for optimal performance.

4.4 Supplementary Information

Synthesis of SP-DA-PEG. The synthesis of the SP-DA- was prepared according to the procedure provided in Chapter 2

Sample preparations. The photoactive surfactant selected for this work is a spiropyran-based photo-isomerizable molecule (SP-DA-PEG). SP-DA-PEG can easily dissolve into toluene liquids by vortexing and sonication.

Light sources. In the bubble experiment, a custom-built multiline Argon Ion UV laser (351.1+363.8 nm, beam diameter of 1.3 mm) is used with a beam diameter of 1.3 mm and light intensity of 44 mW/mm^2. The fiber-coupled UV LED and white LED are directly bought from Thorlabs, Inc. (M365FP1-365 nm, 9.8 mW Fiber-Coupled LED, and MCWHF2-6200 K, 21.5 mW Fiber-Coupled LED) A high intensity UV lamp (100 W over a lamp area of 216 mm × 140 mm, UVP High Intensity Lamp, Analytik Jena) is used to fully transform the SP isomers in 0.1 mM SP-DA-PEG solutions into the MC isomers so as to measure the bubble departure volume in pure MC solutions. A 532 nm green laser (5 mW, GMY-532-5F3-PP, Lasermate Group, Inc) is used to expedite the reverse photo-isomerization of SP-DA-PEG molecules in the bubble experiment.

Droplet and bubble experiments. A stainless steel tube with four glass windows is fabricated using the CNC milling machine and a round hole with a diameter of 0.6Hi mm is fabricated at the tube bottom using a mechanical drilling rig. The round hole is connected to a syringe pump and sealed by Dow Corning High Vacuum Grease. All experimental

glasswares are cleaned by sonication in water and isopropyl alcohol to prevent contamination by residual surfactant molecules and dust. Droplet is equilibrated for about 1 min before recording. For droplet manipulation with UV LED, the LED is placed about 2 cm away from the side of the droplet. For the bubble experiment, the UV LED is mounted around 2 cm above the air bubble. Videos are recorded from the side using Canon EOS 80D.

Pendant drop measurements. All measurements related to the surface tension or interfacial tension were carried out on the Theta Flex Tensiometer from Biolin Scientific. This instrument uses a high-speed camera to capture the outline of drops and bubbles. The pendant drop method is then used to calculate the surface tension or interfacial tension dynamically.

Particle tracing. To demonstrate the flow pattern inside the toluene droplet, we added conductive silver-coated hollow glass microspheres (900 kg/m^3, 25-65 μm, Cospheric LLC) into 0.1 mM toluene solutions before filling into the syringe. The particle-containing solution is then injected into DI water and the droplet volume is tuned to make sure the droplet stays pinned after UV irradiation. The particle density is close to that of the toluene solution such that the effect of gravity or buoyancy on the motion of those microspheres is negligible. The Argon Ion UV laser was used to trigger the photo-Marangoni flow within the droplet and all video frames were recorded using the Canon EOS 80D.

Finite element simulations. We capture the outline of the droplet right before it departs and assume that the droplet is in a quasi-steady state. The computational domain is axisymmetric (6 mm $\times$ 12 mm) and the flow is laminar due to low Reynolds number. The governing equations are continuity and Navier-Stokes equations:

129

(4) For simplicity, we used a fixed interface where Marangoni stresses are balanced by viscous stresses, consistently with previous work on interfaces with surfactant[37]. The curvature-dependent Laplace pressure is also considered and applied to the droplet[12],

(5) where Π is the stress tensor, $\vec{n}$ is the unit outer normal vector, $\vec{t}$ is the unit vector tangential to the interface and ∇_s is the gradient along the interface. The operator δ represents the difference across the

$$\nabla \cdot (\rho \vec{u}) = 0$$
$$\nabla \cdot (\rho \vec{u} \vec{u}) = - \nabla p + \nabla \cdot (\mu \nabla \vec{u}) + \rho \vec{g} \; \vec{t} \cdot \nabla_s \gamma = \delta(\vec{t} \cdot \Pi \cdot \vec{n})$$

interface. No slip boundary condition is applied to the walls in the computational domain except the droplet bottom where an inlet boundary condition is applied and the top wall where an outlet boundary condition is enforced.

Temperature rise of droplets due to direct laser heating

To eliminate the possible effect of thermal Marangoni effect induced by the direct laser on the toluene droplet, we carried out finite element simulations to study the temperature change of the toluene droplet when it is heated by the UV laser. The droplet outline is directly extracted from our experiments on a 11 μL droplet. A uniform volumetric heating is applied on the top region of the droplet at t = 0 s to mimic the laser heating, since surfactants exist both in the bulk and the interface. The heating power is set to be 0.06 W. The temperature change of the toluene droplet before the droplet departure at t = 0.38 s is shown in Figure S2. Despite the high laser power density (2.8 W/cm²), the temperature rise of the toluene droplet is limited to 0.25 °C in 0.38 s.

130
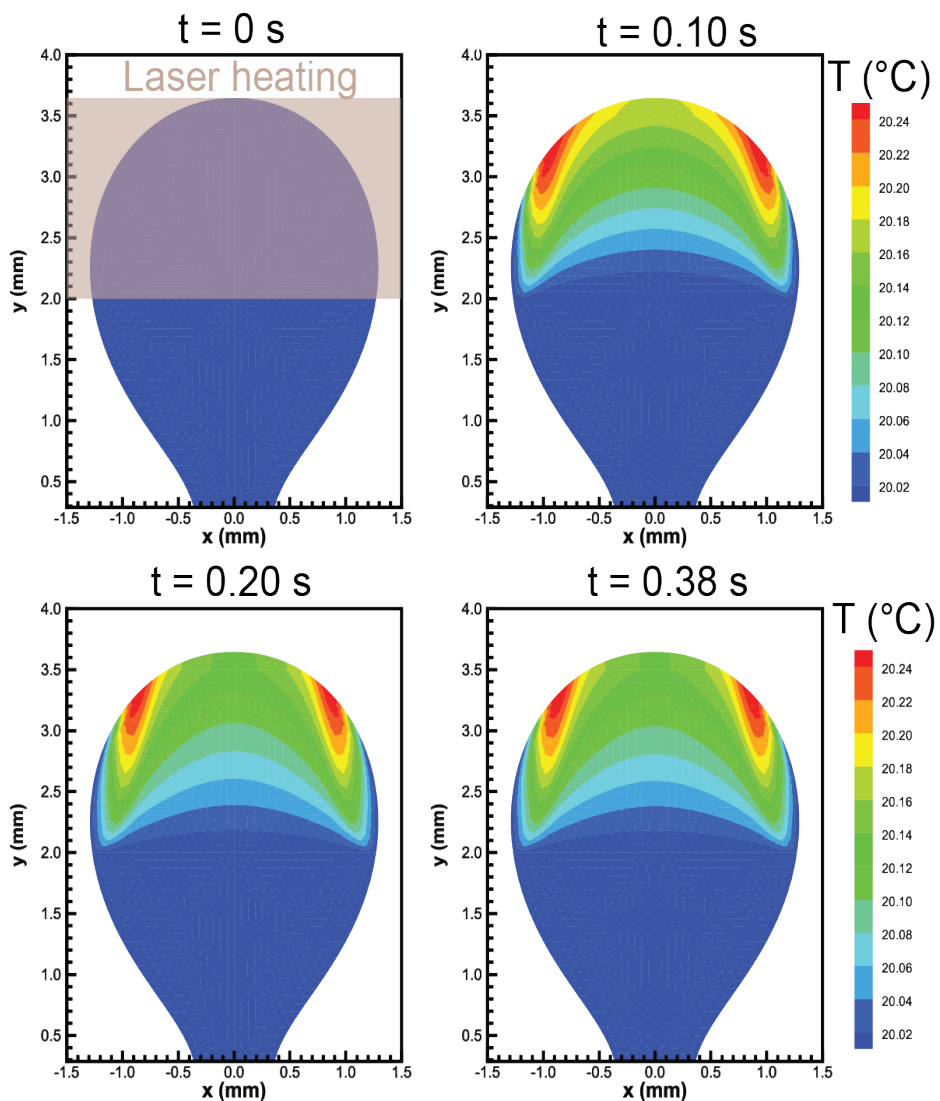
Figure S1. The temperature contours of the toluene droplets under direct laser heating before departing.

We further measured the temperature rise of the toluene droplet using a K-type thermocouple probe. The experimental setup is shown in Figure S3a. In this time, we generate a small toluene droplet that could not depart even with the photo-Marangoni effect. A K-type thermocouple probe is placed in the top region of the toluene droplet and the temperature is recorded once per second. In Figure S3b, it is shown that the droplet

temperature is fluctuating around 23.2 °C. This is because the droplet temperature quickly reaches its equilibrium distribution within 1 second according to our simulation results.
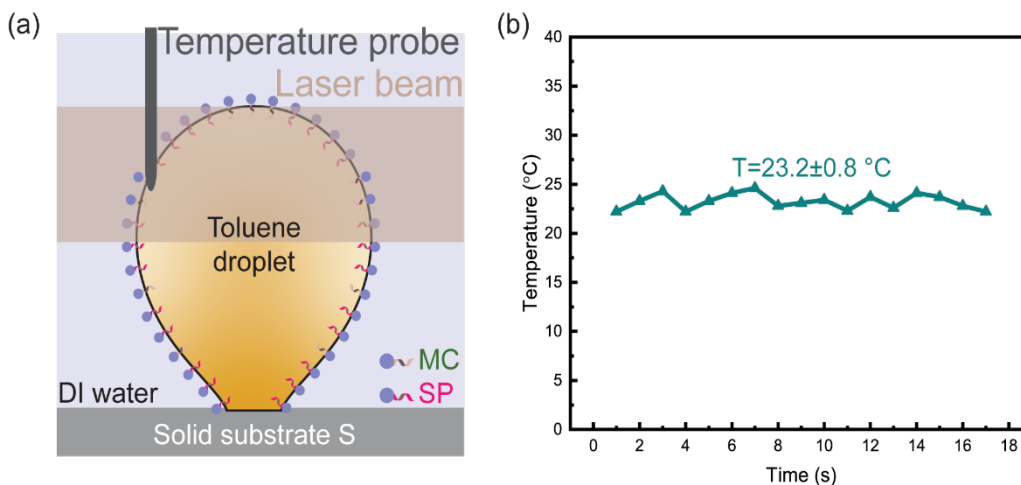
Figure S2. Measuring the temperature rise of the droplet top. (a) Experimental setup to measure temperature of the top of the toluene droplet. (b) The measured temperature change after the UV laser is turned on.

Temperature rise of bubbles due to UV LED irradiation

The departure of air bubbles immersed in the 0.1 mM toluene solution is also subject to the possible effect of thermal Marangoni flow. Therefore, we used a K-type thermocouple probe to measure the temperature variations of the toluene solution after the UV LED is turned on, as shown in Figure S4. After one minute of direct UV LED heating, the solution temperature is increased only by 0.5 °C. Therefore, the effect of temperature variations on bubble dynamics can be neglected.
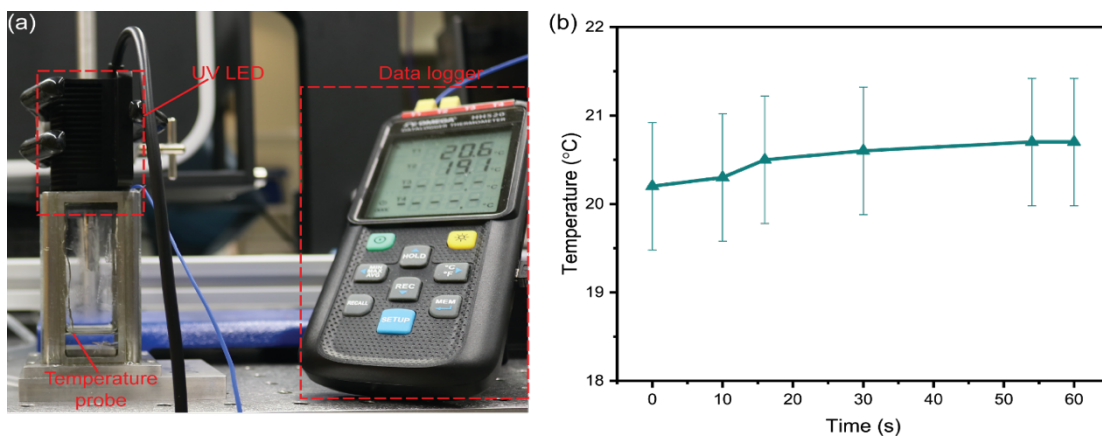
Figure S3. Measuring the temperature rise of 0.1 mM toluene solution due to UV LED heating. (a) Experimental set-up. (b) Temperature change of the toluene solution.

Effect of apparent contact angle

As discussed in the manuscript, in the extreme case of microgravity applications, or of immiscible fluids with matched densities where buoyancy is negligible, the criterion for the photo-Marangoni force to overcome the totality of the pinning surface force is $\frac{\Delta\gamma}{\gamma} \gtrsim$ $\sin^2\varphi$, where φ is the contact angle, $\Delta\gamma$ is the difference in surface tension across the droplet, and γ is the surface tension at the droplet base. It can be seen that the lower the contact angle φ, the easier for this criterion to be satisfied since the right-hand-side of this equation is smaller.

To experimentally verify the effect of the apparent contact angle φ, we compared the departure behaviors of a toluene drop and an m-xylene drop in water. Figure S5a presents time-lapse images of a toluene droplet (0.1 mM SP-DA-PEG) solution departing in $t_{dt} = 2.04$ s. The droplet has a volume of 10.98 mL and a UV laser with intensity of 29.08 mW/mm² is applied on the top of the droplet. The apparent contact angle is measured to be $\varphi_t = 43.2°$. In Figure S5b, we produced a 0.1 mM m-xylene droplet in DI water. The droplet has a

133

volume of 11.33 mL and an apparent contact angle of $\varphi_t = 50.9°$. Figure S5b shows that the

m-xylene droplet departs from the substrate in $t_{d,x} = 3.26$ s, a 60% percent increase

compared to t_{dt}. Since m-xylene and toluene share similar physical and interfacial properties

(density, viscosity, surface tension, etc) due to their similar molecular structure, if we

assume that the interfacial tensions of m-xylene-water and toluene-water are similar, the

increase of the apparent contact angle leads to a stronger vertical component of the pinning

force ($F_{pin,vertical} \sim \gamma d_b \sin^2\varphi$) and hence delays the droplet departure.
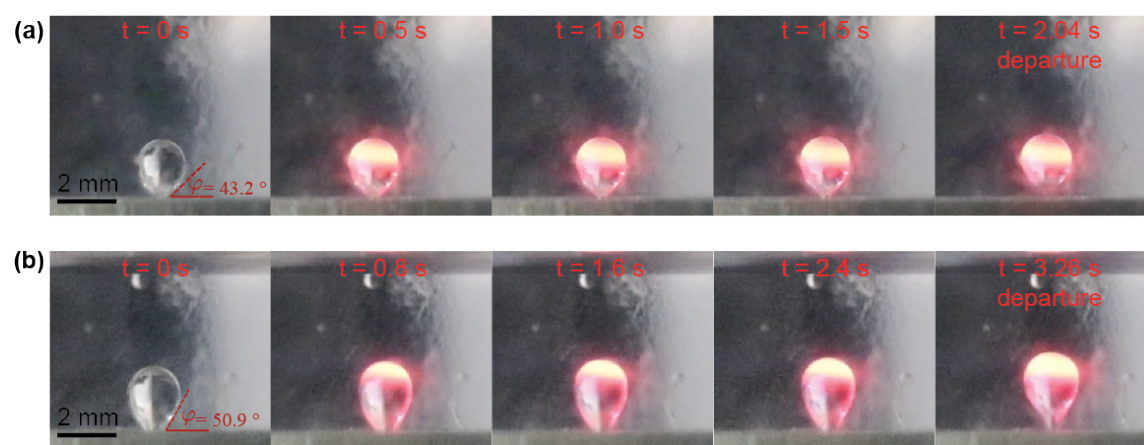
Figure S4. Time-lapse images of droplet departure with different contact angles. (a) The toluene droplet

exhibiting an apparent contact angle of 43.2° departs in 2.04 s. (b) The m-xylene droplet exhibiting an apparent

contact angle of 50.9° departs in 3.26 s.

Supplementary Movies . Movies can be found at *ACS Cent. Sci.* 2022, 8, 2, 235–245.

Copyright 2022. American Chemical Society

Supplementary Movie 1

Description: **Swift departure of the toluene droplet activated by a UV laser**. A

toluene

solution droplet (0.1 mM SP-DA-PEG) is irradiated by an Argon Ion UV laser

(351.1+363.8 nm,

beam diameter of 1.3 mm, incidental light power density of 44 mW/cm^2) and the video is

recorded by a Canon EOS 80D camera. The movie is played in real time.

Supplementary Movie 2

Description: **Flow visualization inside a 0.1 mM toluene solution droplet**. A toluene

solution droplet is irradiated by an Argon Ion UV laser (351.1+363.8 nm, beam diameter of

1.3 mm, incidental light power density of 44 mW/cm^2) and the video is recorded by a

Phantom VEO 640L camera. The movie is played at 4X speed. Particles are flowing

downward near theinterface and moving upward near the center. Particle circulation is

immediately expedited by the Marangoni convection once the UV laser is turned on.

Eventually the droplet departed.

Supplementary Movie 3

Description: **Flow visualization inside a 0.1 mM toluene solution droplet**. A toluene

solution droplet is irradiated by an Argon Ion UV laser (351.1+363.8 nm, beam diameter of

1.3 mm, incidental light power density of 44 mW/cm^2) and the video is recorded by a

Phantom VEO 640L camera. The movie is played at 4X speed. Particles are flowing

downward near the interface and moving upward near the center when the UV laser is

turned on the photo-Marangoni flow takes effect.

Supplementary Movie 4

Description: **Droplet departure under UV irradiation at different heights**. A toluene solution droplet (11.5 μL, 0.1 mM SP-DA-PEG) is irradiated by a fiber-coupled UV LED (M365FP1, Thorlabs, Inc.). On the left panel, the UV LED is aligned at the top of the droplet. On the right panel, the UV LED is aligned at the bottom of the droplet. Both videos are played at 5X speed.

4.5 References

1. Cho, H. J., Preston, D. J., Zhu, Y. & Wang, E. N. Nanoengineered materials for liquid–vapour phase-change heat transfer. *Nat. Rev. Mater.* **2**, 16092 (2016).

2. Kim, H. *et al*. Water harvesting from air with metal-organic frameworks powered by natural sunlight. *Science* eaam8743 (2017) doi:10.1126/science.aam8743.

3. Lu, Z. *et al*. Ultrahigh Hydrogen Evolution Performance of Under-Water "Superaerophobic" MoS2 Nanostructured Electrodes. *Adv. Mater.* **26**, 2683–2687 (2014).

4. Cao, Z., Zhou, J., Wei, J., Sun, D. & Yu, B. Experimental and numerical study on bubble dynamics and heat transfer during nucleate boiling of FC-72. *Int. J. Heat Mass Transf.* **139**, 822–831 (2019).

5. Jaikumar, A., Rishi, A., Gupta, A. & Kandlikar, S. G. Microscale Morphology Effects of Copper–Graphene Oxide Coatings on Pool Boiling Characteristics. *J. Heat Transf.* **139**, (2017).

6. Zhao, Q., Cui, H., Wang, Y. & Du, X. Microfluidic Platforms toward Rational Material Fabrication for Biomedical Applications. *Small* **16**, 1903798 (2020).

7. Prashanth, S., Subbaya, K., Kundachira, N. & Sachhidananda, S. Fiber Reinforced Composites - A Review. *J. Mater. Sci. Eng.* **6**, 1–6 (2017).

8. Liu, Y., Andrew, M., Li, J., Yeomans, J. M. & Wang, Z. Symmetry breaking in drop bouncing on curved surfaces. *Nat. Commun.* **6**, 10034 (2015).

9. Feng, S. *et al.* Tip-induced flipping of droplets on Janus pillars: From local reconfiguration to global transport. *Sci. Adv.* **6**, eabb4540 (2020).

10. Liu, Y. *et al.* Pancake bouncing on superhydrophobic surfaces. *Nat. Phys.* **10**, 515–519 (2014).

11. Chen, L. *et al.* Thermal-responsive hydrogel surface: tunable wettability and adhesion to oil at the water/solid interface. *Soft Matter* **6**, 2708–2712 (2010).

12. Maass, C. C., Krüger, C., Herminghaus, S. & Bahr, C. Swimming Droplets. *Annu. Rev. Condens. Matter Phys.* **7**, 171–193 (2016).

13. Miljkovic, N., Preston, D. J., Enright, R. & Wang, E. N. Electric-Field-Enhanced Condensation on Superhydrophobic Nanostructured Surfaces. *ACS Nano* **7**, 11043–11054 (2013).

14. Wang, W. *et al.* Multifunctional ferrofluid-infused surfaces with reconfigurable multiscale topography. *Nature* **559**, 77–82 (2018).

15. Choi, K., Ng, A. H. C., Fobel, R. & Wheeler, A. R. Digital Microfluidics. *Annu. Rev. Anal. Chem.* **5**, 413–440 (2012).

16. Hao, C. *et al.* Electrowetting on liquid-infused film (EWOLF): Complete reversibility and controlled droplet oscillation suppression for fast optical imaging. *Sci. Rep.* **4**, 6846 (2014).

17. Zhu, Y., Antao, D. S., Xiao, R. & Wang, E. N. Real-Time Manipulation with Magnetically Tunable Structures. *Adv. Mater.* **26**, 6442–6446 (2014).

18. He, S., Meng, Y. & Tian, Y. Correlation Between Adsorption/Desorption of Surfactant and Change in Friction of Stainless Steel in Aqueous Solutions Under Different Electrode Potentials. *Tribol. Lett.* **41**, 485–494 (2011).

19. Li, J., Ha, N. S., Liu, T. 'Leo', van Dam, R. M. & 'CJ' Kim, C.-J. Ionic-surfactant-mediated electro-dewetting for digital microfluidics. *Nature* **572**, 507–510 (2019).

20. Cho, H. J., Mizerak, J. P. & Wang, E. N. Turning bubbles on and off during boiling using charged surfactants. *Nat. Commun.* **6**, 8599 (2015).

21. Lv, C., Varanakkottu, S. N., Baier, T. & Hardt, S. Controlling the Trajectories of Nano/Micro Particles Using Light-Actuated Marangoni Flow. *Nano Lett.* **18**, 6924–6930 (2018).

22. Xiao, Y. *et al.* Moving Droplets in 3D Using Light. *Adv. Mater.* **30**, 1801821 (2018).

23. Seshadri, S. *et al*. Influence of polarity change and photophysical effects on photo

    surfactant-driven wetting. *Langmuir* (2021).

24. Setaro, A., Bluemmel, P., Maity, C., Hecht, S. & Reich, S. Non-Covalent

    Functionalization of

    Individual Nanotubes with Spiropyran-Based Molecular Switches. *Adv. Funct.*

    Mater. **22**,

    2425–2431 (2012).

25. Klajn, R. Spiropyran-based dynamic materials. *Chem. Soc. Rev.* **43**, 148–184 (2013).

26. Kathan, M. & Hecht, S. Photoswitchable molecules as key ingredients to drive

    systems

    away from the global thermodynamic minimum. *Chem. Soc. Rev.* **46**, 5536–5550

    (2017).

27. Bailey, S. J. *et al*. Norbornadiene Chain-End Functional Polymers as Stable, Readily

    Available Precursors to Cyclopentadiene Derivatives. *Macromolecules* **53**, 4917–

    4924

    (2020).

28. St. Amant, A. H. *et al*. Norbornadienes: Robust and Scalable Building Blocks for

    Cascade

"Click" Coupling of High Molecular Weight Polymers. *J. Am. Chem. Soc.* **141**, 13619–13624

(2019).

29. Stauffer, C. E. The Measurement of Surface Tension by the Pendant Drop Technique. *J.*

    Phys. Chem. **69**, 1933–1938 (1965).

30. Chang, C.-H. & Franses, E. I. Adsorption dynamics of surfactants at the air/water interface:

    a critical review of mathematical models, data, and mechanisms. *Colloids Surf.*
    Physicochem. Eng. Asp. **100**, 1–45 (1995).

31. Saien, J. & Akbari, S. Interfacial Tension of Toluene + Water + Sodium Dodecyl Sulfate from (20 to 50) °C and pH between 4 and 9. *J. Chem. Eng. Data* **51**, 1832–1835 (2006).

32. Zhang, Q. *et al.* Light-Guided Surface Plasmonic Bubble Movement via Contact Line De-Pinning by In-Situ Deposited Plasmonic Nanoparticle Heating. *ACS Appl. Mater. Interfaces* **11**, 48525–48532 (2019).

33. Yang, Z., Wei, J., Sobolev, Y. I. & Grzybowski, B. A. Systems of mechanized and reactive droplets powered by multi-responsive surfactants. *Nature* **553**, 313–318 (2018).

34. Hanif, N. M. *et al.* The Composition of Surfactants in River Water and its Influence to the Amount of Surfactants in Drinking Water. **17**, 6 (2012).

35. Kabir, E., Kumar, P., Kumar, S., Adelodun, A. A. & Kim, K.-H. Solar energy: Potential and future prospects. *Renew. Sustain. Energy Rev.* **82**, 894–900 (2018).

36. Raymo, F. M. & Giordani, S. Signal Processing at the Molecular Level. *J. Am. Chem. Soc.* **123**, 4651–4652 (2001).

37. Peaudecerf, F. J., Landel, J. R., Goldstein, R. E. & Luzzatto-Fegiz, P. Traces of surfactants can severely limit the drag reduction of superhydrophobic surfaces. *Proc. Natl. Acad. Sci.* **114**, 7254–7259 (2017).

5. Self-regulating photochemical Rayleigh-Bénard convection using a highly-absorbing organic photoswitch

Abstract

We identify unique features of a highly-absorbing negatively photochromic molecular switch, donor acceptor Stenhouse adduct (DASA), that enable its use for self-regulating light-activated control of fluid flow. Leveraging features of DASA's chemical properties and solvent-dependent reaction kinetics, we demonstrate its use for photo-controlled Rayleigh-Bénard convection to generate dynamic, self-regulating flows with unparalleled fluid velocities ($\sim$mm s^{-1}) simply by illuminating the fluid with visible light. The exceptional absorbance of DASAs in solution, uniquely controllable reaction kinetics and resulting spatially-confined photothermal flows demonstrate the ways in which photoswitches present exciting opportunities for their use in optofluidics applications requiring tunable flow behavior. This chapter was adapted with permission from *Nat Commun.* **2020**, 11, 2599. Copyright 2020 Nature.

5.1 Introduction

Photoswitches can also be used to drive photothermal control of fluids by taking advantage of the easily tunable switching kinetics and the large changes in spectral absorption afforded by negative photoswitches such as DASA. In this chapter we explore how this effect can be leveraged for self-regulation in fluids. Autonomous control of liquid motion is vital to the development of new actuators and pumps in fluid systems. Though current systems provide effective control over flow, autonomous control of fluid motion (i.e., without external manipulation) is inaccessible *via* the chemistries used in these approaches. Self-regulated fluid pumping is, in its current form, most commonly accomplished *via* the establishment of local gradients of solutes resulting from a chemical reaction.[1,2] However, many of these systems are limited by the depletion of the chemical source which is used to generate flow, production of harmful byproducts, and their working environment. Self-regulation is advantageous where manipulation of flow is desirable without external manipulation or complex chemistry. As such, in this chapter we investigate how high-absorbing, negatively photochromic molecular switches might be used to overcome these limitations.

Generally, irradiating highly-absorbing particles or molecules in a solution locally heats the solution, and in turn can result in Rayleigh-Bénard convection, in which thermal gradients generate buoyancy-driven flow. However, in the case of such photothermal Rayleigh-Bénard convection under constant, continuous irradiation (i.e., a constant rate of energy input) of an otherwise closed system, establishing a steady state requires a negative feedback that retards the rate of Rayleigh-Bénard convection as the total energy in the system increases over time. In the case of a high-absorbing, non-bleaching dye or particle, where a

143

photothermal gradient is established, the negative feedback is the heat loss to the surrounding environment due to heat transfer through the confining walls. Absent this external energy loss, there is no mechanism by which to dynamically decrease the amount of irradiant photon energy that is converted to heat (other than to externally decrease the intensity of incident light). By contrast, the use of negatively photochromic molecules, which can reversibly switch from high-absorbing and colored state to non-absorbing and clear state upon irradiation provides an internal negative feedback mechanism: as the light intensity increases, more bleaching occurs, which limits the total amount of irradiant energy that can be converted to heat and, therefore, produce a temperature gradient. These negative feedback properties critically rely on the reversibility of the bleaching reaction and its ability to establish and sustain a concentration gradient of the photothermal material and enable spatially-varying absorbance in solution that is dynamically maintained. As such, self-regulation can be established and maintained internally by the photoswitching properties of the molecule. Furthermore, variable extrinsic factors (e.g., concentration) known to alter characteristics of the photoreaction (e.g., reaction rate) serve as control "knobs" that, in turn, also enable control over the behavior of the Rayleigh-Bénard convection by dynamically tuning the bleaching profile of the photochrome.

For this work, we utilize DASAs, which allow us to understand and exploit the factors that govern self-regulated fluid flow. In this chapter, we report how combining our understanding of DASAs' photoswitching kinetics with an ability to control physicochemical conditions such as molarity, solvent, and light intensity enables both controlled and self-regulating fluid motion in organic solutions. The system operates as

follows: by irradiating a solution containing DASA with visible light (**Figure 1b**) a

controlled bleaching front (i.e., a growing non-absorbing region) is generated, which enables

the local manipulation of solution temperature (**Figure 1c**) which in turn incites a time-

varying thermal gradient and thus Rayleigh-Bénard convection (**Figure 1d**). These

convective flows are inherently self-regulated via the complex interplay between the

photochemical conversion kinetics and high absorption, enabling a novel method of control

over fluid motion. The careful manipulation of the reaction kinetics of a photoswitch

uniquely enables the bleaching front progression to dictate the flow behavior observed in

solution. This degree of control is presently inaccessible via other methods and, thus, using a

negatively photochromic molecular photoswitch such as DASA opens new avenues for the

use of high-absorbing photoswitches in applications for self-regulated fluid pumping and
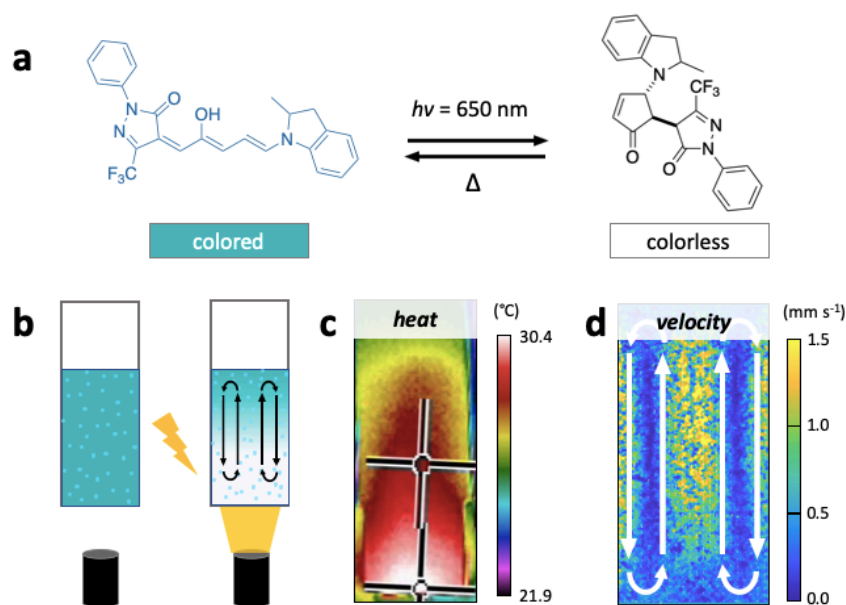
mixing.

Figure 5.1 Donor-acceptor Stenhouse adducts for photothermal control of fluid flow a, DASA-CF3-PI switching under visible light irradiation from an extended, colored, open form to a compact, colorless, closed form. b, Schematic of experimental setup for convective particle tracking. Light shone on the bottom of a quartz cuvette causes DASAs to switch to the colorless form, while also generating c, heat gradients and d, fluid flows due to convection in toluene. Reproduced with permission from Nat Commun. 2020, 11, 2599. Copyright 2020 Nature.

5.2 Results

5.2.1 DASA switching kinetics.

In order to drive dynamic, photochemically-regulated fluid flows we focused on the newly developed third generation DASA bearing a CF_3 pyrazolone-based acceptor and a 2-methyl indoline donor[3] (referred to hereafter simply as DASA-CF_3-PI) due to its high molar absorptivity and tunable forward and reverse switching kinetics in organic solvents. Though DASA-CF_3-PI switches from its colored, open form to a bleached, closed form (**Figure 1a, 2a**) in both toluene and chloroform, the tunability of this behavior arises from solvent- and concentration-dependent photoswitching kinetics. The following studies highlight the dynamic control of flow behavior by varying solvent, concentration, and light intensity. Specifically, this DASA derivative exhibits a faster backward photoreaction in toluene than in chloroform, as evidenced by reverse rates of reaction (k_{back}) of 0.046 s^{-1} and 0.035 s^{-1} in toluene and chloroform, respectively, at 10 μM (Figure 2b, Supplementary Note 1). This difference in k_{back} is intensified at high concentrations—as DASA-CF_3-PI exhibits a stronger concentration-dependence in toluene than in chloroform—leading to an even faster back reaction.[4] The bleaching front velocity (**Figure 2c**) and solvent-dependent switching

combined with DASA's high molar absorptivity (**Figure 2d**), can be exploited to generate sharp thermal gradients at the interface between the bleached and non-bleached portions of the solution that drive convective flows (Fig 2a). Varying light intensity also has an effect on the magnitude of observed thermal gradients.

5.2.2 Molar absorptivity drives thermal gradient.

In its colored form, the high molar absorptivity of DASA enables the effective conversion of light energy to heat, which in turn drives fluid motion. Using UV/Vis spectroscopy, we determined the molar absorptivity of DASA-CF$_3$-PI in toluene, chloroform, and dichloromethane to be $118,820 \pm 516$ M^{-1} cm^{-1}, $88,867 \pm 300$ M^{-1} cm^{-1}, and $129,190 \pm 490$ M^{-1} cm^{-1}, respectively (**Supplementary Figure 2**). For comparison, we determined the molar absorptivity of highly-absorbing, commercially available organic dye Nile Red to be $38,000$ M^{-1} cm^{-1} and that of a non-bleaching DASA analog to be $70,500$ M^{-1} cm^{-1} (**Supplementary Figure 3**). To demonstrate the dramatic changes in temperature enabled by the absorbance of DASA-CF$_3$-PI, solutions of varying concentration in chloroform were irradiated for ten minutes using a 214 mW cm^{-2} white light source (**Figure 3a**). From these experiments, we observe 2 °C temperature changes in solvent without dye due to the heat from the light source and up to 12 °C in the presence of DASA-CF$_3$-PI (**Figure 3b**). Furthermore, infrared imaging illustrates a temperature gradient established throughout the solution within tens of seconds of irradiation (**Figure 3c**). Above 2 mM, however, increasing the DASA-CF$_3$-PI concentration fails to further increase the solution temperature, as a rapid back reaction impedes the penetration of light and thus absorbance of the small molecules responsible for generating heat.
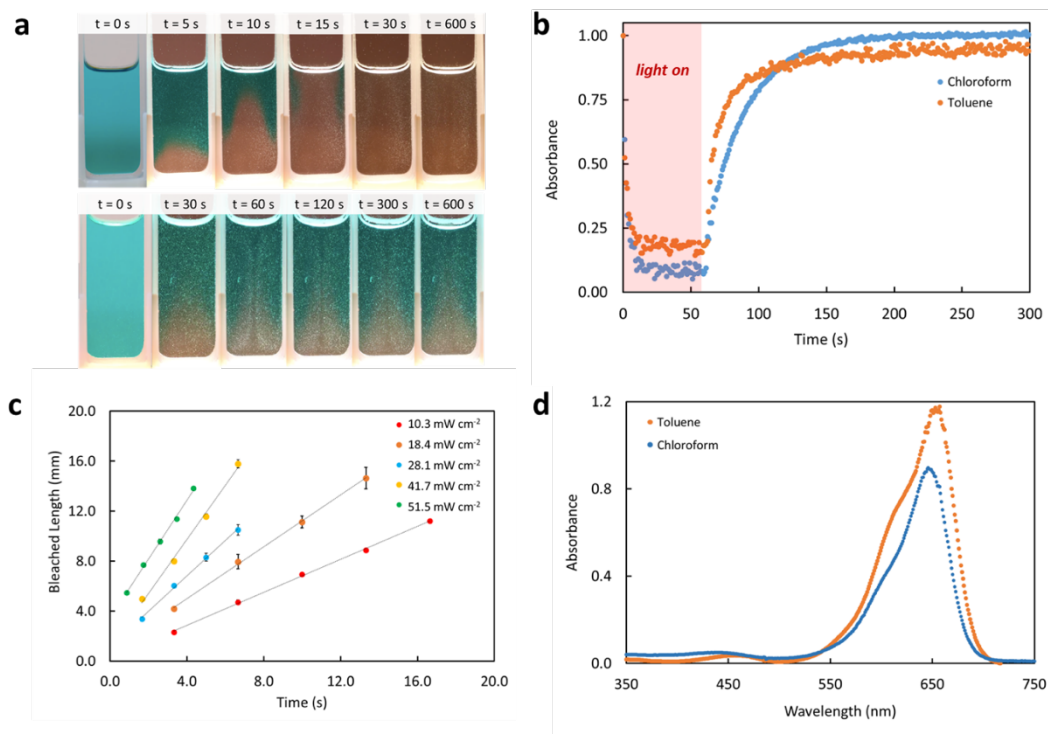
Figure 5.2 Photochemical properties of DASA-CF3-PI in chloroform and toluene. a, Bleaching front progression through 0.25mM DASA-CF3-PI in chloroform stabilized with 0.75% ethanol (top) and toluene (bottom) irradiated with 25 mW cm-2 light. b, Reversible switching kinetics of DASA-CF3-PI in chloroform and toluene at 10 μM. c, Bleaching front length versus time for 0.125mM DASA in chloroform, where the slope provides a measure of the front velocity. D, Absorbance of DASA-CF3-PI in toluene and chloroform at 14 μM. Reproduced with permission from Nat Commun. 2020, 11, 2599. Copyright 2020 Nature.
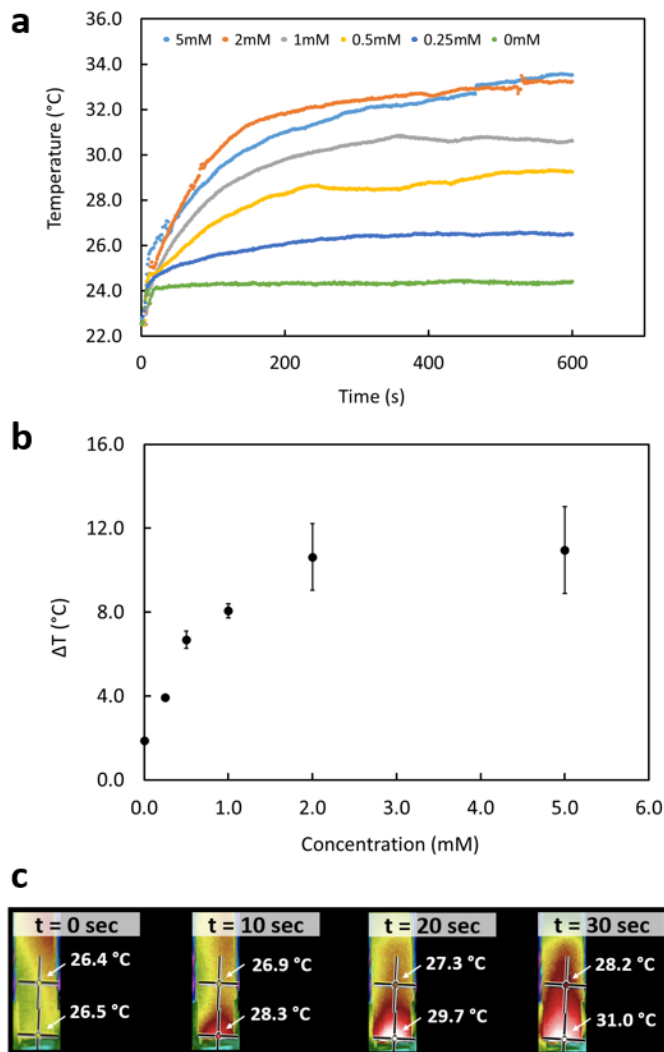
Figure 5.3. Photothermal temperature changes due to DASA-CF3-PI in solution. a, Average heating of chloroform solutions with varying concentrations of DASA-CF3-PI using 214 mW cm-2 white light. b, Change in temperature as a function of DASA-CF3-PI concentration from t=0s to t=600s. Average values are plotted with error bars calculated from the standard deviation of replicate measurements (N=3). c, Thermal images of heat gradient established in the first 30 seconds of irradiation of 2mM DASA-CF3-PI in chloroform, as measured with an IR camera. Note, the camera's auto-adjust feature prevents the use of a consistent legend for the temperature, so numeric values for two locations are shown. Reproduced with permission from Nat Commun. 2020, 11, 2599. Copyright 2020 Nature.

5.2.3 Control of bleaching front.

Using the experimental configuration depicted in Supplementary Figure 1, we found that solutions of DASA-CF$_3$-PI in chloroform at low concentrations (e.g., 0.25 mM) exhibit a well-defined bleaching front (i.e., a growing zone of bleached solution) that propagates through the entire volume of the solution similar to those previously studied.[5] However, this behavior is different from that in toluene, where the bleaching front begins to propagate through the solution but is then halted at some non-zero height due to a competitive back reaction (**Figure 2a**). Understanding the bleaching behavior is critical, as DASA's absorbance—and thus, its ability to generate heat—falls steeply once it has transitioned from the colored to colorless state (**Figure 2b**). The time- and length-scales over which these solutions bleach can be analyzed to predict characteristics of the flow behavior and tune the system for self-regulation.

The bleaching profile corresponds to a sharp gradient in concentration of the open form of DASA-CF$_3$-PI between a bleached zone (A) and unbleached zone (B). Because of the large disparity in photoabsorption efficiency between the open and closed forms of DASA-CF$_3$-PI (**Figure 2b**), the heat generation that drives the convective flow is primarily produced in the unbleached (i.e., colored) zone where the concentration of the open form is significantly greater than the closed form. As such, we expect that the total rate of energy input that drives photothermal convection will be proportional to the average net rate of photoreaction in the bleached zone and the fraction f of the container volume occupied by the unbleached zone, $f = (H - h_I)/H$, where H is the total fluid height and h_I the height of the bleaching front (i.e., colorless zone). Therefore, to a first approximation, we also expect

that the time variation of the magnitude of the maximum convective velocity will qualitatively track with the speed at which the bleaching front advances—i.e., $dv_{max}/dt \propto df/dt \propto -dh_I/dt$. It is therefore of critical importance to understand the kinematics of the bleaching front, and the influence of the various coupled transport processes present in the system.

The velocity of the front depends on the net rate of reaction (forward and backward), mass transport to and from the bleaching front, and convection due to flow and diffusion. By restricting the analysis to only the bleaching front itself, we expect that concentration gradients in the bleached and unbleached regions will be small, such that the diffusive flux is negligible compared to the convective flux. Making this and other simplifying assumptions and solving for the interface velocity yields Eq. (1) (full derivation, **Supplemental Note 2**).

$$v_I = v_{fluid} + \frac{\delta r_{I,open}}{\Delta N_{I,open}} \tag{1}$$

Here, $\Delta N_{I,open} = N_{A,open} - N_{B,open}$ is the change in open DASA-CF$_3$-PI molar concentration across the bleaching front, δ is the thickness of the transition in concentration between the bleached and unbleached regions, and $r_{I,open}$ is the net rate of the reaction, defined in Eq. (2).[4]

$$r_{I,open} = \sigma(N_{I,open}) \cdot \phi_{OC}(N_{I,open}) \cdot I(h_I) \cdot N_{I,open} - k_{back}(N_{I,open})$$
$$\cdot [N_o - N_{I,open}] \tag{2}$$

151

Note that the forward reaction rate is governed by the absorption cross-section σ, the quantum efficiency for photoconversion between the open and closed form ϕ_{OC}, the irradiation intensity at the bleaching front I, and the concentration of open DASA-CF$_3$-PI at the bleaching front $N_{I,open}$. The back reaction is dictated by the rate constant of the backward photoconversion k_{back} and the concentration of the closed form of DASA-CF$_3$-PI $(N_o - N_{I,open})$. The reverse rate constant is calculated by fitting the experimental absorbance recovery of DASA after irradiation is ceased to a decaying exponential function.[4] Substituting Eq. (2) into (1) results in Eq. (3).

$$v_I = v_{fluid} + \frac{\delta}{\Delta N_{I,open}} \left\{ \sigma \cdot \phi_{OC} \cdot I(h_I) \cdot N_{I,open} - k_{back} \cdot \left[N_o - N_{I,open} \right] \right\}$$

(3)

Eq. (3) reveals the unique features that are imparted to the photothermal convection due to a reversible photochemical reaction such as that enabled by DASA-CF$_3$-PI. When k_{back} is small (e.g., in chloroform) the velocity of the bleaching front (which is distinct from, but is influenced by, the underlying convective fluid velocity, as indicated in Eq. (1)) is always positive and the bleaching front will grow to fill the volume of the container. Once completely bleached, no further energy due to photothermal processes is generated—allowing the thermal gradient to dissipate and convective flow to be "turned off." By contrast, if k_{back} is sufficiently large (e.g., in toluene) the location of the bleaching front can reach a dynamic steady state dictated by the self-regulating balance between 1) the photothermal convection and forward reaction in the unbleached zone, and 2) the back

152

reaction in the bleached zone. Thus, using toluene and chloroform, we demonstrate distinct flow behaviors that take advantage of differences in DASA's back reaction rates. Unlike other photothermal systems, DASA's solvent-dependent back reaction kinetics offer unique modular control over dynamic and self-regulating flows in solution.

5.2.4 Nonlinear relationship between concentration and fluid velocity.

Examining the fluid motion in quartz cuvettes containing identical concentrations of DASA-CF_3-PI to those used in the temperature studies, we observed a nonlinear relationship between the strength of convection at early times and DASA-CF_3-PI concentration. This relationship arises as a result of the coupled relationship between the back-reaction kinetics of DASA-CF_3-PI and Beer's Law. As solutions containing DASA-CF_3-PI are irradiated with visible light, the drastic changes in temperature depicted in Figure 3a incite buoyancy-driven Rayleigh-Bénard convection. The strength of this convection can be analyzed by quantifying the speed of flows generated in solution using particle image velocimetry (PIV) to track the motions of neutrally buoyant silica spheres (average diameter = 10 μm). Specifically, 400 μL of solution was pipetted into a cuvette, allowed to settle in the absence of light, and then illuminated from below and recorded using a digital camera (**Supplementary Video 2**). Velocity fields were then calculated from the video using open source PIV software (**Supplementary Figures 4, 5**).[6] These experiments allow us to quantify DASA's remarkable ability to increase fluid motion in a given solution to several mm s^{-1} using only millimolar concentrations of DASA-CF_3-PI and commercially available solvents.

153

Although DASA demonstrates efficient photoswitching capabilities in both toluene and chloroform at low concentrations, the rate of back reaction drastically increases above an optimal concentration.[7] This increased rate implies the rapid reversion of DASA-CF$_3$-PI molecules from a closed, colorless to an open, colored form even in the presence of constant light. With most of the species in the high-absorbing open form, a masking effect is observed (**Figure 4a**) which limits light penetration in the depth of the solution and thus the population of irradiated/switched species. This effect is reflected in the PIV analysis as a continuous decrease in maximum fluid velocity with increasing concentration of DASA-CF$_3$-PI (**Figure 4b).** As a result, there exists an optimal concentration for which light can fully penetrate a solution to establish appreciable convective flow. We estimate this concentration to be 0.5 mM, where the convective flow reaches maximum fluid velocity of ~3.1 mm s^{-1}. While differences in experimental conditions make direct comparison challenging, this fluid velocity is orders of magnitude higher than those reported for common plasmonic particle systems which sustain micrometer per second velocities at similar photon fluxes.[8,9] These experiments establish that light attenuates exponentially as the concentration of the absorbing species increases, and highlight concentration as yet another tunable parameter by which fluid velocity may be controlled.
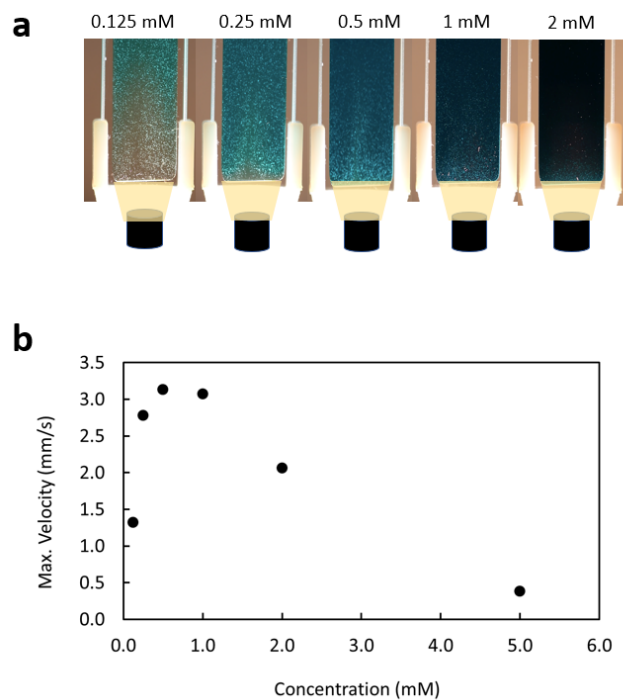
Figure 5.4. Non-linear concentration dependence of particle velocity. a Concentrations ranging from 0.125 mM to 2 mM of DASA in toluene shown from left to right after 10 s of irradiation with 46 mW cm-2 light. b, Particle velocities as a function of concentration show the nonlinear dependency on concentration. Above 0.5 mM, the dark solution exhibits a masking effect that limits light penetration and, as a result, limits particle velocity. Reproduced with permission from Nat Commun. 2020, 11, 2599. Copyright 2020 Nature.

5.2.5 Bleaching front dictates self-regulating fluid motion.

The nonlinear coupling of both solvent- and concentration-dependent photoswitching kinetics and high absorption properties enables unprecedented self-regulation of photothermal flows. Irradiating a solution of a given concentration and solvent incites a photothermally-driven flow which creates a dynamic equilibrium at the bleaching front in which the consumption of photoreactants is stoichiometrically replenished by the flux of regenerated photoreactants from the bleached zone. To illustrate this balance, we present two distinct self-regulating flow behaviors using 0.25 mM solutions of DASA-CF$_3$-PI in chloroform and toluene, respectively, irradiated using variable light intensity (**Supplementary Figure 6, 7**).

In chloroform, an effective self-extinguishing behavior enabled by the careful tuning of the reaction kinetics of DASA-CF3-PI dictates the self-regulating flow behavior. Specifically, the rate of forward reaction is significantly greater than that of the reverse reaction—allowing the bleaching/photoswitching front to propagate through the solution unimpeded. As such, the bleached zone will eventually grow to fill the fluid volume, and the photothermal convection will cease after the thermal gradient dissipates—providing an effective "off-switch" for the photothermal convective flows, even as the light remains on (**Figure 2a, 5c**). The time at which the "switch" occurs can be approximated from the bleach front velocity using Eq. (3) and changes in temperature. In the first eight seconds, the temperature of the solution rises as the bleaching front progresses through the cuvette (Figure 5b, inset). At roughly the same time (~10 seconds), the maximum velocity and the maximum temperature difference are achieved. The brief, initial rise in temperature (**Figure**

5b, inset) is due to the high absorbance of DASA. However, as the solution bleaches

(**Figure 5a**) and the light input remains constant, the temperature gradually decreases and

eventually plateaus. This characteristic behavior in chloroform—i.e., a steep rise followed

by a decrease in maximum velocity and temperature—occurs irrespective of light intensity

(**Supplementary Figure 7**), although the intensity variations enable control of fluid flow

dynamics. Increased light intensity leads to faster absorption and thus higher peaks in

maximum velocity, but also a faster bleaching of the DASA solution. This repeatable

behavior combined with control over tunable parameters (e.g., light intensity), make this

type of switch uniquely amenable to systems in need of dynamic pumping under constant

light irradiation and/or spatially precise zones of light penetration. The self-extinguishing

behavior is achieved without additional stimuli or changes in concentration and can thus be

leveraged for applications that require a fluidic feedback loop.

By contrast, in toluene, where k_{back} is sufficiently fast and $N_{I,open}$ is large everywhere, the

front accelerates due to both the large net forward reaction and induced photothermal

convection due to absorption by the open form. As the rate of the forward reaction (dictated

by the quantum yield of DASA-CF$_3$-PI in toluene) is less than the rate of back reaction,

however, the convective fluid velocity term (v_{fluid}) is balanced by the reaction velocity

term. This balance results in a static bleaching front (i.e., $v_I = 0$, see **Figure 5a**), which in

turn allows for a steady state thermal gradient, and thence a constant fluid velocity that is

maintained over ten minutes (**Figure 2a, 5c**). In measuring the temperature changes in the

system, we similarly find an initial increase in temperature of approximately 0.6 °C within

the first two minutes that rapidly stabilizes to a steady-state value for over ten minutes of

study. This self-regulation is uniquely imparted by the reversibility of the photoreaction of the DASA-CF$_3$-PI system and a matching of forward and backward reaction kinetics. Other high-absorbing dyes and DASAs are presented for comparison (**Supplementary Figures 8, 9**) to demonstrate the rapid rate and magnitude of convective flow uniquely imparted by using a negative photoswitch with tunable backward kinetics. This second characteristic fluid behavior—i.e., a dynamically stabilized fluid velocity—is amenable to fluid systems in need of controlled, constant velocity. Further, the magnitude of the velocity plateau can be adjusted by tuning the light intensity (**Supplementary Figure 7**).
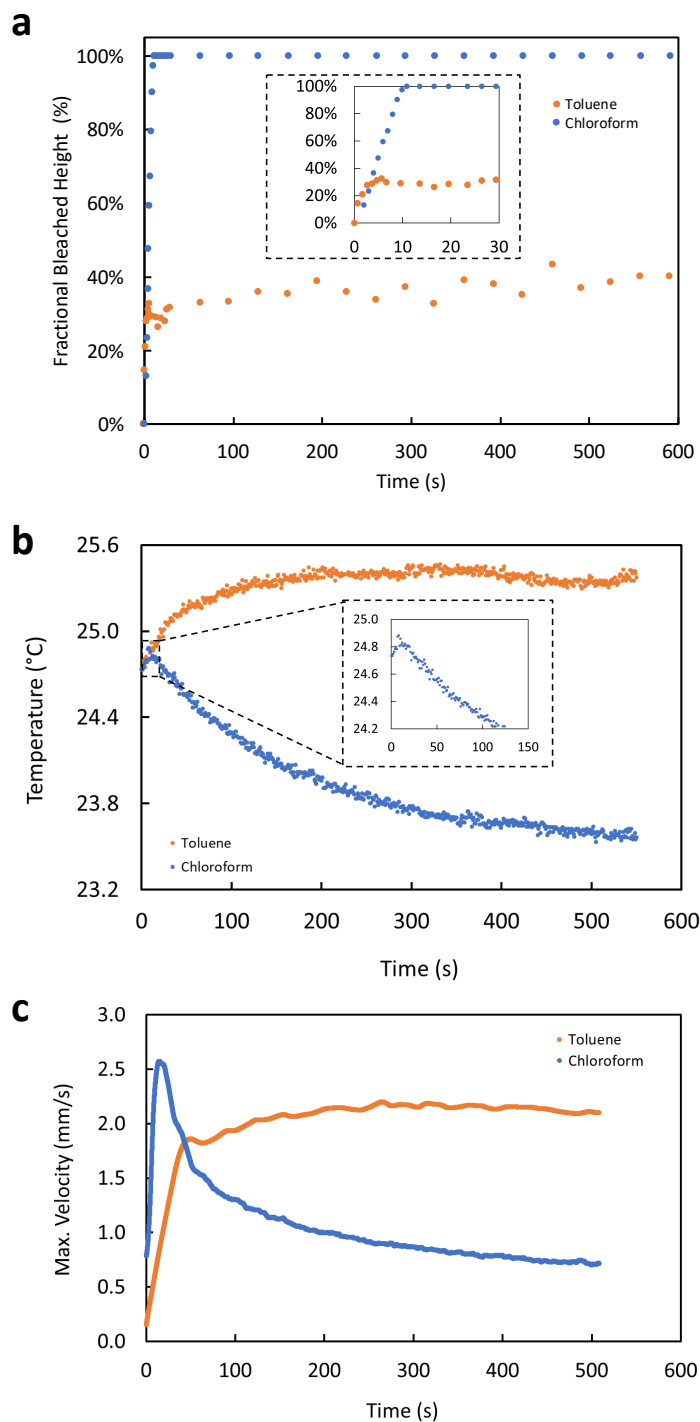
Figure 5.5. Comparison of fluidic and thermal behavior of 0.25mM DASA in chloroform and toluene irradiated with 46 mW cm-2 white light. a, Percent of bleached volume (i.e., height of the bleach front / total wetted length) versus time. Inset depicts the same curves from 0 to 30s. b, Temperature changes over time for toluene and chloroform. Inset depicts the initial spike and then decline in temperature exhibited by DASA in chloroform. c,

Maximum velocity vs. time plots illustrate characteristic velocity trends. See Supplementary Note 3 Percent of bleached volume (i.e., height of the bleach front / total wetted length) versus time. Inset depicts the same curves from 0 to 30 s. Reproduced with permission from Nat Commun. 2020, 11, 2599. Copyright 2020 Nature.

5.2.6 Localized fluid motion.

By localizing the light intensity to a point of interest, we create a pathway by which particles can be advected via a spatially addressed photothermal gradient. To demonstrate this effect, we show the locally directed motion of particles using a red LED ($\lambda = 617$ nm, 21 mW cm^{-2}) to illuminate a 0.25 mM solution of DASA-CF$_3$-PI in chloroform. Visual inspection of particle trajectories demonstrate that we can direct particles along the path of light propagation with just a few seconds of irradiation (**Figure 6, Supplementary Video 3**). Due to a heat-induced decrease in local fluid density, buoyancy effects enable spatially-localized flow, irrespective of the spatial orientation of the light source. As a result of these buoyancy effects, we see from the bleaching that an upward flow is established within seconds after the light source has been removed. The fast reverse kinetics allows for the color to return almost immediately, thus enabling the use of the same solution to direct particles along multiple trajectories.
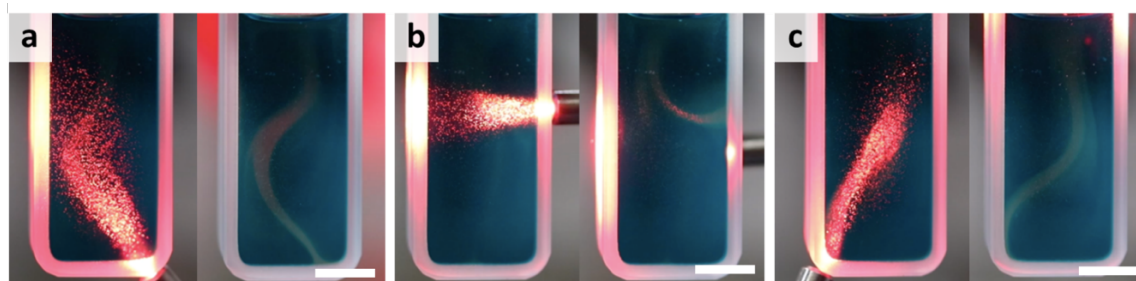

Figure 5.6. Spatially precise convective flows. a-c (left panels), Irradiating one portion of the cuvette using a red LED light. a-c (right panels), convective flows that ensue due to irradiation. The same solution was used for all experiments depicted above (Supplementary Movie 3). Reproduced with permission from Nat Commun. 2020, 11, 2599. Copyright 2020 Nature.

5.3 Conclusion

By leveraging our understanding of DASA's reversible switching kinetics, we have demonstrated the ability to harness the photochemical response of a negatively photochromic switch to control bleaching and consequently photo-thermal gradients in differing solvents to drive programmed fluid motion. The tunable rate of the back reaction of DASA offers a unique handle by which we can control the self-regulatory properties of the system. Additionally, we can estimate the timescale over which a maximum velocity may be achieved as a function of the relative rates of the photochemical reaction and the propagation of the thermal gradient it produces. As such, we unlock a powerful mechanism by which fluid motion can be controlled using a negatively photochromic molecular switch with highly tunable reaction kinetics. For solvents in which DASA-CF$_3$-PI has a fast back reaction, the dynamic steady state achieved in solution produces a self-regulating thermal gradient that can drive fluid flow at a constant velocity. In solvents in which DASA bleaches rapidly and has a slow back reaction, it enables as an effective "off-switch" after the solution has entirely bleached and the thermal gradient dissipates. To our knowledge, this is the first system to demonstrate a self-regulatory degree of control as a result of a photochemical reaction. With careful tuning of reaction kinetics, other high-absorbing negatively photochromic switches can be similarly tailored, providing access to self-regulating control using different wavelengths of irradiation and solvents (Supplementary Figure 9). This versatile control and tunability provides unrivaled access to fluidic applications requiring high fluid velocities ($\sim$mm s^{-1}), controllable fluid behaviors, and operation in a range of chemical environments—all achievable using low intensity visible light.

5.4 Supplementary Information

Supplementary videos can be found at Nat Commun. 2020, 11, 2599. Copyright 2020 Nature.

Supplementary **Video 1** | **Bleaching front of 0.25 mM DASA in chloroform.** Cuvette was irradiated using 41.7 mW cm^{-2} of white light shone through a bandpass filter ($\lambda = 650 \pm$ 40 nm).

Supplementary **Video 2** | **Convection of 0.25 mM DASA in toluene (video speed, 10x).** Left panel depicts the video recording of the convection. Right panel depicts a heat map video of the same video, generated via particle image velocimetry analysis (Canon EOS Rebel T5i, 100mm f/2.8 macro lens, magnification 1x).

Supplementary **Video 3** | **Localized fluid motion in 0.25 mM DASA in chloroform.** A red LED is used to irradiate a cuvette of solution at different points in space.

5.4.1 Experimental Methods

Chemical selection

Chloroform stabilized with 0.75% ethanol and toluene (99.8%) were purchased and used without further purification from Sigma Aldrich. Donor-acceptor Stenhouse adducts were synthesized as described in the procedure previously reported in literature. For each

experiment, the compound was dissolved in solutions from fresh bottles of chloroform stabilized with ethanol or toluene and diluted to the desired concentrations.

Light source

A Schott Ace 150 W fiber optic white light source was chosen for all experiments herein due to its broad coverage of the absorbance spectrum of DASA-CF$_3$-PI and other molecules discussed in this work (Supplementary Figure *3*). In addition, it supplied light fluxes otherwise inaccessible with the use of LEDs available to us.

Characterization

Molar absorptivity of photoswitches and dyes were calculated using spectra obtained with UV/Vis spectrophotometry in triplicate for five concentrations of dye/switch in solvent. Each stock concentration of DASA was prepared 24 h in advance in order to ensure that the photostationary state was reached. All measurements were taken using a standard quartz cuvette with 1 cm pathlength. The photoinduced optical absorption kinetics were measured using a pump-probe setup following previously reported procedures.

Temperature analysis

Heat changes were obtained using a Phidget 4-Input Temperature Sensor in conjunction with the K-Type Teflon Bead Probe Thermocouple (accurate to ±2 °C). Temperatures were measured at the top, middle and bottom of the cuvette to calculate the absolute and temperature differentials over the course irradiation. Infrared images were obtained using a FLIR E60 IR camera accurate to ±2% of reading.

<u>Imaging</u>

A Canon Rebel SL2 (100 mm f/2.8 Macro USM fixed lens, 1x magnification, 29.97 frames per second) was used to image photoreactions occurring in the UV/Vis quartz cuvette. The setup for these reactions is depicted in Supplementary Figure 1. Note that we define the positive u-direction to be against gravity (Supplementary Figure 1). This is later relevant in Supplementary Note 2.

<u>Particle Image Velocimetry</u>

Video records of photoreactions inside the UV/vis cuvette were then segmented into individual grayscale frames based on the camera's frame rate (i.e., 29.97 FPS) using MATLAB code. These frames were then used to perform particle image velocimetry (PIV) using open-source code from Thielecke and Stamhuis.[1,2] Prior to analysis, the region of interest was specified as a rectangle inside of the wetted region of the cuvette where flows occur (Supplementary Figure 4). Next, a fast-Fourier transform (FFT) window deformation algorithm was selected and four interrogation areas of decreasing window size (i.e., 64, 32, 16, and 8 pixels) were used to analyze the motion of particles (Supplementary Figure 4), according to published protocols.[3]

The published protocols also recommend post-processing of data to remove erroneous vectors and ensure accurate calculation. This is achieved by surveying a scatterplot of the horizontal and vertical velocities, and removing calculated vectors determined to be outliers. Graphically, this is achieved by selecting a boundary outside of which the data are outliers

and will be removed (Supplementary Figure 5). Visually, the incongruity of these erroneous vectors is confirmed by surveying plots of vector fields overlaid on each analyzed image.

The remaining velocity data were interpolated to provide values at all coordinate points. The data for each frame were then exported as text files containing four columns: the u-coordinate, v-coordinate, and associated u- and v-velocities of the fluid. These data were then analyzed using separate, custom-written MATLAB code that analyzes the positive v-velocities (i.e., opposing gravity) of each frame, and stores the highest value—i.e., the maximum velocity—at each point in time. These values of maximum velocity are then plotted against time to produce the curves in Supplementary Figures 6 and 7.

5.4.2 Supplementary Note 1

Studies of the backward photoreaction of DASA-CF3-PI in toluene and chloroform are restricted to dilute solutions of DASA-CF3-PI due to the high extinction coefficient of DASA and the limitations of the apparatus detector.

5.4.3 Supplementary Note 2

In general, the shape and location of the concentration gradient in the bleaching front depends in a complex way on the illumination profile in the container, the resulting bleaching reaction kinetics, and the convective mass transport of DASA-CF3-PI, which is carried along by the flow produced as a result of the Rayleigh-Benárd convection. However, if all we seek is the location of the front and its motion in time, then the problem can be simplified by restricting the analysis solely to the bleaching front itself.

Consider that the bleached zone near the bleaching front is maintained at a relatively constant concentration $N_{A,open}$ of open DASA-CF3-PI, and that the unbleached zone near the bleaching front is maintained at a relatively constant concentration $N_{B,open}$. For simplicity, we assume that the concentration varies from $N_{A,open}$ to $N_{B,open}$ over a distance, δ, that is much smaller than both the height of the bleaching front h_I and the fluid height H. Under this assumption, the bleaching front can be treated as a fictitious interface between "phases" A and B, at which a step change in N_{open} occurs due to the photoreaction across the thickness δ. If h_I is appreciably far from the bottom of the container, then we can assume that in phase A the photoreaction has reached local equilibrium, such that no photoreaction occurs, resulting in quasi-steady state mass transport for the interface. The

location of the interface therefore advances with a quasi-steady velocity $\boldsymbol{v}_I = dh_I/dt$, where h_I is the height of the interface.

The general boundary condition for mass transfer of chemical species i across an interface between a general fluid phase A and fluid phase B in vectorial form is given by a molar mass balance of species i at the interface, and can be written without loss of generality:[4]

$$\frac{dN_{I,i}}{dt} = \left\{ \left[\boldsymbol{j}_{A,i} + N_{A,i}(\boldsymbol{v}_A - \boldsymbol{v}_I) \right]_I - \left[\boldsymbol{j}_{B,i} + N_{B,i}(\boldsymbol{v}_B - \boldsymbol{v}_I) \right]_I \right\} \cdot \widehat{\boldsymbol{n}}_I - r_{i,I} \qquad (S1)$$

where $N_{X,i}$ is the concentration of species i in phase X, $\boldsymbol{j}_{X,i}$ is the diffusive flux of species i in phase X, and $\boldsymbol{v}_X$ is the fluid velocity in phase X. $\widehat{\boldsymbol{n}}_I$ is the outward pointing normal vector (defined here as pointing into phase B), and subscript I denotes that the quantity is evaluated at the interface. Here, $\boldsymbol{v}_I$ is the velocity of the location of the interface, which in general need not be equal to $\boldsymbol{v}_{A,I}$ or $\boldsymbol{v}_{B,I}$ because it represents the rate of change in location of the interface rather than a fluid velocity. The curly bracketed term represents the total net molar flux of species i to/from the interface (either from diffusion or convection), and $r_{i,I}$ is the net reaction rate (in units of $mol\ (volume \cdot time)^{-1}$) of species i.

We now make a number of other simplifying assumptions for our bleaching system. Because we already assumed that the interface remains quasi-steady, the left hand side of Eq. (S1) is identically zero. Momentum continuity across the fictitious interface requires that $\boldsymbol{v}_{A_I} = \boldsymbol{v}_{B_I} = \boldsymbol{v}_{fluid}$. Furthermore, we assume DASA is dilute in solution, such that Fick's

law can be used for $j_{X,i}$. Finally, we will assume that the bleaching front is symmetric about

the vertical centerline of the container, and restrict our analysis to the centerline, such that

the problem reduces to a one-dimensional problem in the vertical (negative v) direction.

Under these assumptions and applying the interfacial balance to open DASA-CF3-PI,

Eq. (S1) simplifies to:

$$0 = \left(N_{A,open} - N_{B,open}\right)\left(\boldsymbol{v}_{fluid} - \boldsymbol{v}_I\right) + \left(\frac{\partial D_{open} N_{A,open}}{\partial z}\Big|_I - \frac{\partial D_{open} N_{B,open}}{\partial z}\Big|_I\right) +$$

$\delta r_{open,I}$ (S2)

The first term in Eq. (S2) represents the net convection of DASA to the interface due to

the convective flow. The second term represents the net diffusion of DASA to the interface

due to concentration gradients in the bleached and unbleached regions. We expect that such

gradients will be small, such that the diffusive flux is negligible compared to the convective

flux and will be ignored in subsequent analysis. Making this assumption and solving for the

interface velocity gives

$$\boldsymbol{v}_I = \boldsymbol{v}_{fluid} + \frac{\delta r_{I,open}}{\Delta N_{I,open}} \text{ (S3)}$$

where $\Delta N_{I,open} = N_{A,open} - N_{B,open}$ is the change in open DASA concentration across

the interface. Note that Eq. (S3) assumes nothing about the rate of reaction (or, for that

matter, the illumination), and so it will apply to any general reacting system that creates a

quasi-steady reaction front of the sort that we have assumed here. To apply this prediction

specifically to the DASA system, we use the expression for the net rate of photochemical reaction developed by Lui et al.,[5]

$$r_{I,open} = -\sigma(N_{I,open})\phi_{OC}(N_{I,open})I(h_I)N_{I,open} + k_{back}(N_{I,open})[N_o - N_{I,open}]$$
(S4)

where σ is the absorption cross-section, ϕ_{OC} the quantum efficiency for photoconversion between the open and closed form, $I(h_I)$ the irradiation intensity at the bleaching front, k_{back} the rate constant for the backward photoconversion, and N_o the total concentration of DASA (including open and closed forms) in solution, which remains constant everywhere because the photoreaction is unimolecular. Eq. (S4) explicitly notes the functional dependence on N_{open} of the various photokinetic parameters (these will be suppressed in the equations to follow). Note that, because our analysis treats the bleaching front as a concentration discontinuity, the concentration of the interface $N_{I,open}$ at which the rate is evaluated remains undefined. However, since we have already assumed that no net photoreaction occurs in the bleaching zone, a reasonable choice would be $N_{I,open} = N_{A,open} - c\Delta N_{I,open}$, where c is either 0 or 0.5.

Substituting Eq. (S4) into Eq. (S3) gives

$$\boldsymbol{v_I} = \boldsymbol{v_{fluid}} + \frac{\delta}{\Delta N_{I,open}}\{\sigma\phi_{OC}I(h_I)N_{I,open} - k_{back}[N_o - N_{I,open}]\} \quad \text{(S5)}$$

From this equation, it may appear at first glance that we have lost any time dependence of the problem. However, many of the parameters (chiefly v_{fluid} and $I(h_l)$) are implicitly time dependent, both because the bleaching front is advancing through a non-uniform velocity and irradiation field, and because these fields themselves are time-varying. Therefore, solving Eq. (S5) to obtain the entire time-dependence of the front velocity requires solving the full complex coupled mass, heat and flow transport problem, which is not presented in its entirety here.
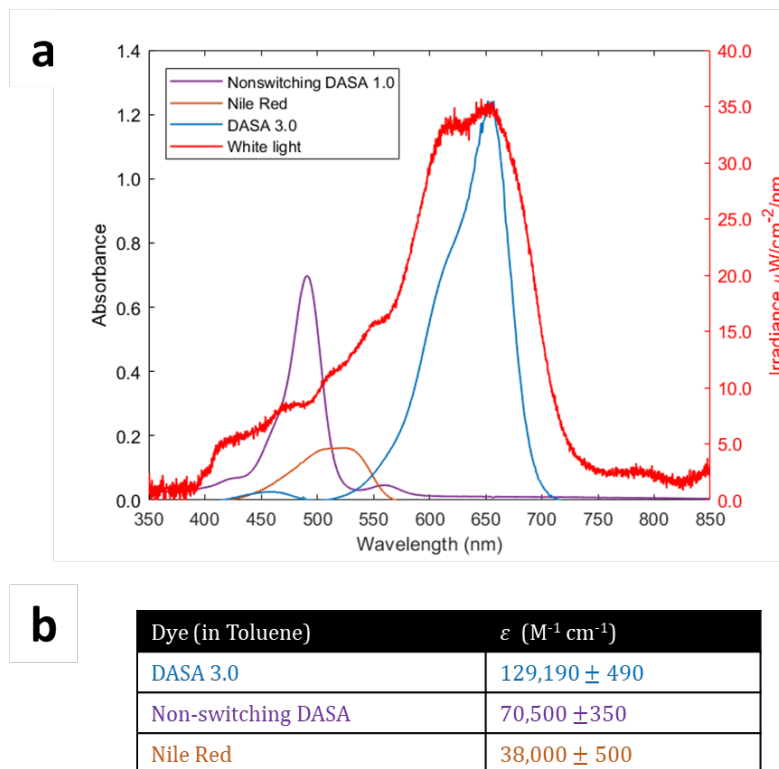
5.4.4 Supplementary Note 3

Nonzero fluid velocities seen at time $t = 0$ s in Figure 5a are likely the result of our imaging set up. Though solutions containing DASA are allowed to settle for two minutes prior to irradiation, as soon as the cuvette is exposed to the white light, it takes several hundreds of milliseconds before the digital camera used in this experiment is able to adjust to the new brightness in its field of view. As such, the particle image velocimetry (PIV) analyses begin only as the camera has adjusted to the light, at which time the photoreaction is already under way—resulting in a nonzero fluid velocity.
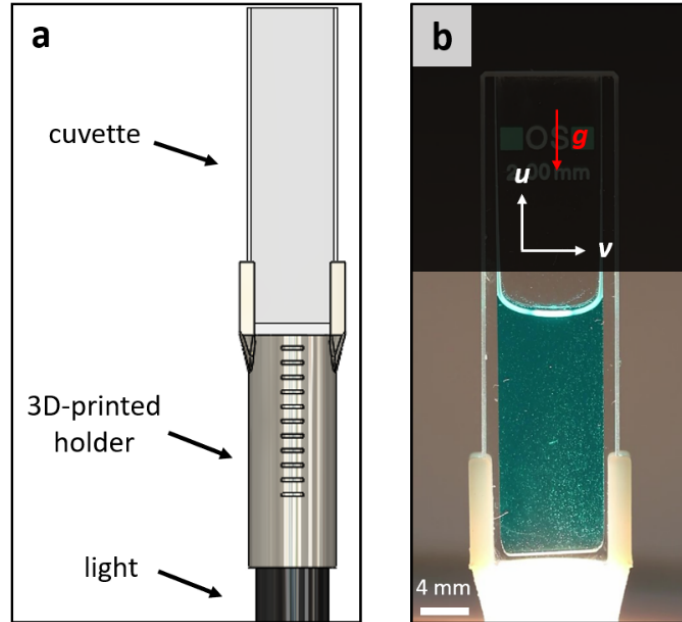
Supplementary Figure 1 | Experimental setup used for UV-vis cuvette studies. a, Labeled SolidWorks rendering of setup. **b**, Image of setup with *u*- and *v*-coordinates labeled. As well as the gravity vector, *g*.
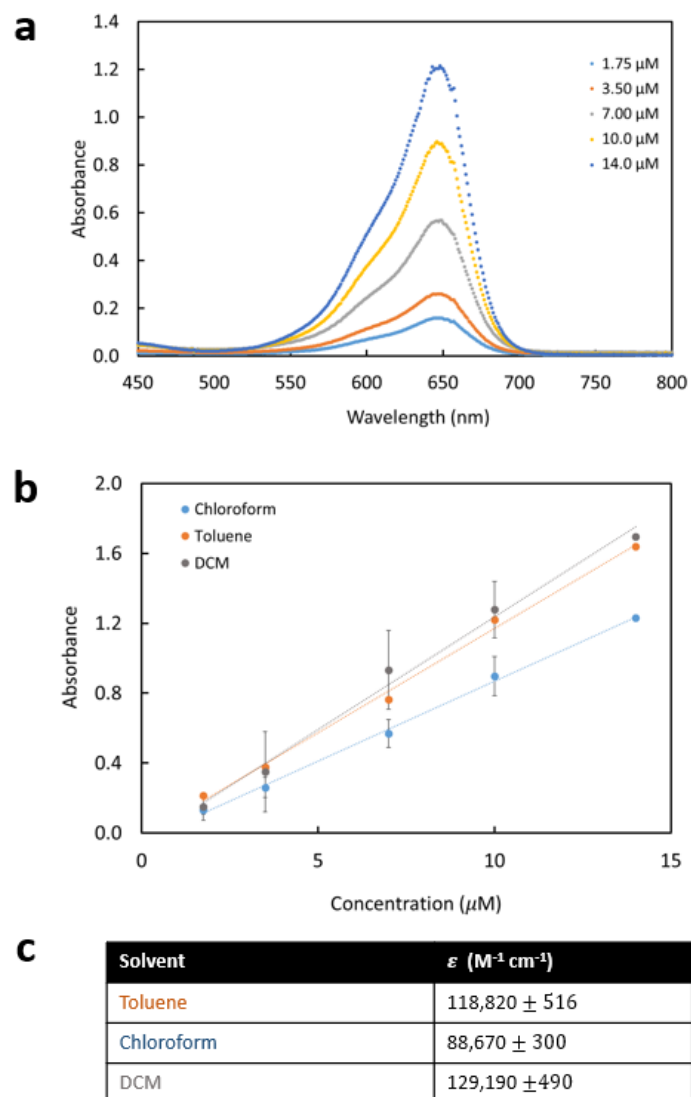
Supplementary Figure 2 | Molar Absorptivity of DASA-CF3-PI in toluene, chloroform and dichloromethane. a, Representative absorption spectra obtained with UV-Vis spectrophotometry for various concentrations of DASA-CF3-PI in chloroform. Maximum absorption is plotted for each concentration in toluene, chloroform and dichloromethane **b,** from which the slope of the line is used to determine molar absorptivity according to Beer's law ($A = \varepsilon bc$, where ε is molar absorptivity, b is path length and c is concentration). **c,** Molar absorptivity values are reported for all solvents in the table.

a

b

| Dye (in Toluene)	ε (M^{-1} cm^{-1})
DASA 3.0	$129{,}190 \pm 490$
Non-switching DASA	$70{,}500 \pm 350$
Nile Red	$38{,}000 \pm 500$

Supplementary Figure 3 | Molar Absorptivity comparison of high-absorbing dyes and DASA-CF3-PI. a, (Left axis) Representative absorption spectra obtained with UV-Vis spectrophotometry for 10 µM of DASA-CF3-PI, non-switching DASA and Nile red in toluene. (Right axis) Absolute irradiance measurement of the white light source using a USB 4000-UV-Vis spectrometer (OceanOptics, Inc., USA). **b,** Molar absorptivities are determined at maximum absorption for each dye and reported for comparison.

174
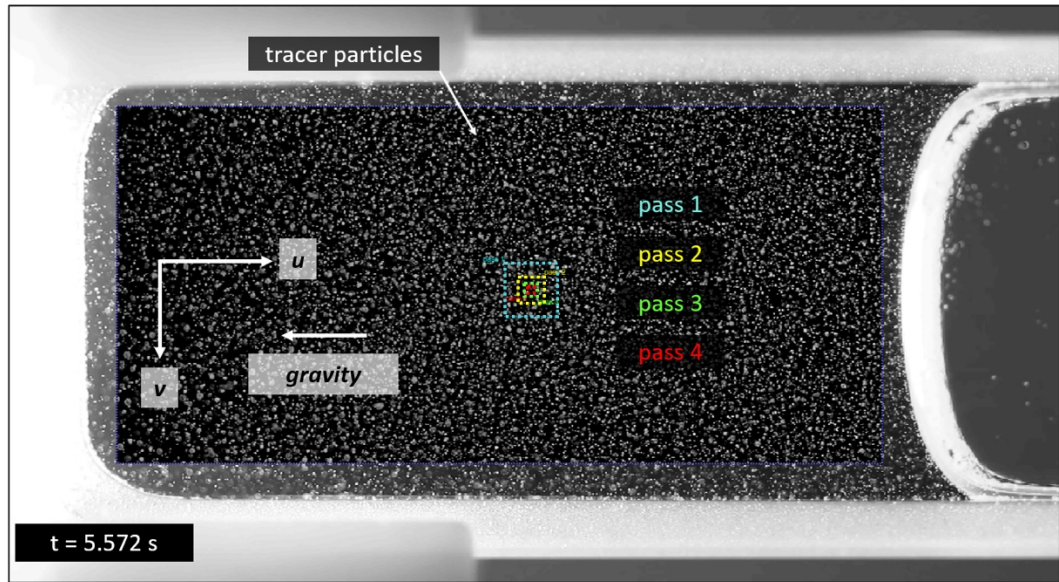
Supplementary Figure 4 | Region of interest and window size selection, as executed in PIVLab.

Speckles are tracer particles in space.
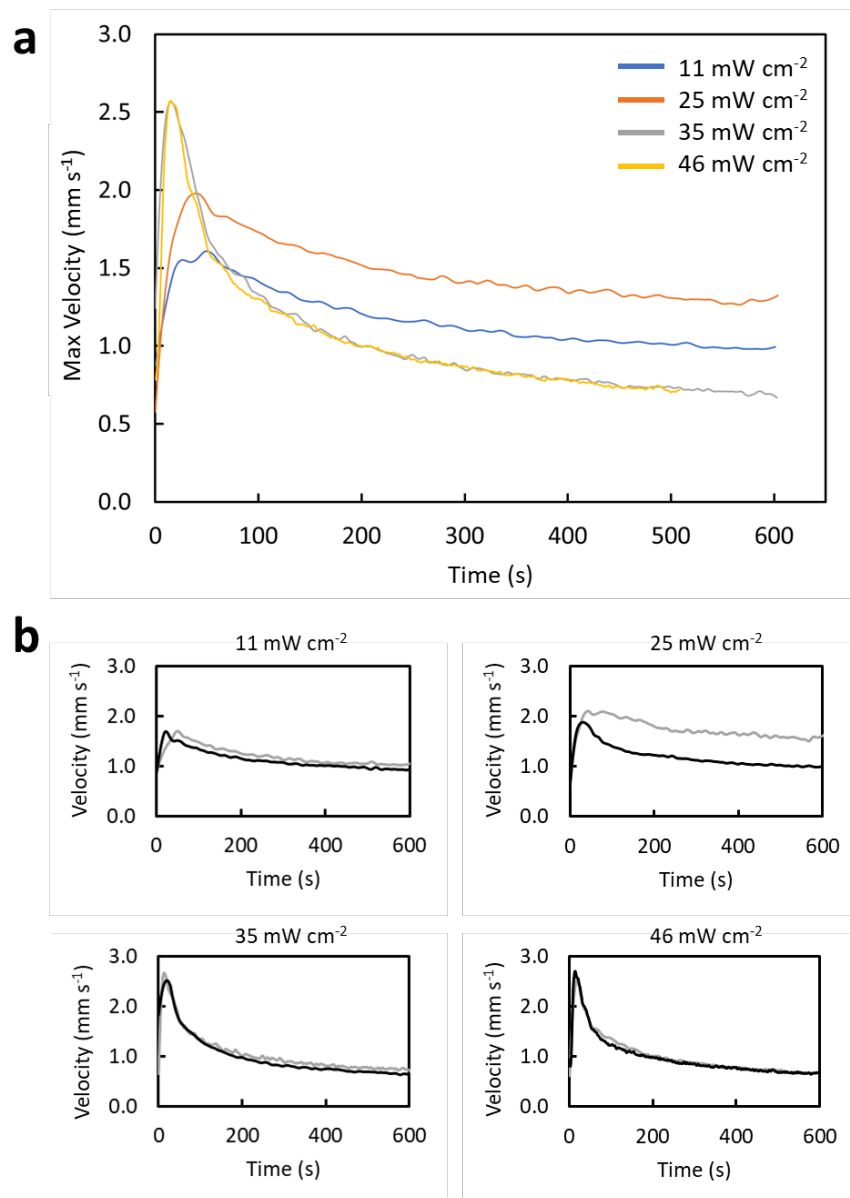
Supplementary Figure 5 | Maximum velocity data for 0.25 mM DASA-CF3-PI in chloroform irradiated at varying intensities. a, Average curves of differing intensity. **b**, Duplicate runs at each light intensity.
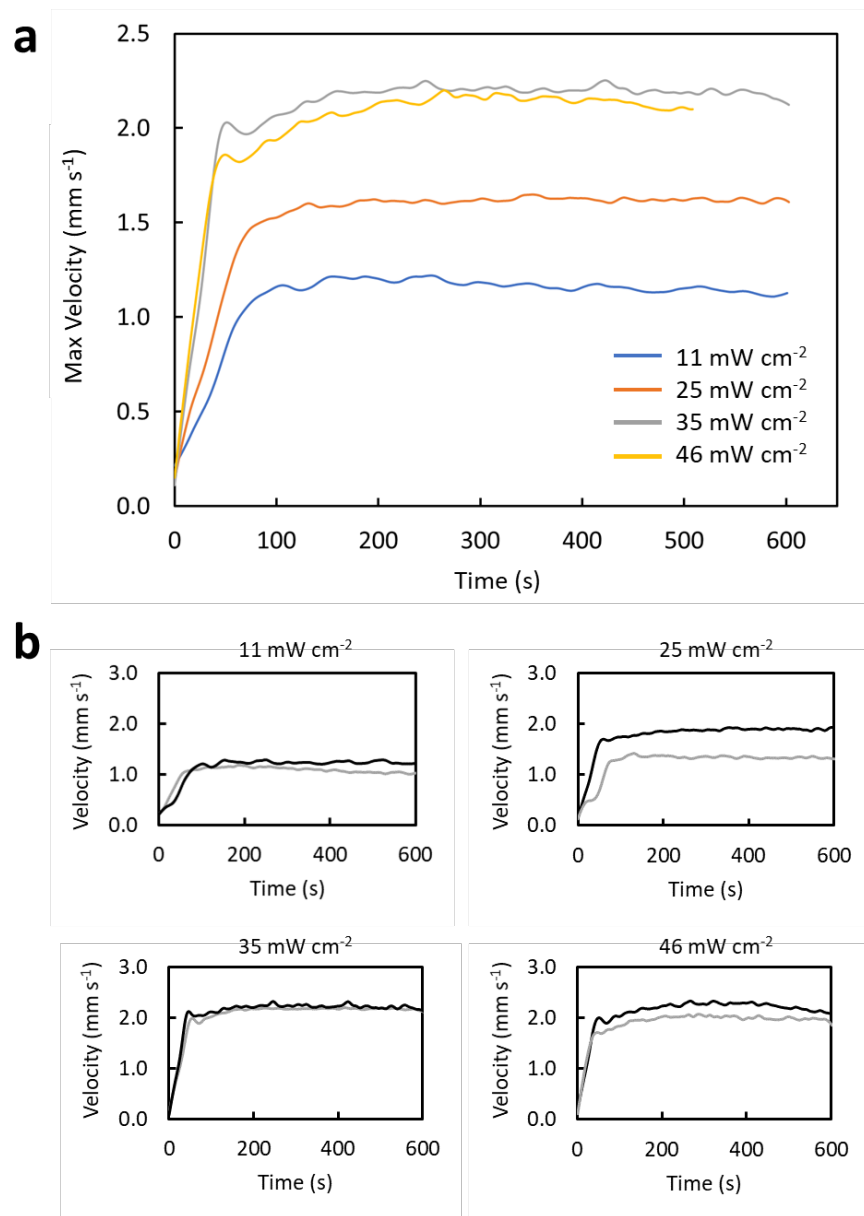
Supplementary Figure 6 | Maximum velocity data for 0.25 mM DASA-CF3-PI in toluene irradiated at varying intensities. a, Average curves of differing intensity. **b**, Duplicate runs at each light intensity.
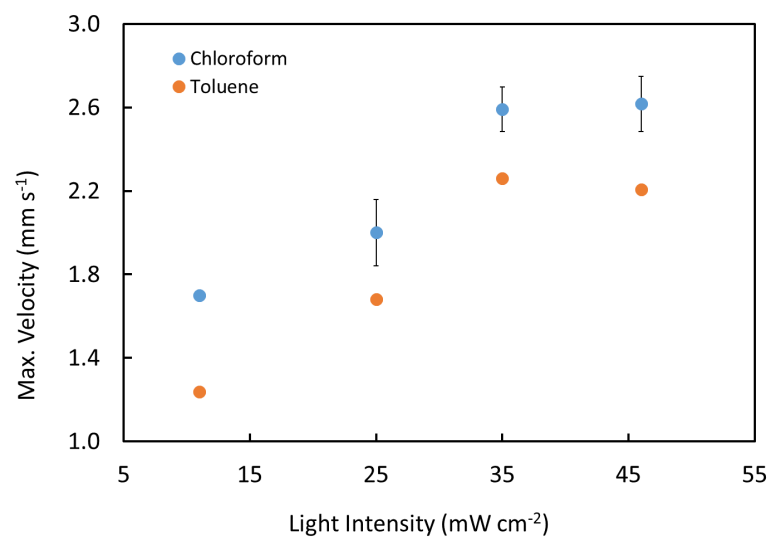
Supplementary Figure 7 | Maximum velocity achieved vs. light intensity for DASA-CF3-PI in chloroform and toluene. Error bars: standard deviation, N=2. Note that in some cases the error bars are smaller than the marker size.
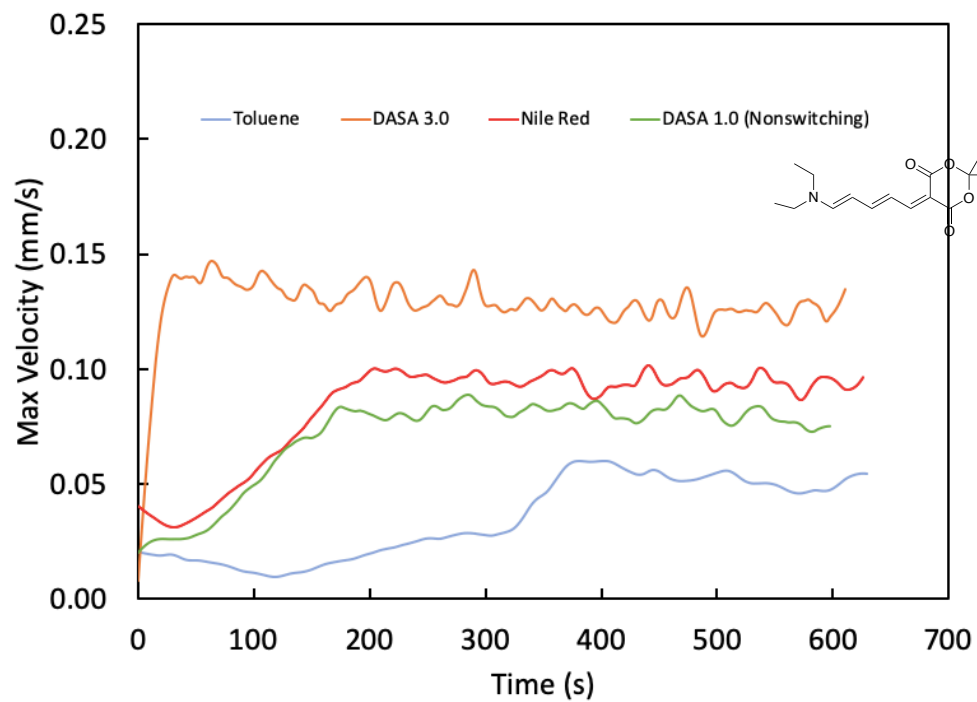
Supplementary Figure 8 | DASA-CF3-PI and dye comparison. Velocity profiles for 0.25 mM DASA-CF3-

PI, Nile red and Non-switching DASA in toluene at 6.34 mW cm^{-2}.

179

a

b
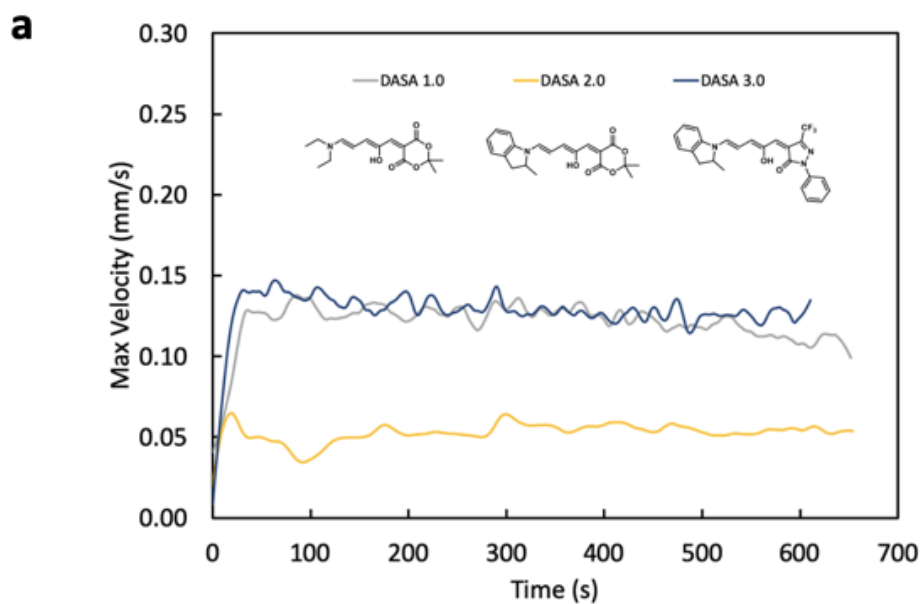
DASA	ε (M⁻¹ cm⁻¹)	% open	Half life t₁/₂	Abs. max
DASA 3.0	118,200	>95%	40s	655 nm
DASA 2.0	107,000	31%	3240s	580 nm
DASA 1.0	102,000	>95%	100s	545 nm

Supplementary Figure 9 | DASA 1.0, 2.0 and 3.0 comparison. a, Velocity profiles of 0.25mM of each generation DASA in toluene at 6.34 mW cm⁻² light intensity. **b**, Representative details regarding molar absorptivity, thermal equilibria and switching kinetics of each DASA in toluene.[6]

5.5 References

1.Zhou, C., Zhang, H., Li, Z. & Wang, W. Chemistry pumps: A review of chemically powered micropumps. *Lab on a Chip* **16**, 1797–1811 (2016).

2.   Merindol, R. & Walther, A. Materials learning from life: Concepts for active, adaptive and autonomous molecular systems. *Chemical Society Reviews* **46**, 5588–5619 (2017).

3.   Hemmer, J. R. *et al*. Controlling Dark Equilibria and Enhancing Donor-Acceptor Stenhouse Adduct Photoswitching Properties through Carbon Acid Design. *Journal of the American Chemical Society* **140**, 10425–10429 (2018).

4.   Lui, B. F. *et al*. Unusual concentration dependence of the photoisomerization reaction in donor–acceptor Stenhouse adducts. *Photochemical & Photobiological Sciences* 1587–1595 (2019) doi:10.1039/c9pp00130a.

5.   Dolinski, N. D. *et al*. A Versatile Approach for In Situ Monitoring of Photoswitches and Photopolymerizations. *ChemPhotoChem* **1**, 125–131 (2017).

6.   Thielicke, W. & Stamhuis, E. J. 42-489-1-Pb. (2014).

7.   Lui, B. F. *et al*. Unusual concentration dependence of the photoisomerization reaction in donor–acceptor Stenhouse adducts. *Photochemical & Photobiological Sciences* 1587–1595 (2019) doi:10.1039/c9pp00130a.

8.   Tansi, B. M., Peris, M. L., Shklyaev, O. E., Balazs, A. C. & Sen, A. Organization of Particle Islands through Light-Powered Fluid Pumping. *Angewandte Chemie - International Edition* **58**, 2295–2299 (2019).

9.   Feldmann, D. *et al*. Manipulation of small particles at solid liquid interface: Light driven diffusioosmosis. *Scientific Reports* **6**, 1–10 (2016).

5.5.1 SI References

1. Thielicke, W. and Stamhuis, E.J. (2014): PIVlab – Towards User-friendly, Affordable and   Accurate Digital Particle Image Velocimetry in MATLAB. *Journal of Open Research Software* 2(1):e30, DOI: http://dx.doi.org/10.5334/jors.bl.

2. Thielicke, W. and Stamhuis, E. J. (2014): PIVlab - Time-Resolved Digital Particle Image Velocimetry Tool for MATLAB (version: 2.01).

http://dx.doi.org/10.6084/m9.figshare.1092508.

2. Thielicke, William. (2019, April 28). PIVLab Tutorial. Retrieved from

https://pivlab.blogspot.com/p/blog-page_19.html.

3. Lui, B. F. et al. Unusual concentration dependence of the photoisomerization reaction in donor–acceptor Stenhouse adducts. *Photochem. Photobiol. Sci.* 1587–1595 (2019).

4. Leal, L G. Advanced Transport Phenomena: Fluid Mechanics and Convective Transport Processes. Cambridge: Cambridge University Press. (2007).

5. Hemmer, J. R. et al. Controlling Dark Equilibria and Enhancing Donor-Acceptor Stenhouse Adduct Photoswitching Properties through Carbon Acid Design. J. Am. Chem. Soc. 140, 10425–10429 (2018).

6. Phase change actuation using Donor-Accepter Stenhouse Adducts

Abstract

We identify environmental effects of polar additives on the control of the switching kinetics of a highly-absorbing negatively photochromic molecular switch, donor acceptor Stenhouse adduct (DASA) that enable its use for phase change actuation. The use of methanol in order to maintain the blue, open DASA conformation in solvents such as toluene allow for maximum temperature changes to be observed. The rising temperature in turn leads to evaporation of the additive and the switching behavior of the DASA is regenerated. In controlling when the DASA will lose its ability to absorb through vapor-liquid equilibrium of the additive, we foresee the ability to cyclically generate and dissipate heat under constant irradiation. Leveraging features of DASA's chemical properties and solvent-dependent reaction kinetics, we demonstrate its use for photo-controlled temperature changes which in turn can be leveraged for the development of oscillating materials under constant irradiation. Modeling of the binary phase mixture of methanol and toluene allow for an assessment of the properties and conditions that govern steady state and oscillatory behaviors and lay the foundation for the creation of smart materials that have dynamic behaviors under constant irradiation. Future work will continue upon these understandings in order to create smart actuators.

6.1 Introduction

Stimuli-responsive materials present an opportunity to build smart actuators that can be remotely controlled and provide access to new behaviors such as oscillation under constant irradiation. The development of liquid-vapor phase-change actuators for soft robots allows us to consider a new method by which we may utilize light responsive molecules, specifically photoswitchable molecules which have recently begun to be used for photothermal actuation.

As seen in Chapter 4, negatively photochromic molecular switches such as DASA can be used to drive fluid flow due to its high molar absorptivity. This property can be further exploited for the generation of mechanical work and to develop soft robot actuators. This chapter explores the possibilities afforded by the system through the control of DASA in fluid systems governed by the environment, the rate, the extent of DASA switching and the lifetime of the closed form. In certain solvents or at high concentrations, switching may be prohibited by the change in the energy landscape thus causing the DASA to behave more like a high-absorbing dye.[36–40] In solvents where DASA switches completely at high concentration, the system will rapidly become clear, thus losing its ability to absorb light and generate heat. Recent work shows that with DASA we can use small quantities of polar additives to control the rate and extent of switching. Despite the control afforded by the switching properties of DASA, applications have yet to be developed in the field of soft robotics to use DASA as a smart fuel source. Additionally, the complex coupled relationship

between the switching kinetics and heat generation open the door for control of actuating systems under constant irradiation through careful design of a self-regulating system.

In this chapter, we propose that using DASA in combination with vapor-liquid equilibrium of additive and solvent, we may achieve oscillation under constant irradiation in an actuator system through the use of additives for control of both heat generation and reaction kinetics. In the present study, we explore how a self-contained system can generate and dissipate heat under illumination conditions by changing mixture composition and the absorbance of the systems, thereby laying the groundwork for future actuator-based applications. For these proof-of-principle studies we will use a polar additive with a low boiling point to control how long the DASA remains in the open, blue, high-absorbing form. This additive will first serve as a control knob to maximize the ability of DASA to convert light into heat by serving as an absorbing photothermal dye in a high-boiling solvent. The binary solvent system will then absorb light to generate heat and the temperature of the solution will continue to rise until the low boiling point additive is evaporated off. After the additive is removed, the DASA solution will switch to the closed, non-absorbing state and therefore no longer generate heat, thus presenting the opportunity to shut down an actuator under constant irradiation. This system has the potential for oscillation if the additive is reintroduced into the system as a result of the temperature changes induced by the DASA switching or reintroduced manually. This capacity is highly desirable in soft robotic systems- an increasing number of which use heat engines to drive their locomotion. In this chapter, we present coupling of the enthalpic requirements with the photo-reaction that we

185

hope will allow for the future design and engineering of an actuator system that can exploit DASA as a photothermal oscillator.

6.2 Experimental methods

Chemical selection. Toluene (99.8%) and methanol were purchased and used without further purification from Sigma Aldrich. Donor-acceptor Stenhouse aducts were synthesized as described in the procedure previously reported. For each experiment, the compound was dissolved in solutions from fresh bottles of toluene diluted to the desired concentrations and kept in the dark.

Kinetic analysis. The photoinduced optical absorption kinetics were measured using a pump-probe setup described in previously reported studies.[41] Studies herein were performed in a demountable liquid cell with variable pathlengths (6um- to 1mm), UV-grade fused silica windows (WAD-U22) and an optical table sample slide holder (HSS-OTE) purchased from Harrick Scientific Products Inc. In addition to characterizing the kinetics of the photoreactions, these experiments also provide a measurement of the photostationary state, i.e., the fractional conversion of the photoswitch to the conformer of the molecule comprising the switched state.

Absorbance tracking. Videos of quartz cuvettes containing DASA solutions were recorded in order to track absorbance changes over time using a Canon Rebel SL2 (100 mm f/2.8 Macro USM fixed lens, 1x magnification, 30 frames per second). Experimental setup

includes a cuvette with light shining from below and a camera stationed directly in front of the solution in order to observe changes in color afforded by the switching induced by irradiation. Videos were then divided into grayscale images using MATLAB code and the average luminance is tracked over the course of an experiment. See supporting information for details.

Light source. A Schott Ace 150 W fiber optic white light source was chosen for all experiments herein due to its broad coverage of the absorbance spectrum of DASA (**Supplementary Figure 3**). In addition, it supplied light fluxes otherwise inaccessible with the use of LEDs available to us.

Temperature analysis. Infrared images were obtained using a FLIR E60 IR camera accurate to ±2% of reading. Thermal energy was supplied to the system via a flexible polyimide heater plate (IcStation) coupled to a benchtop voltage source. Temperature was probed using a K-type thermocouple (ThermoWorks, K-36X) and read using a thermocouple amplifier (Adafruit, MAX31855) and microcontroller (Arduino UNO) with +/- 0.5 C accuracy.

6.3 Results

Previous work with DASA has shown the strong effect of the environment on the ability of the molecule to undergo switching to the closed, clear, non-absorbing form.[36,42] In this

study we exploit the use of an additive to control absorbance changes which in turn affect the heat generating capabilities of a fluid system with the goal of developing smart actuators.

We prove this additive control by developing a quasi-quantitative method for quantifying color changes in response to the additive during live experiments. This method is accessible *in situ* during any live experiment and circumvents the issues associated with using low concentrations and inaccurate conditions in UV-Vis experiments to allow for more application-relevant information to be obtained to determine the necessary conditions for engineering a system for a desired application.

In order to better envision the applications of this additive control, we perform phase change analysis and provide a model of how the system behaves as a function of parameters we can vary. Using thermodynamic modeling of the associated binary vapor-liquid equilibrium (VLE) of the solvent and additive, we aim to combine knowledge of the factors that govern heat transfer with those that control the reaction kinetics. We posit that this analysis will enable us to leverage the system for soft robotics applications through control of parameters that dictate the phase change behavior in the binary mixture.

6.3.1 DASA selection

For an adaptable system of this kind to be actualized, we need a photoswitch that is highly-absorbing, switches at high concentration and has kinetics that are tunable with small quantities of a low boiling point, polar additive. To achieve this, we focus on a newly

developed DASA molecule. This fused ring DASA molecule allows for switching at high concentrations in nonpolar solvents and is highly stable to degradation, making it an ideal candidate for this work. With an initially high open form equilibrium in a variety of nonpolar solvents and a high molar absorptivity, this DASA has potential to be used for photothermal applications. In its open conformation, this DASA is blue and switches to a clear, closed enol form upon irradiation with red light (**Figure 1a**). We find that polar additives, such as methanol, can be used to alter the environment such that the photothermal stationary state is reduced and the rate of the reverse reaction is increased. Unique to DASA is the role of the additive on altering the rate determining step. The rate determining step for thermal reversion (i.e., closed form to open this DASA is typically the B-A transition (**Figure 1b**) but as the polar additive is introduced the energy requirements shift such that the rate determining step is changed to the C-B transition. As a result of the change in energy landscape induced by the methanol, we can see nonlinear effects on the back reaction rate (**Supplementary Figure 6**). This sensitivity allows us to utilize methanol as a low-boiling additive to control the switching kinetics (**Figures 1c, 1d**). Further analysis and calculations regarding the changing energy landscape is required in future studies.

For the goal of creating a phase change actuator, we are interested in incorporating an additive with a low boiling point that can be removed above a certain temperature such that new kinetics are obtained. Methanol, whose boiling point is 64.7 C, is an ideal candidate at low volumes. The effects of the additive can be precisely tuned by altering the volume of methanol, the intensity of light and the depth of the cell. From pump probe UV-Vis measurements we determine the rate of reaction as well as the photothermal stationary state

at varying concentrations of methanol. We see that as the quantity of methanol increases, switching becomes more limited for a 0.125mM solution of DASA in (**Figure 1**).
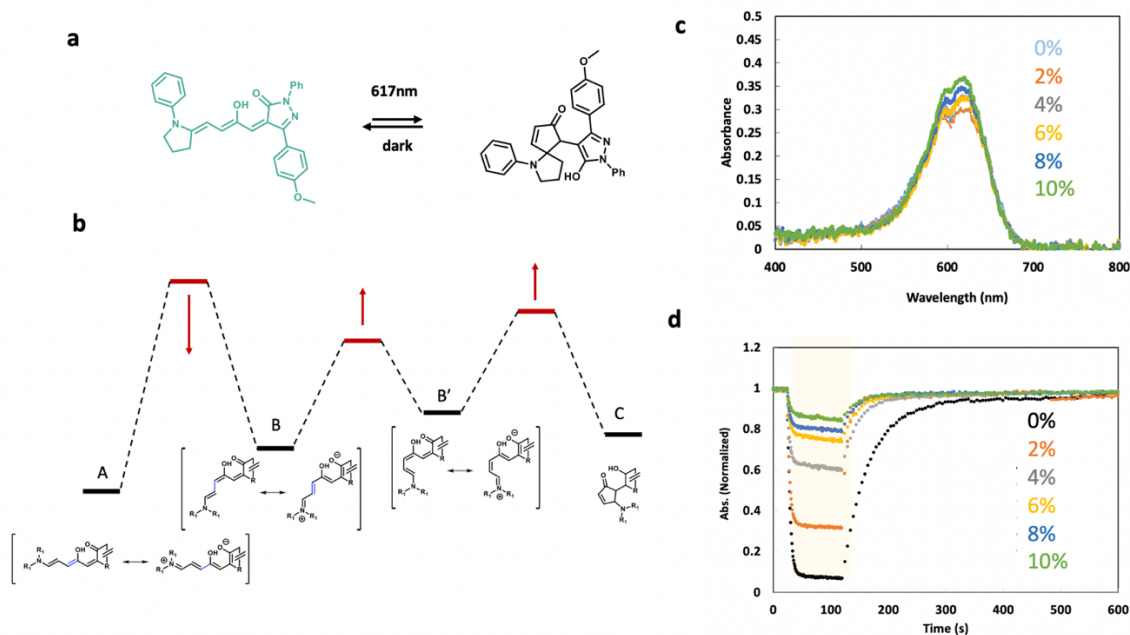

Figure 6.3. a) photoswitching mechanism of DASA from the open, colored form to the closed clear isomer under irradiation conditions. b) simplified changing energy landscape for DASA in the presence of polar additives, with the A-B transition state decreasing in energy and the B-B' and B-C transitions increasing. The changing energy landscapes contribute to the additive effects on the rate of the forward and back reaction of DASA with polar additives. The isomerization occurring between A-B is light driven and each consecutive step is a thermally driven process. In order for the DASA to lose color, the B-C transition must occur which leads to the loss in conjugation and consequent loss of color. Pump probe UV-vis measurements of c) absorbance and d) kinetics for a 0.125mM solution of DASA in toluene with varying volume % of added methanol.

6.3.2 Changes in photothermal behavior induced by the additive

We know from previous work that the high molar absorptivity of DASA in its colored state leads to impressive heating. By adding a solvent that prevents bleaching, we can retain the highly absorbing state and thus can maintain heating for longer timescales. In carefully selecting this additive such that it has a lower boiling point than that of the primary solvent, the heat changes induced by the absorption of the mixture can lead to preferential evaporation of the additive and resulting depletion of the additive from the solvent. After the methanol has evaporated, the DASA solution can now bleach and will absorb much less light to generate heat. We find that with DASA in toluene with methanol added we can reach temperature changes of nearly 30 °C over 3 minutes. At high concentrations, the DASA does not completely bleach even in the absence of methanol (**Figure 2a**) and therefore still generates heat; this temperature change can be decreased by lowering the initial concentration of DASA such that more switching occurs. We note that the heating rate change seems to further support the change in energy landscape driven by the increased presence of methanol. We look to modeling to provide theoretical support for designing a system that would allow this temperature change to be utilized to drive phase change for actuation.
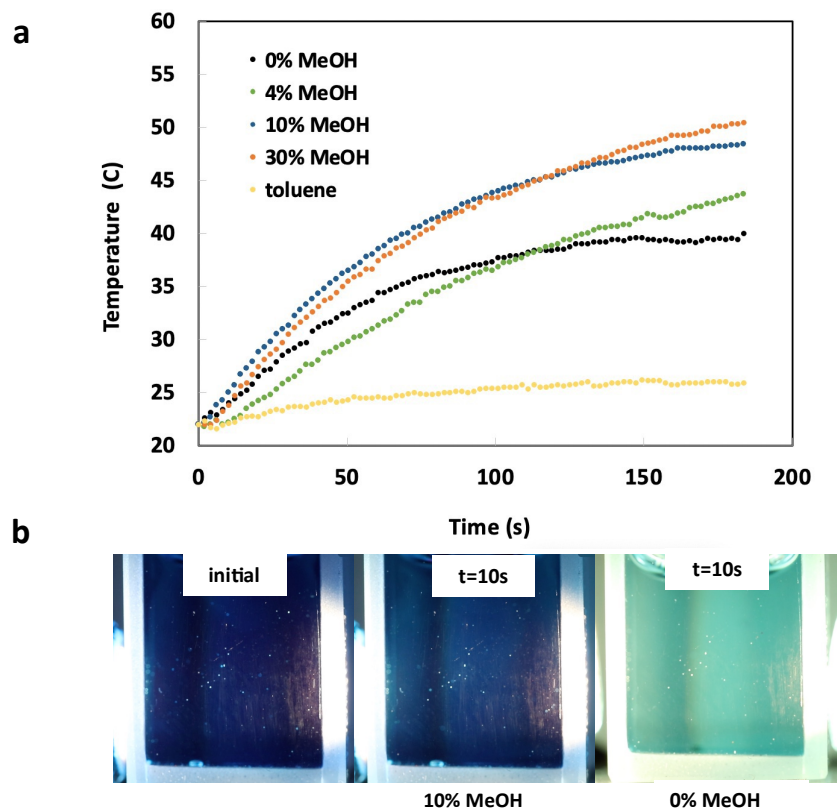
Figure 6.4. a) heating of 0.25mM DASA in toluene with increasing amount of methanol using the white light source. The temperature is measured by placing a thermocouple in the center of the cuvette containing the DASA solution and total temperature changes were confirmed using an IR camera. b) video stills taken from experiments in which white light shining from the sides of a 0% MeOH solution leads to significant switching of DASA and 10% MeOH maintains the dark blue color under irradiation (glare due to camera angle). For this DASA molecule at the high concentrations, some color remains after irradiation even without methanol present. At lower concentrations, more bleaching occurs but overall temperature changes with methanol are decreased. Video stills are taken after 30 seconds of irradiation.

6.3.3 Heating requirements for phase change and altered kinetics

As shown in Figure 2(a), DASA in a binary methanol/toluene solvent induces

temperature changes up to approximately 30 °C. The data shown in Figure 2(a) begins from

ambient conditions, so the system remains a liquid and the methanol volume fraction in the

liquid phase (x_{MeOH}) stays constant. However, for higher starting temperatures (>50 °C),

photothermally-induced boiling of the solvent is possible, and x_{MeOH} will change as a

function of the system temperature. As the switching of DASA is dependent of x_{MeOH},

predicting temperatures required to attain specific values of x_{MeOH} is of use here. This

information can be obtained through the use of temperature-composition (T-xy) diagrams,

which were produced for a binary mixture of toluene and methanol using the non-random

two-liquid (NRTL) thermodynamic model with parameters included in the Supplementary

information. This model assumes ideal gas behavior, but accounts for non-ideal interactions

in the liquid phase of the system. Methanol is a polar molecule that undergoes hydrogen

bonding with itself, so this mixture is expected to exhibit non-ideal liquid-phase behavior.

Calculations to obtain the diagrams and details of the model used are provided in the

Supporting Information. From these calculations, a T-xy diagram for a binary mixture of

methanol and toluene is provided in Figure 3a where liquid volume fractions of methanol

are varied from 0 to 1, and the corresponding vapor volume fractions and temperatures are
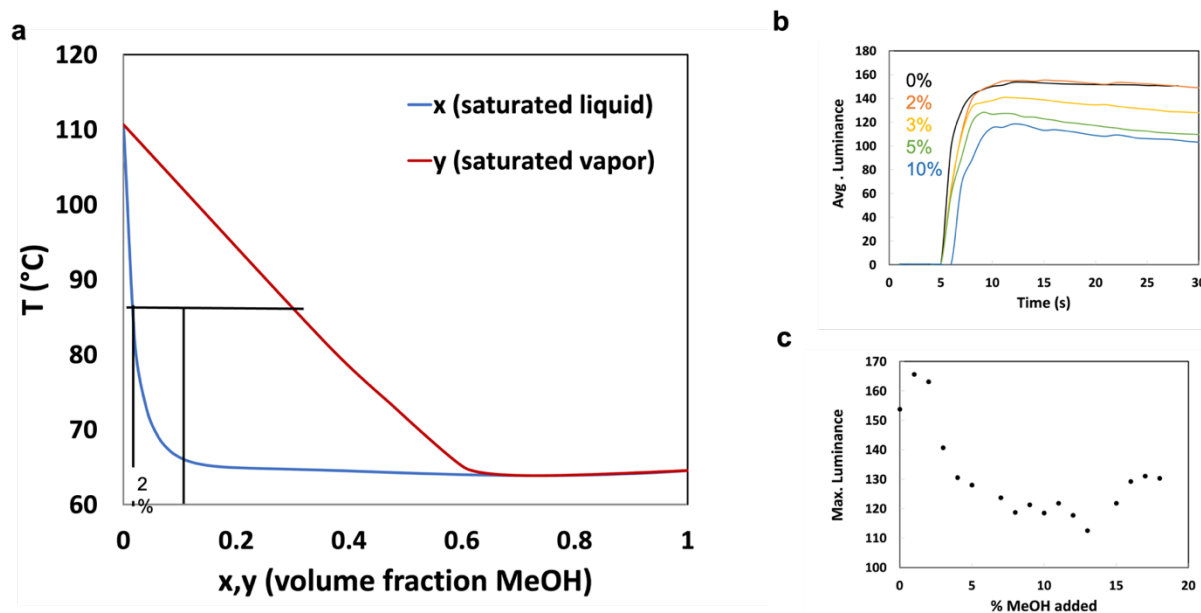
obtained.

Figure 6.5. a) Temperature composition (T-xy) diagram for toluene with varying mole fraction of methanol. Note that while the methanol/toluene binary mixture forms an azeotrope at approximately 82 mol% MeOH, experiments in this work use < 20 mol% MeOH so this is not an issue. b) the changing average luminance over time with varying amount of methanol and c) the max luminance with added amounts of methanol. The luminance measurements allow us to determine at what composition of methanol in toluene the additive effect no longer plays a role. This is found to be below 2% methanol.

To determine x_{MeOH} experimentally, we quantify absorbance changes in solution via a correlated metric — luminance. Experiments were video recorded with the same light source in all of them, and analyzed by converting them to grayscale and summing their luminance. In Figure 3b and 3c we characterize the MeOH concentrations that are sufficiently dilute such that switching occurs. These studies indicate that the effect of the additive occurs with >2 vol% methanol in a solution of 0.25 mM DASA and toluene. We find that below 2 vol%

the effect of the additive is negligible on the switching of DASA. The T-xy diagrams can be used to predict the temperatures that are required to attain x_{MeOH}; a 10 mol% MeOH solution will begin to boil at 73 °C, though all the methanol will not boil off until a temperature of 110 °C is attained. We need to raise the temperature of the overall solution to 85 °C in order to reach a composition of 2% MeOH. This is consistent with experimental observations that show that only when a solution containing 10% MeOH is heated to above 85°C, enough of the solvent evaporated such that the DASA is now able to switch (**Figure 4**) . We demonstrate this by first heating the solution to 62 °C and then supplying light to drive the remaining 25 °C temperature change (**Figure 4a**). After the light drives the temperature to reach 87 °C, the solution is now able to switch in toluene and appears light blue in color, similarly to just 0.25 mM DASA in toluene; this indicates that less than 2% of methanol remains, as predicted by the T-xy diagram. After the light is turned off the solution cools back to 65 °C and the light is again turned on for a second cycle. We find that the solution changes color immediately and the temperature rises only 14 °C which is the equivalent to the temperature change observed in the absence of methanol (**Figure 4a**).
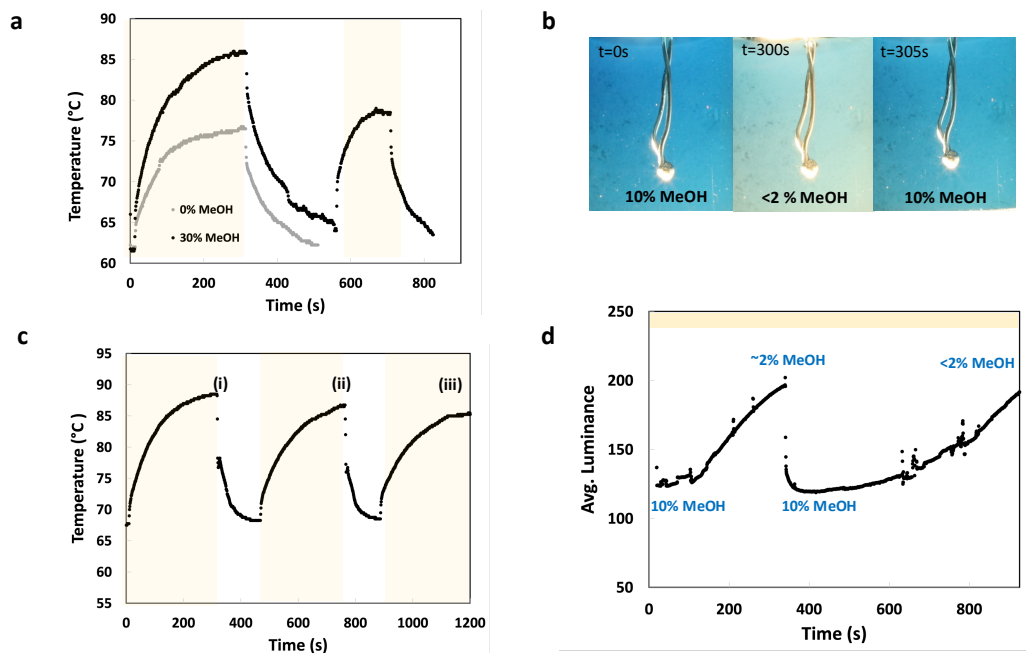
Figure 6.4 a) Heating of DASA in toluene with 30% MeOH using white light to drive evaporation of MeOH. By comparison with a sample containing no methanol (gray) we see that the peak temperature in the second cycle after the methanol has in theory been removed is similar to that of the case in which no methanol is present. Both starting temperatures are different but the change in temperature for both cases is 14 C. This teaches us that the methanol has been removed and now the heating is the same as when DASA switches alone in toluene b) Optical images of the sample immediate after the light is turned on, after 300 seconds of irradiation and immediately after the re-introduction of 10% MeOH under constant irradiation. In the image stills, the initial temperature is 66 C and rises to 86 C in the second panel at which point we see that most of the color of the solution is gone corresponding to the removal of MeOH. . c) Temperature changes observed with irradiation by white light with 10% methanol reintroduced at i, ii and iii and light subsequently turned off to cool. d) the corresponding absorbance tracking to confirm the return of all color and reversion to the open form of DASA.

As a proof of concept, to demonstrate the potential for oscillation due to the evaporation

and reintroduction of methanol, we perform studies in a quartz cuvette in which we boil off

methanol and analyze the changes induced after manual reintroduction. The insight obtained

from the experimental absorbance analysis, combined with temperature data, paints a clear

picture of the cyclical switching kinetics in the disappearance of additive as it vaporizes and

is re-introduced

Here, we use these studies to confirm that when re-introducing methanol, we can get

cyclical behavior of both color and heating. After the methanol is evaporated following

irradiation, 10% methanol is added back to the now-clear solution and the DASA switches

immediately back to the open form and regains its blue color under constant irradiation

(**Figure 4b**). The cyclization heating process begins again and the newly-added methanol

begins to evaporate. To confirm that the amount of heating induced by the reintroduction of

methanol is the same, we perform the same experiments but turn the light off between each

cycle to measure the change in temperature afforded by methanol re-introduction. We see

that with 3 cycles the temperature change is repeated (**Figure 4c**).

Using the grayscale tracker, we observe that in 0.25 mM DASA in toluene, the methanol

sufficiently evaporates such that the solution is no longer absorbing (**Figure 4d**). After 10%

is reintroduced, the color immediately returns to that of the original solution and the heating

process occurs again, leading to the cycling of the color. This is confirmed over at least 3

cycles before some degradation of the DASA begins to occur. The degradation is due to

extended exposure to high heating and can be potentially avoided by identifying a

197

compatible solvent mixture with a lower boiling point in future studies. In a carefully designed system, the re-introduction of the additive can be driven by the cooling induced by the lack of absorbance or an alternative reintroduction method relying on the collection and reintroduction of a specific volume of methanol. We look to thermodynamic modeling to guide the requirements for careful design of an actuator system that may exploit this additive-induced control of heat generation for oscillation.

6.3.4 Energetic requirements and dynamics of phase change for soft-robotic applications

The potential for the combination of additive-dependent photothermal actuation of DASA with binary solvent VLE to produce cylical behavior can best be understood by looking to enthalpy calculations of VLE that constrain the coupled relationship between the heat/mass transport and photoreaction kinetics in the photothermal system. The energetic requirements required to drive phase change and subsequently attain certain compositions in the vapor and liquid phase can be obtained using enthalpy-composition (H-xy) diagrams, which are generated according to methods outlined in the Supporting Information. We use these model calculations in order to establish predictive measures for attaining particular behaviors in a system that simultaneously undergoes photoswitching and phase change, in hopes that new actuators can be built to leverage these properties. In developing models for this system, the energy flows both in and out of the system must be considered. The source of energy input to the system is the heat absorbed by DASA, while heat is removed from the system due to conduction and convection through the fluid and container walls.
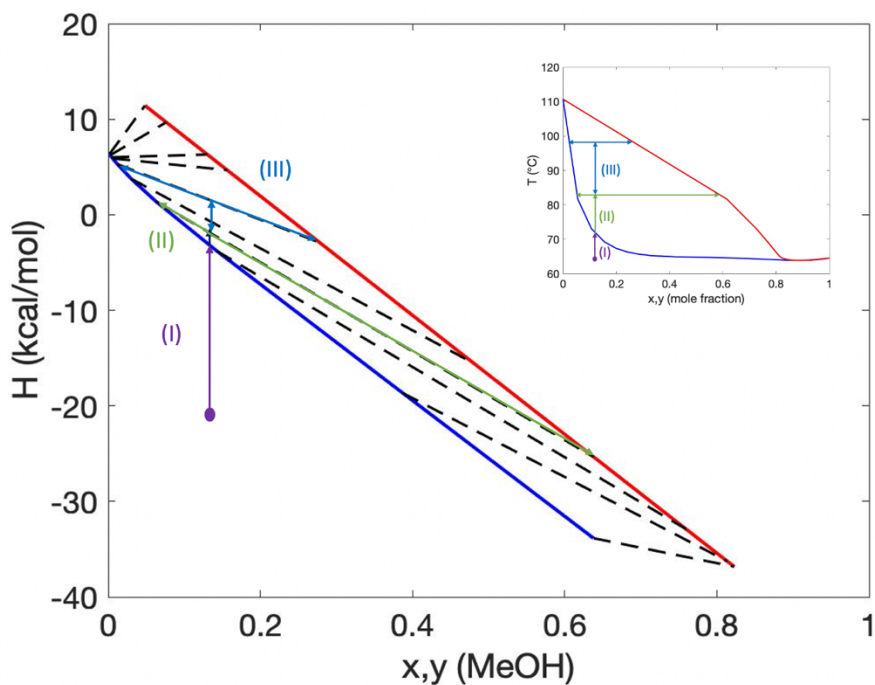
Figure 6.5 (i) System is irradiated by light; temperature increases but the system remains at a constant composition and stays entirely liquid. DASA remains in its open form. The energy needed to produce the temperature change $\Delta T = T2 - T1$ is given by $\Delta H = H2 - H1$. (b) Continued light input causes the temperature to increase, the methanol/toluene mixture enters the two-phase region. The methanol concentration in the liquid phase is decreased but is above the critical methanol concentration that allows photo-switching to occur. Thus, DASA is still in its open form. (iii) Phase separation continues to occur. Methanol concentration in liquid phase decreases to the critical methanol concentration where DASA begins switching to its closed form; in this form, DASA doesn't absorb light.

The energy input to the system is directly related to the concentration of open-form DASA and is a function of the properties of the DASA molecule such as molar absorptivity and quantum efficiency on a per molecule basis, as well as the percentage of DASA in its open form.

As seen in Figure S5, the percentage of open-form DASA decreases as a function of

MeOH concentration in the liquid phase. The Txy diagram additionally allows for the

prediction of temperatures required to attain specific values of x_{MeOH}. These two data sets

can be used concurrently to relate the percentage of open form DASA to system

temperature, which allows us to calculate the heat input to the system (q_{in}) as a function of

temperature.

Similarly, the energy removal from the system (q_{out}) required to condense a

specified amount of the vapor phase can be calculated using concepts in heat transfer.

Namely, if the temperature within the system is assumed to be spatially uniform, and the

conduction through the container walls is assumed to be negligible, q_{out} can be calculated

using the following equation:

$$q_{out} = hA(T - T_{air}) \, (1),$$

where h is the convective heat transfer coefficient of air, A is the system surface area,

and T_{air} is the ambient air temperature. Knowing the relative magnitudes of heat transfer

into and out of the system not only enables predictions of system behavior, but can also

inform system design, as $h, A,$ and T_{air} can all be tuned. Therefore, the combination of the

Hxy diagram presented in Figure 5, and the analysis above allow users to predict system

temperatures and DASA concentrations required to achieve energetic requirements to drive

phase change.

However, this analysis does not contain information regarding the timescales over which

these changes take place. Understanding the transient behavior of energy transfer in and out

is of key importance, as it dictates the nature of the system response. Thus, heat and mass

transfer analysis must be used in tandem with the Hxy diagrams to examine the dynamics of this system. The key timescales dictating the transient behavior of the phase change and photoswitching behavior are:

(1) The time required for heat to be dissipated from the system once the DASA switches to its closed form (τ_{heat}),
(2) The time required for re-condensed methanol to diffuse through the liquid phase of the system (τ_{diff}), and
(3) The time for DASA to switch back into its open form once the methanol concentration is increased above its critical value (τ_{rxn}).

Knowing the relative magnitudes of these timescales is therefore important in designing systems utilizing these binary solvents to exhibit certain long-time behaviors. These timescales can be estimated using mass and energy balances, as outlined in the Supporting Information. τ_{heat} is estimated assuming that the conductive heat transfer is negligible, and that heat dissipation is primarily from convective heat transfer into the surrounding air. This timescale has the following form:

The time required for heat to be dissipated from the system once the DASA switches to its closed form (τ_{heat}),

(4) The time required for re-condensed methanol to diffuse through the liquid phase of the system (τ_{diff}), and
(5) The time for DASA to switch back into its open form once the methanol concentration is increased above its critical value (τ_{rxn}).

Knowing the relative magnitudes of these timescales is therefore important in designing systems utilizing these binary solvents to exhibit certain long-time behaviors. These timescales can be estimated using mass and energy balances, as outlined in the Supporting Information. τ_{heat} is estimated assuming that the conductive heat transfer is negligible, and that heat dissipation is primarily from convective heat transfer into the surrounding air. This timescale has the following form:

$$\tau_{heat} = \frac{\rho V C_p}{hA} \quad (2)$$

Where ρ is the liquid phase, V is the reaction volume, C_p is the heat capacity of the liquid phase, h is the convective heat transfer coefficient of air, and A is the system surface area in contact with the ambient environment. For this system, we assume that the reaction vessel is a cylindrical system, so the volume and surface area can be expressed as a function of the vessel height (L) and radius (R):

$$\tau_{heat} = \frac{\rho \pi R^2 L C_p}{h 2 \pi R L} = \frac{\rho R C_p}{2h} \quad (3),$$

The system mass and surface area both increase with the size of the system, but this timescale can be lowered by increasing A through the inclusion of grooves or fins on the surface. The convective heat transfer coefficient be increased by introducing the forced convection of air across the surface of the system (using a fan), which can also be used to decrease τ_{heat}.

The diffusive time scale for methanol through the system is similarly obtained using analogous concepts in mass transfer:

$$\tau_{diff} = \frac{L^2}{D} \quad (4)$$

Where L is the characteristic length scale of the system (in this case, the height of the liquid in the container), and D is the diffusion coefficient of methanol in toluene. The selection of the liquid height is deemed to be appropriate, given that the methanol concentration gradient is expected to develop vertically, with x_{MeOH} decreasing as the distance from the vapor-liquid interface increases. In this case, the diffusion time can be increased by changing the geometry of the container to increase L.

Finally, τ_{rxn} can be obtained by examining the reverse rate expression of the

photoreaction, which was developed in Ref. 31:

$$r = k_{back}[N_o - N_{I,open}] - \sigma\phi I N_{I,open} \text{ (5)},$$

where r is the reaction rate (in units of mol L^{-1}s^{-1}, σ is the irradiation cross section, ϕ is

the quantum yield, I is the light intensity, $N_{I,open}$ is the concentration of open-form DASA,

k_{back} is the rate of the back reaction (conversion from closed to open-form DASA), and N_o

is the total concentration of DASA in the solution. $N_{I,open}$ can be related to N_o using the

following expression:

$$N_{I,open} = p_{open}N_o \text{ (6)}$$

This expression can be substituted into (4) to yield the following simplified expression:

$$r = [k_{back}(1 - p_{open}) - \sigma\phi I p_{open}]N_o \text{ (7)}$$

To obtain a reaction time scale from the rate expression, the following expression can be

used:

$$\tau_{rxn} = \frac{1}{k_{back}(1 - p_{open}) - \sigma\phi I p_{open}} \text{ (8)}$$

This timescale expression is more complex than the other two, as it is a direct function of

the percent of open-form DASA, which is related to the methanol content and temperature

of the system as discussed earlier. The methods described to establish the relationships

between p_{open}, x_{MeOH}, and T can additionally be applied to equation (7) to make estimates

for the reaction timescale.

To enable an easier comparison between the other timescales, we assume that the

irradiation area (σ) is approximately the same as the area for heat transfer in equation (3):

$$\tau_{rxn} = \frac{1}{k_{back}(1 - p_{open}) - 2\pi RL\phi I p_{open}} \quad (9)$$

The comparison of τ_{diff} and τ_{rxn} is important in understanding whether the conversion of DASA to its open form is diffusion- or reaction-limited. This can be examined by taking the ratio of τ_{diff} to τ_{rxn}; if this ratio is greater than one, the reverse photoreaction is diffusion limited, and if it is less than one, it is reaction limited:

$$\frac{\tau_{diff}}{\tau_{rxn}} = \frac{L^2[k_{back}(1 - p_{open}) - 2\pi RL\phi I p_{open}]}{D} \quad (10)$$

From the analysis performed above, we see that the reverse reaction will almost always be diffusion limited. Thus, the two relevant timescales to compare are τ_{diff} and τ_{heat}.

The relative values of these timescales dictate the behavior of this system. If the conversion of DASA to its open form is much faster than the rate of heat dissipation, then the temperature drops slowly enough to allow for the system to attain some steady state in which the heat dissipation through conduction and convection is balanced by the heat input from some percentage of DASA being converted back to its open form.

If the heat dissipation and conversion to open-form DASA are of relatively the same magnitude, then the system is expected to exhibit a slight overshoot in temperature before the temperature drops to some steady state value and the heat dissipation is balanced by heat generation from DASA in its open form.

Finally, if heat is dissipated quickly relative to the conversion of DASA back to its open form (which occurs at a rate dictated by some combination of τ_{diff} and τ_{rxn}), then the system temperature can drop before the open-form DASA begins generating heat and raising the temperature once again. This leads to oscillatory behavior, where the system goes

through cycles where the temperature rises, DASA switches to its closed form, temperature drops, and then DASA switches to its open form once again. The possibility for oscillation under constant irradiation is highly promising and allows for the future of soft robotics and actuators to include photoresponsive molecular switches as a fuel source.

Thus, the ratio of τ_{heat} to τ_{diff} can be obtained:

$$\frac{\tau_{heat}}{\tau_{diff}} = \frac{\rho R C_p D}{2hL^2} \quad (11)$$

In the ratio above, ρ, C_p and D are inherent to the system and are only changed by varying the system temperature, while h, R, and L are design parameters. Equation (11) serves as a design constraint, which can be used to predict which of the three different cases the system will follow. These key situations, as well as potential ways to achieve these design requirements are summarized in Table 1 below.

Table 1 – Summary of the effects of relative heat dissipation and diffusive timescales.

Outcome	Ratio of heat and diffusive timescales	Strategies to obtain this ratio
Steady-state temperature	$\frac{\tau_{heat}}{\tau_{diff}} \gg 1$	Increase the radius of the container, decrease the liquid height.
Steady-state temperature with overshoot	$\frac{\tau_{heat}}{\tau_{diff}} \sim 1$	Depends on the specific values of h, C_p, and D; balance these values by varying R and L

| Oscillatory response | $\dfrac{\tau_{heat}}{\tau_{diff}} \ll 1$ | Increase h by forcing convection using a fan, increase the liquid height, decrease the container radius. |

6.4 Conclusion

With this work we show that there are new possibilities for what can happen in a photothermal process when we have a binary solvent composition whose changes in turn cause the absorbance and the reactivity of the photoswitch to change. We identified an additive response for a negatively photochromic DASA system that maintains absorbance until all of the additive is removed. As a result, we are able to control the heat generation by controlling the temperature of the overall system such that we can boil off a desired amount of the additive for control of kinetics. We find that re-introduction of an additive after the evaporation leads to an instant reversal of the DASA molecule to the open, absorbing form such that the cycle of heating may begin again. The ability to re-introduce color in this way opens the door for the creation of oscillating actuation systems under constant irradiation that rely only on the relationship between the temperature changes driven by the evaporation and re-introduction of an additive. We develop a model such that future studies may tune properties of this or other photoswitching binary phase systems to create actuators for soft robots that are self-regulated. Using the enthalpy diagrams to carefully design a system will allow for control over the factors that govern heat transfer and kinetics to optimize their

complementary role for creative use. Additionally, we develop a method by which both heating and the kinetics of the solution can be tracked in real-time thus allowing for more specificity of control during experiments and better coupling of the rates of switching with that of heat generation. These contributions enable the possibility for oscillating work to be performed in sunlight or any constant light source and move forward our understanding of the photothermal capability of DASA for the future development of soft actuating systems.

6.5 Supporting Information

Chemical selection. All chemicals were obtained from Sigma Aldrich, TCI Europe or Fisher Scientific and, unless otherwise noted, all reagents were used as received without further purification. DASA was prepared following published protocols by Julie Peterson. Toluene (99.8%) and methanol were purchased and used without further purification from Sigma Aldrich. Donor-acceptor Stenhouse adducts were synthesized as described in the procedure previously reported. For each experiment, the compound was dissolved in solutions from fresh bottles of toluene diluted to the desired concentrations and kept in the dark.

Light source. A Schott Ace 150 W fiber optic white light source was chosen for all experiments herein due to its broad coverage of the absorbance spectrum of DASA (**Supplementary Figure 3**). In addition, it supplied light fluxes otherwise inaccessible with the use of LEDs available to us.

Temperature analysis. Infrared images were obtained using a FLIR E60 IR camera accurate to ±2% of reading. Thermal energy was supplied to the system via a flexible polyimide heater plate (IcStation) coupled to a benchtop voltage source. Temperature was probed using a K-type thermocouple (ThermoWorks, K-36X) and read using a thermocouple amplifier (Adafruit, MAX31855) and microcontroller (Arduino UNO) with +/- 0.5 C accuracy.

6.5.1 Absorbance tracker

Videos of quartz cuvettes containing DASA solutions were recorded in order to track absorbance changes over time using a Canon Rebel SL2 (100 mm f/2.8 Macro USM fixed lens, 1x magnification, 30 frames per second). Experimental setup includes a cuvette with light shining from below and a camera stationed directly in front of the solution in order to observe changes in color afforded by the switching induced by irradiation. Videos were then divided into grayscale images using MATLAB code and the average luminance is tracked over the course of an experiment.

An algorithm was written in MATLAB by Luke Gockowski to analyze light intensity changes in a cuvette over time, serving as a rapid-turnaround, accessible proxy for UV/vis characterization under experimental conditions i.e. independent of light intensity, concentration. The input to the algorithm is a video of a photochemical reaction taking place inside of a thin, rectangular cuvette. The user then chooses a rectangular region of interest— either identical to that of a video previously analyzed (enabling fair comparisons across several videos) or hand-picked.
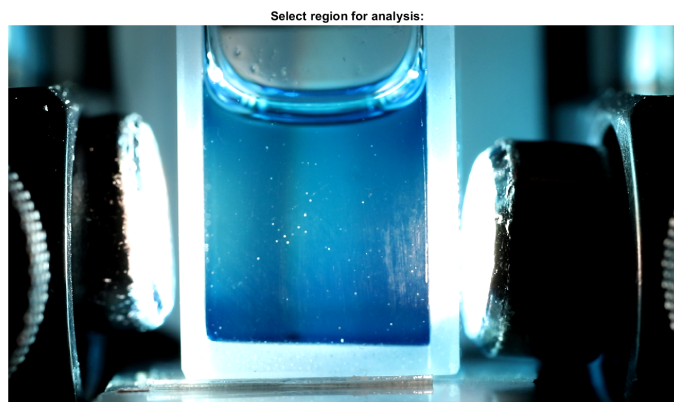
Figure S6 Sample starting image for region selection for absorbance tracker obtained using a Canon

camera.

It was found post-experiment that small, undesirable particulates (dust, fibers, etc.) were attached to surface of the cuvette facing the camera. Here, some post-processing was done to remove these undesirable specks. The image was converted to grayscale, a mask comprising the locations of the specks was created by binarizing the image via an adaptive threshold, this mask was dilated to expand the region surrounding the specks, and finally the image was smoothed and filled using surrounding pixel information (see images below).
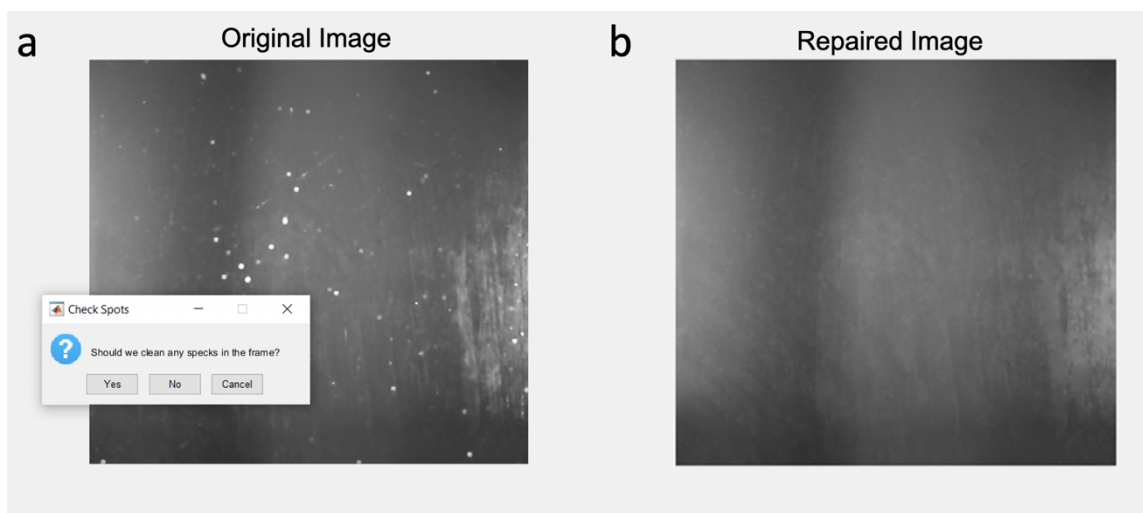
Figure S7 Repair image clear of dust particles adhered to the quartz cuvette

Upon user approval of the "repaired" image, a frame-by-frame analysis of the video can commence. The user selects an interval of N frames between each image to be analyzed — thus, setting the time resolution of the analysis. In each frame pulled from the video of the experiment, some processes are applied and measurements are taken:

1. Capture time data based on frame number and video frame rate.
2. Convert the image to grayscale.
3. Crop the image to the region of interest.
4. Smooth the specks using the same mask developed earlier.
5. Measure net light intensity in the frame.
6. Measure average light intensity in the frame.
7. Measure the standard deviation of the light intensity.

Light intensity is found simply by summing the vector values comprising the images. MATLAB's native "rgb2gray" function was used to convert images to grayscale. This function converts RGB images to grayscale by eliminating the hue and saturation information while retaining the luminance. Luminance is a photometric measure of the luminous intensity per unit area of light traveling through the lens of the camera. We observe two metrics to gain information about the dynamic nature of our system:

Average light intensity quantifies the precise, though not necessarily accurate sum of light transmitted through the cuvette by taking the average of the grayscale values (i.e., on a scale from 0-255) of all pixels in the frame. It has a lower bound of 0 (indicating an image comprising 100% black pixels) and an upper bound of 255 (indicating an image comprising 100% white pixels). This serves as a precise, though not necessarily accurate, proxy for transmittance.

Standard deviation of light intensity serves as an indicator of the spatial distribution of luminance. I.e., a photochemical reaction that allows for spatially homogenous transmittance of light (e.g., a fully bleached solution) would have a relatively low standard deviation compared to a photochemical reaction that incites spatially heterogenous transmittance of light (e.g., a partially bleached solution).

Once these metrics have been quantified via a for-loop-based frame-by-frame analysis, they are plotted (**Figure S4**).
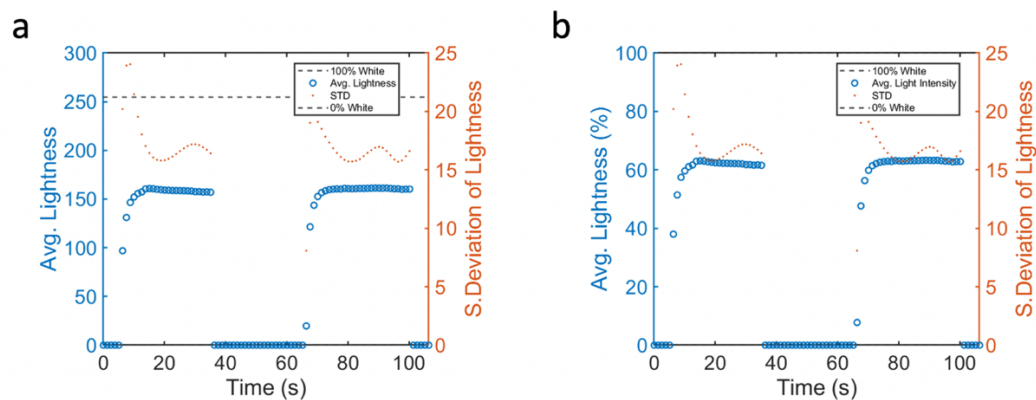

Figure S8 Plotted lightness for a given sample over time including measures of standard deviation.

6.5.2 DASA Characterization

The photoinduced optical absorption kinetics were measured using a pump-probe setup described in previously reported studies. Studies herein were performed in a demountable liquid cell with variable pathlengths (6um- to 1mm), UV-grade fused silica windows (WAD-U22) and an optical table sample slide holder (HSS-OTE) purchased from Harrick Scientific Products Inc. In addition to characterizing the kinetics of the photoreactions, these experiments also provide a measurement of the photostationary state, i.e., the fractional conversion of the photoswitch to the conformer of the molecule comprising the switched state.

Using pump probe UV-Vis spectroscopy, we determine the switching properties of DASA in toluene at various concentration of methanol using a 617nm LED and a cell of 1mm path length. In a 0.125mM sample, the photostationary state increases with increasing

amount of methanol added. Additionally, the initial absorbance rises with this increase as the equilibrium is pushed toward the open form of DASA.
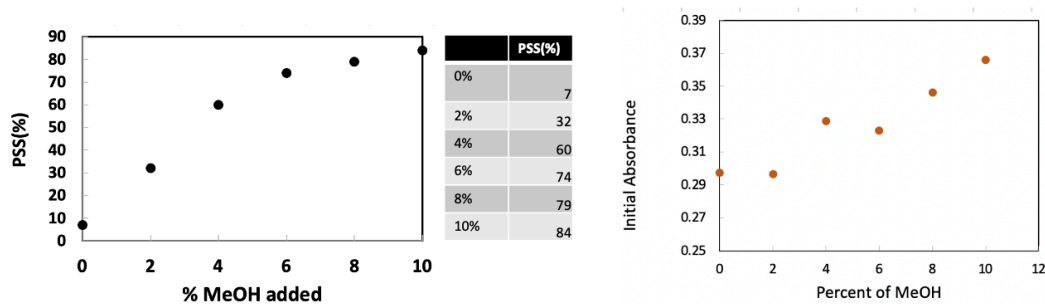

Figure S9. Photostationary state relative to the volume % of methanol added and the corresponding effect on the initial absorbance.

We further track the change in the rates of the back reaction over time. As a result of the shifting energy barriers, we see that first there is an increase in the rate of the back reaction followed by a decrease above a certain volume percent of added DASA. This range is small enough that it will not affect the photothermal heating experiments but demonstrate the importance of careful understanding of the switching properties of any additive on the energy landscape of DASA.

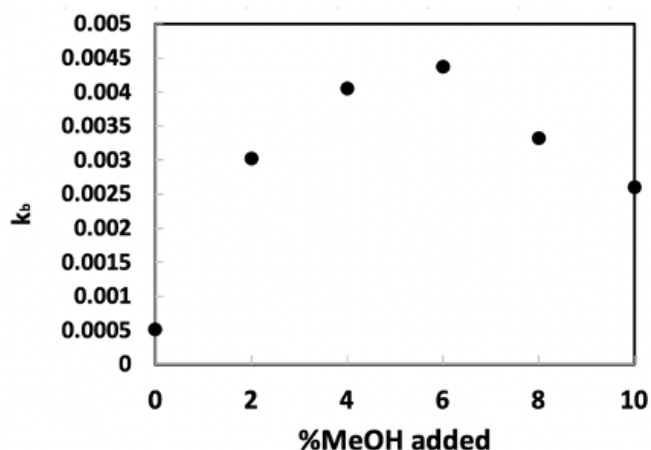|	kb
0.125 0%	0.000517
2%	0.0030205
4%	0.0040557
6%	0.0043693
8%	0.0033243
10%	0.00260413

Figure S10 Rate of back reaction for a 0.125mM solution of DASA in toluene with changing volume % of methanol.

Identical studies were performed for 0.25mM DASA in toluene with varied amounts of methanol added. Again, we see a rise in the initial absorbance and the photostationary state.

For comparison, we track and compare the switching kinetics for solutions up to 0.5mM DASA in toluene. Without methanol, we find comparable switching kinetics indicating that this DASA is less sensitive to changes in concentration compared to previous iterations. Additionally, the rates of the back reaction and photostationary state follow the same trend for all concentrations. These properties inform our selection of concentration range; since less DASA is required to achieve the same behavior and generate a substantial amount of

214

heat we perform experiments using 0.125 and 0.25mM DASA but anticipate similar effects at higher concentrations.
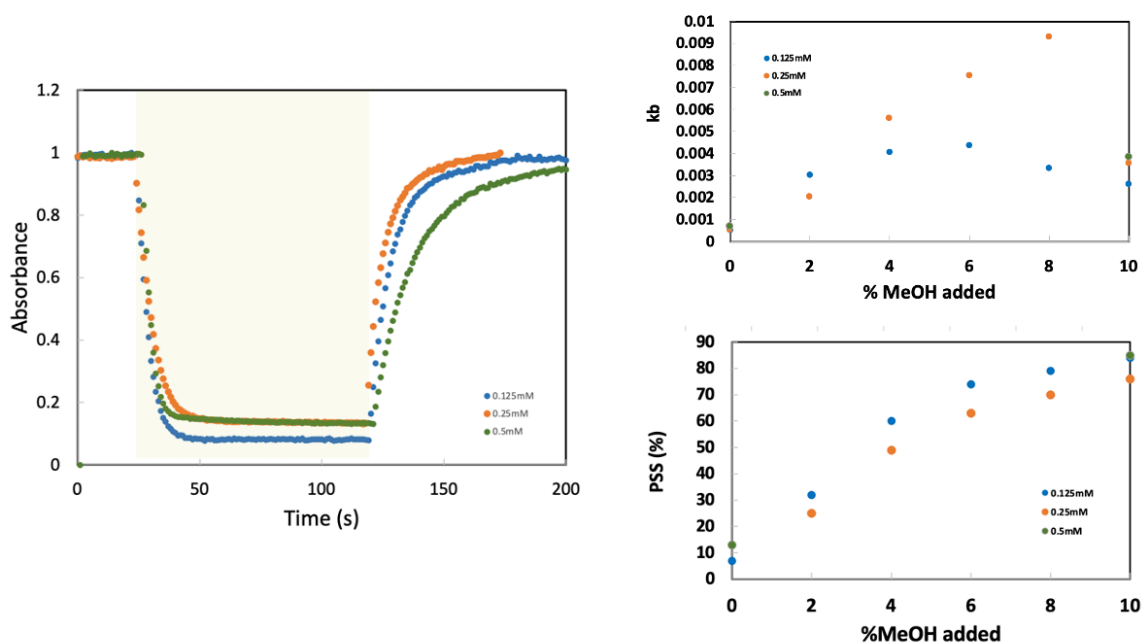

Figure S7 a comparison of a) switching kinetics b) rate of back reaction and c) change in photostationary state of 0.125, 0.25 and 0.5 mM DASA in toluene with increasing concentration of added methanol.

To characterize the effect of switching in experimental conditions we use the absorbance tracker to measure the change in light intensity with increasing concentration of methanol in a 0.25mM DASA solution. We see that with 0- 2% added methanol there is no noticeable difference but above this value we see a change in absorbance which eventually levels off

above 5%. The range is more narrow in experimental conditions than using the pump probe

due to the increased path length in experiment (1cm) and the light source used (white light).
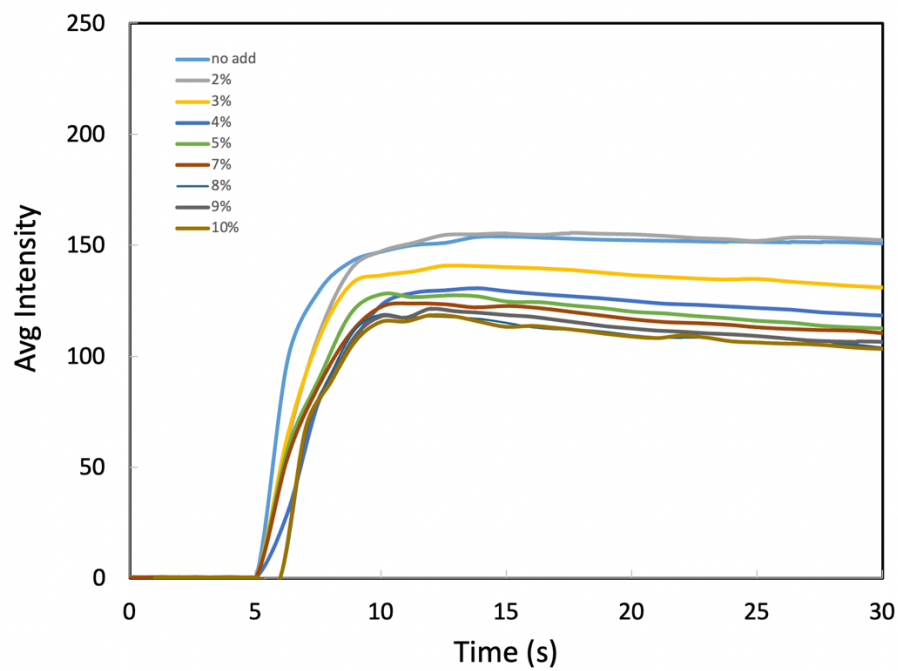

Figure S8 Absorbance tracking of average light intensity for a 0.25mM solution of DASA in toluene with increasing concentration of methanol.

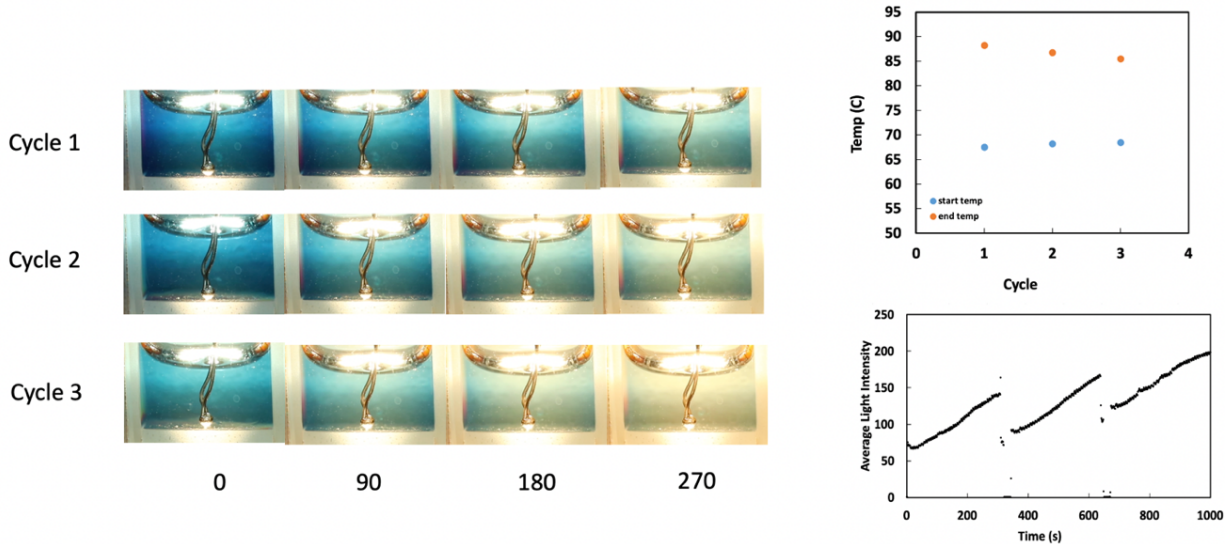## 6.5.3 Evaporation of methanol under irradiation

Figure S9 a) optical images of a cuvette containing DASA with methanol at increasing time (seconds) corresponding to increase in temperature and thus decrease in methanol due to evaporation. For the sample, the temperature before and after irradiation are provided (b) as well as the change in absorbance (c) with each new addition of methanol. The temperature change is less drastically affected than the overall absorbance.

Degradation studies were performed to track the change in heat and switching observed for solution of 0.125mM DASA in toluene with 10% methanol. The initial temperature was 65C for the experiments the light supplied led to an increase in up to 25C for the first cycle. We see from these experiments that after the first cycle in which methanol evaporates off, after the methanol is reintroduced the absorbance decreases appreciably with each cycle. Additionally, the amount of heat generated also decreases albeit less significantly. It is likely that after irradiation and continuous heating to 90C, the DASA is decomposing. We limit the exposure for the reported experiments to the length of two cycles.
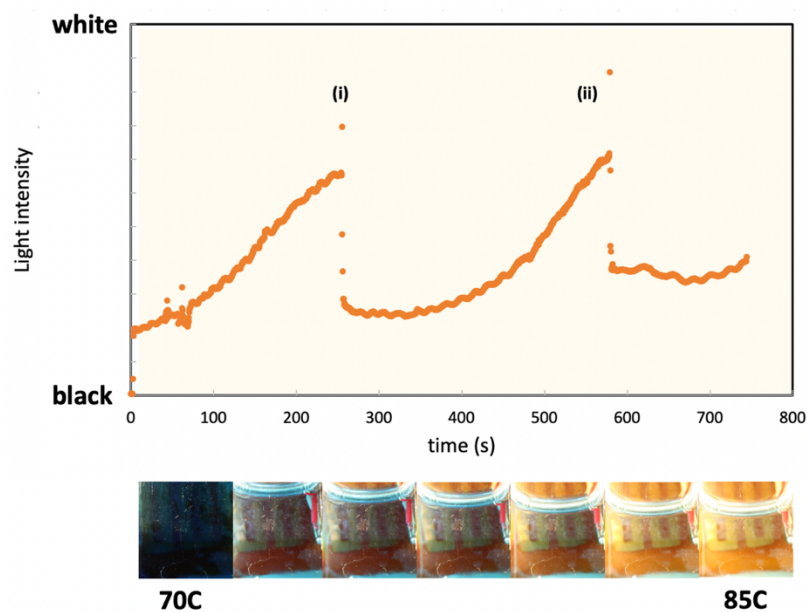
Figure S10 a) absorbance tracking of a solution of 0.125mM DASA in toluene with 10% methanol initially and added in at sec. b) corresponding stills from a video showing the change in transparency afforded by the evaporation of methanol and corresponding change in switching.

For a 0.125mM sample of DASA in toluene with 10% methanol, we explore the potential to use this system as an optical window. Initially prior to irradiation the solution is dark blue in color, allowing very little light through which obscures the shape behind the sample. As the solution heats up and we track the decreasing absorbance, we see that the shape comes into clear focus and light is able to pass through the cuvette. When methanol is added back into the solution the color goes blue and opaque once again, followed by a repeat in heating and transparency. Opportunities for actuation can exist where the transparency

afforded by the kinetic shifts of DASA are what control the on/off capability of light driven process occurring behind the window.

6.5.4 Binary phase diagram modeling

All modeling was performed by Vedika Shenoy.

The switching of DASA is dependent on the methanol concentration in the liquid phase (x_{MeOH}), so predicting temperatures required to attain specific x_{MeOH} via a Txy diagram is of use here. DASA is added in small concentrations (< 1 mM), so this system is approximated as a binary methanol/toluene mixture. Temperature-composition (Txy) diagrams were produced for a binary mixture of toluene and methanol using the non-random two-liquid (NRTL) thermodynamic model. This model assumes ideal gas behavior, but accounts for non-ideal interactions in the liquid phase of the system. Methanol is a polar molecule that undergoes hydrogen bonding with itself, so this mixture is expected to exhibit non-ideal liquid-phase behavior. The NRTL model equation for a binary system is as follows:

$$\frac{G^E}{x_1 x_2 RT} = \frac{G_{21}\tau_{21}}{x_1 + x_2 G_{21}} + \frac{G_{12}\tau_{12}}{x_2 + x_1 G_{12}} \ (1),$$

$$G_{12} = \exp(-\alpha\tau_{12}) \ (2),$$

$$G_{21} = \exp(-\alpha\tau_{21}) \ (3),$$

$$\tau_{12} = \frac{b_{12}}{RT} \ (4),$$

$$\tau_{21} = \frac{b_{21}}{RT} \ (5).$$

In the expressions above, α, b_{12}, and b_{21} are parameters that are specific to the pair of species in the mixture, and do not vary with composition and temperature. x_1 and x_2 refer to

liquid phase mole fractions of species 1 and 2 in the mixture, R is the gas constant, and T is the system temperature. G^E is the excess Gibbs free energy of the mixture, which is the Gibbs energy of a solution in excess to what it would be if the mixture behaved as an ideal solution. This model is used to calculate activity coefficients (γ_1 and γ_2) via the following expressions:

$$\ln(\gamma_1) = x_2^2 \left[\tau_{21} \left(\frac{G_{21}}{x_1 + x_2 G_{21}} \right)^2 + \frac{G_{12}\tau_{12}}{(x_2 + x_1 G_{12})^2} \right] \quad (6)$$

$$\ln(\gamma_2) = x_1^2 \left[\tau_{21} \left(\frac{G_{12}}{x_2 + x_1 G_{12}} \right)^2 + \frac{G_{21}\tau_{21}}{(x_1 + x_2 G_{21})^2} \right] \quad (7)$$

For a specified range of liquid concentration of component 1 (x_1), these activity coefficients can be used to calculate the corresponding vapor concentration of component 1 at the same temperature (y_1) using modified Raoult's Law:

$$y_1 P = x_1 \gamma_1 P_1^{sat} \quad (8),$$

where P is the total system pressure, and P_1^{sat} is the pure component saturation pressure of species 1, which is calculated according to the Antoine equation:

$$\log_{10}(P_1^{sat}) = A_1 - \frac{B_1}{T + C_1} \quad (9),$$

where A_1, B_1, and C_1 are species-specific tabulated constants.

Given the temperature dependence of activity coefficients and saturation pressures, solving these equations to obtain Txy diagrams requires an iterative solution. Therefore, these calculations are performed using Aspen Plus, which has databases containing the relevant parameters for methanol and toluene. Liquid mole fractions of methanol are varied from 0 to 1, and the corresponding vapor mole fractions and temperatures are obtained.

Enthalpy-composition (Hxy) diagrams are also generated to provide information about the energy inputs to the system required to achieve a specified separation. Liquid-phase (h_L) and vapor-phase (H_v) enthalpies are calculated using the following formulas:

$$h_L(T, x_i) = \sum_i x_i C_{p_{L,i}}(T - T_{ref})\ (10)$$

$$H_V(T, y_i) = \sum_i y_i[\lambda_i + C_{p_{V,i}}(T - T_{ref})]\ (11)$$

In the equations above, x_i refers to the liquid-phase mole fraction, y_i is the gas-phase mole fraction, λ_i is the latent heat of vaporization of each component at T_{ref}, and $C_{p_{L,i}}$ and $C_{p_{V,i}}$ are the liquid and vapor heat capacities of each component, respectively. The Txy and Hxy diagrams are generated for a system pressure of 1 atm and can be seen in Figure 1 below.
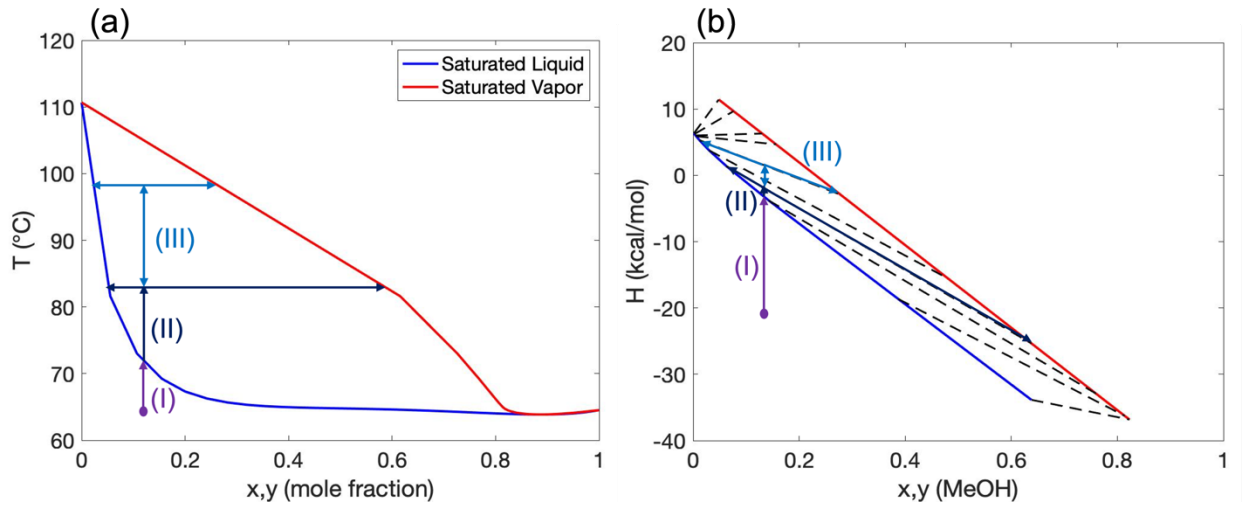

Figure S11 Txy (a) and Hxy (b) diagrams for a binary methanol/toluene system at 1 atm. The dashed lines in (b) are tie lines indicating vapor and liquid phases in thermal equilibrium.

In Figure S12, the "x" line gives the equilibrium compositions of the liquid phase and is also referred to as the bubble point curve, as it describes the temperature at which the first drop of a liquid mixture begins to vaporize. The "y" line gives the equilibrium compositions of the vapor phase and is alternatively referred to as the dew point curve, as it describes the temperature at which the first drop of a gaseous mixture condenses. Mixtures with compositions and temperatures that fall within these two lines will spontaneously phase separate into a liquid and vapor phase. For example, a mixture with the temperature and composition dictated by point Z' in the diagram above will phase separate into a liquid phase with composition x_1 and a vapor phase with composition y_1, with both phases at the same temperature as Z'.

The relative amounts of the vapor and liquid phase can be obtained from this Txy diagram via the Lever Rule, which is as follows:

$$f_L = \frac{y_1 - z_1}{y_1 - x_1},$$

$$f_V = \frac{z_1 - x_1}{y_1 - x_1},$$

where f_L and f_V refer to the liquid and vapor fractions, respectively. Thus, while the liquid and vapor compositions are set by equilibrium, the relative amounts of liquid and vapor can be tuned by changing the composition of the one-phase mixture.

Finally, as the mole fraction of methanol increases, the boiling point of the mixture — described by the bubble point curve — is seen to decrease. Methanol has a lower boiling point

than toluene, so increasing concentrations of methanol cause mixtures to boil at a lower temperature.

There are three key regions shown in Figure S12: (I) refers to the heating of a subcooled binary mixture to its saturation temperature, (II) indicates the continued boiling of the mixture, leading to changes in liquid and vapor compositions. In (I) and (II), DASA is in its open form, and absorbs light which in turn drives the heating of the solution. (III) indicates the region in which a critical value of x_{MeOH} is reached such that DASA switches to its closed form and the system begins to cool down.

Analysis of the transport phenomena governing the system is also necessary to predict the relative timescales of heat and mass transfer within the system.

Heat Transfer Analysis

The transient heat transfer out of the system can be examined by writing an energy balance around the system boundaries; in this case, the system is defined as the liquid and vapor phases of the binary mixture, as well as the container.

$$\rho V C_p \frac{dT}{dt} = q_{in} - q_{out},$$

where m is the system mass (take this to be the liquid mass), C_p is the heat capacity of the system (take this to be the heat capacity of the liquid phase), and q_{in} is the heat flow into the system, and q_{out} is the heat flow out.

In this system, the q_{in} term is the energy input due to the open-form DASA absorbing light. Therefore, once the DASA switches to its closed form at a critically low x_{MeOH}, the system stops absorbing heat and $q_{in} = 0$. In this case, the energy balance simplifies to:

$$\rho V C_p \frac{dT}{dt} = -q_{out}$$

To simplify this problem, we assume that the heat transfer out of the system is primarily due to convection of heat from the surface of the system/container:

$$\rho V C_p \frac{dT}{dt} = -hA(T - T_{air}),$$

where h is the convective heat transfer coefficient of air, A is the system surface area, and T_{air} is the ambient air temperature. Equation (14) is a 1° ODE, and can be solved using separation of variables:

$$\frac{1}{T - T_{air}} dT = -\frac{hA}{\rho V C_p}$$

$$\int_{T_{max}}^{T} \frac{1}{T' - T_{air}} dT' = -\frac{hA}{\rho V C_p} \int_{0}^{t} dt'$$

$$\ln\left(\frac{T - T_{air}}{T_{max} - T_{air}}\right) = -\frac{hA}{\rho V C_p}$$

$$\frac{T - T_{air}}{T_{max} - T_{air}} = \exp\left[-\frac{hA}{\rho V C_p} t\right]$$

The characteristic timescale for heat transfer out of this system is then given by:

$$\tau = \frac{\rho V C_p}{hA}$$

To examine the possible values for this timescale, C_p is approximated as the liquid heat capacity of pure toluene (which is valid given that DASA switches to its closed form for methanol mole fractions of ~ 0.02) and h is taken to be 40 $\frac{W}{m^2 K}$ which is characteristic of free air convection across a surface. The ratio of mass to surface area is varied to examine how this timescale for heat transfer changes.

224

6.6 References

1.   Liu, G. L., Kim, J., Lu, Y. U. & Lee, L. P. Optofluidic control using photothermal nanoparticles. *Nature Materials* **5**, 27–32 (2006).

2.   Lahikainen, M., Zeng, H. & Priimagi, A. Reconfigurable photoactuator through synergistic use of photochemical and photothermal effects. *Nature Communications* **9**, 1–8 (2018).

3.   Ndukaife, J. C. *et al*. Photothermal heating enabled by plasmonic nanostructures for electrokinetic manipulation and sorting of particles. *ACS Nano* **8**, 9035–9043 (2014).

4.   Gelebart, A. H., Vantomme, G., Meijer, E. W. & Broer, D. J. Mastering the Photothermal Effect in Liquid Crystal Networks: A General Approach for Self-Sustained Mechanical Oscillators. *Advanced Materials* **29**, (2017).

5.   Gelebart, A. H., Vantomme, G., Meijer, E. W. & Broer, D. J. Mastering the Photothermal Effect in Liquid Crystal Networks: A General Approach for Self-Sustained Mechanical Oscillators. *Advanced Materials* **29**, (2017).

6.   Ma, H. *et al*. Flexible, all-inorganic actuators based on vanadium dioxide and carbon nanotube bimorphs. *Nano Letters* **17**, 421–428 (2017).

7.   Meder, F., Naselli, G. A., Sadeghi, A. & Mazzolai, B. Remotely Light-Powered Soft Fluidic Actuators Based on Plasmonic-Driven Phase Transitions in Elastic Constraint. *Advanced Materials* **31**, (2019).

8.   Kang, D. J., An, S., Yarin, A. L. & Anand, S. Programmable soft robotics based on nano-textured thermo-responsive actuators. *Nanoscale* **11**, 2065–2070 (2019).

9.   Vesperinas, A., Eastoe, J., Jackson, S. & Wyatt, P. Light-induced flocculation of gold nanoparticles. *Chemical Communications* 3912–3914 (2007) doi:10.1039/b710502a.

10.   Tansi, B. M., Peris, M. L., Shklaev, O. E., Balazs, A. C. & Sen, A. Organization of Particle Islands via Light-Powered Fluid Pumping by Gold and Rutile Nanoparticles. **16802**, 1–6 (2019).

11.   Palacci, J., Sacanna, S., Steinberg, A. P., Pine, D. J. & Chaikin, P. M. Living Crystals of Light-Activated Colloidal Surfers. *Science* **339**, 936–939 (2013).

12.   van Oosten, C. L., Bastiaansen, C. W. M. & Broer, D. J. Printed artificial cilia from liquid-crystal network actuators modularly driven by light. *Nature Materials* **8**, 677–682 (2009).

13.   Ikeda, T., Mamiya, J. I. & Yu, Y. Photomechanics of liquid-crystalline elastomers and other polymers. *Angewandte Chemie - International Edition* **46**, 506–528 (2007).

14.   Iqbal, D. & Samiullah, M. H. Photo-responsive shape-memory and shape-changing liquid-crystal polymer networks. *Materials* vol. 6 116–142 (2013).

15.   Liu, Y. *et al.* Humidity- and Photo-Induced Mechanical Actuation of Cross-Linked Liquid Crystal Polymers. *Advanced Materials* **29**, (2017).

16.   Lu, X. *et al.* Liquid-Crystalline Dynamic Networks Doped with Gold Nanorods Showing Enhanced Photocontrol of Actuation. *Advanced Materials* **30**, (2018).

17.   Kohlmeyer, R. R. & Chen, J. Wavelength-selective, IR light-driven hinges based on liquid crystalline elastomer composites. *Angewandte Chemie - International Edition* **52**, 9234–9237 (2013).

18. Lu, X., Guo, S., Tong, X., Xia, H. & Zhao, Y. Tunable Photocontrolled Motions Using Stored Strain Energy in Malleable Azobenzene Liquid Crystalline Polymer Actuators. *Advanced Materials* **29**, 1–7 (2017).

19. Martella, D. *et al*. Light activated non-reciprocal motion in liquid crystalline networks by designed microactuator architecture. *RSC Advances* **7**, 19940–19947 (2017).

20. White, T. J. *et al*. A high frequency photodriven polymer oscillator. *Soft Matter* **4**, 1796–1798 (2008).

21. Gelebart, A. H. *et al*. Making waves in a photoactive polymer film. *Nature* **546**, 632–636 (2017).

22. Ulrich, S. *et al*. Visible Light-Responsive DASA-Polymer Conjugates. *ACS Macro Letters* **6**, 738–742 (2017).

23. Zhu, M. Q. *et al*. Spiropyran-based photochromic polymer nanoparticles with optically switchable luminescence. *Journal of the American Chemical Society* **128**, 4303–4309 (2006).

24. Jin, Y., Paris, S. I. M. & Rack, J. J. Bending materials with light: Photoreversible macroscopic deformations in a disordered polymer. *Advanced Materials* **23**, 4312–4317 (2011).

25. Livshits, M. Y. *et al*. Generating Photonastic Work from Irradiated Dyes in Electrospun Nanofibrous Polymer Mats. *ACS Applied Materials and Interfaces* vol. 10 37470–37477 (2018).

26. Singh, S. *et al*. Spatiotemporal Photopatterning on Polycarbonate Surface through Visible Light Responsive Polymer Bound DASA Compounds. *ACS Macro Letters* **4**, 1273–1277 (2015).

27.   Narumi, K. *et al*. Liquid Pouch Motors: Printable Planar Actuators Driven by Liquid-to-Gas Phase Change for Shape-Changing Interfaces. *IEEE Robotics and Automation Letters* **5**, 3915–3922 (2020).

28.   Lee, H. J. & Loh, K. J. Liquid vaporization actuated soft structures with active cooling and heat loss control. *Smart Materials and Structures* **30**, (2021).

29.   Li, X., Duan, H., Lv, P. & Yi, X. Soft Actuators Based on Liquid-Vapor Phase Change Composites. *Soft Robotics* **8**, 251–261 (2021).

30.   Lee, J. *et al*. Programmable Bilayer Actuator Driven by Visible Light Using Donor – Acceptor Stenhouse Adducts. 1–8.

31.   Seshadri, S. *et al*. Self-regulating photochemical Rayleigh-Bénard convection using a highly-absorbing organic photoswitch. *Nature Communications* **11**, 1–8 (2020).

32.   Helmy, S., Oh, S., Leibfarth, F. A., Hawker, C. J. & Read De Alaniz, J. Design and synthesis of donor-acceptor stenhouse adducts: A visible light photoswitch derived from furfural. *Journal of Organic Chemistry* **79**, 11316–11329 (2014).

33.   Helmy, S. *et al*. Photoswitching using visible light: A new class of organic photochromic molecules. *Journal of the American Chemical Society* **136**, 8169–8172 (2014).

34.   Hemmer, J. R. *et al*. Controlling Dark Equilibria and Enhancing Donor-Acceptor Stenhouse Adduct Photoswitching Properties through Carbon Acid Design. *Journal of the American Chemical Society* **140**, 10425–10429 (2018).

35.   Hemmer, J. R. *et al*. Tunable Visible and Near Infrared Photoswitches. *Journal of the American Chemical Society* **138**, 13960–13966 (2016).

36.   Sroda, M. M., Stricker, F., Peterson, J. A., Bernal, A. & Read de Alaniz, J. Donor–Acceptor Stenhouse Adducts: Exploring the Effects of Ionic Character. *Chemistry - A European Journal* **27**, 4183–4190 (2021).

37.   Lerch, M. M., Wezenberg, S. J., Szymanski, W. & Feringa, B. L. Unraveling the Photoswitching Mechanism in Donor-Acceptor Stenhouse Adducts. *Journal of the American Chemical Society* **138**, 6344–6347 (2016).

38.   Mallo, N. *et al*. Structure-function relationships of donor-acceptor Stenhouse adduct photochromic switches. *Chemical Science* **9**, 8242–8252 (2018).

39.   Lui, B. F. *et al*. Unusual concentration dependence of the photoisomerization reaction in donor-acceptor Stenhouse adducts. *Photochemical and Photobiological Sciences* **18**, 1587–1595 (2019).

40.   Lerch, M. M. *et al*. Tailoring Photoisomerization Pathways in Donor-Acceptor Stenhouse Adducts: The Role of the Hydroxy Group. *Journal of Physical Chemistry A* **122**, 955–964 (2018).

41.   Hemmer, J. R. *et al*. Controlling Dark Equilibria and Enhancing Donor-Acceptor Stenhouse Adduct Photoswitching Properties through Carbon Acid Design. *Journal of the American Chemical Society* **140**, 10425–10429 (2018).

42.   Clerc, M. *et al*. Promoting the Furan Ring-Opening Reaction to Access New Donor–Acceptor Stenhouse Adducts with Hexafluoroisopropanol. *Angewandte Chemie - International Edition* **60**, 10219–10227 (2021).

7. Directions for future work and conclusion

This chapter describes numerous findings that present an opportunity for future exploration by scientists looking to take advantage of photoswitchable small molecules and surfactants for the control of fluid interfaces and actuation systems.

7.1 SP-DA-PEG continued studies

Much remains unknown and unexplored regarding the spiropyran-based surfactant we have synthesized including the switching pathways and the possible avenues of control of SP-DA-PEG. Here we present some preliminary studies that open the door for exciting possibilities for use with fluid flow and in nanoemulsion systems.

7.1.1 Cosurfactant effects on interfacial tension

To better understand the spiropyran surfactant and the co-surfactant effects first encountered in the studies from Chapter 2, we performed interfacial tension measurements at varying concentrations of charged co-surfactant SDBS. Through this preliminary work, we discovered interesting and unexpected interfacial responses to the presence of SP-DA-PEG and SDBS. These experiments were conducted on the tensiometer in a 1mM SP-DA-PEG solution in toluene with a water droplet containing SDBS of various concentrations.

In the presence of the charged co-surfactant, we observe particularly unusual behaviors of the SP-DA-PEG at concentrations of SDBS higher than 0.125mM.
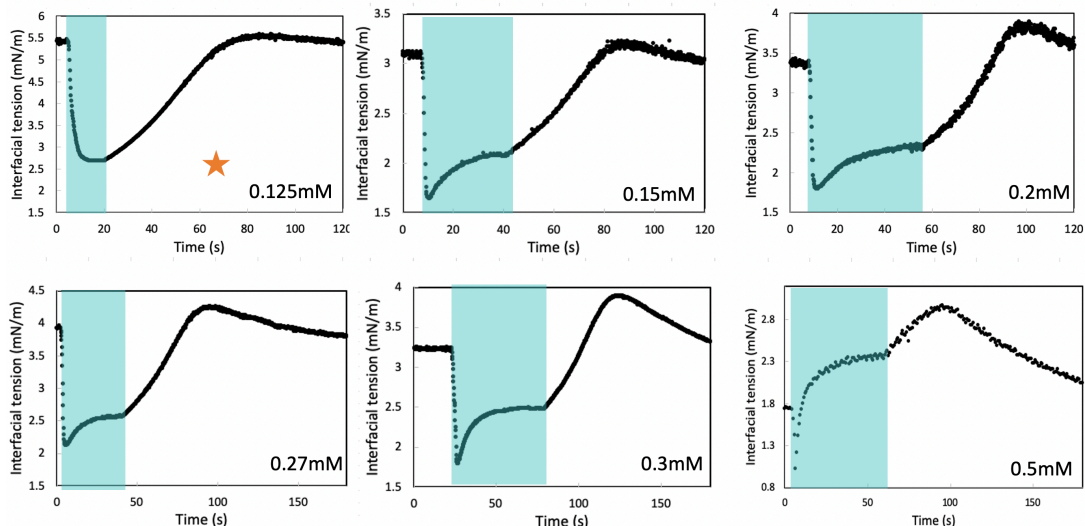

Figure 7.11 Interfacial tension measurements between toluene and water for various concentrations of SDBS in water ranging from 0.125mM to 0.5mM at constant concentration of 1mM SP-DA-PEG in toluene. At higher SDBS concentration, the interfacial tension undergoes a multi-step process indicating an effect of the co-surfactant on the switching properties of the photo-surfactant.

As shown in Figure 1, at 0.125 mM SDBS, the behavior is as expected; upon UV light irradiation, the interfacial tension decreases and plateaus as the spiropyran converts to the merocyanine form. After the light irradiation is removed the interfacial tension rises back to the original value. However, above 0.15mM we observe multiple steps and very different behavior. Between 0.15mM and 0.3 mM SDBS, light irradiation results in a near instantaneous drop in the interfacial tension, after which it begins to rise and eventually plateaus. Interestingly, this change in interfacial tension occurs all while under constant irradiation. After it plateaus the light is turned off and the interfacial tension rises, overshooting the initial equilibrium interfacial tension and finally returning to the original

value. This behavior suggests that the interaction between the SP-DA-PEG and the co-surfactant is mechanistically complicated and thus the effect on the interfacial properties is highly dependent on the relative concentration of each.
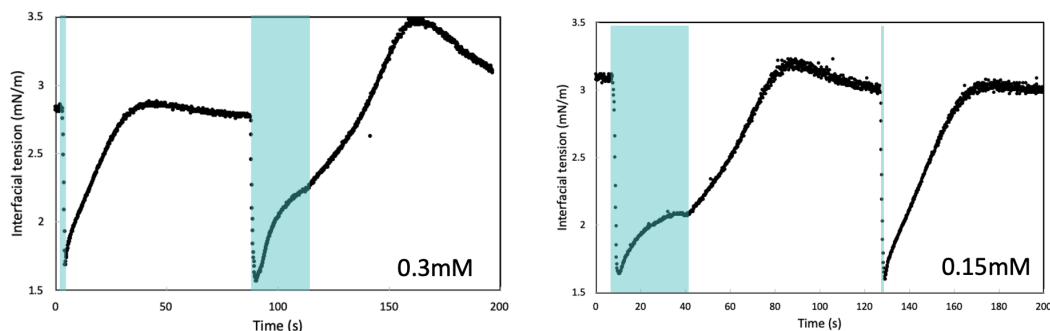

Figure 7.12 Interfacial tension measurements for (left) 0.3mM SDBS, with light pulsed first for 1 second and then for longer and (right) 0.15mM SDBS where initially the light is supplied for a longer time followed by a 1 second pulse.

Additionally, we find that the amount of time over which the droplet is exposed contributes to the behavior observed, particularly in the reverse reaction. For concentrations of 0.3mM and 0.15mM shown in Figure 2, we look at what occurs when light is supplied for only one second compared to long intervals (20 seconds or longer). Regardless of if the short exposure is first or second, we always see that the overshoot behavior is observed after the longer exposure. This suggests the possibility that the longer exposure might lead to the formation of a merocyanine isomer that opens pathways for the reverse reaction to access an additional spiropyran isomer.
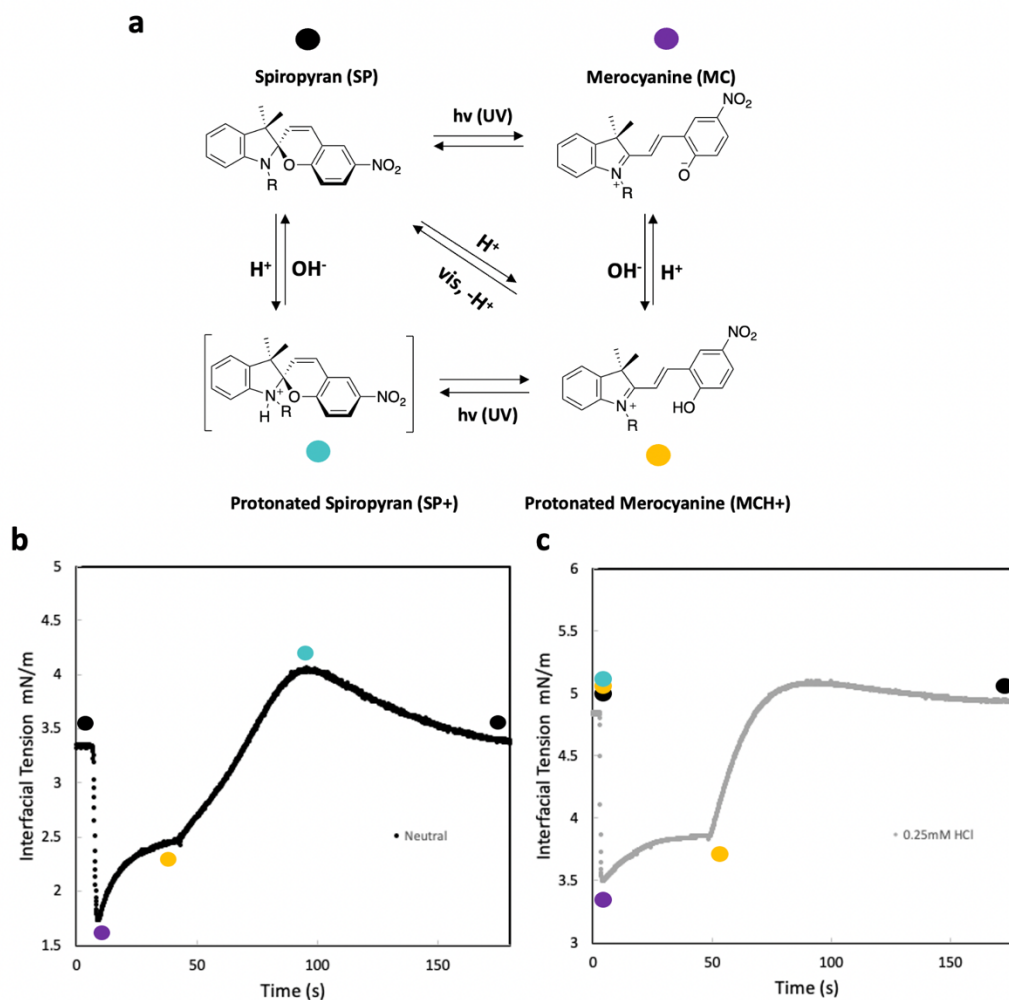
Figure 7.26 a) proposed mechanism of Spiropyran switching.) interfacial tension

measurements for a) 0.25mM SDBS in water and 1mM SpiroPEG in toluene and c) with

0.25mM HCl in water with the corresponding proposed isomer.

In order to potentially understand the effect of the co-surfactant on the mechanism and to

better conceptualize what might be occurring with the charged co-surfactant, we add

0.25mM HCl to the water. We believe that what is occurring in the 0.15-0.3mM range is as

follows; when the solution is irradiated, the spiropyran is converted first to the zwitterionic

MC but is quickly protonated to the MCH+ form which is stabilized. After the light is

233

removed it transitions back to the SP by going through the protonated spiropyran transition state (SP+), ultimately losing the proton and returning to the stable spiropyran form in which it began. To support this hypothesis, we test using acidic condition; under these conditions we would expect that the protonated merocyanine will be favored and the zwitterionic form will be short lived. In the acidic environment we also suspect that the initial equilibrium will be shifted such that it is a mixture that contains some of the merocyanine as well as the protonated spiropyran, since the environment will favor these more polar species. We see in looking at these data that the equilibrium is in fact higher than 0.25mM SDBS with neutral water and the same behavior is observed in the form of the initial spike to low interfacial tension before the stabilization at the more polar form. The reverse reaction has less of an overshoot, but we hypothesize that this is because the equilibrium state contains some of the protonated spiropyran already and so the stabilized interfacial tension is consistently higher. Further studies are needed in order to confirm these mechanistic hypotheses.
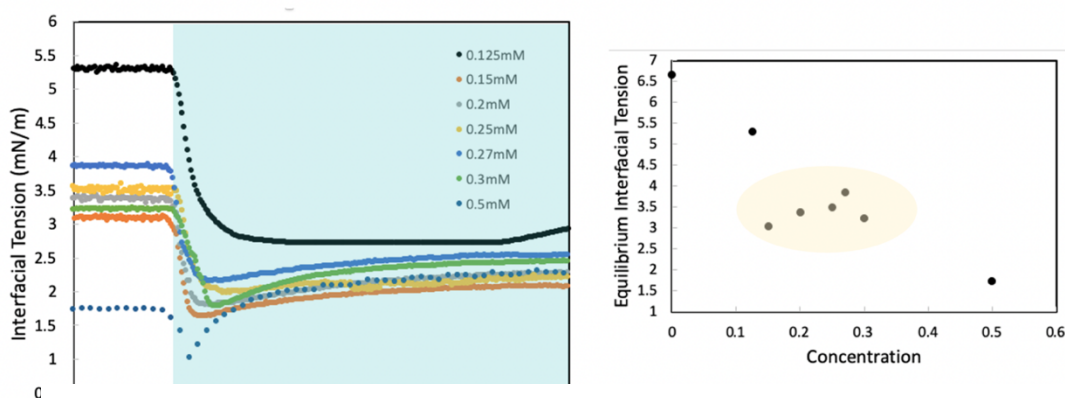

Figure 7.27. Nonlinear concentration dependence of initial equilibrium interfacial tension. Within the range of 0.15-0.3mM, the system equilibrates to roughly the same interfacial tension whereas a large change is observed for 0.5mM and 0.125mM.

234

We see there is a nonlinear concentration dependence on the initial equilibrium which might hint at the presence of micelles and an interesting stabilization process due to the co-surfactant. We observe that in the range of 0.15-0.3 mM SDBS, the equilibrium interfacial tension and undershoot/overshoot behavior is roughly the same. However, above 0.3mM, we have a drop in the initial interfacial tension and the droplet is highly unstable. Below 0.15mM the interfacial tension at equilibrium increases by ~1.5mN/m and the light driven overshoots are not observed. We suspect that in the case of less charged co-surfactant the conversion does not undergo alternate switching pathways but simply converts between the SP->MC forms which suggests that the charged co-surfactant is responsible for the observed multi-step switching behavior. Quite curious is the behavior above 0.5 mM where we find that under irradiation, the interfacial tension rises above the initial equilibrium. It is possible that in the 0.5mM case, which poses the biggest question, we are operating above the critical micelle concentration and therefore the behavior reflects what might occur if micelles instead of free surfactants are sitting at the interface.

The range over which the behavior is observed is centered around the critical micelle concentration of SDBS in water which is reported as 0.3mM. This value is likely to shift in the presence of the SP-DA-PEG cosurfactant and, as such, more studies need to be done to confirm the critical micelle concentration and the significance of this concentration range. A better understanding of this might allude to how micelles sitting at the interface might compare to free surfactant molecules on the reaction process. Further exploration needs to be done to take advantage of the potential of isolating steps in the switching mechanism or simply to select a concentration that allows for the greatest degree of predictability and

235

interfacial control. The co-surfactant effects remain relatively unexplored and open many doors for the control of interfacial properties.

7.1.2 Nanoemulsion control using SP-DA-PEG

Revisiting the motivation for the work as discussed in chapter 1, we sought to explore the potential to drive nanoemulsion instability with the knowledge gained around the large polarity change of the spiropyran based photosurfactant as well as the co-surfactant effects. After the studies performed in chapters 2 and 3 revealed the importance of both co-surfactant and the extent of the polarity change to drive interfacial tension change, we looked to make nanoemulsions with SP-DA-PEG. Since we saw with the droplet studies that SP-DA-PEG leads to droplet breakup as a result of the large change in interfacial tension, we anticipated that it may serve as a good co-surfactant for the breakup of nanoemulsions.
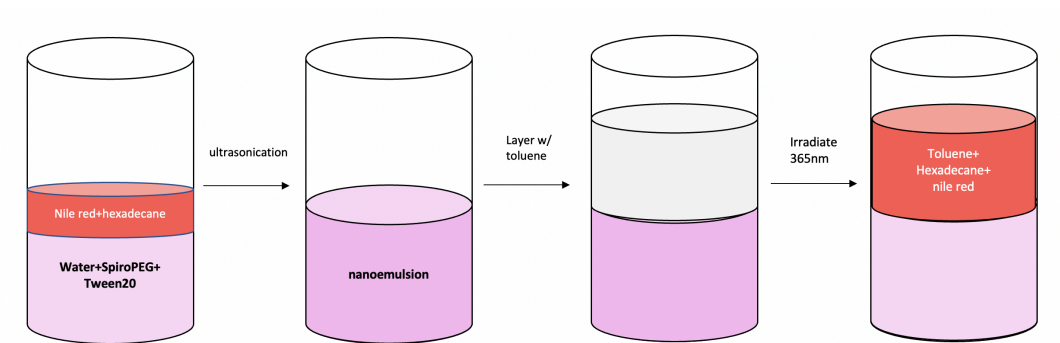

Figure 7.15. Cartoon depiction of the experimental procedure for forming nanoemulsions to test for light-induced breakage.

For the nanoemulsion experiments, the procedure for investigation is in accordance with both those reported by the Helgeson group and refined by us to create a stable nanoemulsion system with this specific surfactant. Of interest is an oil in water nanoemulsion, where the co-surfactant initially resides in the water phase. As such I selected an inner oil phase of hexadecane in which the SP-DA-PEG is not soluble. To the hexadecane, Nile red was added to be able to detect its release using visual analytical techniques. In the water phase, 1mM SP-DA-PEG was used in conjunction with 10mM Tween 20 as the stabilizing co-surfactant. The samples were ultrasonicated in an ice bath to control for temperature after which the nanoemulsions were measured to be roughly 200nm. To these nanoemulsion solutions, a toluene layer was then added such that we could test for phase separation after irradiation; the hexadecane containing Nile red would be expected to separate into the organic phase, and the concentration could be determined. The samples were irradiated for 10 minutes, and the toluene layer was then collected for UV-vis measurements. After constructing a calibration curve of Nile red in toluene, we used the UV-vis measurements to determine how much of the encapsulated oil was released from the irradiation and nanoemulsion breakage.
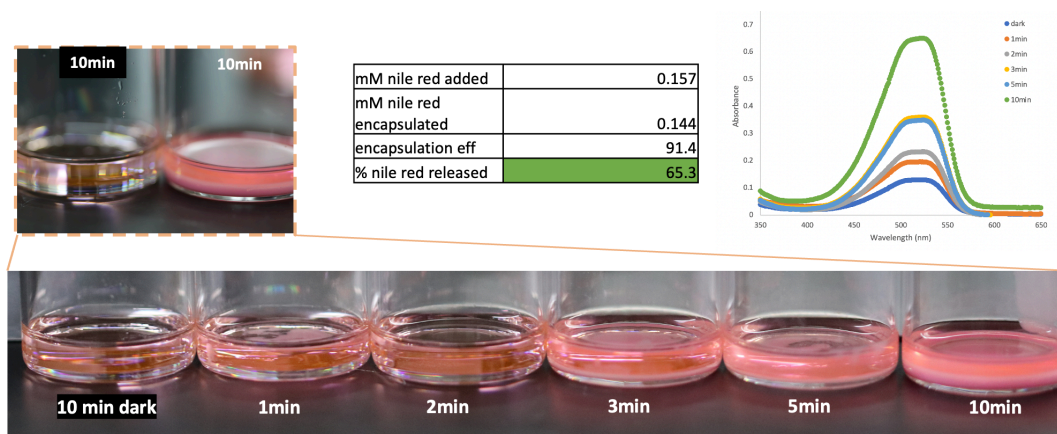
mM nile red added	0.157
mM nile red encapsulated	0.144
encapsulation eff	91.4
% nile red released	65.3

Figure 7.16 Experimental results showing the toluene layer after up to 10 minutes of irradiation compared with 10 minutes in the dark. With increasing time, there is an increasing amount of Nile Red phased into the toluene layer from the hexadecane inner phase. The UV vis data shows quantitatively the amount of Nile Red released and calculations based on the calibration curve indicate about 65% is released after 10 min of irradiation.

We find from these experiments that after 10 minutes of exposure to 365nm light, we can release 65% of the encapsulated oil. While this is promising, we have not been able to optimize the nanoemulsion composition such that the results are consistent with each emulsification attempt to get reproducible results. This results from the heating occurring during the ultrasonication, the uncertainty regarding how much of each co-surfactant is required as well as the penetration depth of irradiation. One presiding challenge is that we are not able to determine experimentally what is occurring at the interface; we are not certain about whether the photosurfactant is initially in the bulk or at the interface and, therefore, cannot accurately determine what happens to it after irradiation. As a result, we also have challenges in determining how much of the photo-surfactant should be used to drive the desired changes. From section 6.1.1 we see how the co-surfactant effects play a

significant role in the switching behavior and so a charged co-surfactant such as SDBS presents a possible alternative co-surfactant. In our first attempts of using SDBS under the same conditions we find that it was not possible to make a stable nanoemulsion. In these instances, the droplet size is always large and that the internal phase is never fully encapsulated. We are confident that further work can be done to perfect the composition needed to create an SDBS/SP-DA-PEG nanoemulsion that would allow for the co-surfactant effects to be explored. Additionally, better and more consistent modes of characterization are also required.

Preliminary experiments also suggest that salt (NaCl) has a releasing effect on nanoemulsions containing SP-DA-PEG even in the absence of light. It is possible that the salt functions similarly to the SDBS but further investigations need to be conducted regarding the effect of other additives on the multiple stimuli-responsive SP-DA-PEG emulsion systems. With the new knowledge and advances in our understanding of the co-surfactant effects, it is possible to optimize nanoemulsion breakage for desired applications.

7.2 Specific programming of fluid flow using high absorbing photoswitches

The reversible conversion of spiropyran to merocyanine is driven by two wavelengths of light. In organic solvents such as toluene, the SP->MC conversion occurs with UV light (lambda max:365nm) while the reverse reaction of SP->MC is driven by visible light (lambda max: 530nm). The response to multiple, discrete wavelengths of light allows for opportunities to have more precise control over fluid motion. In previous studies of

photothermal driven fluid flow using DASA, we control the bleaching front through factors such as concentration and light intensity. Using the spiropyran molecule, we can control the bleaching front by using dual wavelengths of light; this allows us to program a given boundary to set the convection speed for a given system and to stop or start the motion under constant illumination.
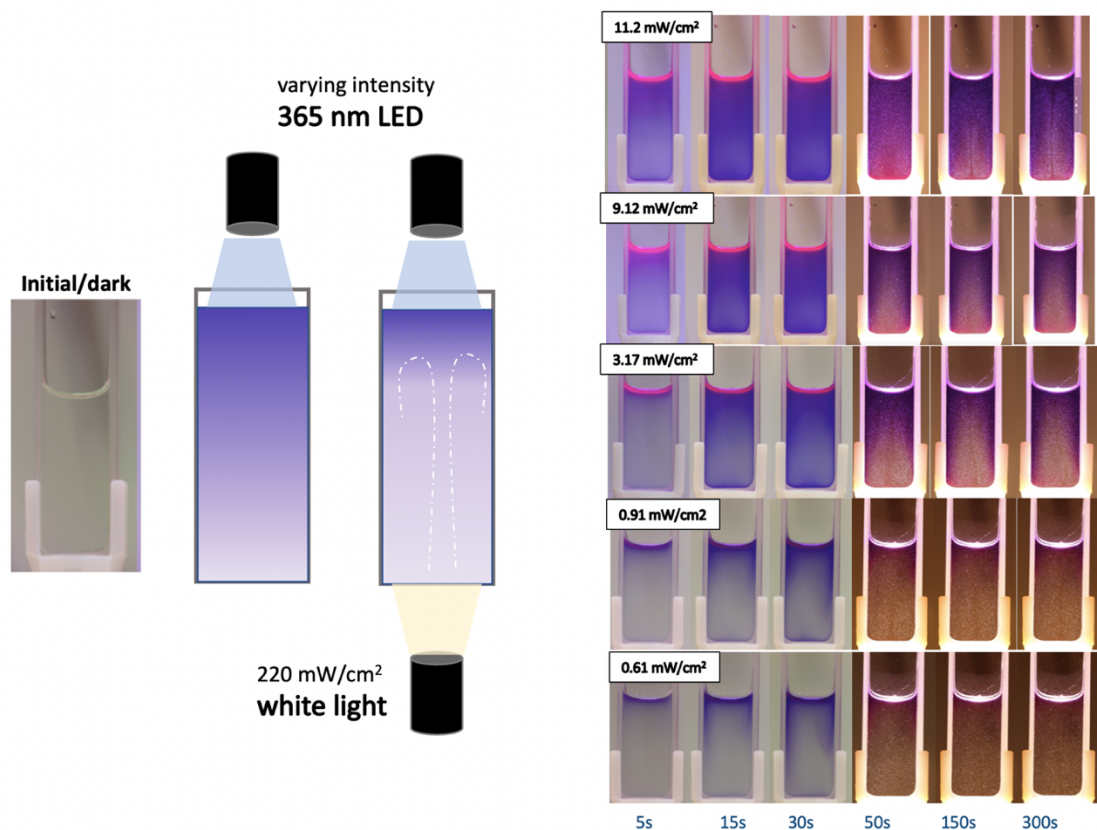

Figure 7.17 cartoon schematic showing the experimental setup. (right) different light intensities of UV irradiation from above with the white light turned on after 30 seconds.

In the experiments shown in Figure 7, 365nm light is initially supplied from the top of a cuvette to convert the initially clear SP solution the purple MC form. After the solution has been irradiated using different intensities of UV light for 30 seconds, the white light is

supplied from the bottom in order to drive the Rayleigh-Bénard convection similarly observed for DASA molecules. The two lights can be used to establish a location for the flow as the absorbing region is programmed by the intensity of the UV light and the initial conversion. Here, the UV light can pre-program a specific path of flow in the solution. This opens a future for studies in microfluidics and fluid pumping and mixing to enable flow in very specific locations using light.
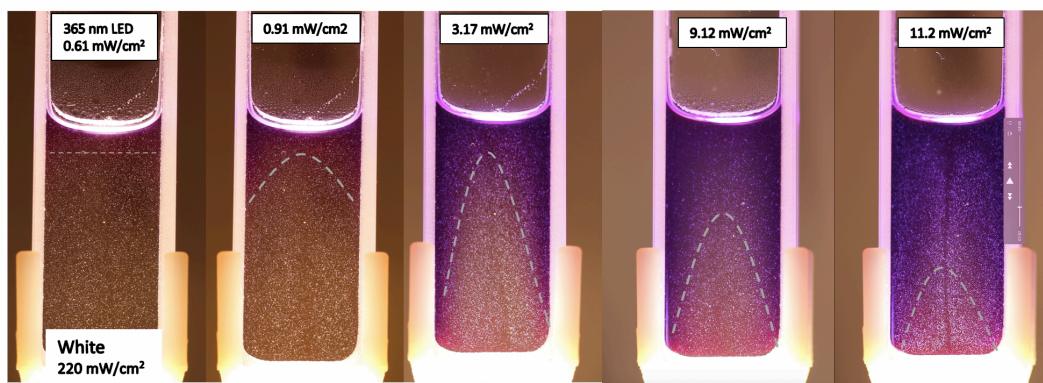

Figure 7.18 Visuals captured after 1 minute of irradiation with both wavelengths to compare the different boundaries set by using the dual wavelengths of varying intensity and different locations of flow.

This can also be accomplished in DASA solutions using additves. Here we expand on the work done in Chapter 6, using additives to alter the switching kinetics of DASA combined with our knowledge and ability to generate fluid flows. In Figure 9 a boundary is established between the switched and unswitched DASA as a result of an additive (HFIP) of differing density being added subsequently to an irradiated solution of DASA in toluene. In this instance, the HFIP drives the clear, closed DASA back to the colored, open form such that only in the top half of the cuvette is the high absorbing DASA present. When the white light is supplied from below, we observe rapid flow behavior localized in this region.

Significant exploration can be done to understand and optimize the layering by relating the density of the addition to the diffusion and heat transfer. Using just additives with variable density we can explore how the flow behavior can be programmed to a clearly defined, specific region within a more complex system for mixing, fluid pumping or reaction processes.
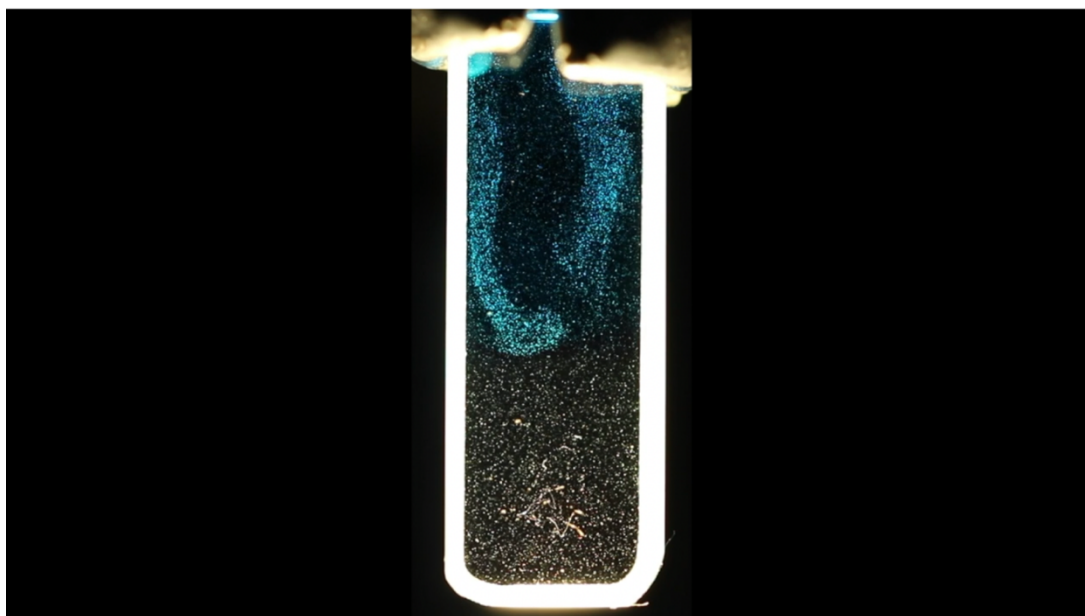

Figure 6.19. Flow observed in the upper half of a cuvette in which white light is irradiating from below and HFIP converts only the top half of the unmixed solution to the open, highly absorbing DASA form. Video on youtube: https://youtu.be/vnbsaBfa4PM.

7.3 Soft muscle development

Based on the photothermal studies shown in Chapters 4 and 5, future work looks to take advantage of the relationship between the engineering and photochemistry to develop

photothermal actuating systems. As shown, the high molar absorptivity of DASA leads to light-induced heating that drives both fluid motion and phase change behavior. Much like a dye, DASA can be used to generate heat in fluid systems, however our understanding of the switching behavior of DASA allows for highly specific tunability for complex applications of this work. Preliminary proof of concept demonstrations have been done to show that DASA can rapidly heat to generate a phase change in dichloromethane, which is a solvent in which the DASA of interest does not switch. Here, DASA behaves as a high absorbing dye and enables rapid heating and lifting of a weight of up to 1 kg in an LDPE soft muscle pouch.
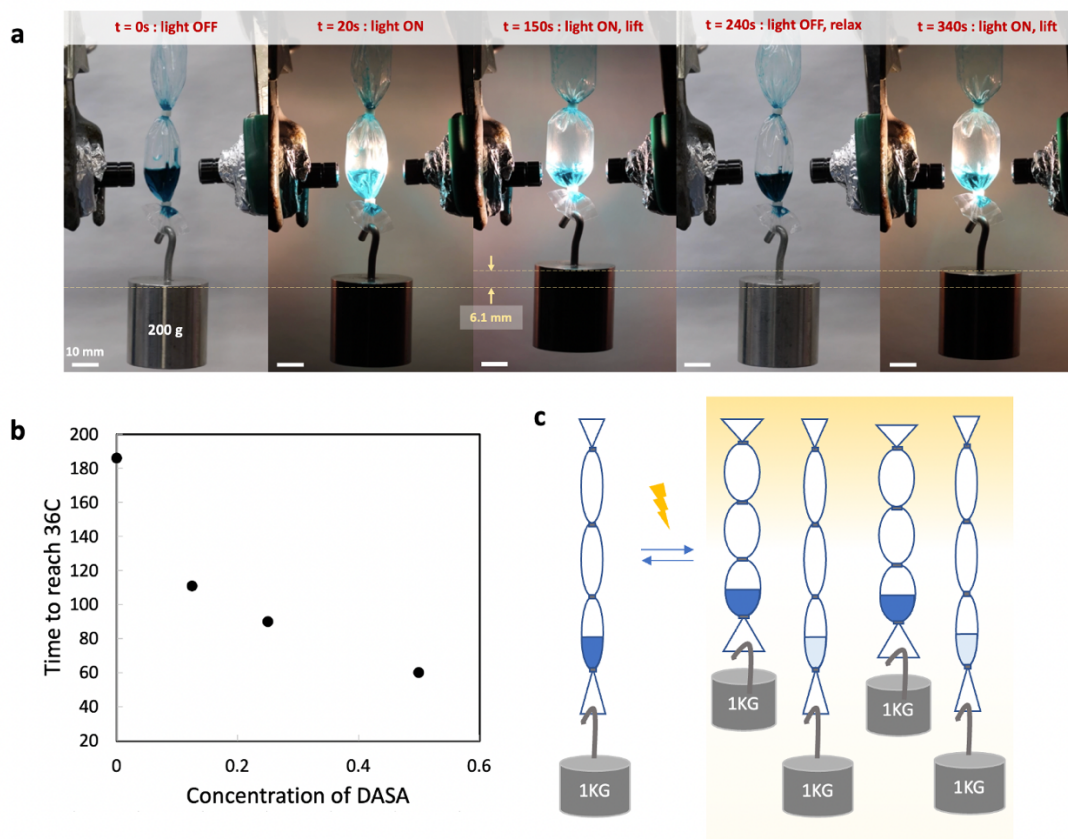
Figure 7.20 a) Soft muscle lifting of a 200g weight using 1mM DASA in dichloromethane. B) Heating data showing the amount of time it takes for a solution containing various concentrations of DASA to reach 36C in DCM under irradiation using white light. c) Proposed goals for oscillatory work under constant irradiation.

Future work aims to take advantage of the photochemistry in order to enable self-regulatory actuation under constant irradiation. Using the thermal analysis performed in Chapter 5, new possibilities can be achieved in which the binary mixture and relative change in kinetics drives complex behaviors such that oscillation can be achieved. The potential to develop a system that can turn itself on and off under constant visible light irradiation opens the possibility to use the sun to do work in this way. Using small amount of material and

solvent as well as solar energy, the future for this work is an investment in conservation of resources to work toward an environmentally conscious future.

7.4 Concluding remarks

With this work I aim to move the fields of chemistry, chemical engineering, and mechanical engineering to think and incorporate tools from beyond the antiquated lines that separate each discipline and to look towards a future that puts accessibility at the forefront. To be truly impactful, research must be interdisciplinary not only in name but in action, and with that comes admittance of what we cannot do alone, acknowledgment of who paved the way and a re-evaluation of what counts as knowledge. I am grateful for the opportunities I have forged and have been provided that have allowed me to experience true collaboration within and beyond the lab. My research has been informed directly by the insights I gained from friends, advocacy work and the life experiences I have had. I believe that the future of photoswitchable fluid systems for actuation and mechanical work is promising, with ample space to grow and uncover curious paths beyond those articulated here. I hope that this dissertation has provided a port off which future scientists can jump to pursue anything that to them is interesting, whether it seems to be possible or not.